Resonance-based Electro-Optic Sensing: Innovative Techniques for Sensitivity and Bandwidth Enhancement in Minimally Invasive Vector Microwave Field Imaging

by

Dong-Joon Lee

A dissertation submitted in partial fulfillment
of the requirements for the degree of
Doctor of Philosophy
(Electrical Engineering)
in The University of Michigan
2009

Doctoral Committee:

Research Scientist John F. Whitaker, Co-chair
Professor Thedore B. Norris, Co-chair
Professor Herbert G. Winful
Associate Professor David A. Reis

To my family.....

ACKNOWLEDGEMENTS

First of all, I would like to thank my gracious advisor, Dr. John F. Whitaker for his continuous guidance and support throughout my graduate program at Michigan. It was a great pleasure to work with him and he is certainly a model advisor, truly deserving the greatest respect. I have enjoyed working with him, and deeply appreciate his contribution to this work. I am also grateful to my previous advisor Prof. Almantas Galvanauskas who opened the world of optics to me and guided me to the successful completion of the Ph.D qualification exam. I should appreciate Prof. Jeong-Jin Kang who never saved his contributions and fruitful discussions on microwave devices and analyses for prolific publications with him. I also thank Profs. Ted Norris, Herbert Winful in the department of Electrical Engineering, as well as Prof. David Reis in the department of Physics, for joining my dissertation committee and providing valuable feedback.

It has been a great experience to meet and become good friends with my many colleagues at the Center of Ultrafast and Optical Science (CUOS). I am very grateful to my dearest lab fellows, Dr. Bianca Jackson, Galen Chen, and senior fellow Dr. Kyoung Yang and Matthew Crites at Opteos inc. They showed unfailing willingness to help throughout all aspects of my graduate studies, including being my great personal English tutors. I also have good memories at my Korean friends. Especially, I would especially like to thank Sang-June for sharing the tough times as well as good, and Sang-Hyun, Myoung-Kyu, Tae-Il, Hyo-Il and Dong-Sook for their good friendship throughout my time in Ann Arbor. My acknowledgement would not be complete without mentioning the staff members of the CUOS and EECS department for their dedication and for their assistance over the past years.

Most importantly, I would like to express the deepest gratitude to my family. Their unconditional love and emotional support have been the greatest motivation for me

to keep progressing during these years. My special thanks to wife, Hee-Ju, my parents, parents-in-law, and my lovely daughters, Chae-Eun and Chae-Young to whom I dedicate this thesis with much love.

TABLE OF CONTENTS

CHAPTER

LIST OF TABLES

Table

LIST OF FIGURES

Figure

LIST OF APPENDICES

Appendix

ABSTRACT

The electro-optic sensing/sampling (EOS) technique has gained great attention over the last decade as a valuable diagnostic tool for high-speed circuits and microwave sensing/imaging due to unique features such as inherently low invasiveness, ultra-broad bandwidth, and high spatial and temporal resolution for the detection of vector microwave fields. Despite these beneficial aspects of EOS, there still remain challenges to be overcome in the existing methodology. The primary one is low sensitivity, originating from the inherently tiny figure of merit in EO materials. In addition, the invasiveness increases for higher frequency applications as the size of very fast electronic devices becomes comparable to that of the sensor probes. Furthermore, the conventional reflective mode of the EOS configuration also demands the arguably cumbersome polarization management and optical alignment associated with an expensive and delicate mode-locked pulsed laser.

This dissertation presents novel methods to address the various challenges of the unique features in the EOS systems. The sensitivity is enhanced by > 10 dB with Fabry-Perot resonance-based techniques, and this is accomplished with simplification of the optical implementation compared to the conventional methodology (chapters 2 and 3). For high frequency sensing of vector microwave fields, a novel electrical down-conversion technique is presented (chapter 4) and compared with the recently introduced and thus more conventional photonic technique (chapter 5). Both down-mixing techniques are optimized through the application of a new carrier suppression method, enhancing the signal-to-noise ratio up to 10 dB (chapter 6), and the merits and shortcomings of the two techniques are discussed (chapter 7). The results suggest employing the photonic down-conversion scheme for higher frequency sensing (*i.e*, the broader bandwidth). Another technique to expand the bandwidth, utilizing higher-order harmonics of the photonic local oscillator, is also presented. Up to three times the sensing bandwidth, using the second- or third-order harmonics can be readily achieved. Such expansion of the bandwidth is enough to cover even up to the millimeter-wave regime with additional carrier suppression to increase the signal-modulation depth (chapter 8). Finally, the least invasive fiber-based probe that has been envisioned to date, with greater accessibility to devices tested with millimeter-wave sensing, has been developed through miniaturization of the probe size (chapter 9). This dissertation demonstrates a number of innovative techniques that realize the most simple and efficient, minimally invasive, high frequency EO measurement system developed to date.

CHAPTER 1

INTRODUCTION

1.1 Foreword

In accordance with the dramatic success and explosive demand for wireless communication systems based on microwave technology, there have been rapid developments in high-speed, radio frequency engineering over the past few decades. This endlessly rising growth in the information and communication market is requiring even more rapid development of high-speed electrical engineering that will be needed to meet the global demands for wireless ubiquitous networks.

The wireless communication technology heavily relies on microwave circuits and antennas to implement sophisticated transmitter/receiver systems. The systems have evolved into compact and miniaturized modules by virtue of the monolithic microwave integrated circuits (MMIC) technology. The functional bandwidth of MMIC has been extended to the millimeter wave regime to utilize the technically challenging higher frequency bands to accommodate growing communication channels.

In the design and analysis of microwave devices, it is often desirable, if not necessary, to have detailed information on the characteristics and potential effects of the local electromagnetic radiation. While the far-field pattern is of primary concern, as the distance from the antenna to the observer is typically much greater than the largest dimension of the transmitting antenna, in the near-field region measurements are still useful in testing for electromagnetic compatibility and interference (EMC/EMI), measuring specific absorption rate, creating far-field patterns from a compact range environment, and diagnosing failures in microwave integrated circuits [1-3].

For compact higher frequency applications, microwave and millimeter wave circuits and antennas (as well as arrays of their antennas) are becoming faster and more complicated, thus accurate measurement methods have become increasingly important. Near-field electrical measurement and diagnostic techniques have served as powerful tools in the design and analysis of high frequency antennas or circuits where complete field-pattern and polarization characterizations would be beneficial. Near-field information from guided-wave or radiating devices has the potential to provide the actual detailed electromagnetic field distributions that conventional scattering-parameter measurements, using a vector network analyzer and on-wafer probing, [4] cannot.

Although existing microwave near-field scanners have been used for such measurements, their results are typically limited because they are not able to operate non-intrusively in the reactive near-field region of a device-under-test. Furthermore, microwave scanning systems generally must be accompanied by associated numerical post-processing methods to enable a conversion of the measured quantity into the electromagnetic field [5]. This requires computing the relative spatial localization of the electric charges and current surface densities directly from the mapped pattern of the probe signals. Ideally, measurements could be made at circuit internal nodes or in the reactive near field at the interior of an antenna, and not via either port-based connections or metallic probes that must be positioned a number of wavelengths from an antenna.

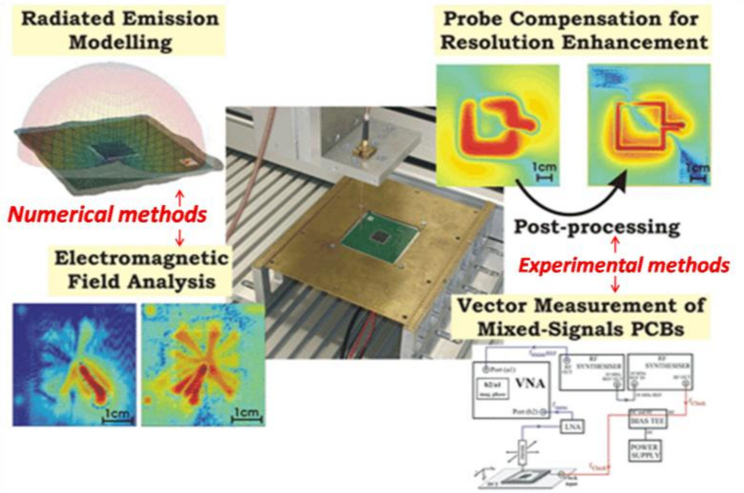

Figure 1.1: Current non-photonic methods for near-field measurement (Left: numerical methods), (Center: photograph of an electromagnetic near-field scanner), (Right: an experimental near-field scanning system) [from: www.izm.fraunhofer.de].

To address these issues, significantly less invasive, direct-sensing methods that use photonic-assisted near-field-probes and nonlinear-optical techniques have been proposed and implemented [6-8]. As the most popular of these methods, electro-optic sensing (EOS) exhibits a large measurement frequency range, low intrusiveness, and high spatial resolution [9]. Using probes fabricated purely from dielectric materials and interrogated by optical beams allows for non-contact, non-destructive, and high-impedance – yet high-frequency – probing to be performed at internal nodes of microwave integrated circuits and even within the reactive near fields of antennas and arrays. Thus, the full amplitude and phase information of individual unit cell or its arrays can be used for detailed characterization of the device performance.

1.2 Brief principle of EO sensing

Electro-optic sensing (or sampling) (EOS) has become a standard technique for the near field measurement of electronic devices because of its large bandwidth and low invasiveness, as well as its fine temporal and spatial resolution. The sensing relies on the electro-optic effect associated with the sensor crystals, which have variable refractive indices in response to the applied electric fields. The tiny modified indices, due to the fields, perturb the original transmissions, so that the amount of modulation indicates the strength of the fields.

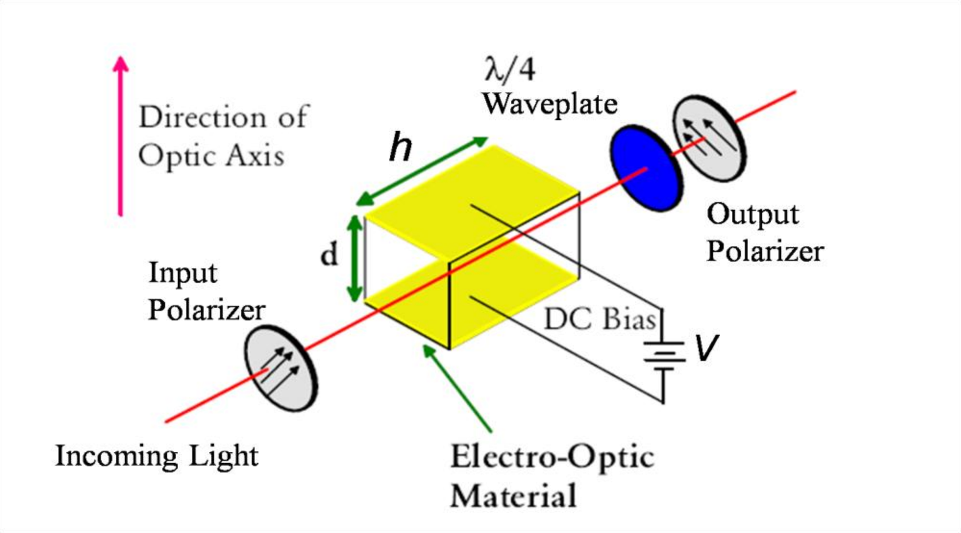

Figure 1.2: Transverse electro-optic modulator [from Ref.10].

Electro-optic modulation and sensing (EOM/EOS) are a combined utilization of laser technology and the Pockels effect. With this effect, a small change in the refractive index properties of a material will be caused by the application of an external electric field to it. This change is linearly proportional to the strength of the applied field. A light beam propagating through a length, *h*, of an electro-optic material will undergo a phase retardation. If such a material were to be placed in-between a pair of crossed polarizers, as in Fig. 1.2, the linear electro-optic effect is seen as a modulation of the light intensity passing through the system.

$$\delta_{eo} = \frac{\pi}{\lambda}\left(n_e^{\,3} r_{33} - n_o^{\,3} r_{13}\right) V \frac{h}{d} \qquad (1.1)$$

The voltage induced additional phase retardation, δ_{eo}, for a transverse x-cut $LiTaO_3$ electro-optic modulator is described in Eq. 1.1, where λ is the wavelength of the optical beam, n_e and n_o are the extraordinary and ordinary refractive indices respectively, r_{33} and r_{13} are the appropriate electro-optic coefficients, V is the applied voltage across a distance d, and h is the interaction length. (A detailed theoretical review is to be presented in chapter 2.) The observed intensity modulation is in Eq. 1.2.

$$I_0 = I_i \sin^2\left(\frac{\delta_{eo}}{2}\right) \qquad (1.2)$$

The applied voltage, *V*, can be DC or sinusoidal (time-varying) in nature. While commercial electro-optic modulators operate in the GHz regime, modulators operating at THz frequencies have been demonstrated [11]. The maximum modulation frequency is determined by the resonance and electro-optic properties of the electro-optic material, the physical design of the modulator, and the parameters describing the laser beam.

With electro-optic modulators, a known intense electric field is applied across the material to result in the desired modulation of the optical laser light. Electro-optic sampling or sensors effectively reverse the process, resulting in a transducer-like arrangement. An electro-optic material is placed near the device-under-test (DUT) that is radiating electromagnetic fringe fields. When a laser beam passes through the material, the fringe fields modulate the beam. If the DUT and electro-optic material, the probe, are placed between crossed polarizers, this modulation is seen as a change in the point to distinguish between two types of electro-optic materials; transverse and longitudinal [12]. In transverse (x-cut) material, as shown in Fig. 1.2, the optimal alignment for the electro-optic modulation is when the direction of the electric field is normal to the propagation of the optical beam. With longitudinal (z-cut) materials, the electric field is parallel to the propagation of the optical beam, placing a pair of transparent electrodes onto the two material interfaces that the light passes. Thus, a transverse material, such as x-cut $LiTaO_3$ or GaAs (110), would be used to detect the horizontal component of the DUT's electric fringe field, while a longitudinal material, such as BSO or a different orientation of GaAs (100), would be sensitive to the normal component. In both cases, the electric field of interest is parallel to the optical axis of the crystal. With the proper choice of probe orientation and optical input polarization, EOS measurements can properly distinguish between two orthogonal electric field components, a measurement characteristic known as cross-polarization suppression capability [13-17]. This type of EOS is known as the non-contact external EOS. A comprehensive summary of the various types of electro-optic sampling is located in the later chapters of this thesis.

1.3 EO sensing with Harmonic-Down-Mixing in a pulse-modulated laser

One very successful method for high-speed EO sensing is the harmonic-mixing technique, which utilizes higher-order harmonics of the repetition rate in a pulsed laser [1,2,9]. For instance, a train of ultrafast laser pulses with carrier frequency f_c (or λ_c in wavelength) is basically a convolution of a single pulse and a sampling function, which is evenly spaced by the inverse of repetition rate. The frequency view of the pulse train is a multiplication of each Fourier spectrum pair of the respective single pulse and the sampling function as illustrated in Fig. 1.3 Usually, the repetition rate is very fine by several orders, compared to the spectral bandwidth of a laser pulse. For example, in our previous lab work, the pulse width was ~100 fs and the corresponding bandwidth was 10 nm at 900 nm wavelength (=333.33 THz) [1,2,9]. The replica pulses were repeated precisely every 80 MHz. Fortunately, phase-locked loop (PLL) technology exists that allows the repetition rate of the laser to be synchronized with a 80 MHz reference source, as is done with the Spectra Physics Lock-to-Clock system that is available with their Tsunami Ti:Sapphire ultrafast laser system. This phase-lock is accomplished through the addition of a servo motor and piezoelectric actuator on a mirror in the laser cavity. The PLL electronics constantly adjusts the length of the laser cavity to keep the repetition rate well stabilized at f_0 = 80 MHz.

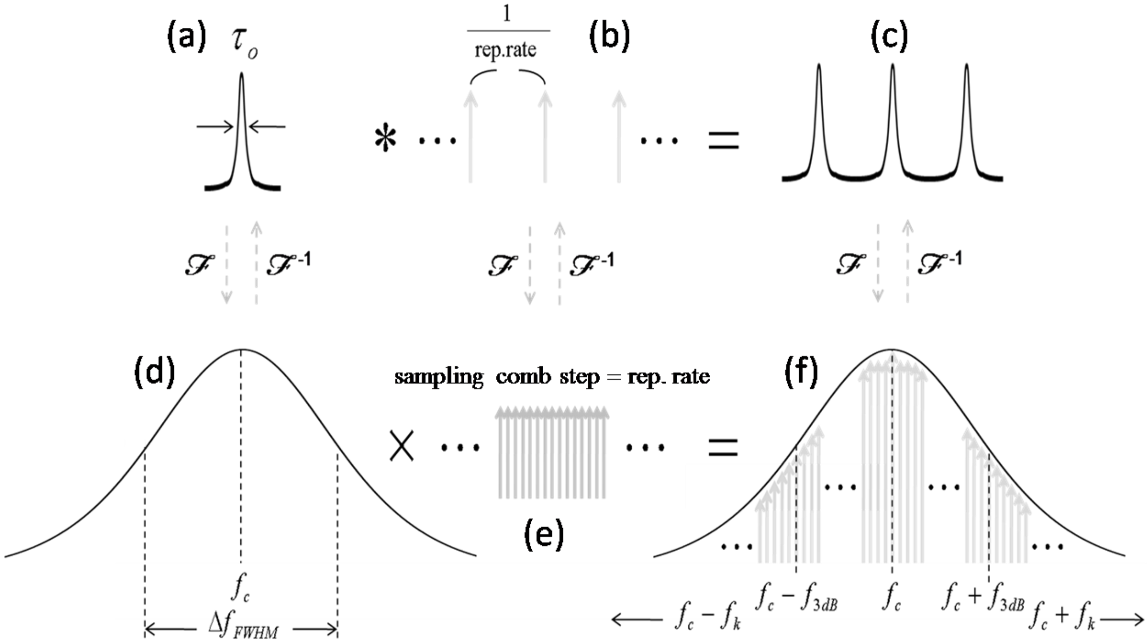

Figure 1.3: Origin of higher–order harmonics in pulsed trains. (a) single-shot pulse (b) sampling trains (c) pulsed trains (d)~(f) frequency spectrum of (a)~(c) (τ_o: pulse width, f_c: carrier frequency, Δf: 3dB bandwidth).

This fine 80 MHz of spectral comb is filled under the entire spectrum as shown Fig. 1.3 (f). The 3 dB bandwidth frequency f_{3dB} covers a frequency range out past the 23140th harmonic thus providing a 3 dB measurement bandwidth up to 1.852 THz. Our lab had reported the field distribution of a ~4 GHz patch antenna using the 50th harmonic components [2]. The antenna was driven with a 4.003 GHz cw input to yield a 3 MHz IF signal component. Since the 50th harmonic is only 0.22 % of the bandwidth, the adjacent harmonics are considered virtually flat in such a narrow band. Furthermore, since many of the electro-optic sensors cover beyond the T-Hz bandwidth [18], such ultrafast pulsed lasers enable measurement up to the bandwidth determined by the pulse width and laser wavelength.

Harmonic-mixing is basically a synchronous sampling, where the DUT is driven by a radio-frequency (RF) or microwave CW-wave synthesizer. This technique works when the DUT's synthesizer can be precisely phase-locked to the repetition frequency of the laser.

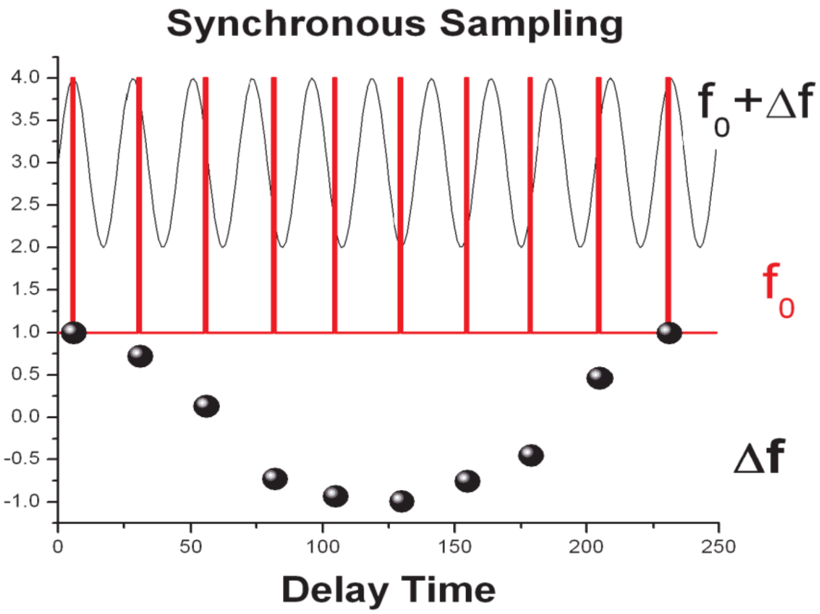

Figure 1.4: Synchronous Sampling via Harmonic Mixing. The RF synthesizer is set at frequency equal to an integer multiple of the laser repetition frequency plus an offset. The probe pulse at frequency, f_0, scans through the RF signal at the beat frequency yielding the sampled signal. [from Ref.10] (The spectral spacing of the sampling comb is drawn exaggerated for convenience).

Once the synthesizer is phase-locked with the laser repetition rate, the frequency of the synthesizer, RF, is set at an integer multiple, *N*, of the laser repetition frequency plus an offset, Δf, such that

$$RF = (N \times f_0) + \Delta f \qquad (3)$$

This synchronous sampling via the harmonic mixing scheme is depicted in Fig. 1.4. The probe pulse at frequency, f_0, scans through the RF signal at the beat frequency, Δf, yielding the sampled signal. When harmonic mixing is utilized, the measurement bandwidth is a function of the bandwidth of the optical probe pulse, optical pulse jitter, and the interaction time between the optical pulse and the RF signal [19].

Placing the DUT (or even a sensor probe) on a two-dimensional raster scanning stage, accumulated data set from each raster-scanned position can reconstruct the image of the measured electric fields. This type of external EOS is known as EO field mapping. The EO probe, with a high-reflective coating on it so as to keep the optics independent of the DUT, is lowered into the fringe fields emanated from the DUT. The relative amplitude and phase of the fringing electric field is measured at a series of data points while scanning. In this manner, a map of the relative changes in the amplitude of the electric field from the DUT can be produced. The same can be done with the phase. The spatial resolution is largely determined by the spot size of the focused probe beam, which is typically less than 10 μm [14]. In addition, the distance between the EO probe and the DUT can be varied from scan to scan, yielding even more information about the performance of the DUT. If one chooses probe crystals with the proper axis orientations, the relative amplitude and phase of all three orthogonal electric field components of the DUT can be mapped out via raster-scanning of the device. Field mapping of microwave waveguides, patch antennas, and horn antennas has been demonstrated [13,14,20]. EO-field mapping provides a valuable method of device characterization, especially for mm-wave integrated circuits and radiating structures.

1.4 Fiber-Based Electro-Optic Field Mapping

In order to ease optical alignment of EOS systems, to enhance positioning ability, and increase measurement flexibility of external EOS, a fiber-based EOS system was developed by Yang [21]. Laser light, after passing through a polarizing beam-splitter, is coupled into a single mode optical fiber as in Fig. 1.5.

In order to manipulate the polarization of the beam while in the fiber, the fiber is wound into two sets of loops, with one set corresponding to a half-waveplate and the other to a quarter-waveplate. The polarization is manipulated by adjusting the tension of the fiber in each set of loops. The cleaved output end of the optical fiber is glued with UV-curable epoxy to a gradient-index (GRIN) lens. The EO probe is attached to the opposite end of the GRIN lens. The purpose of the GRIN lens is to focus the optical beam onto the surface of the probe. Prior to this thesis work, micro-machined GaAs was used as the probe material. (110)-oriented GaAs was used for measurements of tangential fields, while (100)-oriented GaAs was used with normal fields (Fig. 1.5). A high-reflection (HR) layer was deposited on the bottom surface of the probe to reflect the optical beam back. The return beam travels back through the optical fiber and is reflected at the polarization-dependent beam splitter into the detection apparatus. The fiber-based EOS system provides increased positioning ability and measurement flexibility.

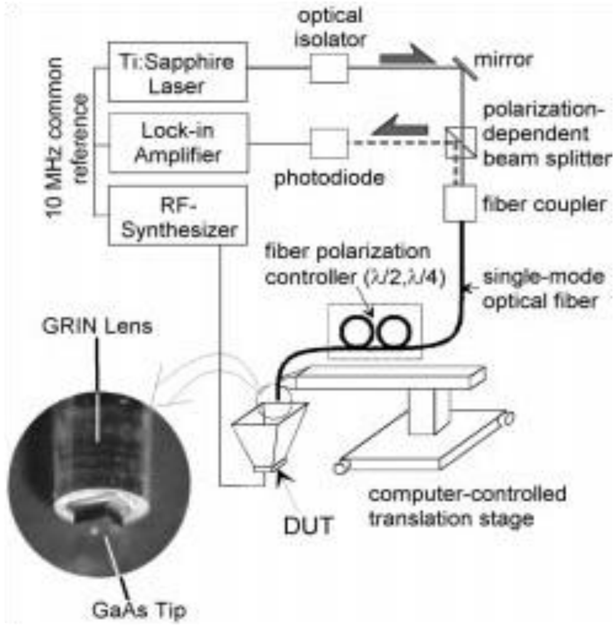

Figure 1.5: Fiber-Based Electro-Optic Sampling System. The GaAs tip (100 or 110) with an HR layer at its bottom surface is mounted beneath a GRIN lens. [from Ref.21]

1.5 Scope and outline of this thesis

This dissertation consists of 10 chapters, and numerous novel methods for improving various aspects of the unique features of EOS systems are covered throughout the chapters. Chapter 1 introduced a motivation and brief description of EOS systems. The combined utilization of an ultrafast laser and Pockels effect yields a successful EOS system through the Harmonic-mixing technique. A brief review of this technique and current limitations were introduced.

Chapter 2 presents a method to apply the intrinsic resonator characteristics of an EO crystal (as a Fabry-Perot etalon) to the EOS applications [23,24]. The etalon or resonator, built on a sensor wafer, also possesses an intrinsic amplitude modulation slope obviating the need for conventional polarization components. The amplitude modulation slope can be significantly increased by building highly reflective layers on both surfaces of a resonator. This resonance-based scheme is especially advantageous for a fiber-based reflective mode of sensing, due to the noise reduction advantage to be discussed in chapter 3 [24]. For both transmissive and reflective configurations, experimental verification with 3 MHz of low frequency micro-strip fringing fields is followed.

Higher frequency sensing, inevitably requires expensive pulsed optical sources to achieve broad sensing bandwidth when down-mixing techniques are used. Chapter 4 presents a novel down-mixing method which does not require optical modulation as a beating source for down-mixing [25,26]. The optical local oscillator (LO) beating source is replaced with a cost-effective electrical source using another frequency synthesizer. Thus, the electrically demodulated RF signal from the fast photodetector is down-converted with the electrical LO component by the square-law of the electrical diode mixer.

Chapter 5 presents another down-mixing technique which does not rely on pulsed lasers. The optical heterodyne mixing technique is another solution for higher frequency sensing, replacing an expensive pulse-based optical beating source with a cost-effective conventional electro-optic modulator for LO light modulation, which is a proven replacement for the electrical LO source [27,28]. Using this down-mixing technique, the resonance-based EO sensing enhancement technique and probe sensor are applied to field mapping of high speed devices. The marriage of this probe and the heterodyne mixing technique enables broadband sampling with high sensitivity.

Chapter 6 presents the performance of a resonance-based down-mixing system, which can be optimized by suppressing the optical carrier more than the signal modulation components [29]. Since the resonance-based sensor probe has heavy spectral dependency on tuning laser wavelengths, the investigation of field mapping evolution as a function of various wavelengths offers optimal spectral bias wavelength. A practical modeling for the optimal bias computation is discussed and the spectral bias optimizations for both the electro-optic modulator and resonator-sensor are presented, respectively.

With carrier-suppressed optimization conditions, the two down-mixing techniques are compared and their merits and shortcomings are discussed in chapter 7 [28]. The results suggest employing the photonic (or electrical) down-conversion scheme for higher (or lower) frequency sensing.

Chapter 8 presents novel techniques to significantly enhance the bandwidth of the Heterodyne mixing technique [30]. The bandwidth is fundamentally determined by the speed-limit of an electro-optic modulator, which generates the optical LO components. This criteria and use are valid in fiber optical communication (*i.e.*, the Radio over Fiber system) where higher-order signal distortion is a big concern in the sense of linear data transmission. However, in the case of EO sensing, the higher-order harmonic components are not detrimental, but rather beneficial, for enhancing the bandwidth, since the LO components only contribute to down-converting the RF signal information without nonlinearity-based signal distortion or invasiveness.

Chapter 9 presents a method to minimize the invasiveness of the sensor probe [31]. Low invasiveness is one of the distinguishing features of the EOS. Avoiding any metallic components in the sensor, such all dielectric nature of the EO material and probe structure is an origin of significantly less invasiveness in near field detection. However, for smaller sized devices with certain resonant frequencies, such as millimeter wave antennas, the conventional size and volume of the sensor probe have enough capacitance to shift the desired characteristics of the original devices. Such crucial fact of invasiveness is investigated comparing with a conventional probe and the improved field images measured with the novel micro-structure probe.

Finally, chapter 10 finishes the thesis by providing the conclusions drawn from the previous chapters and proposals for future work.

CHAPTER 2

RESONANCE-BASED ENHANCEMENT OF ELECTRO-OPTIC SENSITIVITY AND SYSTEM SIMPLIFICATION

2.1 Introduction

In this chapter, an analytical model for enhancing the electro-optic (EO) effect and sensitivity based on resonance advantage is presented. The principles of EO phase retardation are introduced first, and the concept of resonance-based EO phase enhancement over the non-resonance-enhanced case is followed. A theoretical model simulating a Fabry-Perot-based, Pockels-effect probe demonstrates that both the electro-optic phase retardation and modulation-efficiency slope of the optical system can be resonantly enhanced. Consequently, it predicts that electric-field measurements are possible using a configuration that eliminates the polarizer, analyzer, and quarter-wave retarder of typical electro-optic intensity modulators. A simplified electro-optic-sensing system that employs a wavelength-tunable laser diode and an electro-optic-crystal micro-cavity is experimentally demonstrated. An experimental verification of the concept is presented in a transmissive configuration using thin, uncoated, $LiTaO_3$ crystals, and an electro-optic modulation signal that is ~60 dB above the system noise floor is obtained.

2.2 Principles of Electro-Optic Phase Retardation

As illustrated in Fig. 2.1, for an EO crystal with given thickness h, the total round trip phase shift $\delta(\lambda,E)$, as a function of wavelength and electric field, is expressed in Eq. 2.1.

$$\delta(\lambda,E)=\frac{4\pi hn(E)}{\lambda} \qquad (2.1)$$

where $n(E)$ is an intrinsic refractive index n_0 with an electric-field-dependant, small dynamic refractive index change $\Delta n(E)$. It is assumed that the dispersion $n(\lambda)$ is negligible for the relatively narrow tuning band $\Delta\lambda$. Hence, the total phase shift can be re-expressed in Eq. 2.2 with the static and dynamic term.

$$\delta(\lambda,E)=\delta_0(\lambda)+\delta_{eo}(\lambda,E) \qquad (2.2)$$

where $$\delta_0(\lambda)=\frac{4\pi hn_0}{\lambda}$$ and $$\delta_{eo}(\lambda,E)=\frac{4\pi h\Delta n(E)}{\lambda}$$

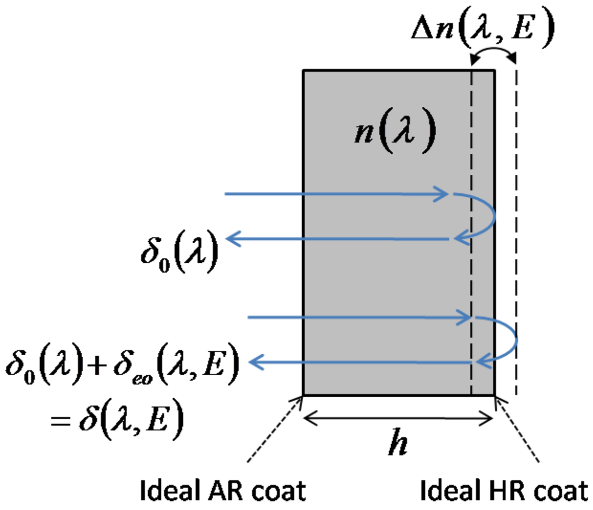

Figure 2.1: Illustration of the round-trip phase delay associated with an EO material.

The majority of the phase shift is $\delta_0(\lambda)$. The amount of transmission is mainly determined by $\delta_0(\lambda)$ and fixed at a particular wavelength. The dynamic phase shift, which is typically much smaller than the static phase shift $\delta_0(\lambda)$, is determined by $\Delta n(E)$. The amount of dynamic phase shift $\delta_{eo}(\lambda,E)$ is heavily affected by the physical properties of

EO crystals as well as the vector electric field *E*. The propagation of optical radiation in a crystal can be described completely in terms of the impermeability tensor η_{ij} ($= \epsilon_0 \epsilon_{ij}^{-1}$). The two directions of polarization, as well as the corresponding indices of refraction (*i.e.*, velocity of propagation) of the normal mode, are found most easily by using the index ellipsoid, as shown in Fig. 2.2.

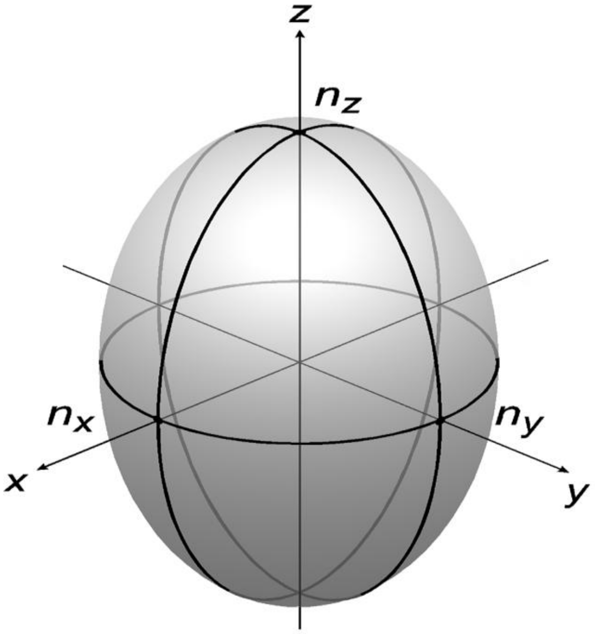

Figure 2.2: Index ellipsoid of a positive uniaxial crystal ($n_x = n_y < n_z$, such as the $LiTaO_3$ that is widely used in this thesis).

The index ellipsoid assumes its simplest form in the principal coordinate system as Eq. 2.3.

$$\frac{x}{n^2{}_x} + \frac{y}{n^2{}_y} + \frac{z}{n^2{}_z} = 1 \qquad (2.3)$$

where the directions *x*, *y*, and *z* are the principal axes - that is, the directions in the crystal along which **D** and **E** are parallel. $1/n^2{}_x, 1/n^2{}_y$ and $1/n^2{}_z$ are the principal values of the impermeability tensor η_{ij}.

According to the quantum theory of solids, the optical dielectric impermeability tensor depends on the distribution of charges in the crystal. The application of an electric field will result in a redistribution of the bond charges and possibly a slight deformation of the ion lattice. The net result is a change in the optical impermeability tensor. This is known as the electro-optic effect. The electro-optic coefficients are defined traditionally as

$$\eta_{ij}(E) - \eta_{ij}(0) \equiv \Delta\eta_{ij} = r_{ijk}E_k \qquad (2.4)$$

where E is the applied electric field. The constant r_{ijk} is the linear (or Pockels) electro-optic coefficient.

From Eqs. 2.3 and 2.4, a generalized expression of the index ellipsoid in a crystal in the presence of an electric field can be obtained as

$$\sum_{i,j} \eta_{ij}(E)x_i x_j = 1 \qquad (2.5)$$

where i,j = 1,2,3. Thus, Eq. 2.5 can be rewritten as

$$\begin{aligned} &\eta_{11}(E)x_1x_1 + \eta_{12}(E)x_1x_2 + \eta_{13}(E)x_1x_3 + \\ &\eta_{21}(E)x_2x_1 + \eta_{22}(E)x_2x_2 + \eta_{23}(E)x_2x_3 + \\ &\eta_{31}(E)x_3x_1 + \eta_{32}(E)x_3x_2 + \eta_{33}(E)x_3x_3 = 1 \end{aligned} \qquad (2.6)$$

where x_1, x_2, and x_3 are identical to the principal axes of the crystal.

By using the permutation symmetries (the detailed explanation can be found in chapter 7 of Ref. 32.), the number of independent elements of r_{ijk} reduces from 27 (3×3×3) to 18 (6×3). Thus the equation of the index ellipsoid in the presence of an electric field can be written

$$\begin{aligned} &\left(\frac{1}{n^2{}_x} + r_{1k}E_k\right)x^2 + \left(\frac{1}{n^2{}_y} + r_{2k}E_k\right)y^2 + \left(\frac{1}{n^2{}_z} + r_{3k}E_k\right)z^2 \\ &+ 2yzr_{4k}E_k + 2zxr_{5k}E_k + 2xyr_{6k}E_k = 1 \end{aligned} \qquad (2.7)$$

where E_k (k = 1,2,3) is a component of the applied electric field and summation over repeated indices k is assumed. Here, 1,2,3 correspond to the principal dielectric axes x, y, z, and n_x, n_y, n_z are the principal refractive indices. This new ellipsoid (Eq.2.7) reduces to the unperturbed ellipsoid (Eq.2.3) when $E_k = 0$. In general, the principal axes of the ellipsoid (Eq.2.7) do not coincide with the unperturbed axes (x, y, z).

The electro-optic tensor r_{ij} (now 6×3) heavily depends on the symmetry class of the crystal. Thus, a choice of an EO crystal gives the unique value of r_{ij}, and this specifies the Eq.2.7. For instance, a $LiTaO_3$ crystal has a crystal symmetry of $3m$. The electro-optic coefficients are in the form of Eq. 2.8.

$$r_{ij}\left(LiTaO_3\right)=\begin{pmatrix} 0 & -r_{22} & r_{13} \\ 0 & r_{22} & r_{13} \\ 0 & 0 & r_{33} \\ 0 & r_{51} & 0 \\ r_{51} & 0 & 0 \\ -r_{22} & 0 & 0 \end{pmatrix} \qquad (2.8)$$

As the electric field is along the optical axis of the crystal, the equation of the index ellipsoid can be written, according to Eq. 2.7, as Eq. 2.9 [32].

$$\left(\frac{1}{n_o^2}+r_{13}E\right)x^2+\left(\frac{1}{n_o^2}+r_{13}E\right)y^2+\left(\frac{1}{n_e^2}+r_{33}E\right)z^2=1 \qquad (2.9)$$

Since $LiTaO_3$ is a uniaxial crystal, $n_x = n_y = n_o$ and $n_z = n_e$. If it is assumed that $r_{ij} << n^{-2}$, and $dn = -(1/2)n^3 d(1/n^2)$ is used, then the new refractive indices due to the perturbation of the ellipsoid by the applied field are

$$n_{x'} = n_o - \frac{1}{2}n_o^3 r_{13}E_z, \qquad n_{y'} = n_o - \frac{1}{2}n_o^3 r_{13}E_z,$$

$$n_{zy} = n_o - \frac{1}{2} n_o{}^3 r_{33} E_z \qquad (2.10)$$

For a beam propagating through $LiTaO_3$ in a direction normal to the *xy* plane, there is no refractive index change and thereby no phase retardation. For the case of light propagating normal to either the *xz* plane or *yz* plane, there is a phase retardation of the form in Eq. 2.11.

$$\delta_{eo}(\lambda, E) = \frac{\pi}{\lambda}\left(n_e{}^3 r_{33} - n_o{}^3 r_{13}\right) hE_z \qquad (2.11)$$

Therefore, for given wavelength and electric field, the physical property of a crystal as well as a proper orientation determines the strength of EO induced phase retardation. The quantity $n_e^3 r_{33}$ - $n_o^3 r_{13}$ is called figure of merit, which is uniquely determined by the physical property of an EO crystal. The figure of merit is a key value that determines the half wave voltage V_π for an EO modulator. The V_π is generally expressed in Eq. 2.12.

$$V_\pi = \frac{d}{h} \frac{\lambda}{(n_e{}^3 r_{33} - n_o{}^3 r_{13})} \qquad (2.12)$$

In the case of a longitudinal modulator, the electrode separation *d* and thickness of the crystal *h* are identical, so the V_π is simply the inverse of the figure of merit at a given wavelength. The small nature of Pockels effect gives small values of EO coefficients. For $LiTaO_3$, $r_{13} = 7.0\ pm/V$ and $r_{33} = 30.3\ pm/V$. Hence, for instance, the V_π at 900 nm is *~3721 V* with the refractive indices $n_e = 2.18$ and $n_o = 2.175$.

In case of electro-optic field sensing, it will be more convenient to define a new quantity E_π than V_π because ambient electric fields cause the phase retardation in EOS systems whereas applied voltages do for EO modulators. Since $V = Ed = Eh$, E_π is simply expressed in Eq. 2.13.

$$E_\pi = \frac{\lambda}{h(n_e{}^3 r_{33} - n_o{}^3 r_{13})} \qquad (2.13)$$

The value of E_π for 1mm thickness of $LiTaO_3$ is *~3721 V/mm*, and this value can be lowered with a thicker crystal or shorter laser wavelength, even by different materials with higher EO coefficients.

2.3 Concepts of Resonant EO Systems

As previously introduced in chapter 1, in the conventional embodiment of an EOS field-measurement system, the probe light beam passes through the EO medium, situated between a pair of crossed polarizers, and the light intensity varies with the strength of the applied field. This polarizer/analyzer pair creates an EO-efficiency slope for the modulator that follows the derivative of the function $sin^2(\Gamma/2)$ with respect to Γ, which is the phase retardation – typically very small – induced by the applied field. A quarter waveplate shifts the operating point to an essentially linear operating regime at a 50% transmission point. Here the function has its steepest slope, $0.5(sin\Gamma)/\Gamma$, which approaches 0.5 for minute values of Γ [32]. While small EO-retardation values have been enhanced via resonance phenomena such as the Fabry-Perot effect for more than a decade [33-36], these techniques have mainly concentrated on increasing the phase within the context of the 'sin^2' efficiency slope of conventional intensity modulation.

In contrast to the conventional EOS modulation method, it has been suggested that in a system employing a resonant EO probe, the polarizers and waveplate may actually be bypassed [37]. In this chapter, we have utilized not only phase retardation, but also the EO-modulation slope of the resonance-based EOS effect. These two crucial relations are modeled, experimentally demonstrated, and compared to the properties of a conventional EOS system. The model demonstrates how the modulation slope can be controlled over a significant range, both through tuning of the laser wavelength and with the addition of distributed Bragg coatings on the faces of the EO medium [35,36]. Extending the model to the experimental regime, we have also been able to prove that the modulation slope can be achieved only through utilization of the Fabry-Perot effect in the EO medium, without the need for the polarizer/analyzer and the quarter waveplate.

A single layer of EO material can act as a Fabry-Perot etalon in which refractive-index discontinuities cause multiple internal reflections and, subsequently, multiple cavity-transmission components. Fig. 2.3 presents the transmission components out of an EO crystal in the presence of electric fields. The electric field after the *n*-th round trip is expressed as in the figure. The summation of these components determines the transmission spectral response, based on the wavelength-dependent phases of the components. The discontinuity at each boundary, due mainly to the refractive indices and Fresnel coefficients associated with the two layers, determines the depth of spectral modulation. The round trip phase delay, δ_{rt} ($= 4\pi nd/\lambda$), which is described in terms of the refractive index, n, material thickness, d, and wavelength, λ, determines the period of the spectral response. Therefore, for a given etalon, the spectral phase delay, $\delta(\lambda)$ determines the amount of transmission between the maximum (unity) and minimum, as determined by the refractive index. Hence, this phase term, $\delta(\lambda)$, can be regarded as a static spectral bias for transmission.

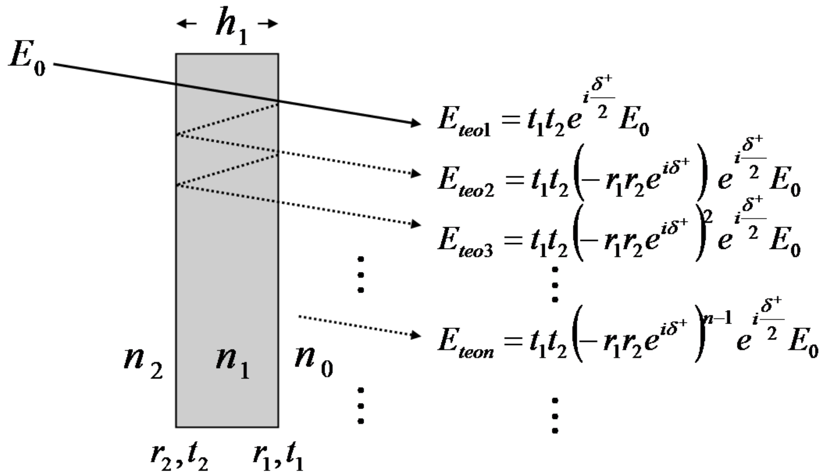

Figure 2.3: Transmission EO components for a single layer (where r and t are Fresnel coefficients for reflection and transmission of electric field).

This static spectral phase becomes perturbed by an additional dynamic phase term $\pm\Delta\delta(\lambda,E)$, which is induced when the EO medium is subjected to an applied electric field (E), due to the Pockels effect. The external vector conditions, such as beam direction and applied field polarity, determine the sign of $\Delta\delta$. This dynamic phase shift resulting from a time-varying electric field produces the amplitude modulation on the transmitted optical beam. The general optical field transmission with modulation, in terms of the modulated phase, $\delta^{\pm}(\lambda,E)$ ($= \delta(\lambda) \pm\Delta\delta(\lambda,E)$), is expressed as $T^{\pm}=t_1t_2\bullet exp(\delta^{\pm}/2)/(1+r_1r_2\, exp(\delta^{\pm}))$, where

$r_{1,2}$ and $t_{1,2}$ are Fresnel reflection/transmission coefficients at the front, or incident, and back interfaces, respectively. Hence, the original power transmittance at a given wavelength λ, $I_t(\lambda)=|T(\lambda)^2|$, is shifted to $I_t(\lambda,E)= T^+(\lambda,E)*T^-(\lambda,E)$. The dynamic modulation, $\Delta I_t(\lambda,E)$ $(=I_t(\lambda,E)- I_t(\lambda))$, is virtually proportional to the slope of the spectral response, $dI_t/d\delta$, while the average amount of transmission is set by the spectral response itself at a fixed static bias.

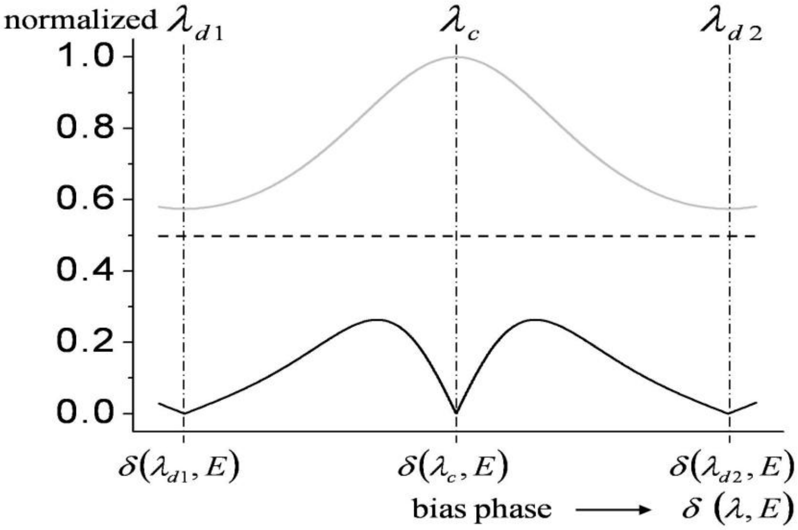

Figure 2.4: Simulation of the transmitted intensity (grey line) and EO signal strength (black line) for a resonance-based EO system relative to the EO signal strength for a non-resonant, single-pass EO probe of the same thickness (flat, dashed line; EO signal is product of slope and EO phase retardation, or 0.5) versus wavelength (all normalized, for one mode).

Simulations were first performed for a $LiTaO_3$ etalon (n = 2.18) over a single mode spacing. This refractive index results in transmission values of 57.5% to 100% at destructive and constructive wavelengths (λ_d and λ_c), respectively (Fig. 2.4, gray curve). This periodic spectral response can be employed in place of the 'sin^2' slope created by a conventional polarizer/analyzer pair. Since the induced EO-phase perturbation is typically minute, the derivative of the spectral transmission in Fig. 2.4 yields the slope for EO amplitude modulation. The slope in such a resonance-based system is shifted by tuning the bias phase (*i.e.*, wavelength), as compared to using a quarter-wave retarder in conventional systems to reach their maximum slope of 0.5 (wavelength independent – dashed line in Fig. 2.4).

The overall EO modulation is then essentially a product of the modulation slope and the EO phase retardation. The highest slope for an uncoated Fabry-Perot-based $LiTaO_3$ etalon is ~ 0.23, which is about half that for conventional EO intensity modulation using the polarizer/analyzer/waveplate combination. Despite this, it is still possible for the resonance-based phase retardation to be stronger due to the interferometric summation of multiple round trips of the optical beam in the EO etalon [33,34]. This allows enhanced phase retardation around λ_c. The intrinsic resonator created by the etalon maintains the photons inside the medium for a longer time compared to the ideal, single-pass configuration. In addition, the identical resonance mechanism results in the spectral shape of the phase retardation being the same as the spectral response of the transmission.

The maximum enhancement can be quantified in terms of $r_{1,2}$, the Fresnel field reflection coefficients at the front and back EO-etalon interfaces. The enhancement is $(1+|r_1r_2|)/(1-|r_1r_2|)$ at all constructive wavelengths, λ_c, compared to the single-pass case (normalized to 1 for convenience). Taking into account such spectral variations of the EO-phase retardation, the simulation of the overall EO-signal strength versus minute phase perturbations for a $LiTaO_3$ etalon is presented in Fig. 2.4 (black line). These quantities are compared to those of a normalized, conventional, $\sin^2$-EOS-modulation configuration (both transmission function and EO signal strength equal to 0.5) using an anti-reflection (AR)-coated $LiTaO_3$ crystal with identical properties.

At λ_c, the enhancement of the resonant EO retardance is a maximum, 32% greater than in the single-pass, conventional-modulation case. However, at this wavelength, no EO signal is expected because of the zero slope in transmission. Similarly, other zero-slope biases, such as destructive wavelengths, λ_{d1}, λ_{d2} (Fig. 2.4), yield no EO signal either. The maximum EO signal exists when the laser is tuned towards the peak of the resonant modulation slope, although this strength is only increased to a level that's 51.6% of that found with the conventional modulation geometry. However, in the latter, since the highest slope and ideal, AR-coated optical components with perfect alignment were assumed, the difference between the EO signals in resonant and non-resonant EOS systems will in reality be even closer. Most importantly, further enhancement of the sensitivity of the resonance-based EOS system, which is possible with judicious use of reflective coatings on the crystal surfaces, is anticipated and to be verified in the next chapter. Furthermore, regardless of any small reduction in EO signal strength, the benefit of eliminating the polarization components required in conventional EO modulation is still realized.

2.4 Simulations of Resonant EO Systems

The methodology to calculate the amount of phase retardation induced by external electric fields is discussed in the previous section. The impact of EO modulation, along with different wavelength, is discussed further in this section. Based on the theory in session 2.1, for LiTaO$_3$, the total round trip phase shift $\delta(\lambda,E)$ in Eq. 2.2 is re-expressed as in Eq. 2.14.

$$\delta(\lambda, E_z) = \frac{4\pi h n_0}{\lambda} + \frac{4\pi h (n_e - n_o)}{\lambda} + \pi \frac{E_z}{E_\pi} \qquad (2.14)$$

The new term in the middle came from the birefringence of LiTaO$_3$, but this term can be neglected for thin LiTaO$_3$ because of its natural weakness of the birefringence (n_e - n_o). Hence, the first term is the only static and most dominant term which determines a spectral response. The wavelength can be considered as an optical bias for the EOS system. The transmission is fixed at a certain set of wavelengths. If there is an external-field-induced dynamic phase perturbation, $\delta_{eo}(\lambda,E)$, the transmitted light intensity is also perturbed.

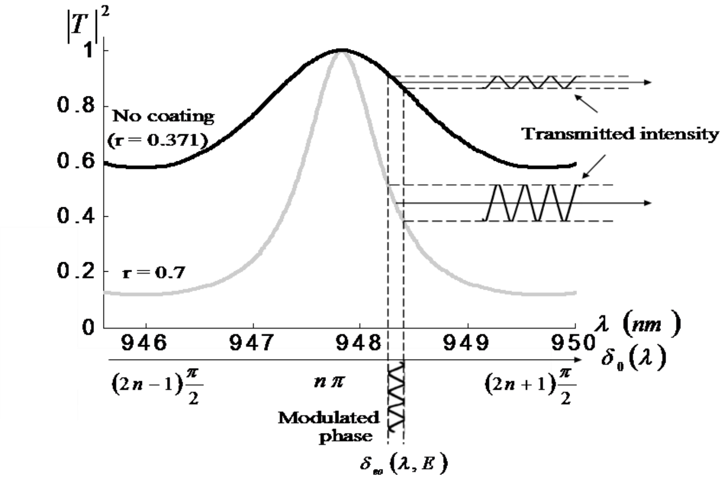

Figure 2.5: Transmittance of EO modulated intensity for different resonance cases.

The most important factor for the amount of modulation can be understood qualitatively by Fig. 2.5. The black plot is one of the modes as in Fig. 2.4 and the gray one is the same sample with a field reflection $r = 0.7$ of a balanced resonator. With the same input signal, the transmitted intensity of the bare sample has less modulation with higher intensity, whereas that of the balanced resonator has the opposite behavior. Apparently, the resonator case is more advantageous for EOS application even though it transmits less light.

The fundamental difference of the modulation amount is originated from the slope of the transmission plot versus phase shifts. In most cases for EOS applications, the input modulation is extremely small, so the whole derivative of transmission plot versus phase shift naturally indicates the efficiency of the EO modulation. Therefore, the amount of modulated transmission is proportional to the amount of input modulation and the slope.

The quantitative amount of resonance based enhancement can be calculated by the marriage of the transmission and phase enhancement theory. First, the EO efficiency – the change of transmission versus infinitesimal phase change – is expressed in Eq. 2.15.

$$\frac{dI_t}{d\delta} = \frac{2(t_1 t_2)^2 r_1 r_2 \sin\delta(\lambda, E)}{\left(1 + (r_1 r_2)^2 + 2 r_1 r_2 \cos\delta(\lambda, E)\right)^2} \tag{2.15}$$

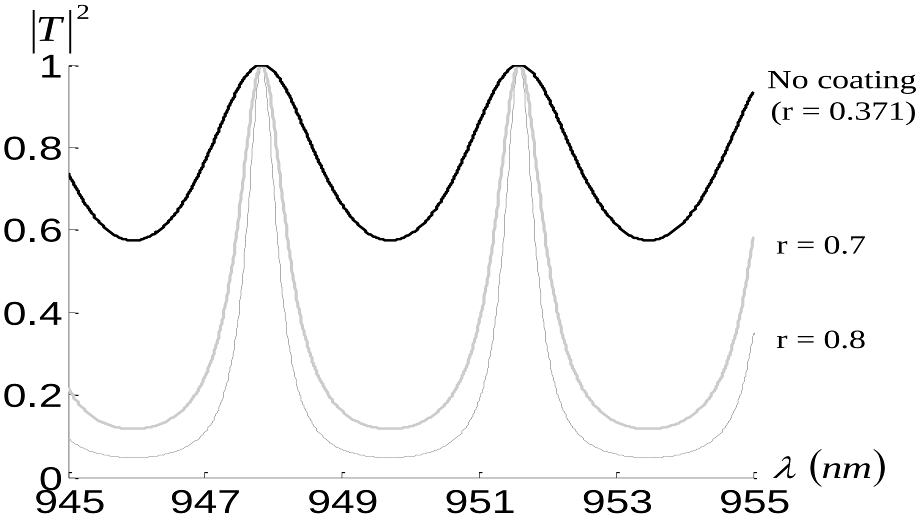

Figure 2.6: Transmittance of a $LiTaO_3$ wafer for various coatings (55 µm thick).

The transmissions for various balanced coatings are presented in Figs. 2.6. The EO phase shift can be calculated by Eq. 2.10, where $T^{+}(\lambda,E)$ (*or* $T^{-}(\lambda,E)$) is the forward (or backward) field transmission as defined previously.

$$\angle I_t^{\pm(1)}(\lambda,E)=\angle T^{+(1)}(\lambda,E)-\angle T^{-(1)}(\lambda,E) \qquad (2.16)$$
$$=\tan^{-1}\left(\frac{1-r_1r_2}{1+r_1r_2}\tan\frac{\delta(\lambda,E)^{+}}{2}\right)-\tan^{-1}\left(\frac{1-r_1r_2}{1+r_1r_2}\tan\frac{\delta(\lambda,E)^{-}}{2}\right)$$

Here, in the case of normal field sensing, only z components ($E = E_z$) affect $\delta_{eo}(\lambda,E_z)$. Usually, the E_z fields are tremendously smaller than E_π, so $E_z = 10^{-4}E_\pi$ is used for the simulation. The shape of δ_{eo} basically follows the transmission with the enhancement factor $(1-r_1r_2)/(1+r_1r_2)$ compared to the single-path phase shift. The results for various balanced coatings are presented in Fig. 2.7 as along with the single-pass results.

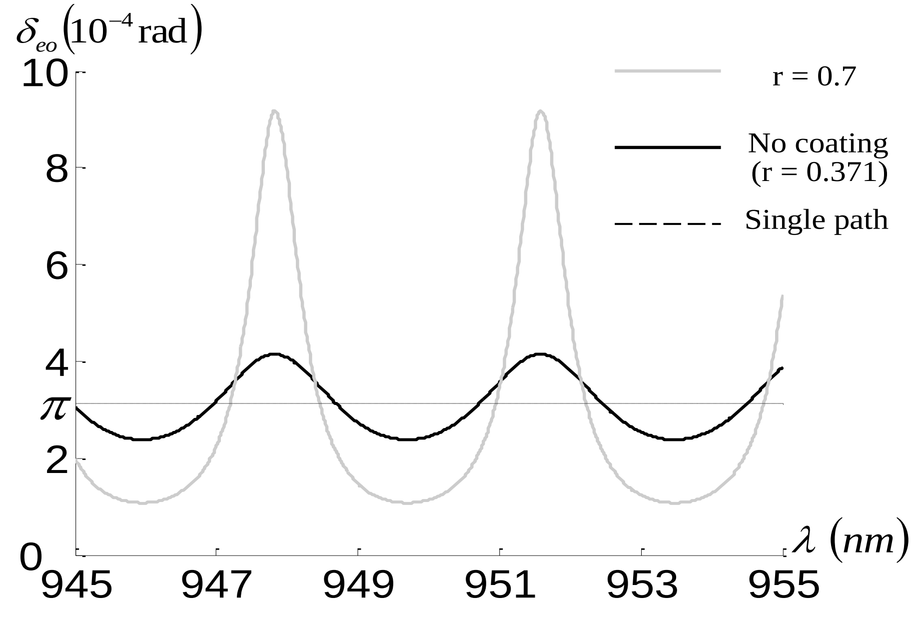

Figure 2.7: EO phase retardations of a $LiTaO_3$ wafer for various coatings (55 µm thick).

The EO strength is proportional to the product of the EO efficiency and EO phase shift. The enhanced phase factor increases the relative contrast of each plot with different coatings, as can be seen in Fig. 2.8.

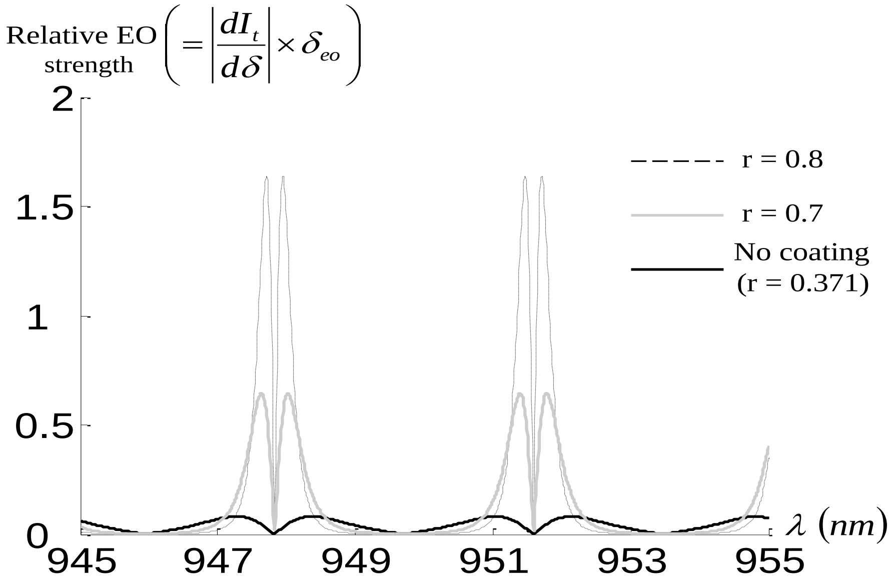

Figure 2.8: Relative EO strength of a $LiTaO_3$ wafer for various coatings (55 μm thick).

Following the same steps, simulations for an EO wafer possessing higher refractive index (GaAs, n = 3.6) with a variety of coatings over a single mode spacing are presented in Fig. 2.9.

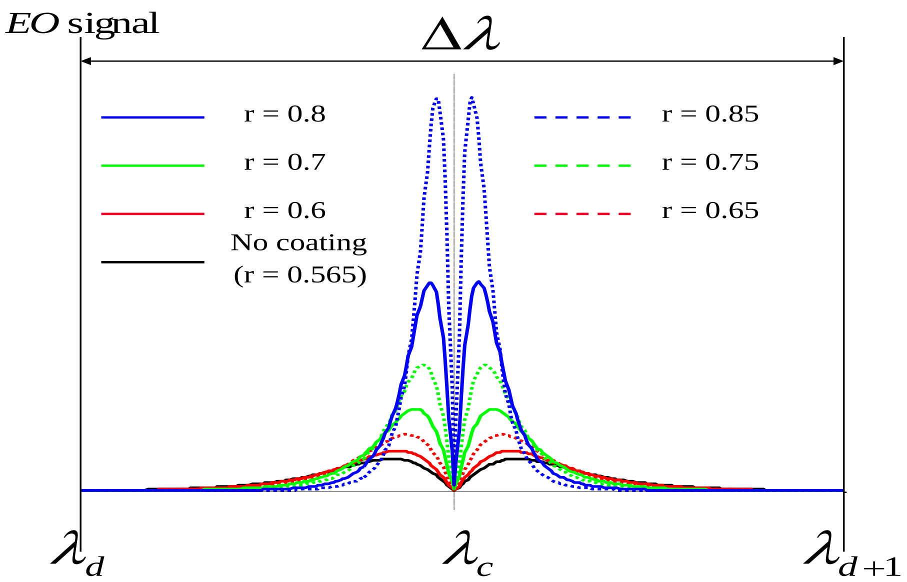

Figure 2.9: Relative EO strength of a GaAs wafer for various coatings.

Thus, as seen in Figs. 2.8 and 2.9, more resonance enhancement is expected with more coatings, but the stronger resonance reduces the enhancement bandwidth.

Furthermore, the sharp ‘spectral holes’ in the middle of the ‘efficient bands’ would be harder to avoid. If the separation of the two bands becomes narrower than a linewidth of a laser, the huge contrast will be washed out. This requires the need for a fine tunable laser with narrow linewidth and good stability.

2.5 Experiments of Transmissive Resonant EO Systems

An experimental scheme for EOS intensity modulation has been assembled as shown in Fig. 2.10. For the $\sin^2$ intensity-modulation scheme, an input polarizer would be set to a 45° linear polarization with respect to the optic axis of the EO probe crystal, and a quarter-waveplate rotated to maximize the transmission of the laser. Adjusting the pair of polarizers and the quarter waveplate are arguably cumbersome procedures. Furthermore, the inherent, static birefringence of $LiTaO_3$ degrades the performance of the waveplate, and further tuning is usually required to maximize the modulation signal. However, through the use of a resonant EO-sensor configuration, one finds that the polarization optics may be removed, and small bias shifts induced by static birefringence may be readily compensated by simply tuning the laser wavelength.

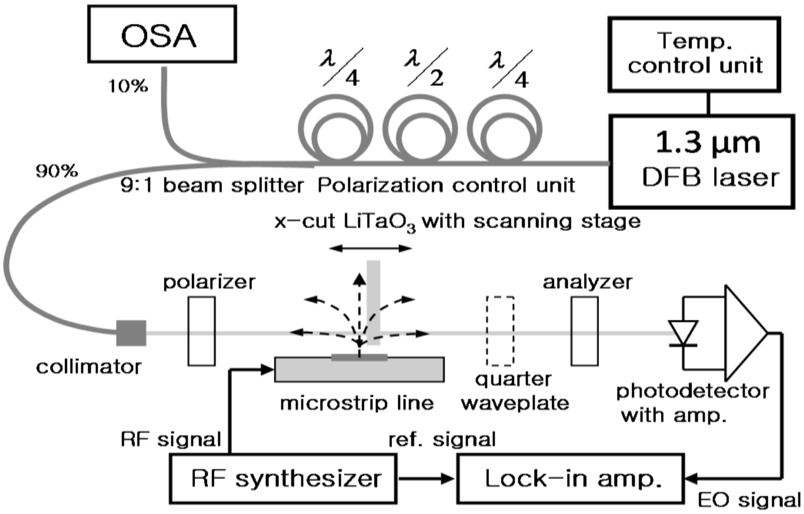

Figure 2.10: Resonance-based EOS system. The components with dashed outlines are required for conventional intensity modulation. The crystal is placed ~ 0.2 mm above the DUT, and the center of the collimated beam waist is ~ 3 mm above the DUT to avoid beam clipping for a full resonance condition. The dashed lines on the DUT represent E-field flux lines.

To demonstrate this, a commercial, distributed-feedback laser diode with a 1305.2 ~ 1309.1 nm temperature tunability range and a 0.02 nm linewidth was used to deliver ~ 3 mW of optical power for EOS interrogation of the electric field above a microstrip-transmission-line used as a device-under-test (DUT). With a mode spacing of 7.16 nm for the 54.64 µm thick, x-cut $LiTaO_3$ wafer, a tuning range of ~ 4 nm covered about one half of a resonant mode. A lateral scan of the microstrip positioned ~ 200 µm under the EO probe allowed the field above and to the sides of the 4-mm-wide top metal strip to be characterized. The crystal was oriented so that it sensed the normal component of electric field.

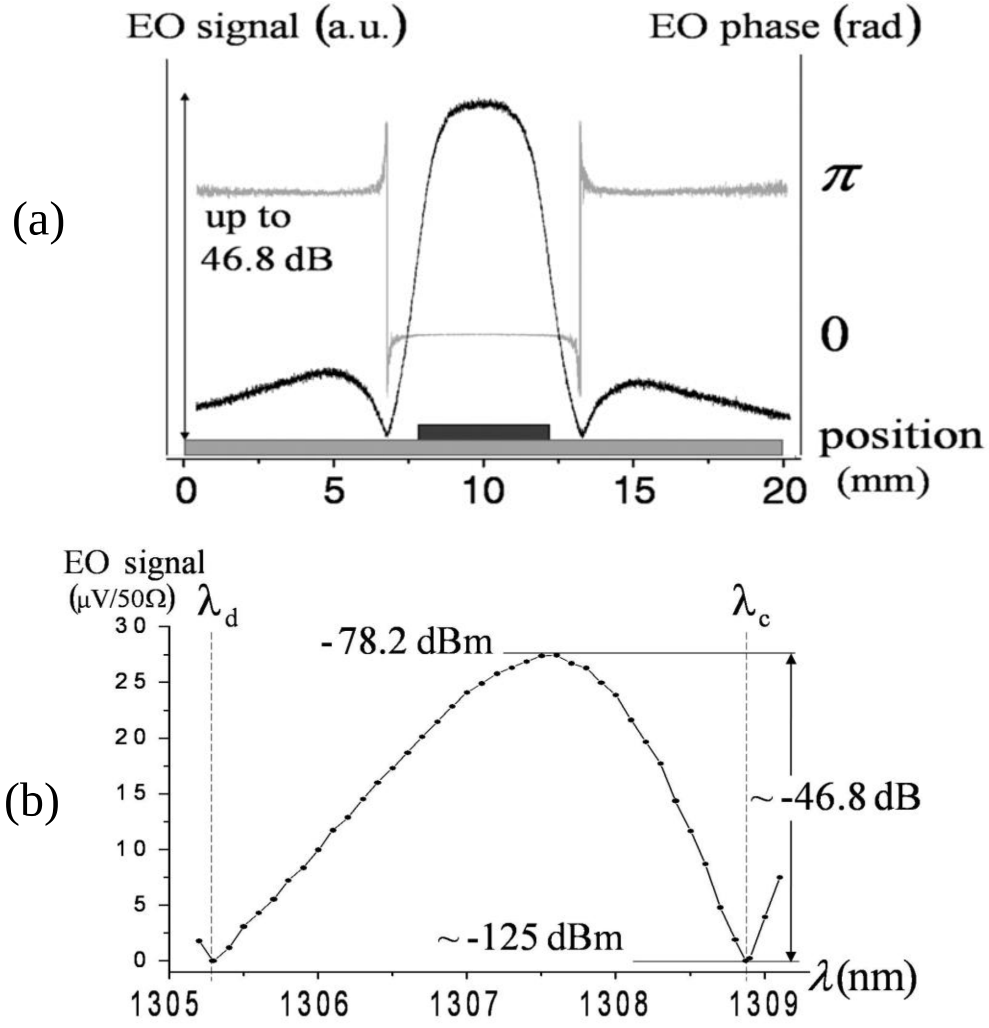

Figure 2.11: (a) The normal component of electric field measured on top of a microstrip transmission line. The black line is the normalized signal magnitude, and the gray line is phase. (b) strength of EO signal for a half mode of the EO-field-strength resonance shown in Fig. 2.4 (for $LiTaO_3$ of 54.64 µm thickness).

Figure 2.11(a) shows a typical EO amplitude and phase signal for the microstrip DUT (driven with 23 dBm input power at 3 MHz). At the edge of the microstrip, where the phase flips, the signal drops to the noise floor. An SNR of 46.8 dB was observed with the laser tuned to the wavelength yielding the maximum spectral slope shown in Fig. 2.4. The thin nature of the EO crystal enabled the resolution of signals down to the -125+/-5 dBm noise level of the system with a sub-millimeter spatial resolution. The bandwidth of the photodetector and the average lifetime of a photon in the etalon are the limiting factors for the bandwidth of this EO measurement. While applications should be possible out to the microwave X-band, the most unique aspect remains the simplification made possible by the reduction of polarization components and the ease of the laser-wavelength tuning.

To characterize the strong spectral dependence of EO sensitivity, the crystal was set in the middle of the DUT top electrode, where it intersected the strongest electric field, and the EO signal was sampled every 0.1 nm as the wavelength was tuned (Fig. 2.11(b)). The signal completely disappeared twice, at destructive (λ_d, ~59% transmission) and constructive (λ_c, ~99% transmission) wavelengths.

Adding a polarizer/analyzer pair does not appreciably improve the resonance-based EO performance, since, in a conventional EOS system, the polarizers create the EO-sensitivity slope, while the crystal only contributes uniform phase retardation. Here, the interplay of phase modulation and slope yields the EO signals that emerge from the analyzer. Since a resonant crystal has a uniquely strong EO phase retardation and slope, the crystal by itself is enough to create ‘the interplay’ for EO modulation.

While thin EO crystals are generally preferred for EOS because they are compact, have a low invasiveness to the device under test (DUT), and have the potential for providing high spatial resolution, they also expand the resonant mode spacings of the etalon, thus allowing better spectral resolution for the Fabry-Perot effect than is possible with thicker crystals. However, a larger EO-modulation signal is expected for thicker crystals, where the maximum EO slope – determined only by the wavelength – remains the same. As the crystal becomes thicker, the number of longitudinal modes and the phase retardation increase linearly, as does the overall EO signal.

With the thicker crystal, the tunable range of the laser now covers multiple cavity modes. Figure 2.12 presents such EO-signal data for a $LiTaO_3$ crystal of 277.10 µm thickness. A simulation is performed using arbitrary electric field and light strength in order to match the results with the experimental scale. The narrow laser linewidth enables nearly the full Fabry-Perot spectral modulation to be maintained even for the thicker $LiTaO_3$ crystal. Thus, the same shape of EO signal strength as seen in Fig. 2.4 is expected. A modulation-signal level about five times higher than that found in the thin crystal of Fig. 2.11(b) is calculated, and the measurement agrees well with this value. A further increase of crystal thickness does not increase the scale factor linearly, as the slope becomes flatter due to poor spectral-resonance resolution for typical laser sources.

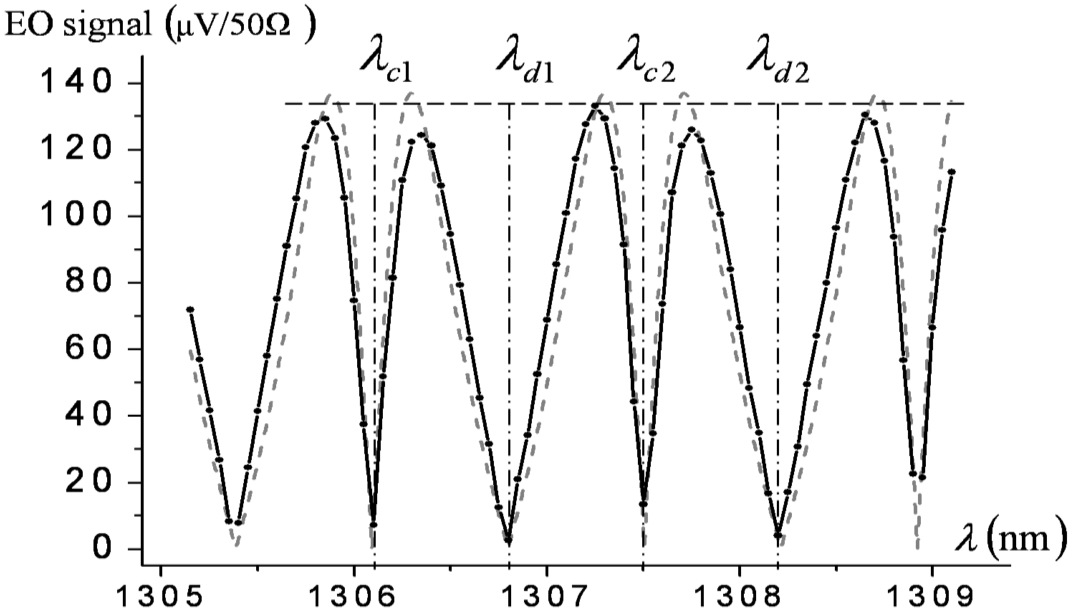

Figure 2.12: Strength of EO signal over several resonant modes of a 277.10 µm thick $LiTaO_3$ probe. The solid black (dashed gray) line is experimental data (simulation), with the maximum signal level (flat dashed) corresponding to -64.5 dBm. Constructive and destructive etalon wavelengths are denoted by $\lambda_{c\,1,2}$ and $\lambda_{d1,2,}$ respectively.

2.6 Summary

A very simple, resonance-based EOS system that requires only a narrow-linewidth diode laser, EO crystal, and photodetector for its optical realization was presented. This new system is suitable for most thin EO crystals, thus the invasiveness can be reduced while maintaining good EO sensitivity by virtue of the resonance advantage for EO retardation enhancement. Not only the system simplification and sensitivity advantages, this resonance-based methodology can be extended to high-frequency sensing as well.

CHAPTER 3

RESONANCE-BASED ENHANCEMENT OF ELECTRO-OPTIC SENSITIVITY IN AN ALL-FIBER-ENCLOSED REFLECTIVE MODE

3.1 Introduction

In the previous chapter, a thin uncoated $LiTaO_3$ wafer was employed as a free-space, transmissive EO sensor. The relatively poor maneuverability and opto-mechanical robustness of the free-space EO sensor have been improved upon in several cases through the use of a reflective, fiber-based probe geometry [3,21,35,38]. Furthermore, the compactness and reliability of such a fiber-based embodiment provide for enhanced spatial resolution and relief from the necessity of tedious optical alignment. As an extension of resonance-based EO sensing technique to the practical reflective mode sensing, a reflective fiber-based EO probe with a built-in microcavity is developed to utilize the advantages of the resonance-based EO sensing scheme. The resonance-based design for electro-optic microwave-field-mapping, which eliminates the need for the polarizer, analyzer, and quarter-wave retarder in its optical-probe-beam path while also exhibiting less laser-induced noise and an enhanced signal-to-noise ratio as compared to conventional single- or double-pass electro-optic intensity modulators, is conceived and demonstrated in this chapter. The measurement approach utilized a high-reflection, resonant-micro-cavity probe and an entirely fiber-enclosed optical-beam path, and thus it had a significantly improved scanning mobility with enhanced convenience. A model for the reflective resonant-probe was proposed and then employed to calculate electro-optic phase retardation and a modulation-efficiency slope, the latter of which was found to indicate that system sensitivity can be optimized via tuning of the input laser wavelength.

This concept was experimentally verified using thin $LiTaO_3$ EO probe crystals configured as balanced resonators, and then an entirely fiber-coupled measurement was demonstrated.

3.2 Theoretical Modeling

In this chapter, first the modeling of the resonance-based, EO sensing concept is extended so that it applies to reflective EO sensing. In this case, the addition of extra distributed Bragg coatings on the faces of the EO medium are considered, and the operating location on the modulation-efficiency slope is found to be controllable over a significant range through tuning of the laser wavelength. Besides the sensitivity enhancement, the resonance-based reflective geometry has an advantage in reducing laser-induced noise, as it needs to deliver fewer photons to a photodetector in order to achieve the equivalent amount of EO-modulation signal.

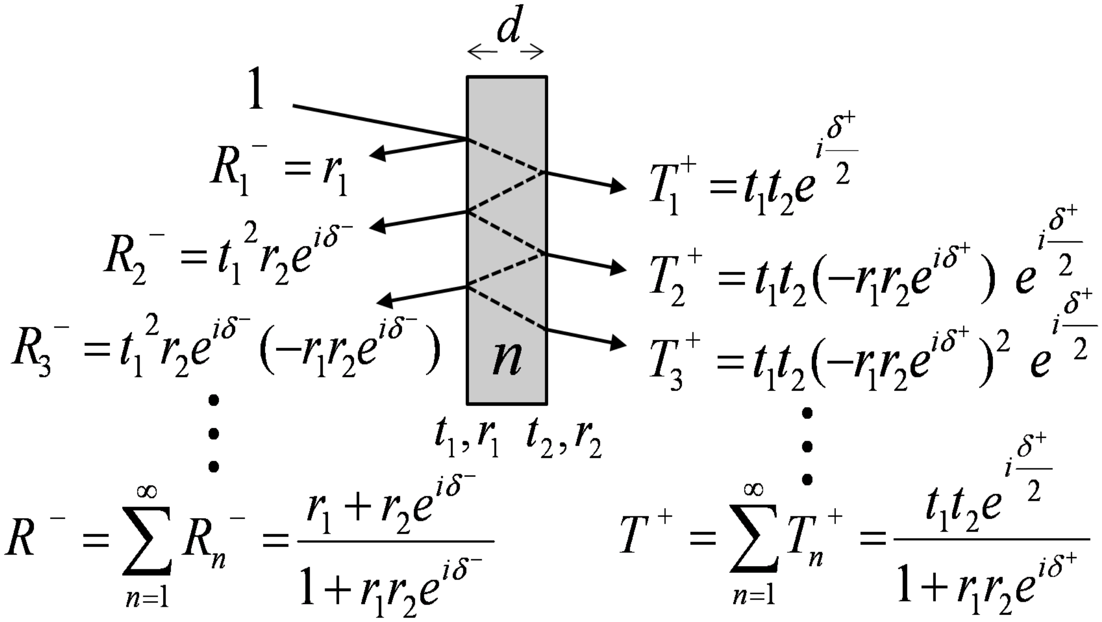

Figure 3.1: Interferometric field components of transmission and reflection from the Fabry-Perot effect in an EO wafer. ($r_{1,2}$ and $t_{1,2}$: Fresnel reflection/transmission field coefficients at the front, or incident, and back interfaces. The incident beam is drawn with a non-normal incidence angle for ease in separating the transmitted and reflected beams).

The modeling of a general, resonance-based EOS system was first described in the previous chapter on a transmissive system [23]. Here, the same methodology is adopted for the quantitative analysis of reflective systems. In EOS systems, a single plate or layer of EO material can act as a Fabry-Perot etalon in which refractive-index discontinuities lead to multiple internal reflections and, subsequently, multiple cavity-transmission components. The index of refraction, n, and the thickness of the EO medium, d, determine a round-trip optical phase delay of the etalon, $\delta = 4\pi nd/\lambda$. When one includes the Pockels effect for the EO sensor, the index is modified to $n \pm \Delta n$ in the presence of a static electric field, causing an additional single pass phase delay, $\Delta\delta = 2\pi\Delta nd/\lambda$. As a result, the single-pass phase delay (*i.e.,* in transmission), including an electric-field-induced EO effect, can be written as $\delta^{\pm}/2 = \delta/2 \pm \Delta\delta$, where the ± indicates the sign of the phase retardation depending on the light direction and polarity of the applied electric field. Thus, as a low-frequency electric field is applied along the optical-axis of an EO wafer, a transmitted optical beam experiences an additional single-path phase retardation, $\Delta\delta$, and the field transmission and reflection will be modified to T^+ and R^-, as illustrated in Fig. 3.1. It should also be noted that the T^+ and R^- have the opposite sign of EO shift due to their opposite propagation direction.

As the refractive index of an EO etalon is changed by an electric field, E, the original power transmittance, $I_t(\lambda)=|T(\lambda)^2|$, and reflectance, $I_r(\lambda)=|R(\lambda)^2|$, at wavelength λ are shifted to $I_t(\lambda,E) = T^+(\lambda,E)*T^-(\lambda,E)$ and $I_r(\lambda,E) = R^-(\lambda,E)*R^+(\lambda,E)$, due to the EO phase retardation. The amount of the transmittance (or reflectance) change, $\Delta I_{t\ (or,\ r)}(\lambda,E)$, strongly depends on the minute phase change $\Delta\delta(\lambda,E)$ that accompanies the bias wavelength and the applied field. The optical-beam wavelength determines the static operating bias-phase, whereas the electric field causes an extra, EO-induced phase. In other words, the wavelength sets the amount of static transmission (or reflection) depending on the spectral response of the etalon, and the amount of transmitted (or reflected) modulation intensity is determined by the slope of the spectral response at the operating wavelength, along with the amount of EO phase modulation. The spectral-response slope, $dI_{t\ (or,\ r)}(\lambda,E)/d\delta(\lambda,E)$, presents the EO transmission (or reflection) sensitivity versus minute changes in the phase and yields the wavelengths that maximize the resonance-based EO signal.

The EO phase retardation for transmission and reflection can be expressed as $\angle I_t = \angle T^+ - \angle T^-$, $\angle I_r = \angle R^- - \angle R^+$, respectively [33,34,39]. These are identical to each other and both have an in-phase (or out-of-phase) shape of the spectral response as in light transmittance (or reflectance). The product of the spectral slope and the amount of EO phase retardation governs the total EO signal strength. Simulations of the reflectance and the spectral slope versus minute phase perturbations for a $LiTaO_3$ probe ($n = 2.18$) are presented in Fig. 3.2, along with the relative EO phase retardation and signal strength. These quantities are also compared to an ideal, conventional, non-resonant, double-pass EOP configuration with the same crystal, but with a 100% high-reflection (HR) coating placed on the second interface (interface 2 in Fig. 3.1).

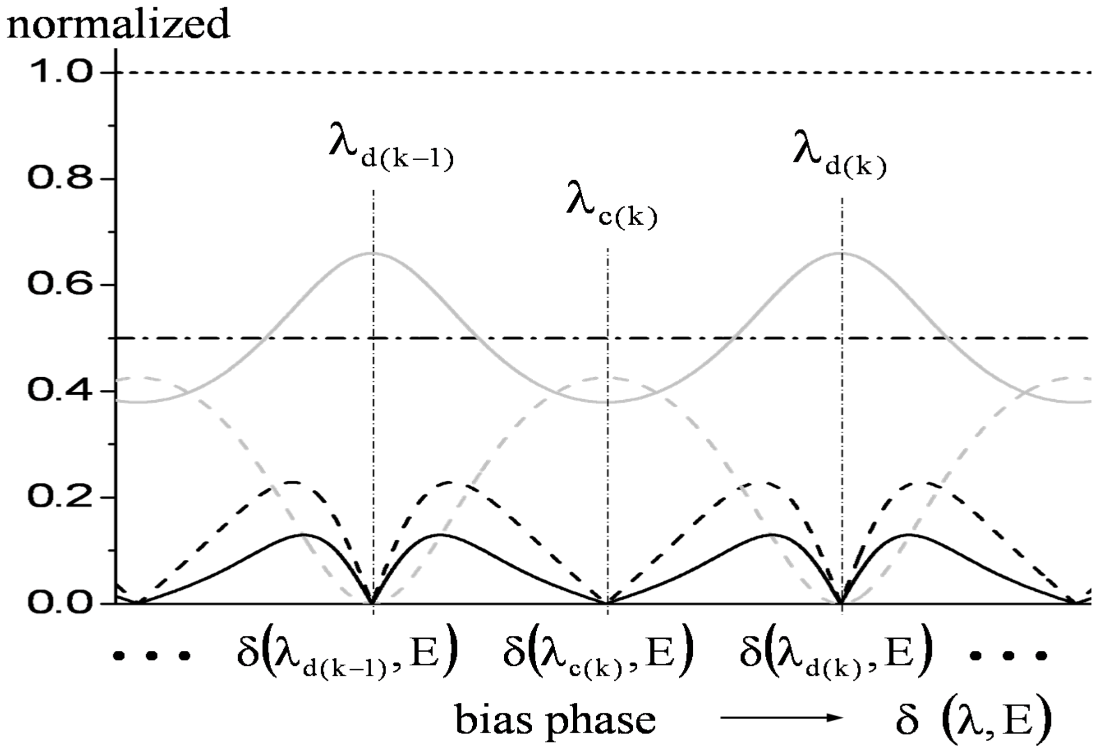

Figure 3.2: Simulations for a reflective, resonance-based, $LiTaO_3$ EOS system (over two etalon modes; no coatings). All quantities plotted versus phase, which varies as a function of laser wavelength and the applied low-frequency electric field. Dashed gray line: normalized reflectance I_{rn}; dashed line: spectral slope $|dI_{rn}/d\delta|$; solid black line: normalized EO signal I_{EOn}; dotted line: normalized EO phase retardation for ideal double-pass case $2\Delta\delta$; solid gray line: relative EO phase retardation versus ideal double pass case $\angle I_r/(2\Delta\delta)$; dash/dot line: I_{Eon} for ideal double-pass case.

Analyzing Fig. 3.2, the normalized EO signal strength in the reflective, resonance-based system is $I_{EOn} = |dI_{rn}/d\delta| \times \angle I_r/(2\Delta\delta)$, and it is observed to have up to ~26% of the EO signal in the ideal, conventional double-pass system. Since I_{EOn} is a normalized relative quantity for input-beam intensity (I_{in}) and double-pass phase retardation ($2\Delta\delta$), the absolute intensity modulation is expressed as $I_{EO} = I_{EOn} \times (2\Delta\delta\ I_{in})$. As the slopes and EO phase retardation for transmission and reflection are respectively out-of-phase ($dI_{rn}/d\delta = -dI_{tn}/d\delta$) and identical ($\angle I_t = \angle I_r$), the EO strengths (*i.e.,* the product of slope and retardation) will be the same for the two cases of the opposite phase and for any wavelength, even though the transmitted and reflected light are complementary ($I_{rn} = 1-I_{tn}$). This indicates that the reflection configuration for EOS systems has the advantage of requiring a lower intensity of light in order to achieve the same EO modulation as the transmissive embodiment. Consequently, there will also be less laser-induced noise in the modulation and the electric-field measurement (Fig. 3.3).

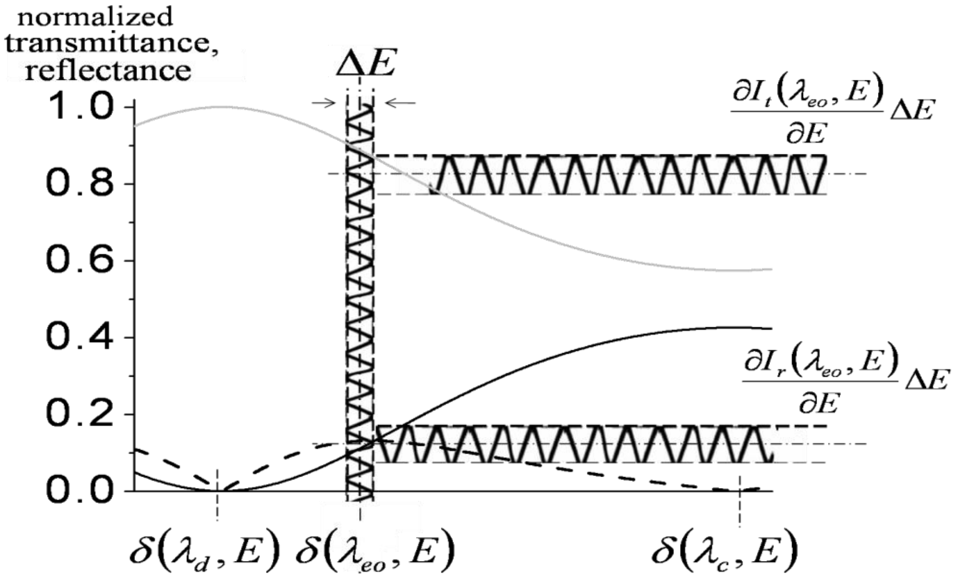

Figure 3.3: Principle of resonance-based EO amplitude modulation for transmission and reflection cases (a half mode for a $LiTaO_3$ etalon with no reflective coatings). Gray line: normalized transmittance; solid black line: normalized reflectance; dashed black line: EO signal strength. Both modulations (exaggerated for ease of observation) have the same amplitude with opposite phase.

3.3 Experimental Demonstration

Experiments have been conducted to highlight the enhanced signal-to-noise characteristics that are possible using thin EO crystals, and the ability to produce a less complicated EOS system by eliminating the polarizer/analyzer pair and the optical-biasing, quarter-waveplate of traditional intensity-modulating probes is demonstrated. Finally, the utility of this novel system is shown to reach to high-frequency field sensing through application of a photonic down-conversion technique.

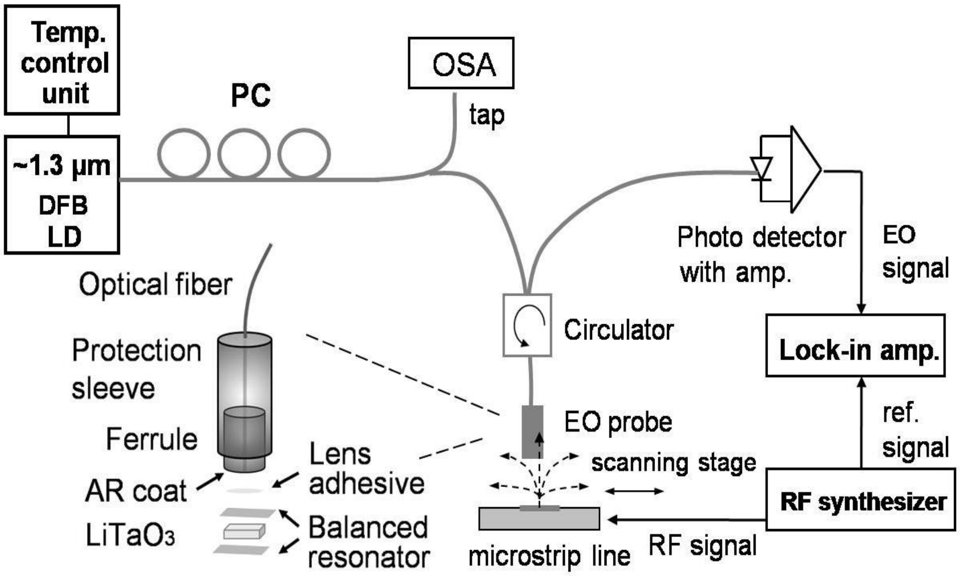

Figure 3.4: Experimental setup of the all-fiber, resonance-based, EO probing system (DFB LD: distributed feedback laser diode, PC: polarization controller, OSA: optical spectrum analyzer). The gray and black lines are optical fibers and electrical connections, respectively. The dashed lines on the DUT are electric-field flux.

An experimental setup that demonstrates the fiber-based amplitude and phase sensing of an RF electric field without the need for conventional, intensity-modulation polarization components is shown in Fig. 3.4. The fiber-based polarization-controller unit sets the incident beam polarization to maximize the induced EO phase retardation associated with the EO probe crystal. A commercial, distributed-feedback laser diode operating at ~1305 nm at room temperature again supplied 3 mW of optical power for interrogating the tangential electric field (with the x-cut $LiTaO_3$) with x-cut above a microstrip-transmission-line serving as the device under test (DUT). The 0.02 nm linewidth and ~0.1 nm/°C of temperature tunability of the laser enabled spectral responses of various thin crystals to be observed versus wavelength with acceptable resolution.

The structure of the fiber-based resonant EO probe is also shown in Fig. 3.4. The approximately index-matched interfaces between the fiber, ferrule, AR coating, and UVcuring adhesive (with $n \sim 1.5$) minimized the discontinuities within the beam path and provided a low optical insertion loss to the probe/etalon. While the resonant-reflection probe had its maximum EO-modulation response at a low reflected intensity (bottom curves in Fig. 3.3), a conventional, double-pass configuration reflects a high intensity from an HR coating on the exposed face of a probe. In the latter, a GRIN lens would be used for collimating or focusing the probe beam into a relatively thick crystal [3,21], while in the former, a thin crystal was mounted directly on the fiber facet [as in 3,35,38]. In the non-resonant configurations, the quarter-waveplate/analyzer polarization components would be required, and typically 50% of the input probe light delivered to the detector, about five times more than for the resonant probe. While a non-resonant system can be operated with power levels reduced from this 50% level [40-42], a greater benefit in signal-to-noise ratio can be realized with the steeper modulation slopes of the resonant techniques. Moreover, in non-resonant, conventional systems, the index mismatch between the fiber/ferrule glasses and the crystal causes detrimental spectral modulation. As a consequence, the trade-off for achieving greater reflection is an increase in the laser-induced noise, or one could say that laser noise is, in practice, more efficiently suppressed in the reflective, resonance-based cases.

The normal field can be measured in one of two ways – using a fiber-based probe that has z-cut probe tips or, as mentioned in chapter 2, using a free space embodiment with x-cut wafers. Here, we iterated and added the reflective version of sensing with the same condition to compare the signal strength as well as noise quality induced by the laser strength on the detector. The $LiTaO_3$ wafer was slightly tilted to break the retro-reflection condition, then the detector was switched to the reflected path. As predicted earlier, each EO signal strength for the reflective/transmissive cases is expected to be the same for any wavelengths while the respective noise is different for each case.

Fig. 3.5 presents the signal-noise comparison between the reflection/transmission cases, with various lock-in time constants at the wavelength (λ_p) which was set to the peak sensitivity bias point. The signal levels were comparable and the transmitted signal was slightly lowered intentionally to better compare the laser-induced noise on the graph. Considering the transmissive/reflective power ratio is ~ 6.7 at λ_p, the noise shown in Fig. 3.4 is reasonable.

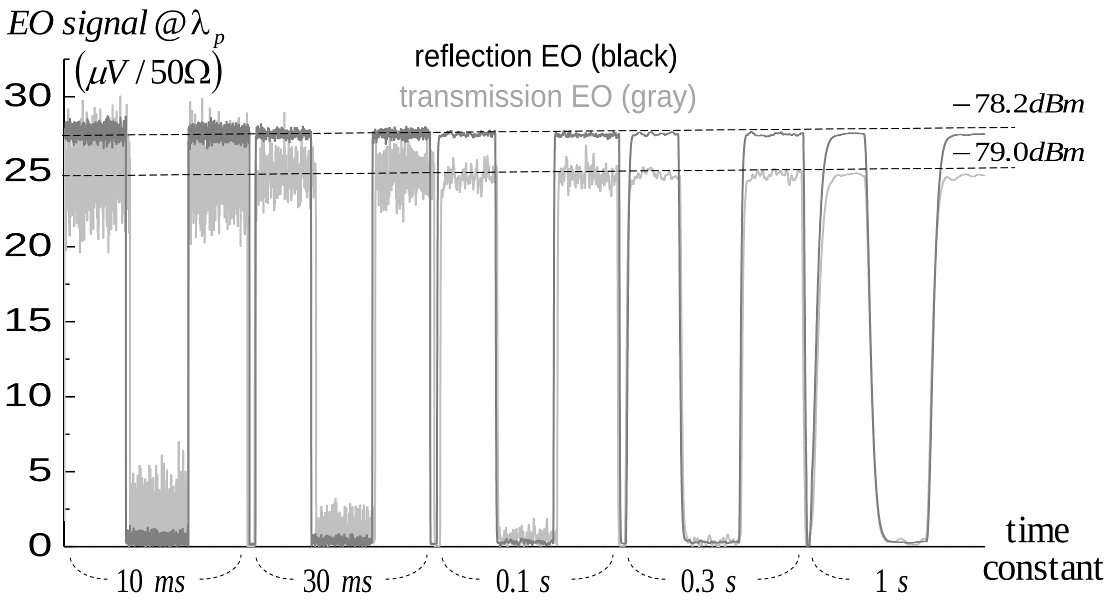

Figure 3.5: Laser noise evolution of transmmissive/reflective EO signal for various instrument time constants (wide and narrow signal dips are under respective RF off and laser off cases to characterize the laser noise).

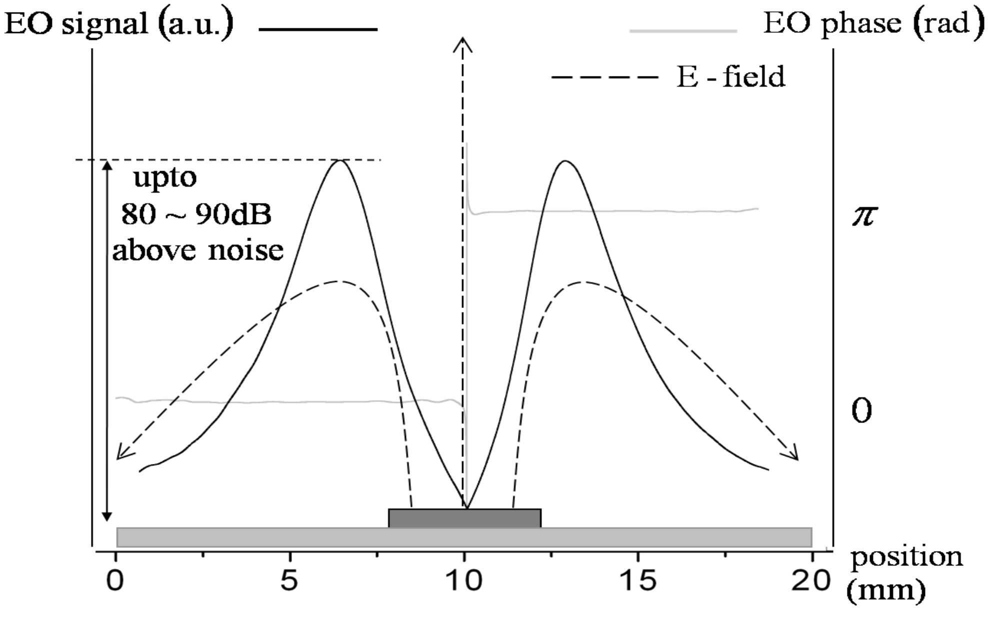

Figure 3.6: Tangential components of E-field from microstrip line.

While conventional quarter-waveplate/analyzer EOS embodiments deliver ~50% of the input light to the detector, the reflective resonance-based systems do less than that for most of the efficient signal band. This suggests the laser-induced noise is more suppressed in the reflective resonance-based cases.

In our test experiment, a 50~55 µm thick, x-cut $LiTaO_3$ wafer was used for the EO probe, since this etalon allowed a full resonant mode in reflected or transmitted intensity to be observed when tuning over several nm of wavelength. This resonant EO probe was configured to sense the tangential EO amplitude and phase signal for the DUT, which was fed with a 23 dBm sinusoidal input at 3 MHz. The microstrip line was scanned laterally under the fiber-based EO probe, revealing the field pattern above and to the sides of the top metal strip. At the middle of the microstrip in Fig. 3.6, where the phase was observed to change by 180°, the amplitude dropped to the noise floor, and a signal-to-noise ratio of ~80 dB was found with the wavelength at the maximum spectral bias in the half-mode window.

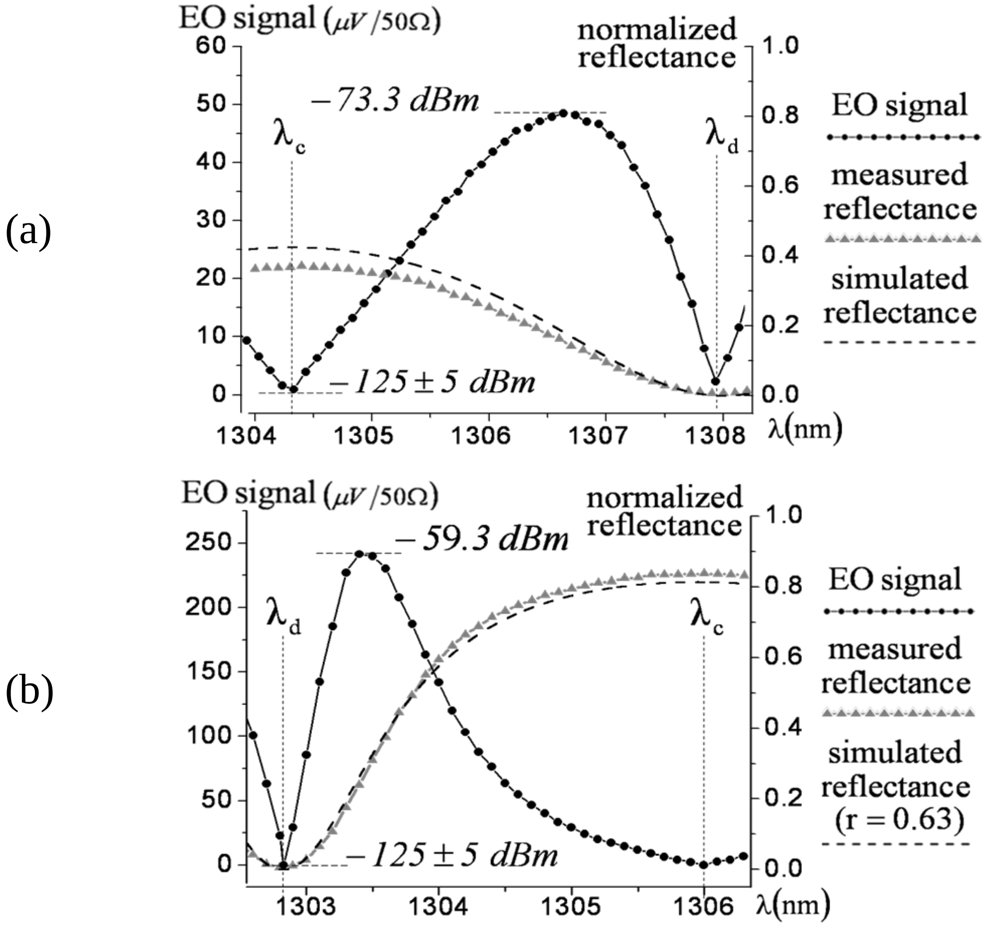

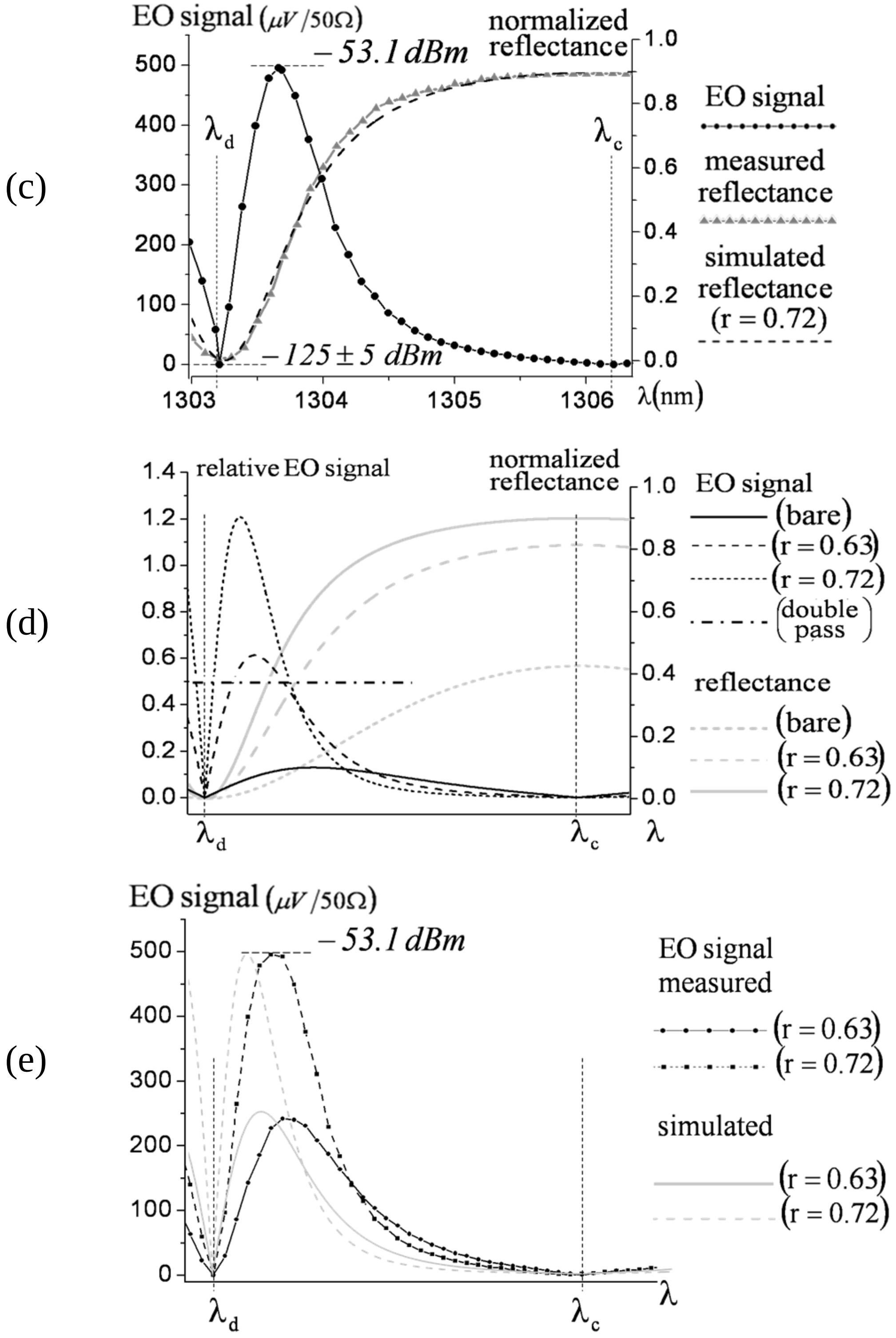

Figure 3.7: EO signal strength and reflectance from probes with various resonant conditions: (a) bare wafer (b) three layers of balanced HR coatings (c) five layers of balanced HR coatings. (d) comparison of computed results for the three probes. (e) normalized comparison of measured and simulated EO signals in (b, c and d).

To characterize the strong spectral dependence of the EO sensitivity, the crystal was positioned so that it intersected the strongest tangential electric field, near the edge of the microstrip top electrode. The EO signal was then recorded every 0.1 nm as the wavelength was tuned, utilizing an uncoated crystal as the etalon. Figure 3.7(a) shows results of the calculated and measured reflectance, as well as the measured EO signal versus wavelength. These signal levels are stated in the RF power levels that are present on the lock-in amplifier at the output of the photodetector, which demodulates the EO signal amplitude and phase from the probe light beam. As expected, the signal completely disappeared twice, at the destructive (λ_d) and constructive (λ_c) wavelengths, as before, and the EO response was found to be maximum at a relatively low reflected intensity. Experimental results shows slightly less spectral resonance than the simulation, since the first round-trip component from the etalon that contains EO retardation couples back to the fiber core with slightly less efficiency than expected.

To make the resonance-based EOS system more sensitive, the spectral slope was increased through judicious use of reflective coatings on the crystal surfaces. To build a balanced resonator, we evaporated three alternating dielectric layers of $ZnSe$ and MgF_2 at quarter-wavelength thickness ($ZnSe/MgF_2/ZnSe$) on both surfaces of a second $LiTaO_3$ plate. Again, because higher-order round-trip components get coupled back to the fiber less efficiently, the HR coatings were found to each yield $r \sim 0.63$ of the Fresnel field reflection coefficient (Fig. 3.7(b)), even though $r \sim 0.82$ was expected. Adding another pair of $MgF_2/ZnSe$ coatings on each face of a third EO plate yielded an experimental r of ~0.72 (Fig. 3.7(c)) [43].

The balanced probes with three and five layers of coatings enhanced the EO signal level approximately five and ten times compared to that of the bare probe, respectively, as seen in Figs. 3.7(b) and 3.7(c). However, the bandwidths of the etalon modes were reduced to 63%, 33% and 23.3% for the three probes with respect to the full (*i.e.,* 100%), flat bandwidth in a non-resonant case. Since the EO wafers used have a 10% thickness tolerance as specified by the manufacturer, the mode separation and resonance wavelengths (λ_d , λ_c) are positioned at different wavelengths. Assuming the same thickness for each probe sample before coating, the calculated relative EO signal strengths and reflectances for the Fresnel field reflections of the three etalons are displayed in Fig. 3.7(d). The maximum normalized EO signal level that can be achieved from the conventional double-pass, non-resonant configuration is 0.5, and the resonant probes with three and five layers of dielectric HR coatings show enhancement factors of ~1.2 and 2.4 times this level, respectively. A comparison of the normalized measured and simulated EO signals in the etalon probes are shown in Fig. 3.7(e). The values are compared at the referenced common λ_d, λ_c for convenience. The measured peak EO signals are observed farther from λ_d than in the simulation cases. This is due to the imperfections in the resonator, particularly at λ_d where, in practice, some amount of light transmission greater than zero exists. This minimum-transmission offset not only indicates the quality of the resonator, but also impacts the shape of the EO-signal plot. Further numerical and quantitative analysis is to be discussed in chapter 6.

Stronger resonant cavities not only enhance the signal strength, but also improve noise quality by requiring less light be delivered to the detector, as discussed previously. For Fig. 3.7(c), the peak EO signal of -53.1 dBm at 3 MHz was observed on the lock-in when only ~20% of the 3 mW input power was used. A simple increase in input power to 7 mW results in 7.3 dB of additional EO-signal enhancement, although further improvement was limited by the laser power and photodetector saturation. As the wavelength approaches λ_d, the signal per unit reflected power will increase significantly. Hence, further signal enhancement would be feasible with high power versions of the laser and detector. An alternate option for signal enhancement is improving the resonator Q factor through thermal expansion of the fiber core, which improves the coupling efficiency [3,35].

3.4 Summary

A resonance-based, fiber-optic EO probe that has been demonstrated to provide enhanced sensitivity over conventional, non-resonant, double-pass EO probes has been presented. An EOS system based on such probes can eliminate the need for the standard analyzer/waveplate sensing configuration and provide improved noise performance by limiting the light intensity needed for photo-detection. The signal-to-noise characteristics can be further increased by enhancing the resonant performance of the EO probes. Using a low-cost, cw-pigtailed laser diode and an all-fiber-guided embodiment, the resonance-based probe provides reliable and simplified optical-system realization.

CHAPTER 4

VECTOR NEAR-FIELD SENSING WITH ELECTRICAL-HETERODYNE DOWN-CONVERSION

4.1 Introduction

Although electro-optic sensing (EOS) has been a promising solution for performing minimally invasive near-field measurements of microwave devices and radiation sources, the price that has historically been paid to realize the unique benefits of EO probing is a requirement for expensive, pulsed lasers (especially for high frequency or fast transient measurement) and a relatively low field sensitivity [1-3,9,21].

To address the sensitivity issue in EO measurements, probe geometries that take advantage of an optical resonance in the EO medium have been developed in chapter 3 [23,24,34,36]. Fabry-Perot etalons and other resonant structures have been demonstrated, with increases in field-sensitivity observed. While in general, the stronger the resonance effect used, the slower the probe response speed (and the lower the frequency range for the probe), for applications at moderate frequencies, the benefits mentioned above are enhanced due to the fact that an inexpensive, continuous-wave (cw) laser diode may substitute for the short-pulse laser.

Measurement systems based on cw optical sources have utilized direct modulation of the light beam in the EO probe, followed by demodulation in a photodetector receiving the return beam. While these initially suffered from a lack of phase-measurement capability, this shortcoming has been mitigated by the use of a down-mixing scheme [1,2,9,11,24-26]. The phase and amplitude of the down-converted electrical signal, which will be proportional to these properties of the signal, are then displayed using a lock-in amplifier or oscilloscope.

This chapter presents a fully vectorial (*i.e*, amplitude-phase), high frequency electro-optic (EO) field-mapping technique that employs a high speed photodetector and electrical mixer to realize practical electrical down-conversion. The method features a continuous-wave laser-diode optical source, an entirely fiber-coupled beam path, a resonance-assisted EO-micro-cavity probe (discussed in chapter 3), and an RF-down-conversion mixing circuit that is shown to be effective for extracting near-field vector RF information. The system is the first of its kind to allow amplitude and phase analysis of signals interrogated with a continuous optical beam and no polarization components in the EO-modulation section. A complete tangential-electric-field characterization in the near field of RFID antennas – small planar loops intended for applications in mobile-reader instruments – is presented to demonstrate the effectiveness of the measurement technique, with a >35 dB signal-to-noise ratio attained.

4.2 Principle and Experimental Setup

The experimental schematic of the reflective, resonance-based EOS network is shown in Fig. 4.1. The optical part of the system is basically a modification of Fig. 3.4 to the optical telecommunication wavelength regime (the optical C-band). Based on computations of the reflected spectrum from a Fabry-Perot etalon, the EO medium, consisting of an x-cut, ~52-µm-thick $LiTaO_3$ plate, had a five-layer high-reflection (HR) coating at ~1560 nm, deposited on its top and bottom faces.

A glass ferrule was used to mate the probe tip with a single-mode optical fiber (Corning; SMF-28). A fiber-pigtailed, distributed-feedback (DFB) laser (Qphotonics: QDFBLD-1550-50), manual polarization controller (Thorlabs: FPC030), optical circulator (Thorlabs: 6015-3-APC), and fiber-pigtailed photodiode (Newfocus: 2117-FC), were then spliced together with the probe to form a continuous, low-loss, enclosed optical path. As the frequency radiated by the DUT directly modulated the probe optical beam in this case, it was necessary for the photodiode to have sufficient bandwidth to resolve the RF or microwave signal. While this is not a serious limitation up to and beyond even Ka-band, until now only scalar measurements have been performed by observing the detected RF-signal amplitude with a spectrum analyzer. Therefore, to also capture the

DUT-signal phase, we have utilized an electronic mixing technique to down-convert the high frequency signal information into a low-frequency IF appropriate for the bandwidth of a lock-in amplifier. The measured amplitude and phase at the IF then directly correspond to those of the signal frequency from the DUT.

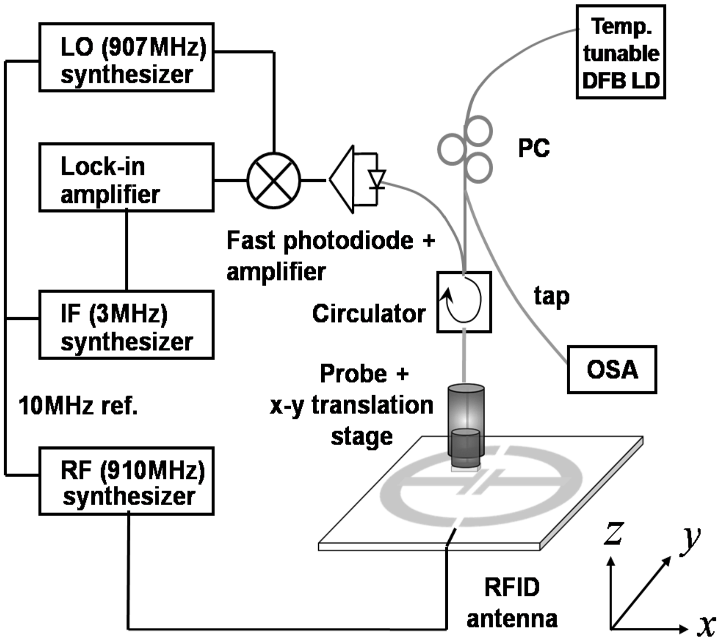

Figure 4.1: Experimental setup of the entirely fiber-coupled, resonance-based EO sensing system. (DFB LD: distributed feedback, cw laser diode; PC: polarization controller; OSA: optical spectrum analyzer). The gray and black lines are optical fibers and electrical connections, respectively.

A qualitative description of the Fabry-Perot-based amplitude modulation that arises from the EO-induced spectral perturbation on the static spectral bias is presented in Fig. 4.2. When the optical phase bias (*i.e.*, the laser wavelength) is set along the reflection-spectrum slope (by temperature-tuning the laser diode), the reflected beam is modulated proportionally with the slope due to the perturbation of the bias by an applied RF field. The DFB laser was set to deliver ~30 mW of optical power with wavelength at λ_{eo} (Fig. 4.2). At this wavelength the reflected power is ~10% of the input beam, to maximize the modulation without exceeding the 3 mW saturation level of the 1-GHz-bandwidth photodiode. At this optical-bias point (*i.e.*, λ_{eo}), compared to a conventional double-pass EO sensor utilizing the same crystal, an enhancement in the system SNR of ≥10 dB has been realized.

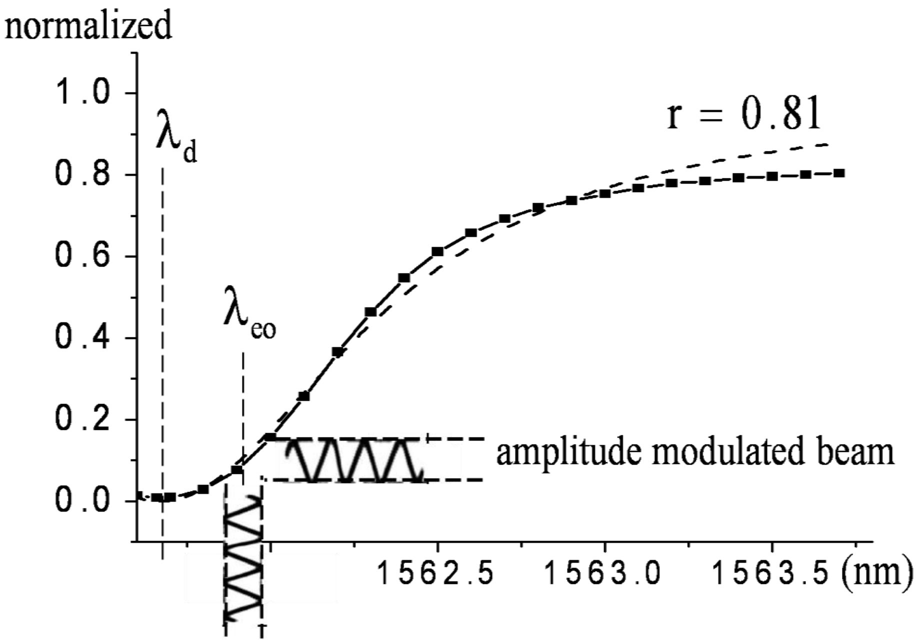

Figure 4.2: Normalized EO-probe reflectance vs. tunable laser wavelength (solid line: experimental reflection; dashed line: fitted reflection with an equivalent Fresnel reflection coefficient of $r = 0.81$). A sinusoidal RF field modulates the refractive indices of the EO medium and hence also the optical phase delay in the micro-cavity. Analogous to a sinusoidal variation in the wave length, this effect of the RF field causes a corresponding sinusoidal reflected-intensity modulation.

4.3 Results and Discussion

To demonstrate the operation of the new EOS technique, we have conducted near-field scans on an RFID antenna designed for use in a mobile handheld scanner at 910 MHz. The RFID DUT (Fig. 4.3) is basically a folded $\lambda_0/2$ dipole antenna that is transformed to a circular structure so its size may be minimized. The RFID antenna adopted the T-match topology to adjust the input impedance of a planar dipole antenna. A capacitively-loaded transmission line added in the middle of the antenna reduces the resonant frequency by providing extra electrical length [25, appendix C].

The resonant frequency of the antenna is measured to be ~910 MHz, which is in the middle of the UHF band for RFID. The resonance frequency could be tuned by manipulating the electrical length of the capacitive load and the size of the parasitic patch on the other side of the substrate. The matching quality was observed to be good, giving ~22 dB return loss at the resonance frequency, as seen if Fig. 4.4. The fiber-based EO probe, positioned on an X-Y, computer-controlled translation stage as shown in Fig. 4.1, scanned the DUT at a separation of ~300 μm, with a 200-μm step resolution. The scanning area is 50 mm×45 mm.

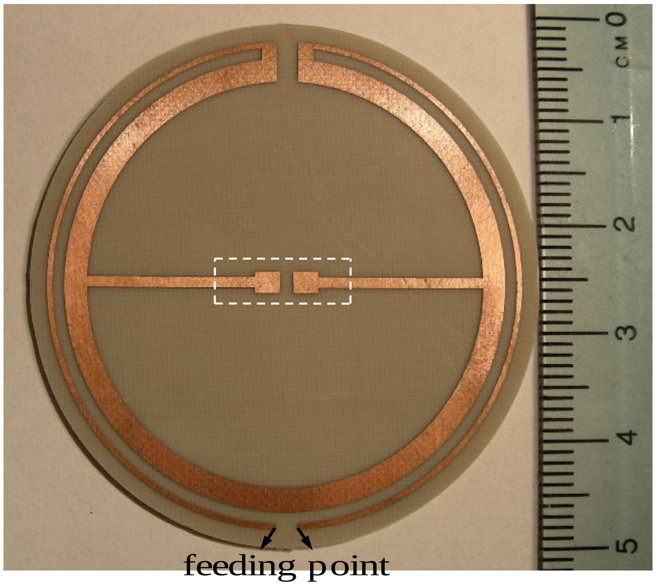

Figure 4.3: Manufactured antenna with capacitively-loaded patch (antenna perimeter = 46.5 mm, board thickness = 0.787 mm, ε_r = 2.2, trace thickness = 0.05 mm), (dashed trace: a tuning patch on the back side of the substrate).

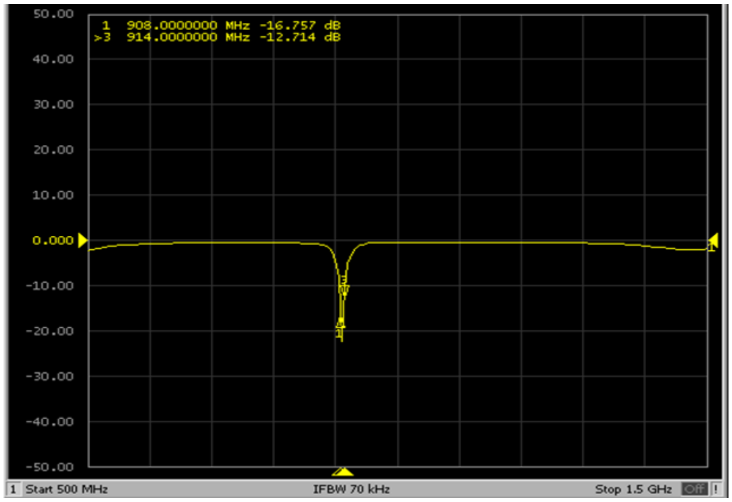

Figure 4.4: Return loss of the manufactured antenna with capacitive loading (0.5 ~ 1.5 GHz, 22 dB return loss at 910 MHz).

This circular RFID DUT consists of two major dipole antennas. The primary one is the folded dipole, at the top of the structure in Fig. 4.3, and the secondary one is the capacitive-loading dipole patch in the middle of the substrate. With a 20 dBm power at the RFID input, an apparent peak signal level (from the demodulated optical sideband at the photodetector output, after amplification) of -45 dBm ± 3dB is observed on the lock-in amplifier at the two terminal ports for both the *x* and *y* components of the electric field (depending on the polarization of the tangential component and slight changes of the probe height or the spectral bias). The primary dipole consistently shows a signal level 1-2 dB larger than the secondary one, as the primary one experiences less return loss due to its smooth circular interconnect traces.

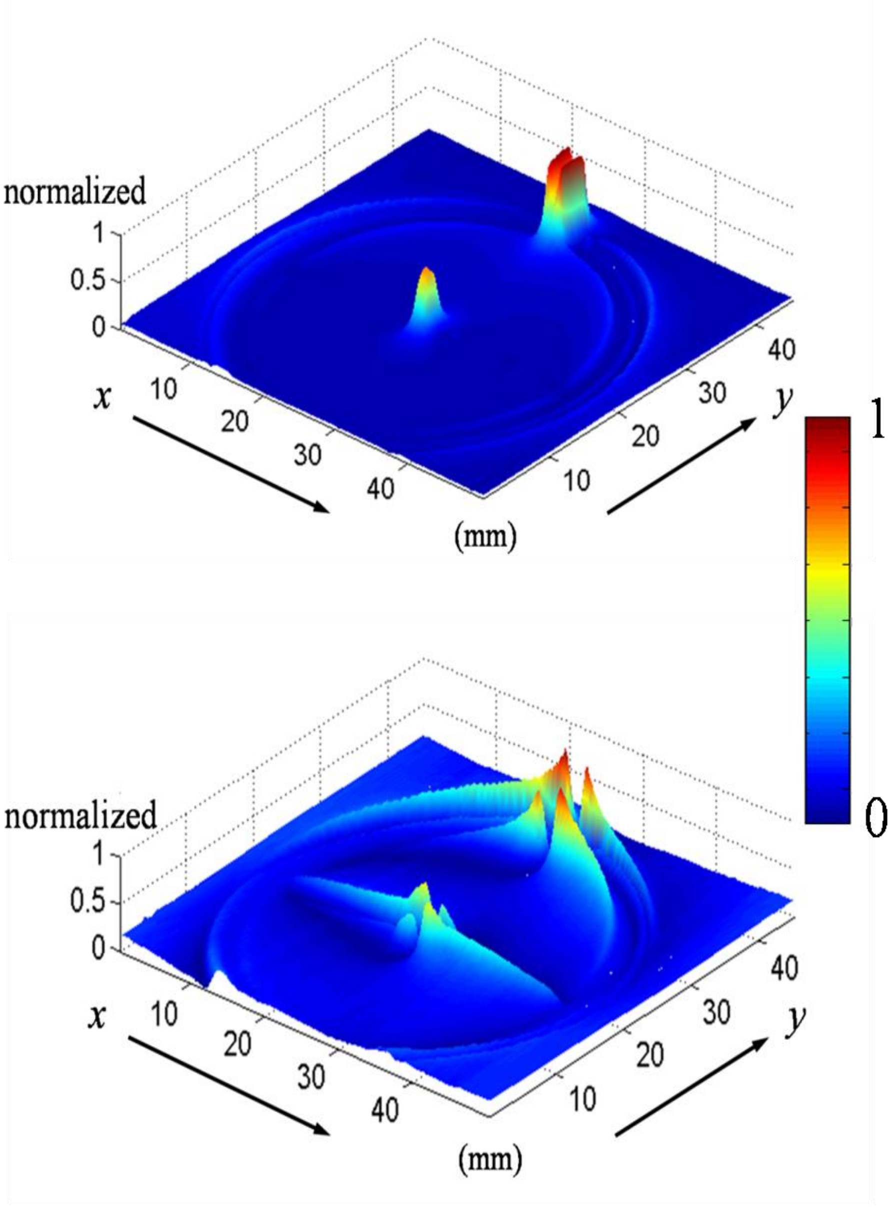

Figure 4.5: Transverse electric near-field distributions over the circular RFID antenna (3D view, normalized, 1 ~ -45 dBm, 0 ~ -85 dBm of photodetector output). (a) amplitude of transverse, *x*-component (b); amplitude of transverse, *y*-component.

An oblique view of the normalized electric-field amplitude is shown in Fig. 4.5 for both transverse field components. The noise level is -85 dBm ± 5 dB, depending on the EMI environment around the experiment. The SNR is thus in excess of 40 dB, which is sufficient for both field mapping and device characterization, and it can be increased by lowering the noise floor with improved shielding methods. The -45 dBm of peak signal level was obtained from electronic down-conversion. A 910 MHz RF signal at -38 dBm, demodulated by the photodiode, is down-converted to a 3-MHz IF (The choice of IF is flexible within the sub-sonic scale) using 0 dBm of a 907 MHz local oscillator (LO). Although the mixer has ~7 dB conversion loss, it does not impact the overall SNR, and the absolute value of the signal can be changed with the LO power level.

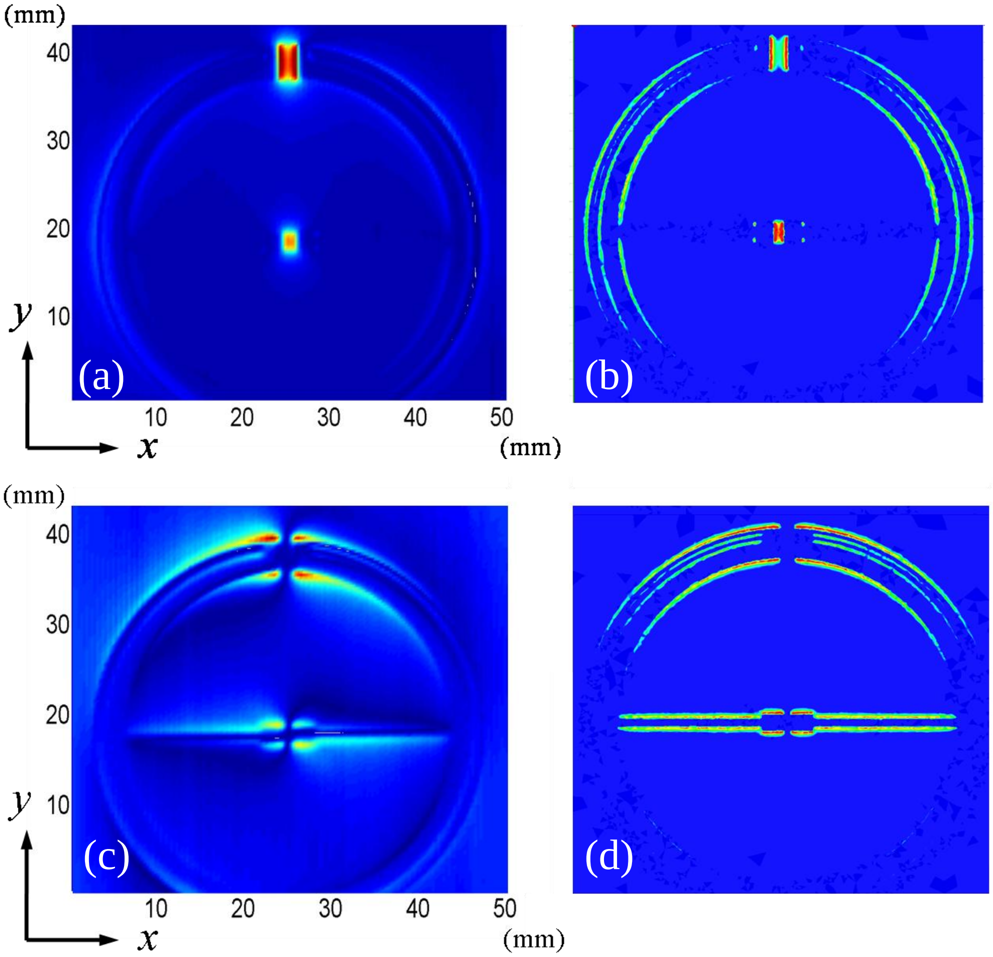

Figure 4.6: Transverse electric near-field distributions over the circular RFID antenna (top view, normalized amplitude with the same scale bar in Fig. 4.5), (a) measured transverse, *x* component; (b) computed transverse, *x* component; (c) measured transverse, *y* component; (d) computed transverse, *y* component. (Simulations were provided by Galen Chen).

The high frequency structural simulator (HFSS), v10, a three-dimensional, full-wave, finite-element method, was used to simulate the electric-field distribution for an ideal version of the circular RFID antenna at the resonant frequency. The HFSS simulated results of two orthogonal, transverse radiation distributions, the *x*-component and *y*-component, with a spatial resolution of 100 µm were shown in Fig. 4.6 (b) and (d), respectively. Considering the simulation was performed under perfect matching condition, as one observes, there is excellent agreement between the simulated and measured fields for both of the transverse components. The circular transmission traces radiate both *x* and *y* electric field components. The *x* (or *y*) component becomes stronger on the circular trace towards the horizontal (or vertical) direction as seen in Fig. 4.6.

The essential benefit of the signal down-conversion is to obtain the amplitude and phase information of the RF signal simultaneously. This is possible by utilizing a lock-in amplifier and an IF that falls within its bandwidth. One can also exploit the narrow pass-band afforded by lock-in detection to isolate the signal at the IF despite the wide bandwidth of the photodiode and its amplifier, the EO sensor, and so on.

The phase information from the RFID-antenna transverse-field components, which can provide valuable information on propagation directions and radiated polarizations, is shown in Fig. 4.7, in 2-D plots. Two predominant phase angles are observed along the two antenna ports, where the pair of dashed lines, at each scale bar, indicates the 180° phase shift. In the two dipole gaps on the plot of the *x*-component of electric field, the signals are seen to be in phase, and thus the polarization that will combine in the far field is identified. The energy in each part of the *y*-component, which is seen to be of high amplitude only at the edges of the microstrip lines, is always out of phase with that of neighboring parts of the *y*-component, indicating that this polarization will destructively combine in the far field.

The amplitude and phase analysis over the entire antenna also provides a detailed characterization of the antenna design. For instance, the 22 dB return loss of the antenna based on network analyzer measurements indicates the matching quality, but does not provide genuine field flows. When the antenna operates at the resonance frequency of 910 MHz with 22 dB return loss, the strongest fields are expected on the two terminal ports at the top and center of the DUT, as observed. The fields at the ports should also diminish rapidly as they propagate away from the terminals, as also seen in Fig. 4.6. The strongest fields are at the end of the horizontal lines (*x*-direction), and the fields drop rapidly and significantly as they move towards the feed side via the circular transmission lines. Therefore, the amplitude and phase analyses of the antenna using this near-field-mapping system are suitable for scrutinizing the matching and the design of the DUT.

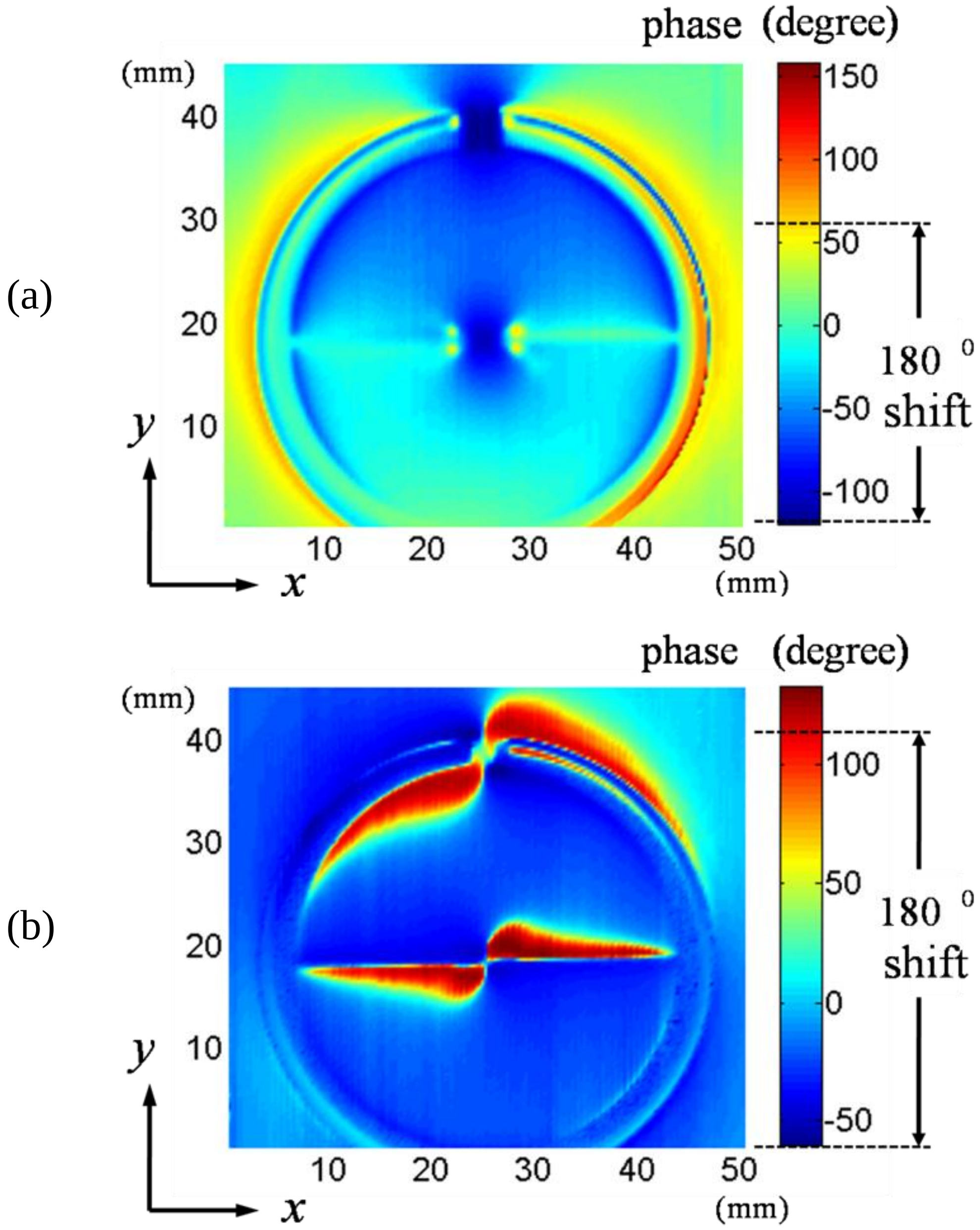

Figure 4.7: Transverse electric-field phase distributions over the circular RFID antenna (top view). (a) phase of transverse, *x*-component; (b) phase of transverse, *y*-component.

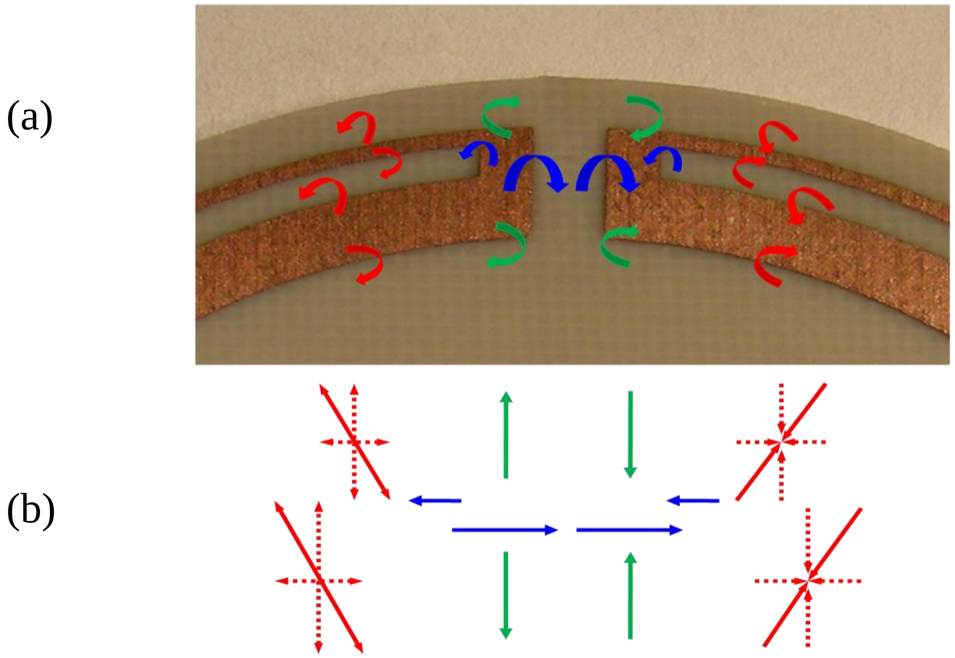

Figure 4.8: Electric near-field distributions over the primary RFID antenna terminal, (a) photograph (b) corresponding transverse vector components.

Concentrating on the most critical parts of the structure based on the full-antenna scans, the measured amplitude of the tangential electric fields for the primary and capacitively-loaded terminals are presented, respectively. The detailed distribution of vector near electric-field on the primary antenna port is presented in Fig. 4.8. The antenna has various transverse components such as *x* (blue), *y* (green) and their combinations (red) as illustrated in Fig. 4.8(b).

The corresponding *x* and *y* transverse vector electric fields ~300 µm above the primary antenna are shown in Fig. 4.9. The electric fields are initial radiation sources that essentially govern the far-fields. The dominant *x*-components (blue) are in phase and the dominant (green) and partial (red) *y*-components are out-of phase. Corresponding amplitude and phase-pair plots appear in Fig. 4.9 (a,c) and (b,d), respectively. Similar analysis and measurement are performed for the secondary capacitively-loaded antenna. Because of its rectangular structure, there are only discrete *x* (blue) and *y* (green) components as seen in Fig. 4.10.

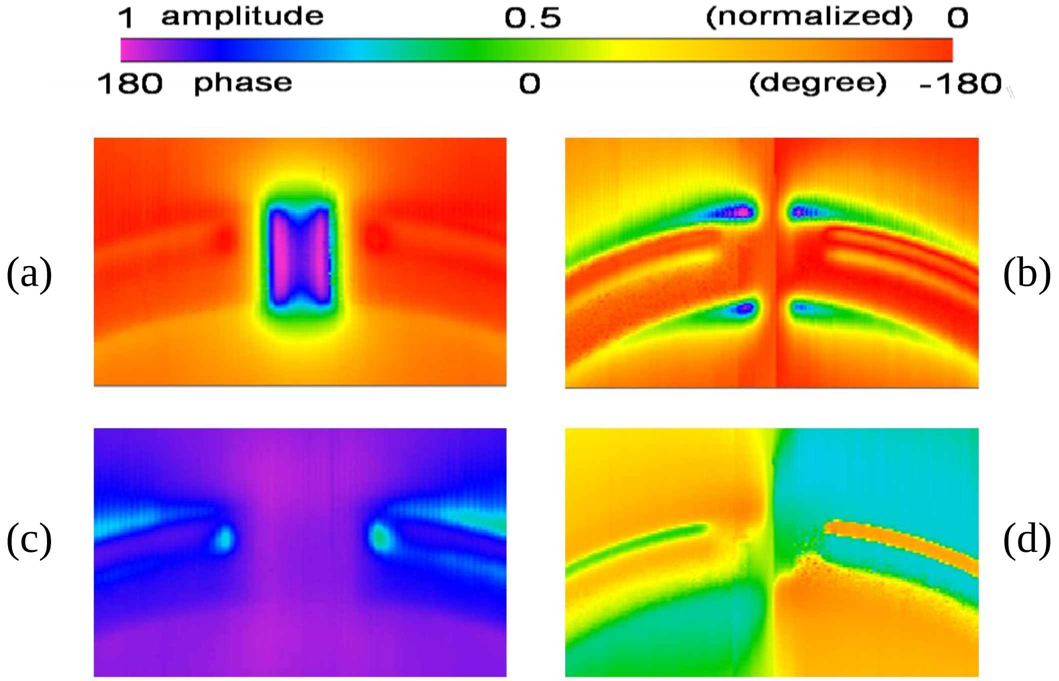

Figure 4.9: Transverse electric-field distributions over the primary antenna terminal, (a) amplitude of transverse, *x* component (b) amplitude of transverse, *y* component (c) phase of transverse, *x* component (d) phase of transverse, *y* component.

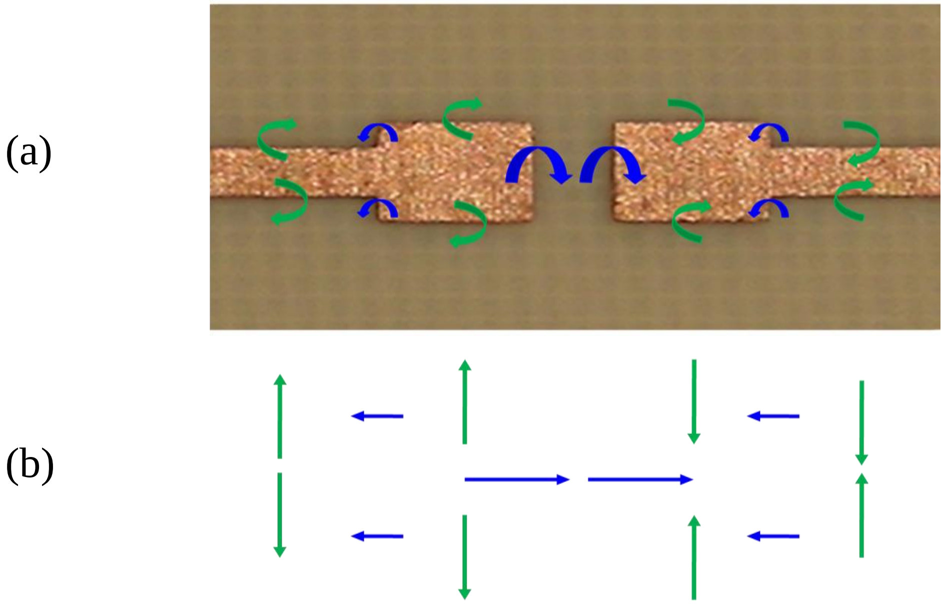

Figure 4.10: Electric near-field distributions over the secondary RFID antenna terminal. (a) photograph; (b) corresponding transverse vector components.

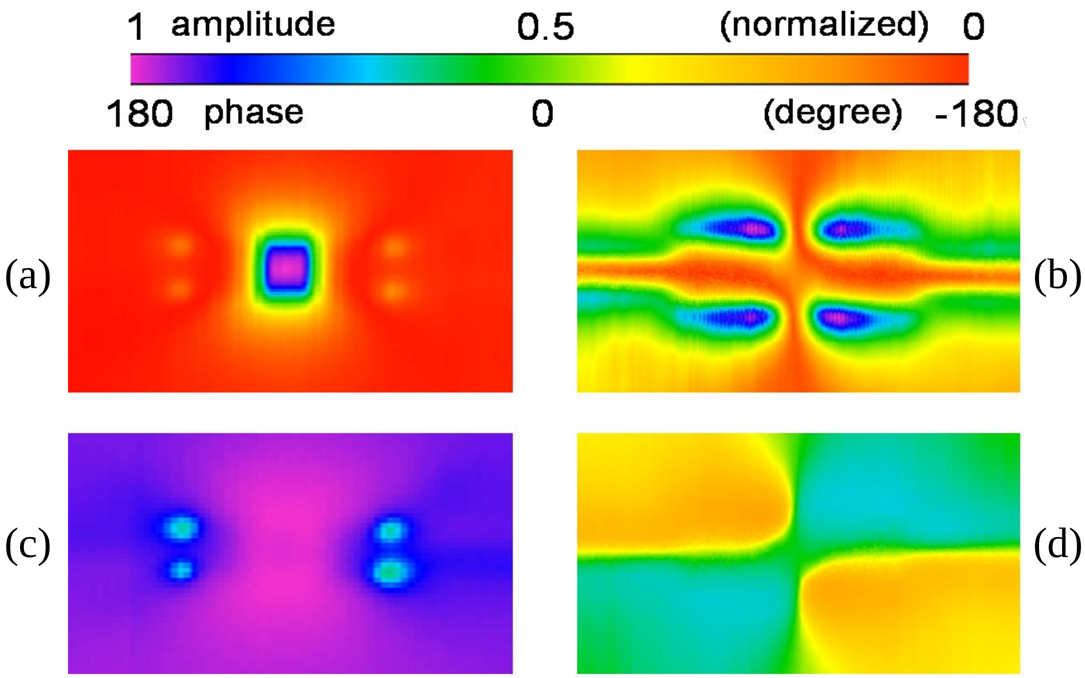

Figure 4.11: Transverse electric-field distributions over the secondary antenna terminal, (a) amplitude of transverse, *x*-component; (b) amplitude of transverse, *y*-component; (c) phase of transverse, *x*-component; (d) phase of transverse, *y*-component.

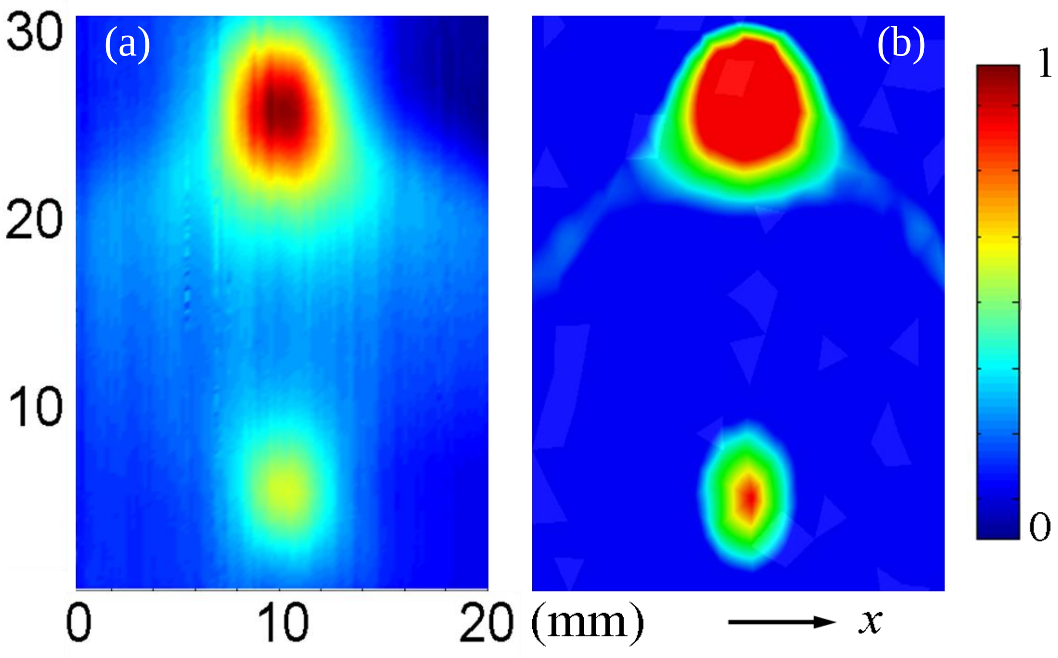

Figure 4.12: Transverse *x* electric-field distributions 5 mm above the two antenna terminals (normalized, 1 ~ -60 dBm, 0 ~ -88 dBm of photodetector output); (a) measurement; (b) simulation.

The strong *x*-direction fields at the two terminals yield evidence of efficient radiation due to good impedance-matching on-resonance. The dominant *x*-components (blue) and *y*-components (green) in the secondary port are in and out-of phase, respectively, as seen in Fig. 4.11 (a,c) and (b,d). Hence, the overall *x*-components are constructively added up whereas the *y*-components are destructively cancelled out as they propagate through air.

To expand the utility of the near-field measurements, the directionality and pattern of the near-field radiation components may also be extracted. For instance, Fig. 4.12 is the *x*-components ~5 mm above the two radiation ports. As opposed to the *x*–components in Figs. 4.9 and 4.11, where individual seminal fields were observed, only the surviving (non-cancelled) dominant field components are radiating from the two ports with the same phase.

The two radiation sources can be considered virtually as a single point source as observed from the far-field, where mainly the linearly polarized *x*-components propagate, while the *y* components will are mainly cancelled. In this case, the antenna behaves like a single folded-dipole antenna, so its radiation pattern would be a conventional, ‘donut-shaped’ pattern. Fig. 4.13 is the radiation pattern (TE plane) of the whole antenna measured with a conventional far-field measurement method. Since the electric field is already specified with the *x* direction, and *z* is the radiation direction for TEM propagation, the *x*-*z* plane is the TE plane. The TE radiation pattern shows slight beam steering which is possibly due to the unbalanced field strength between the primary and secondary ports. Fig. 4.14 is the radiation pattern in the TM plane (*y*-*z* plane). There is no azimuthal angle dependency, as expected. Therefore, the radiation pattern of the proposed antenna, as is shown in Figs 4.13 and 4.14, has the same characteristics of radiation as a conventional folded-dipole antenna.

The antenna gain is 0.04 dBi, and this gives 2.4 m of read range at +30 dBm, which is the typical maximum transmission power level for mobile phones.

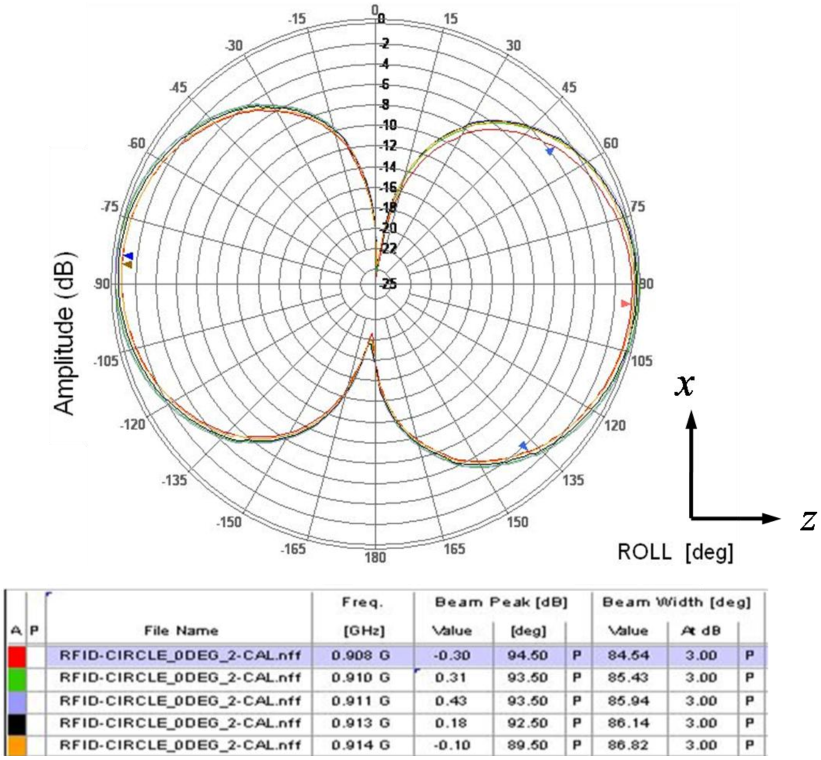

A	P	File Name	Freq. [GHz]	Beam Peak [dB] Value	Beam Peak [dB] [deg]		Beam Width [deg] Value	Beam Width [deg] At dB	
🟥		RFID-CIRCLE_0DEG_2-CAL.nff	0.908 G	-0.30	94.50	P	84.54	3.00	P
🟩		RFID-CIRCLE_0DEG_2-CAL.nff	0.910 G	0.31	93.50	P	85.43	3.00	P
🟦		RFID-CIRCLE_0DEG_2-CAL.nff	0.911 G	0.43	93.50	P	85.94	3.00	P
⬛		RFID-CIRCLE_0DEG_2-CAL.nff	0.913 G	0.18	92.50	P	86.14	3.00	P
🟧		RFID-CIRCLE_0DEG_2-CAL.nff	0.914 G	-0.10	89.50	P	86.82	3.00	P

Figure 4.13: Radiation patterns of the circular RFID antenna (TE plane, 908~914 MHz).

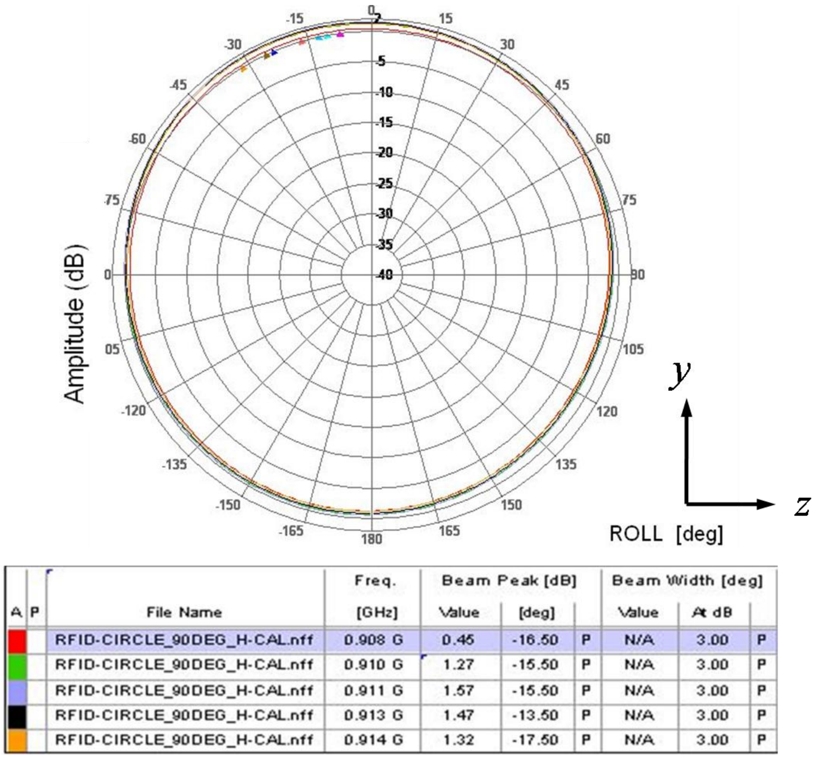

A	P	File Name	Freq. [GHz]	Beam Peak [dB] Value	Beam Peak [dB] [deg]		Beam Width [deg] Value	Beam Width [deg] At dB	
🟥		RFID-CIRCLE_90DEG_H-CAL.nff	0.908 G	0.45	-16.50	P	N/A	3.00	P
🟩		RFID-CIRCLE_90DEG_H-CAL.nff	0.910 G	1.27	-15.50	P	N/A	3.00	P
🟦		RFID-CIRCLE_90DEG_H-CAL.nff	0.911 G	1.57	-15.50	P	N/A	3.00	P
⬛		RFID-CIRCLE_90DEG_H-CAL.nff	0.913 G	1.47	-13.50	P	N/A	3.00	P
🟧		RFID-CIRCLE_90DEG_H-CAL.nff	0.914 G	1.32	-17.50	P	N/A	3.00	P

Figure 4.14: Radiation patterns of the circular RFID antenna (TM plane, 908~914 MHz).

4.4 Summary

A very simplified high frequency electro-optic field-mapping system that employs a high speed photodetector and electrical mixer to realize practical electrical down-conversion was developed. This electrical down-mixing technique, combined with an efficient resonance-based probe, was proven to be suitable for scrutinizing near fields to evaluate the performance of microwave devices or explore the evolution of radiation from the antennas radiating ports. Effective tangential-electric-field characterization in the near field of RFID antennas was demonstrated with a >35 dB signal-to-noise ratio.

CHAPTER 5

EXTENDED-FREQUENCY NEAR-FIELD SENSING WITH OPTICAL-HETERODYNE DOWN-CONVERSION

5.1 Introduction

In order to accommodate rapid increase of the communication channel demand, the bandwidth of modern wireless technology has been greatly expanded enough to cover the entire microwave regime. Thus the finite spectrum that is suitable for the wireless applications can be fully utilized. To characterize near field radiation performance of wireless devices, direct electro-optic (EO) sensing based on continuous-wave (cw) lasers is a good solution, especially for low-frequency-band applications as presented in chapters 2 and 3. For practical, higher-frequency sensing, such as at the ~910 MHz of the mobile phone band, the electrical down-conversion technique was successfully applied to the direct sensing method in chapter 4.

Although direct sensing is a simple and efficient method, its frequency range is fundamentally limited by the speed of the photodetector employed. Since the cost-functional effectiveness of a detector degrades rapidly for higher frequencies, the electrical conversion method, where cw lasers are coupled with fast photodetectors, loses its merit for higher frequency sensing applications. To realize very fast EO sensing with a slow detector, photonic down-mixing is the primary solution. One confirmed method is the so-called harmonic-mixing technique, which utilizes higher orders of harmonic components in an expensive pulsed laser as an optical beating source [1,2,9]. This chapter presents another photonic down-mixing technique that can be effectively achieved by a cw-modulated beam with an amplitude modulator.

This photonic heterodyne-down-mixing technique is applied to a practical, higher-frequency, EOS system using a low-cost, cw-pigtailed laser diode and an all-fiber-guided optical communication embodiment. In addition, the resonance-based probe, used in previous chapters 3 and 4, provides reliable, efficient and simplified optical-system realization. The system is suitable for scrutinizing RF near fields in order to evaluate the performance of high frequency microwave devices. The full vector near field characterization of an X-band patch antenna is provided as an example of the pertinence of the measurement method.

5.2 Experimental System and Results

Unlike the Harmonic-mixing technique [1,2,9], which utilizes the harmonics of the repetition rate of a pulsed laser as a local oscillator (LO), a method proposed by Kuo [44] and improved by Sasagawa [45] has been adopted to our resonance-based technique for high-frequency antenna characterizations. Here, a cw laser is modulated by a conventional electro-optic modulator (EOM), which imparts a sideband onto the optical beam for use as an LO to mix down, within the EO probe, the signal frequency to an intermediate frequency (IF). Combining this mixing process with the cavity-enhancement effect, we present, to our knowledge, the first use of an all-fiber enclosed, resonance-based, heterodyne-down-conversion, EO-sensing embodiment.

Figure 5.1 displays the experimental setup of this new EO field-sensing implementation. An inexpensive, fiber-pigtailed, temperature-tunable, cw laser diode was coupled with the resonant EO sensor, resulting in a significant simplification of the conventional EO optical-polarization-control configuration. That was, the polarizer/analyzer pair and the quarter waveplate employed for nearly all other EO-modulation sensors were eliminated, as previously described in chapters 2 and 3. Modulated laser light (with average power of 8 mW) was delivered to a $LiTaO_3$ probe (balanced 5 layer coating optimized for 1560 nm) having $r = 0.81$, and the EO-modulated beam returning from the probe was routed to the detector through a fiber-optic circulator. The experimental EO signal peak was observed at a wavelength ‘bias’ of 1562.1 nm, where it experienced the highest slope of the modulation response (Fig. 4.2 in chapter 4).

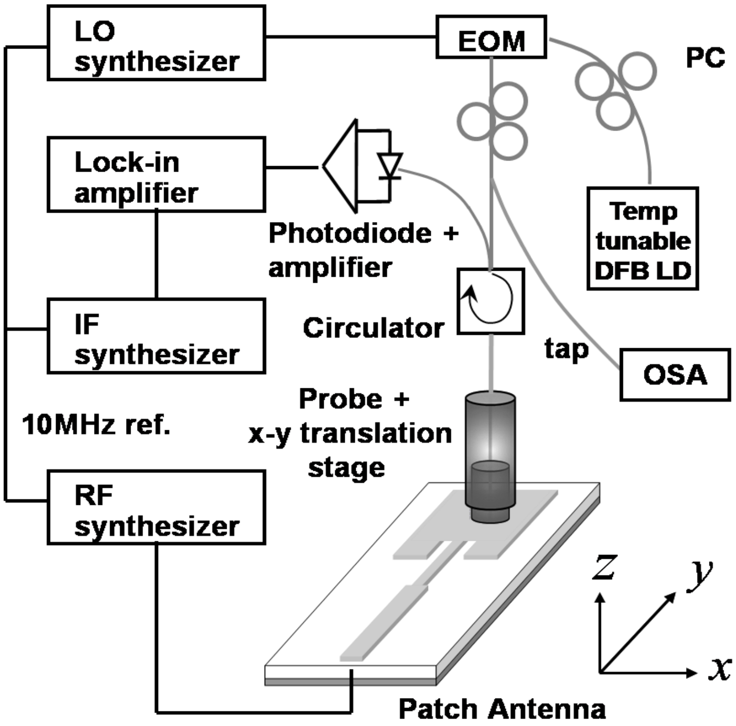

Figure 5.1: Experimental setup of the all-fiber, resonance-based, photonic-heterodyne-down-conversion, EO-probing system using modulated cw light. (The gray and black lines are optical fibers and electrical connections, respectively).

As the wavelength was shifted away from the maximum slope and the destructive wavelength, λ_d, the EO signal was observed to decrease due to the reflection slope becoming more shallow, while noise increased in response to the increased reflected light intensity. The signal and noise levels converge to a finite value as the slope flattens.

Figure 5.2 suggests the limits of the high speed response of the resonant EO probe, as determined by the increasing photon lifetime in the EO etalon with cavity quality factor. The figure is generally valid for an arbitrary thickness of the resonator with balanced reflections of $r = 0.81$. The temporal response shows heavy spectral dependency based on the resonance conditions. For instance, with crystal thickness d, the round trip phase delay is $\delta = 4\pi nd/\lambda$, a function of wavelength which, by its presence in the exponent of the term, $exp(i\bullet\delta)$, governs the duration and shape of a transient response as well as a steady-state response [46, appendix B]. The transient responses typically converge to the steady-state values after several round-trip delays, τ, although the duration of the transient response has heavy spectral dependency. For the 52 µm, resonant $LiTaO_3$ EO probe, the τ value is 756 fs, and the first five to seven round trips are sufficient to nearly reach the full interferometric condition at the peak EO signal wavelength, λ_{eo}. This time scale (~4-5 ps) is sufficiently instantaneous to sample 100 ps of a high-speed periodic signal, such as a 10 GHz RF sinusoid, with high fidelity. It is within this microwave X-band range that we demonstrate the system and resonant probe of Fig. 5.1.

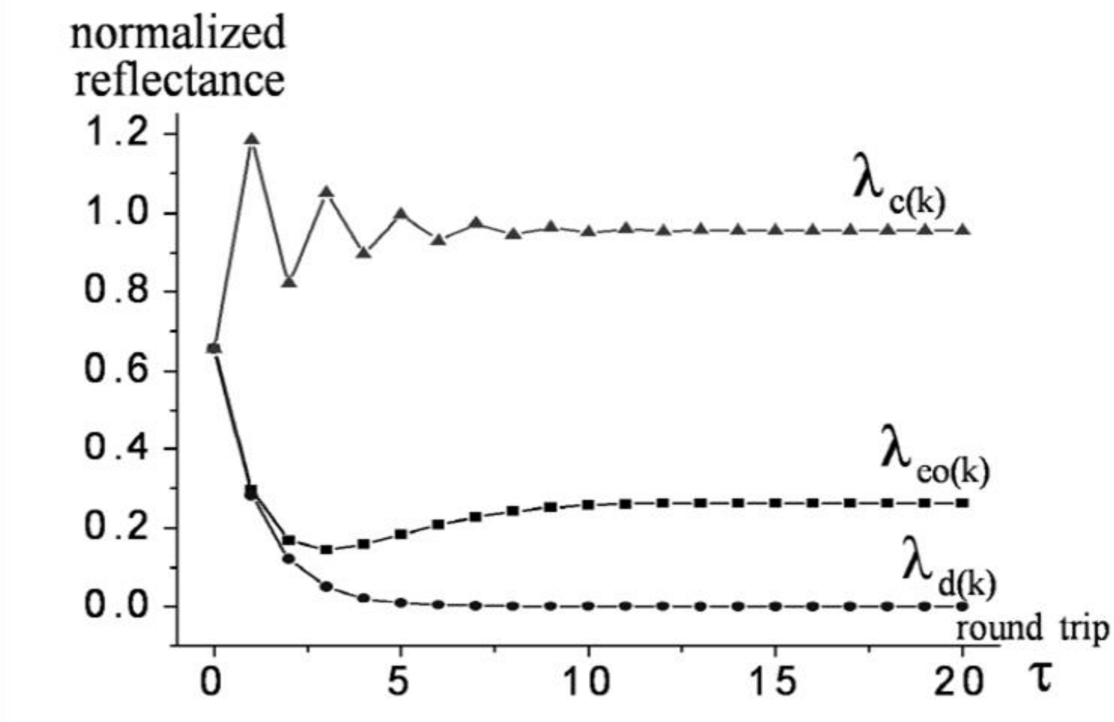

Figure 5.2: Transient reflectance responses of a balanced resonator (r = 0.81) vs. photon round-trips in the etalon at constructive, peak-EO-signal, and destructive wavelengths, respectively (λ_c, λ_{eo} and λ_d).

Numerous field-mapping scans were conducted on a recessed-feed patch antenna with a quarter-wavelength transformer to facilitate impedance matching, and the patterns captured show how the electric near-field distribution can be used to examine the quality of the impedance match and the aperture-level field behavior. To first identify the resonance characteristics of the antenna, the scattering parameter S_{11} was measured over a 2 GHz bandwidth on a network analyzer (Fig. 5.3). The minimum return loss was determined to be 9 dB at a frequency of 10.485 GHz (point **c**).

For the EO characterization, we first measure an arbitrary, highly mismatched frequency (point **a**, at 11.26 GHz) where a VSWR of 32.5 was expected to yield a strong standing-wave pattern. To measure 11.26 GHz, the cw laser wavelength is set at the most efficient bias wavelength (1562.1 nm) and modulated via the external EOM at 11.263 GHz. This provided a 3 MHz IF signal after the optical sideband was mixed with the microwave signal in the EO probe. The resultant measured tangential components of the near electric field at the DUT frequency of 11.26 GHz are presented in Fig. 5.4, along with a photograph of the actual DUT.

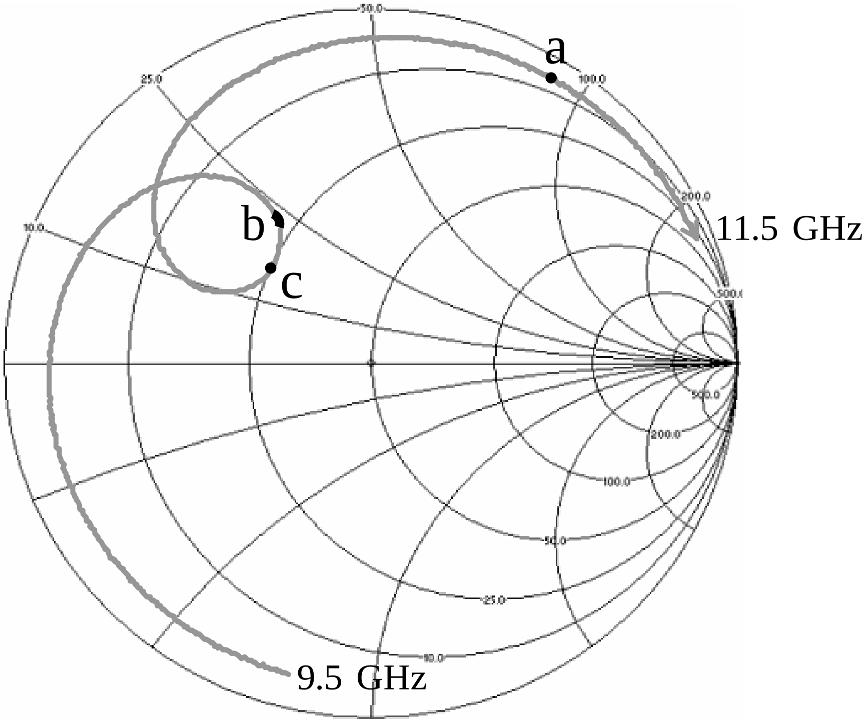

Figure 5.3: S_{11} of the DUT patch antenna. (Point **a**: highly reflective point at 11.26 GHz; point **b**: narrow band close to the minimum return loss at 10.438-10.446 GHz; point **c**: minimum return loss at 10.485 GHz).

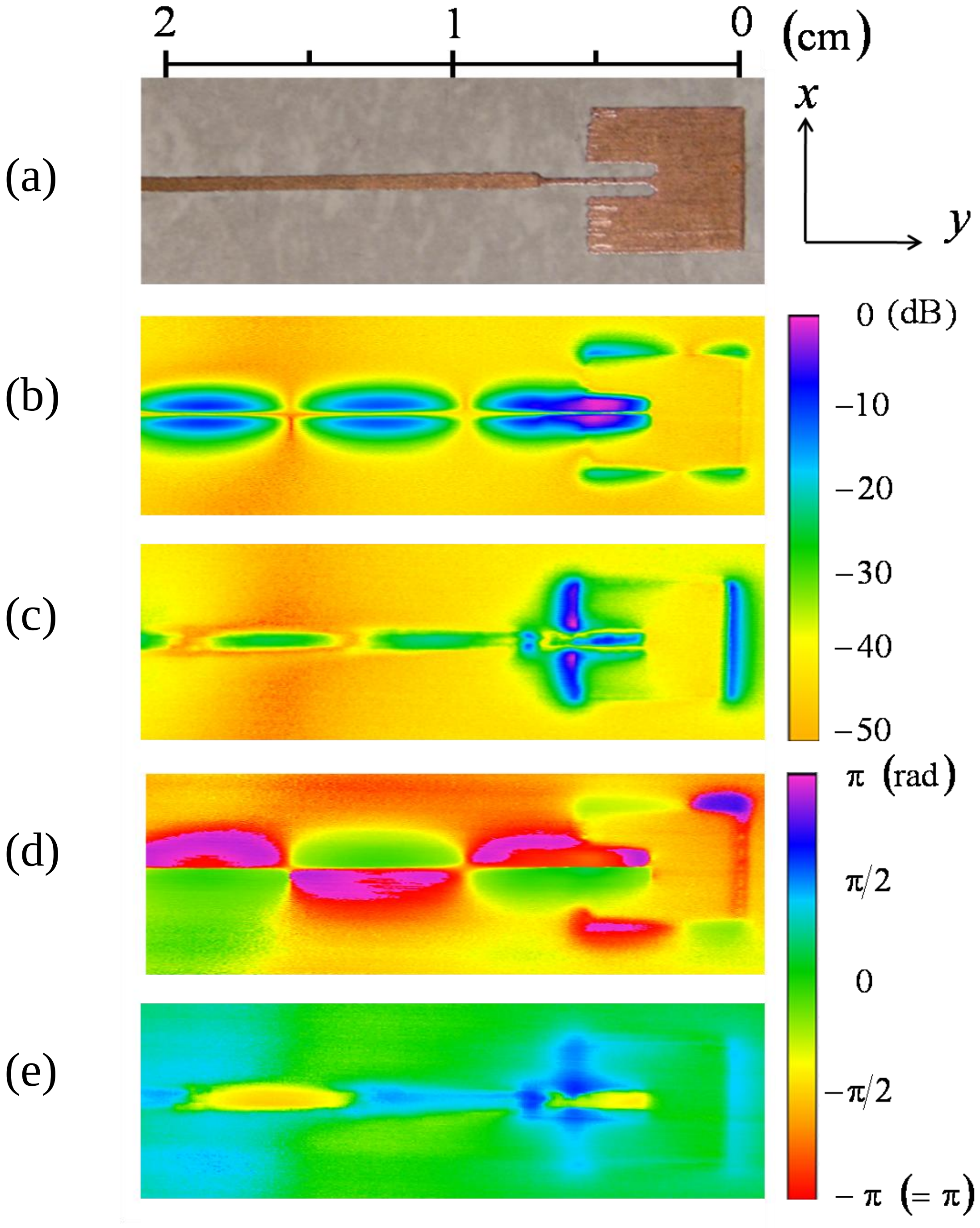

Figure 5.4: Tangential near field patterns of a patch antenna at point **a** (log scale). (a) photograph and dimension of the DUT; (b) amplitude of *x* and (c) *y* electric-field components; (d) phase of *x* and (e) *y* components.

The scan area is 22 mm × 8 mm, and a 40 μm step resolution was used. With such fine scanning steps and a 10 μm spatial resolution for the probe, a sampling area of much less than 100 μm was realized, and the probe easily resolved the 200 μm width of the narrow transformer line. Figure 5.4 (b, c) shows two orthogonal tangential electric-field amplitude distributions at the highly mismatched frequency of point **a**. The probe is nearly 50 μm above the DUT, which is fed with +15 dBm of RF power. As expected, the majority of the input power is not delivered through the matching line and is reflected back to create a strong standing wave. This is observed in the *x* and even *y* components as a higher order mode. Each vector field component shows a 50 dB SNR and the absolute EO-signal-peak point is -36.1 dBm for the *x* component. The phase, also shown in Fig. 5.4(d, e) alternates for each standing-wave peak by 180°, and the 5 mm length of each standing-mode cycle, partially residing in the substrate, is a reasonable spacing for the 11.26 GHz input. The standing pattern decreases significantly as the input frequency approaches the antenna resonance. For instance, the field distributions for the narrow band (10.438~10.446 GHz, VSWR ~2.7) at point **b** are shown in Fig. 5.5. The patch DUT exhibits a stronger and more distributed field pattern for the guided signals, while supporting a diminished standing wave. In addition, the relatively rapid transition over the circular-resistance and parabolic-reactive traces on the Smith chart indicates large impedance changes even over the narrow band.

The S_{11} trace on the chart contains strong impedance evolution versus frequency. In other words, the amplitude and phase of the reflection, S_{11}, is only another transformation of impedance which controls the frequency-dependent signal flow. Although the frequency-dependent device impedance, $Z(\omega)$, governs the radiation characteristics of the antenna, the S_{11} (or $Z(\omega)$) trace from a network analyzer measurement is not enough to explore the detailed, impedance-dependent, full near-field distributions.

The evolution of the field distribution versus the sampled frequencies in band **b** is also demonstrated in Fig. 5.5. The change in symmetry and the variation in signals peaks on the feed line are noted, along with the fact that such a detailed high frequency distribution is virtually impossible for a conventional finite-element-based simulation method to compute quickly.

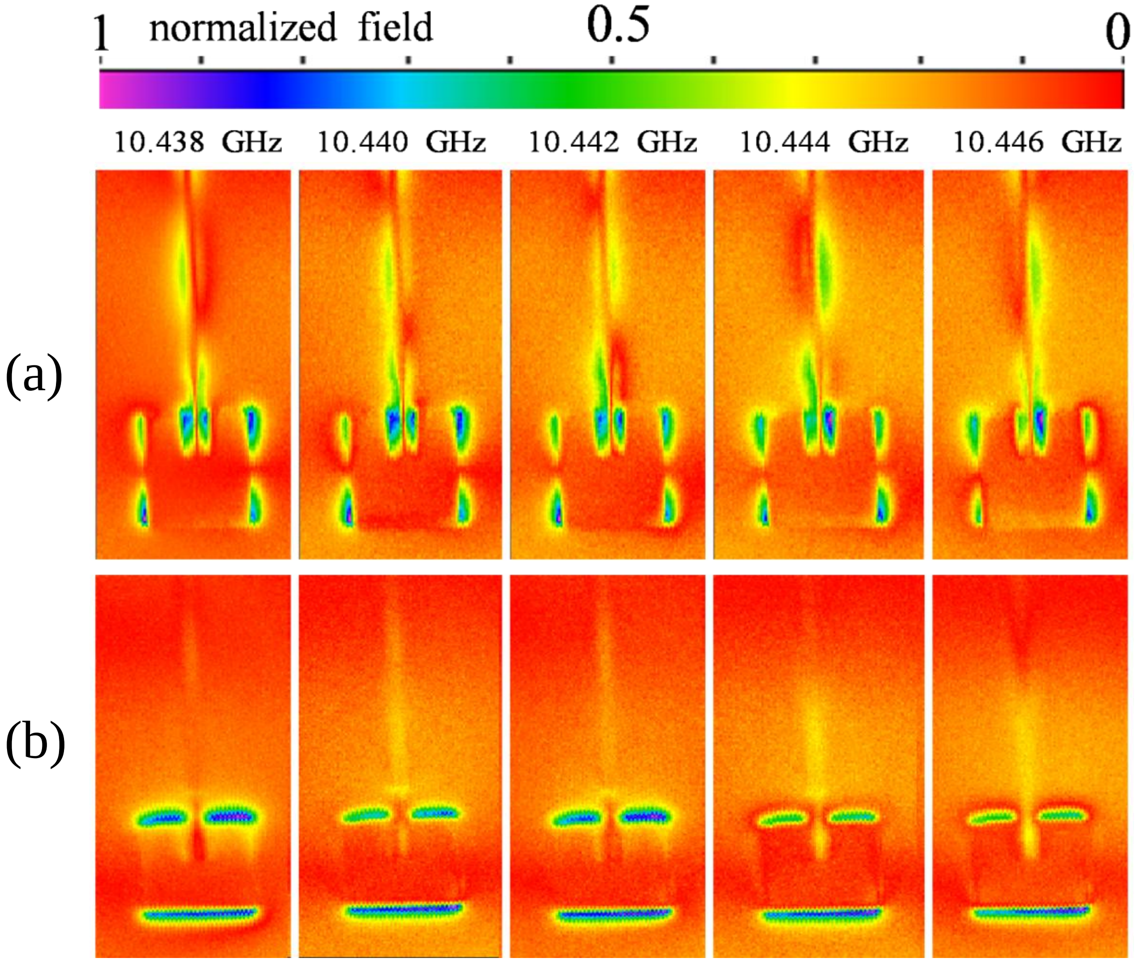

Figure 5.5: Tangential electric near-field patterns of a patch antenna at band **b** (normalized linear scale, 0.1 mm scanning resolution). (a) evolution of *x* component and (b) *y* component of electric field vs. frequency.

The radiation pattern has the lowest return loss at 10.485 GHz (point **c**), and the near-field scan is presented in an oblique view in Fig. 5.6. The most efficient radiation condition does not necessarily promise a uniform distribution of the electric field over the DUT. Since the near field is the fundamental basis of the far-field pattern, the near field can be a crucial clue to the mid- and far-field evolution of radiation. Asymmetric distributions in the near field could cause undesired beam steering and far-field distortion. Such non-uniform fields can be adjusted more evenly by fine frequency tuning, as seen in the 10.442 GHz example shown in Fig. 5.5.

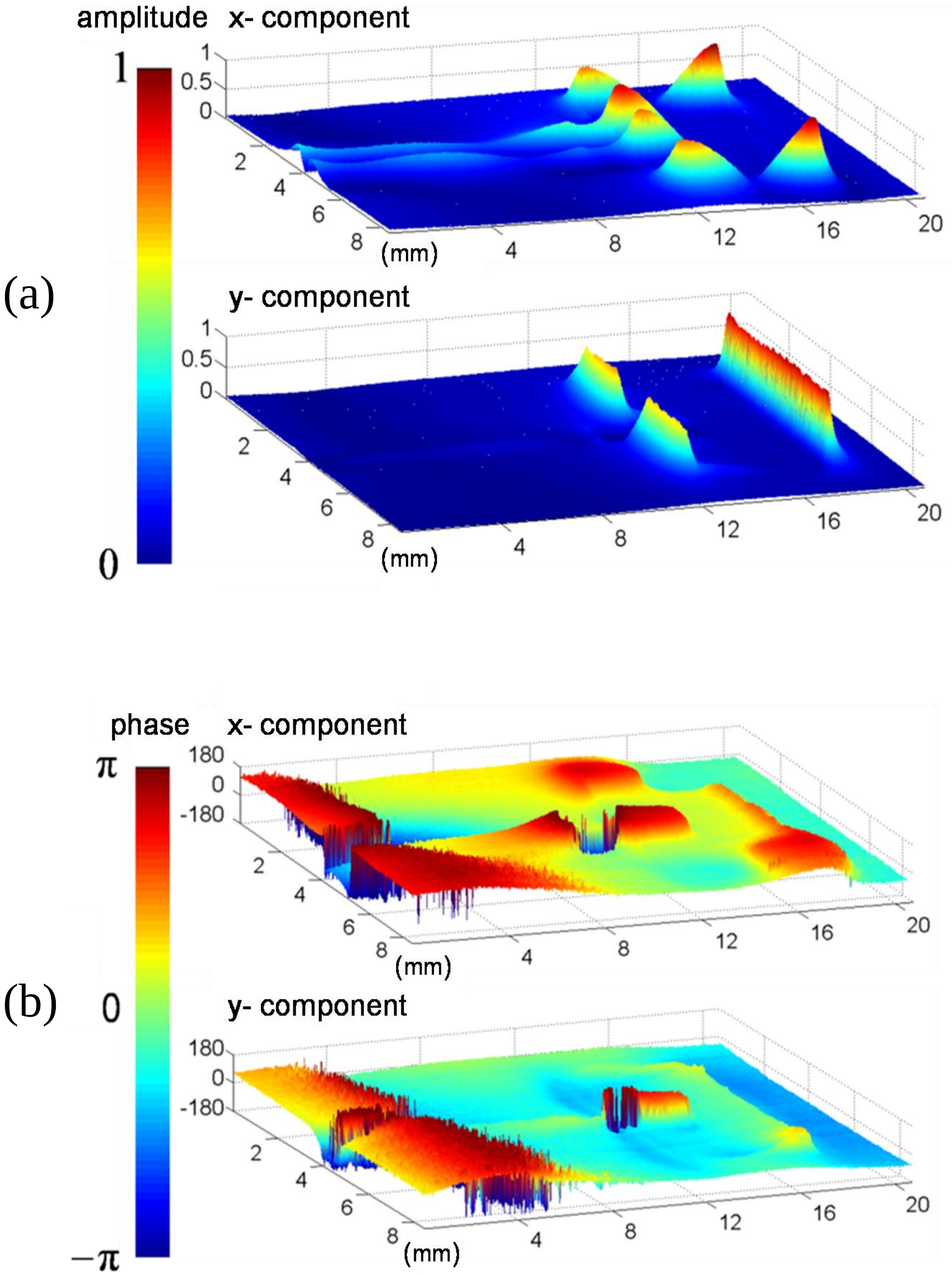

Figure 5.6: Tangential near-field patterns of a patch antenna at point **c** (normalized linear scale, 40 µm scanning resolution). (a) electric-field amplitudes and (b) phases, for both *x* and *y* components (noisy part results from loss of phase lock on lock-in amplifier at low signal amplitude).

Furthermore, this near-field characterization is useful for planar arrayed antenna designs. The interplay of phased-array elements can modify whole-beam-pattern parameters such as directivity or steering. For instance, imaging the patterns of Fig. 5.5 as a five-arrayed-antenna set, the analysis of each unit antenna can be a strong tool for evaluating the desired radiation performance of the whole antenna set.

5.3 Summary

A photonic heterodyne-down-mixing technique was applied to a practical, higher-frequency, electro-optic sensing system that is suitable for scrutinizing RF near fields in order to evaluate the performance of microwave devices. Using a low-cost, cw-pigtailed laser diode and an all-fiber-guided optical communication embodiment, the resonance-based probe provides reliable and simplified optical-system realization. The system offers very detailed full near field distributions for higher frequency radiation devices.

CHAPTER 6

OPTIMIZATION OF DOWN-MIXED SIDEBAND MODULATION

6.1 Introduction

More than 5 dB enhancements of the signal-modulation-depth, compared to the results in the previous chapters, are achieved without increasing the complexity of the system in chapter 5. The modulation sidebands are optimized both in an electro-optic modulator and a micro electro-optic sensor. The principle and method of optimizing operational bias points for the devices are described from the point of view of both an electro-optic modulator and sensor, and their different optimum characteristics for signal-modulation depth, due to their huge scale gap, are presented. The practical limitation for the sensitivity enhancement due to asymmetric field distortions, its solution to compensate distortions, and combined optimization conditions for both electro-optic modulation and sensing are presented by exploring the evolution of field-mapping distributions.

6.2 Optimization Principle

The EO effect, has been an essential and valuable phenomenon for controlling or modulating the transmission of light, imparting sidebands adjacent to the carrier. This is because the phase-modulated light, due to the EO effect, can be transformed into an intensity-modulated output in various ways. One popular method is the interferometric EO light modulation, where the transmission can be controlled within the range of an interference fringe. Typically one of two optical paths is phase-modulated by the EO effect, and thus the intensity of light can be controlled in a huge dynamic range of the interference patterns.

In contrast to the EOM, where intense electric fields are applied across conductive electrodes, in the EOS technique, a considerably lower-amplitude, free-space electric field is introduced across the EO medium without the use of electrodes. As introduced in chapter 1, such small electric fields induce a minute phase retardation that is transformed into a light-intensity modulation through the use of polarization components. The modulated light thus contains information on the applied electric field due to interaction with the light in the EO crystal. By this principle, the characteristics of the applied field could be inferred from the field-dependent light modulation.

The sensitivity-performance of an EOS system is primarily evaluated by its modulation depth (*i.e.,* signal strength over noise or minimum detectable signal). In photonic down-mixing, as described previously, an optical-heterodyne technique is employed in which a light source is 'pre-modulated' in an external EO device [24,30,47,48] before interrogating the signal to be measured in a second EO device (the EO sensor).

The modulation depths are determined by modulation biases that are typically electrical and angular values controlled by a voltage source and waveplate for the EO modulator and sensor cases, respectively. Typically, these biases are set for a half-wave voltage (V_π) and 45 degree for the each case to give transmission values of 50% [32]. In the previous chapters, rather than adopting such a conventional scheme, we used a resonance-based system where a laser wavelength served the role of a spectral bias, replacing the conventional, waveplate-based angular bias [23,24,26,30].

In this chapter, a model for the optimization of both the voltage bias of the external EOM that provides the LO photonic beam and the spectral bias that determines the EO sensor RF modulation characteristics is presented. In addition, a comprehensive experimental survey of the effects of the changes in the 'pre-modulator' DC-voltage bias and the EO-sensor laser-spectrum bias on the ability of the sensor to map microwave electric fields above an antenna is presented. By observing the evolution of the quality of the high-spatial resolution microwave field maps for different modulator operating conditions, practical optimum SNR conditions compared to conventional modulator operating conditions are determined. The large scale difference between huge LO and minute RF sideband modulations causes field distortion in LO sidebands, while the RF sidebands are not affected. To overcome and even utilize the nonlinearity, a novel technique to balance and compensate an asymmetric distortion is presented, with an observed benefit to noise suppression. The practical signal-modulation-depth enhancement range and a procedure for the combined optimization of the LO and EO modulator operating points are also discussed.

6.3 Pre-Modulation Optimization: LO sidebands

In order to optimize the EO sensing of an applied electric field in a heterodyne down-mixing configuration, it was first necessary to optimize the creation of the side band to be used as the LO signal. In such photonic-down-mixing systems, an EO amplitude modulator (*i.e.*, the pre-modulator) produces LO double-side bands on either side of the carrier wavelength. Because the sidebands correspond to modulation strength and frequency, the modulation depth can be specified by the sideband strength per unit carrier power (*i.e.*, carrier-to-sideband ratio). The enhanced modulation depth in the LO sideband will eventually be manifested as a stronger IF signal after mixing with the photonic LO in the EO sensor. The EOS system employed is the same as the photonic-heterodyne one used previously for the high-frequency (X-band) microwave field mapping [24,30]. Again, a cw telecom distributed-feedback (DFB) laser was externally modulated by a conventional Mach-Zehnder EOM (a JDS Uniphase OC-192 device) to impart the LO sidebands onto the optical carrier.

To respond to the microwave fluctuations (or modulations) emerging from an analyzer, the detector has to have sufficient bandwidth to cover the frequency at which the field varies. The photonic-down-mixing technique extracts the same high-speed RF information from the DUT, but after mixing with the LO components on an optical carrier, the signal resides at the lower IF-signal frequency. Thus only a low bandwidth photodetector is required.

It should be noted that the IF component originates from the beating of only the LO and the RF sidebands, and not from the carrier component. Hence, although the strength of the LO/RF sidebands is proportional to the carrier intensity, enhancement of the sidebands by supplying a higher carrier power is not recommended. This is because the carrier, which is usually the dominant intensity of the sensing light beam, is a major source of noise. [23,32]. As a result, it is crucial to maximize the performance of the input light modulation (*i.e.*, the LO) per unit carrier power during heterodyne-based EOS optimization. The ideal modulator for this case would be one having a bandwidth reaching the operating frequency of the DUT, with 100% modulation depth and minimal nonlinearity (*i.e,* spurious-free operation).

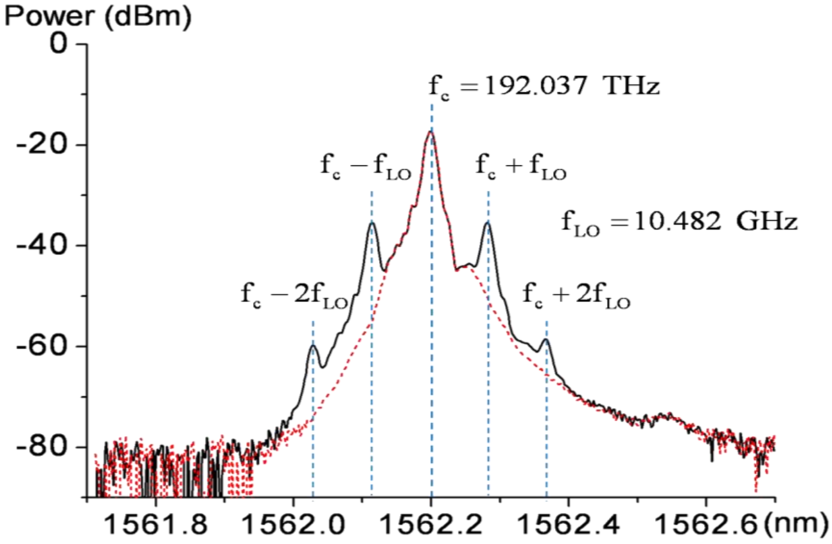

Figure 6.1: Modulated spectrum of the laser at 1562.2 nm from an EOM. (DC bias = V_π, RF driving power = 14 dBm with a 10.482 GHz LO frequency. The dashed red curve is without the RF bias).

Typically, an EOM is operated at the centro-symmetric half transmission voltage V_π to minimize nonlinearity-related higher-order distortions. In our system, the EOM modulates the ~1560 nm band of the DFB laser with an LO frequency of 10.482 GHz. This is done in order that the field from an X-band patch antenna, with a resonant radiation frequency of 10.485 GHz, can eventually be sensed using the photonic-down-mixing method. Thus, the signal at the 3 MHz difference frequency between the LO and RF contains the signal information, and a stronger, or more efficiently modulated optical beam (LO), will serve to increase the IF beat signal from the sensor.

To explore the quality of EO sensing under different bias conditions for the LO-sideband modulation in an EOM, we examined electric fields from an X-band patch antenna using a fiber-coupled, $LiTaO_3$ EO probe. The probe has unique resonant characteristic by means of a balanced Fabry-Perot resonator, as introduced in chapter 3.

As its spectral resonance curve gets perturbed when the EO crystal experiences electric fields, setting the laser line at the most perturbative spectral regime (*i.e.*, the steepest slope) realizes highly efficient and maximized EO amplitude modulations [23,24,26,30]. For instance, the 1562.2 nm laser spectral bias (Fig. 6.1) provides the strongest EO signal, where the laser wavelengths act as EO biases, the same as waveplate-based angular biases in a conventional system.

For higher frequencies, the modulation depth becomes smaller because of its finite EOM bandwidth, and this can be computed from the carrier-to-sideband ratio (CSR). As the laser wavelength at 1562.2 nm is modulated with 10.482 GHz of LO frequency, the corresponding spectra have carrier frequency, f_c (= 192.037 THz) and double-sided modulation bands, f_s (= $f_c \pm f_{LO}$) as shown in Fig. 6.1. The CSR at the V_π bias is 18 dB, which corresponds to ~25.1% of the modulation depth. Although this partial modulation is from the degradation of the EOM performance, the modulation depth can be further increased by reducing the CSR. To realize this, it is important to suppress the carrier while maintaining the modulation as much as possible. For instance, transitions from the typical half transmission bias, $(2n+1)V_\pi$, (*i.e.*, the point ***c*** in Fig. 6.2) to the minimum power bias, $4n\ V_\pi$, (*i.e.*,point ***h*** in Fig. 6.2) reduce the CSR significantly.

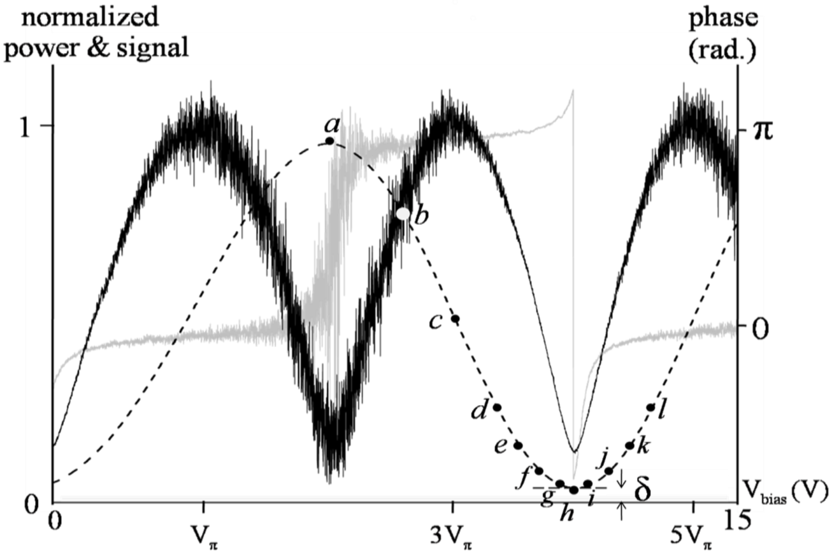

Figure 6.2: Measured transmission power curve for the pre-modulated light beam (dashed line) and the resulting measured EO amplitude (black solid line) and phase (gray solid line) that correspond to the different EOM operating points. (***a-l*** are a selection of discrete DC bias and EOM operating points to be investigated). The actual transmitted power at point ***c*** is 9 mW; the actual peak EO signal level is -52.5 dBm.

Figure 6.2 presents the experimental transmission curve from the EOM and the corresponding EO signal amplitude and phase. The signal was measured at the strongest point over the DUT and each trace is normalized for convenience. Sweeping the DC bias from the EOM 0 to 15 V covers five V_π points and the black and gray traces are EO signal amplitude and phase, respectively, measured during the sweep. The EO signal strength is basically a derivative of the sine-squared modulation curve. Thus, the signals are alternately maximum (minimum) for every odd (even) V_π bias value. The signal toggles its sign (*i.e.*, phase) where it changes the sign of the slope via the turning points (***a*** or ***h***). We set a small measurement time constant (10 ms) on a lock-in amplifier to exaggerate and scrutinize the intensity fluctuation of the signal, which is basically proportional to the laser intensity. For this reason, the signal at the upper half of the transmission curve is considerably noisier than that of the lower half case.

Figure 6.2 explains the strong relationships between both signal and noise and the DC modulation bias. This bias determines the modulation depth (*i.e.,* CSR) and the light intensity (approximately the carrier power). For instance, the signal levels at bias points ***b*** and ***d*** are comparable, but the noise-fluctuations are significantly different due to the three times higher carrier power for the former bias point. In addition, comparing the signal level at the bias yielding the largest EO signal (point ***c***, where the modulator transmission is 50%) and the bias point ***d*** (where the light transmission is decreased by half), the EO signal level drops only 20% even though the light transmission is significantly lower. This indicates that the signal per unit power can be increased by optimizing the bias point. Moreover, since the noise from the laser-intensity fluctuation is proportional to the laser power level, the SNR can be enhanced by increasing the signal portion per unit power.

To explore the optimum modulation per unit power, a practical model was devised. An EOM has a sine-squared transmission curve versus DC voltage bias ($sin^2(V)$), where the laser power governs the carrier strength and its derivative determines the modulation efficiency slope ($|2sin(V)cos(V)|$). As the voltage bias approaches the minimum transmission points ($4nV_\pi$ for integers, n), the ratio of the slope and power, ($|2cot(V)|$), increases significantly, with a singularity arising as $4nV_\pi$ is reached. However, in practice, when RF power at the LO frequency is applied to the EOM, there exists some noticeable minimum power transmission, even at bias values of $4nV_{\pi}$. This is because the LO provides a dynamic bias oscillation around the minimum of the transmission curve, leading to a small 'leakage' transmission that depends on the applied LO power level and frequency. This power portion (equaling δ in Fig. 6.2) is 3.57% ± 1% in our modulator at bias point **h**, when driven with 14 dBm of LO power at a frequency of 10.482 GHz. This practical offset modifies the ideal transfer function to $(1-2\delta)\bullet sin^2(V)+\delta$. This minimum light transmission allows the singularity that would be caused by a slope/power ratio of zero to be avoided. Hence, the peak ratio exists in the region between the EOM bias values $(2n+1)V_{\pi}$ and $4nV_{\pi}$ and close to $4nV_{\pi}$ and it is 2.7 times the value at the conventional, 50% transmission EOM bias of $(2n+1)V_{\pi}$, as shown in Fig. 6.3.

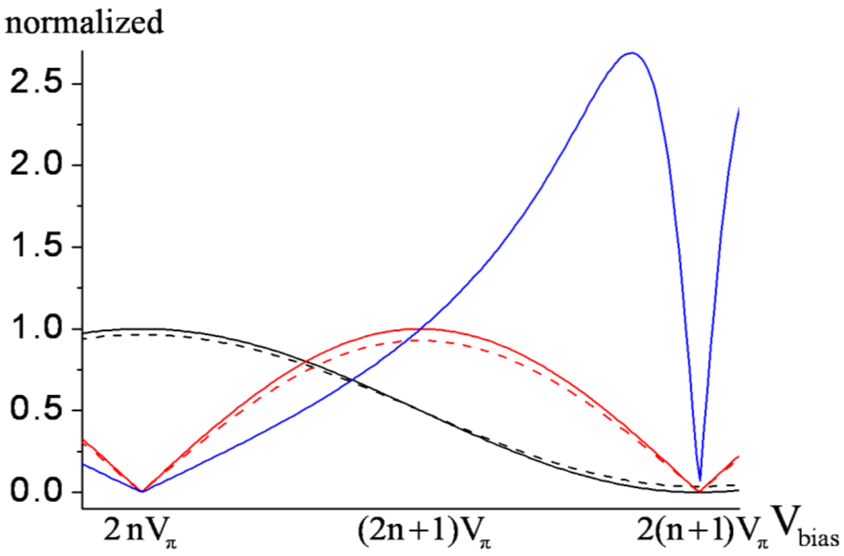

Figure 6.3: Modulation slope (red), transmission curve (black) and normalized signal per unit power (blue) for an EOM such as the device providing a pre-modulation in optical-heterodyne-down-mixing EO sensing. The dashed lines are for practical cases with a δ from Fig. 6.2 of 3.57%.

The practical offset δ heavily impacts the relative peak strength and its position. In addition, nonlinear behavior has to be considered as one shifts the bias toward the peak-modulation-per-unit-power point, due to the asymmetric nature of the slope around that bias. As expected based on the modeling, lowering the bias close to the minimum transmission point increases the modulation per transmitted power, as the carrier components decrease in power faster than the LO side bands. We investigate the evolution of the CSR versus a variety of bias points that are labeled ***a*** to ***l*** in Fig. 6.2. The bias points were set with a 5 dB CSR step, except near each of the inflection points ***a*** and ***h***. The precise modulation depth, M, can be attained from the measured CSR values and the relation $CSR = (2/M)^2$ (Table 6.1).

Table 6.1: Carrier to sideband ratio (CSR) and modulation depth (M) at various DC biases in Fig. 6.2.

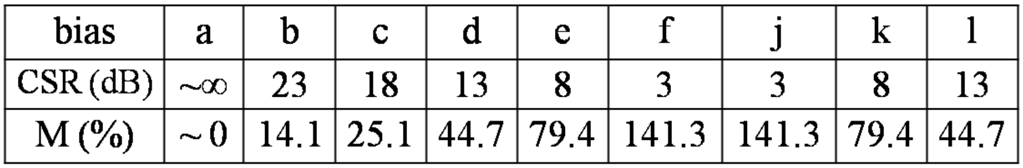

bias	a	b	c	d	e	f	j	k	l
CSR (dB)	~∞	23	18	13	8	3	3	8	13
M (%)	~ 0	14.1	25.1	44.7	79.4	141.3	141.3	79.4	44.7

The modulator used in this work yielded a 25.1% modulation depth at the half-transmission bias, ***c***, whereas a 6 dB CSR would indicate a full (100%) modulation depth for double-sideband amplitude modulation. The biases close to the minimal transmission (for instance: ***f*** to ***j***) yield over-modulation (≥100%). In fact, as the carrier level diminishes and becomes comparable to the two adjacent sideband levels, the beating–interaction between the two sidebands has to be considered, as it also becomes comparable to that of the carrier-sidebands. Since the separation and contrast between beating channels determines the modulation frequency and depth, the beating among the suppressed-carrier and comparable modulation sidebands actually contains both the fundamental (by carrier-sidebands) and second-order-harmonic (by sideband-sideband) modulations. As the sidebands exceed the carrier, such as at both the bias points **g** and **i**, (where the CSR becomes -2 dB), the second-order harmonics become more dominant. Thus the depth for the fundamental-order modulation actually becomes diminished due to the nonlinearity. Further carrier suppression at the bias value **h** reveals a CSR of about -20 dB, making the optimum second-order harmonic component overwhelm the fundamental one [30].

This carrier suppression technique has been known for over a decade to increase modulation depth, and its application to EOS has even been proposed [42,47]. However, conclusive EO-field-scan results and the related limitations of carrier suppression have not been clearly presented or discussed. Here, the practical limitations on modulation-depth enhancement by controlling CSR were developed, along with a remedy to transform and utilize the nonlinearity-based unbalanced results to enhance the sensitivity.

This probe sensing operation typically imparts a minute RF modulation on the carrier, and the final electric field signal is de-modulated as the IF component, which is obtained as a down-mixed product between LO and RF. Thus, the overall EO sensitivity is a combination of the LO and RF. To investigate the optimum condition of LO sideband modulation, we fixed the RF modulation condition at the steepest slope of the spectrum in the probe resonator and changed the bias points from ***a*** to ***l***.

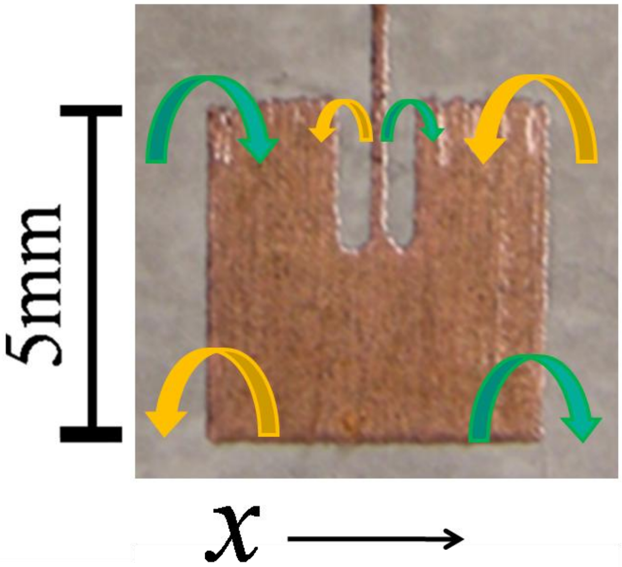

Figure 6.4: Microstrip patch antenna with representative horizontal vector-field fringing flux lines.

To investigate the relative sensitivity enhancement by the bias optimizations, the same DUT antenna used in chapter 5 is adopted. The antenna for RF radiation, annotated with its major horizontal transverse-vector (± *x*-direction) components of electric field, is shown in Fig. 6.4. Six dominant and symmetric horizontal electric-field components are expected near the square edges of the DUT, and to determine the benefit of the decreased CSR and increased depth of pre-modulation in the EOM, the relative strength of the patch-antenna field components was investigated at the modulation bias values shown in Fig. 6.2.

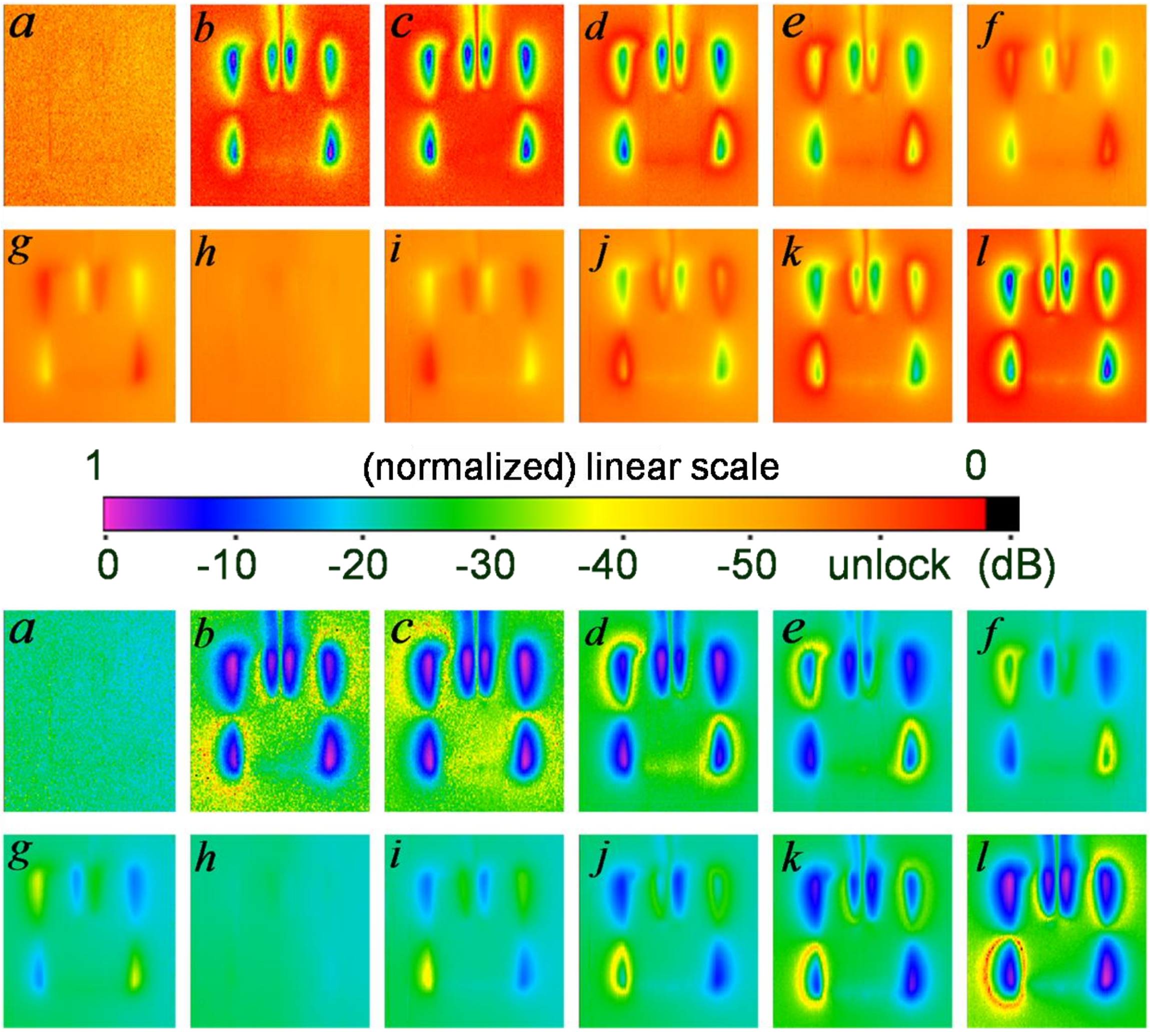

Figure 6.5: Evolution of horizontal transverse electric field mapping at the various DC voltage biases to the EOM in Fig. 6.2 (normalized log scale: 0 dB = -52.5 dBm photo-detected power in the signal at the IF).

In order to explore the optimal EOM DC bias, the evolution of the field distributions was investigated with various DC voltage biases to the EOM. Figure 6.5 presents 12 sets of amplitude electric-field-mapping scans for the patch antenna at the bias values ***a*** to ***l***. The field maps were generated using the method first introduced for circuit characterization, with the modifications described in Sect. 6.2. The experimental configuration of the EO sensor remained unchanged during these trials, so that the impact of the operating point of the EOM pre-modulation only could be evaluated. The fields in Fig. 6.5 are normalized in log scale for analysis convenience. As the bias values shift from the voltage at ***c*** (the 50% transmission point) to that at ***a*** or ***h*** (peak and minimum transmission, respectively), the fields become more distorted. Both these turning points (***a*, *h***) yield no EO signal due to the lack of modulation slope as seen in Figs. 6.2 and 6.3. The point ***h*** should have the least background noise, whereas this noise is maximized at point ***a***. Operation of the EOM at the latter bias also yields no signal, but laser-induced noise and the EO signals exist when the biases are set at a non-zero slope of the EOM.

The maximum EO signal (and thus the largest field amplitude) and a non-distorted, symmetric field are measured at bias point ***c***, which also is at a position where the largest dynamic EOM-drive-voltage oscillations will still yield a linear response. As the bias values shift away from point ***c***, the field distributions in the scans become less symmetric, which is an erroneous result for a simple passive device such as this symmetric antenna. The bias point ***b*** (or ***d***) exhibits a stronger +*x* (or –*x*) directional response, with such an asymmetric pattern occurring because the positively-varying (or negatively-varying) EOM-drive voltages cause a stronger nonlinearity than the oscillation periods directed in the opposite polarity. The nonlinearity becomes most severe as the bias approaches point ***h***. Since moving from point ***a*** to ***h*** corresponds to a descending reflection slope, the phase switches sign when it becomes ascending after passing point ***h***. Thus, the nonlinearities before point ***h*** (descending slope) and after (ascending slope) are identical in degree, but their asymmetric patterns are opposite.

Such nonlinear asymmetric distortion is a fundamentally detrimental limitation, although the sensing mechanism still maintains a relatively strong signal despite its power reductions for bias values near ***h***. For instance, the signal at ***c*** drops by about one half at point ***f***, while the power decreases by about one sixth. This indicates the bias ***f*** has about a three-times stronger signal for the same amount of power, which is expected from Fig. 6.3. This 3 dB CSR point at operating point ***f*** is close to the peak bias. Even though it does show the most efficient signal levels per unit power, the enhanced nonlinearity is accompanied by a noisy signal that originates from higher-order (particularly, the second-order) distorted modulations.

Depending on the bias-vector slope, the sensitivity has a heavy directional dependency. Although it looks detrimental by itself, this nonlinear and unbalanced sensitivity can be overcome and even utilized using the difference in the sensing results of two complementary (*i.e.*, opposite slope) biases. The EO modulations from the ‘mirror biases' (such as the bias pair ***g-i, f-j***, etc) with the same amplitude-modulation slope and opposite polarity contain the common intensity noise components. While the mirror biases have common noise components, they have complementary asymmetric distortions. Therefore, subtracting the amplitude pair would not only cancel the common noise but also compensate and balance the field distortions.

For instance, Fig. 6.6 presents one way that such a nonlinearity-compensating technique can be applied, along with an example of noise cancellation. Figure 6.6(a) is the subtracted amplitude of **g** and **i** (|**g-i**|) on a log scale. The signal-to-noise contrast has been enhanced by at least 10 dB compared to the conventional result at the bias **c** as in Fig. 6.5.

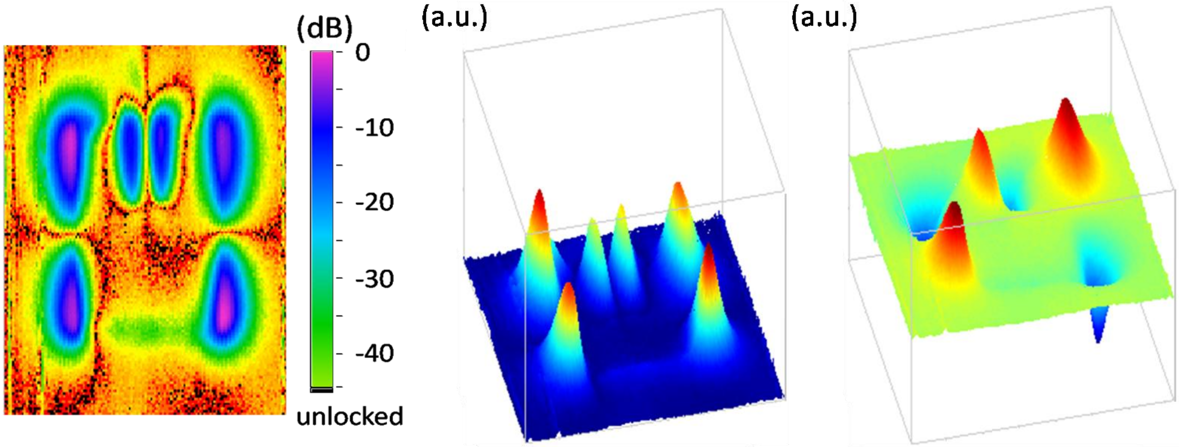

Figure 6.6: Horizontal transverse electric field mapping by subtracted amplitudes at bias **g** and **i** in Fig. 6.5. (a) normalized log scale of |**g-i**|, (0 dB = -62.6 dBm); (b) normalized linear scale of |**g-i**|, (red: max, blue: min); (c) normalized linear scale of **g-i**, (red: max, green: reference, blue: min).

Besides SNR enhancement, the other main advantage of this difference technique is phase capability in a single data set. For example, Fig. 6.6(c) is a linear amplitude-phase plot of **g-i**, with noise normalized as 0 (green), and the respective red and green are amplitude with the opposite phase. Notice that this phase information was extracted from only amplitude information, which has a heavy directional nonlinearity, and thus this technique enables one to extract phase information even when using an intensity-measurement instrument such as a spectrum analyzer, eliminating the need for phase-sensitive instruments like the lock-in amplifier. The down side of this technique would be the need for two complementary data sets that require relatively fine DC bias tuning to realize acceptable complementary conditions.

6.4 EO-Sensor Modulation Optimization

The methodology behind EO sensing is essentially that used in EO modulation, except ambient RF electric fields cause the light modulation rather than a very confined, intense electric field between an electrode pattern. Recalling conventional EOS measurements, induced phase retardations of a small fraction of a degree arise due to external electric fields, and these are transformed into an intensity modulation as the light emerges from an analyzer. A polarizer/analyzer pair creates the sine-squared transmission curve and a quarter-wave plate is used to shift the angular bias. This bias plays the same role as the voltage bias in the EOM pre-modulation case, and it is applied to the same sine-squared intensity-transmission curve. Hence, the angular bias is set typically at the 45° point, which is V_π in the EOM pre-modulation version.

Similar approaches in EOM LO-sidebands SNR optimization have been reported in the conventional sine-squared EOS RF-sidebands case [41,48]. Unlike the pre-modulation-LO-EOM attempt, the optimization technique in EOS was practically useful because the infinitesimal scale of RF modulation makes the any slope on the sine-squared curve 'virtually linear' to mitigate the most detrimental effect - the nonlinearity - in the pre-modulation-LO case. Hence, the modified modeling with practical minimum offset consideration, δ, described in Fig. 6.2, can still be applied to this case with minimal nonlinearity. The peak SNR angular bias was reported to be 88° and it rapidly dropped to zero at the singular bias 90° [41,48], because the minimum transmission δ, which is now determined by a pair of polarizer/analyzer quality (*i,e,.* polarization extinction ratio), is usually smaller than that of the resonator case.

The modulation efficiency slope can be exclusively achieved by the Fabry-Perot resonant effect. The higher resonant slopes achieved with a high-Q resonator structure can have a steeper slope than in the sine-squared modulation case, and thus the modulation per unit power increases more than for the conventional non-resonant cases. In previous chapters, an inexpensive, pigtailed, temperature-tunable, cw laser diode (1560 nm wavelength) was coupled with the resonant EO sensor, resulting in a significant simplification of the conventional EO optical-polarization-control configuration. That is, the polarizer/analyzer pair and the quarter waveplate employed for nearly all other EO-modulation sensors are eliminated. In this case, ~9 mW of modulated cw laser light was delivered to the probe, which is again the 52 µm $LiTaO_3$ plate, coated with five layers of balanced high reflection films at the appropriate telecommunications wavelength. The EO-modulated beam returning from the probe was routed to the detector through a fiber-optic circulator.

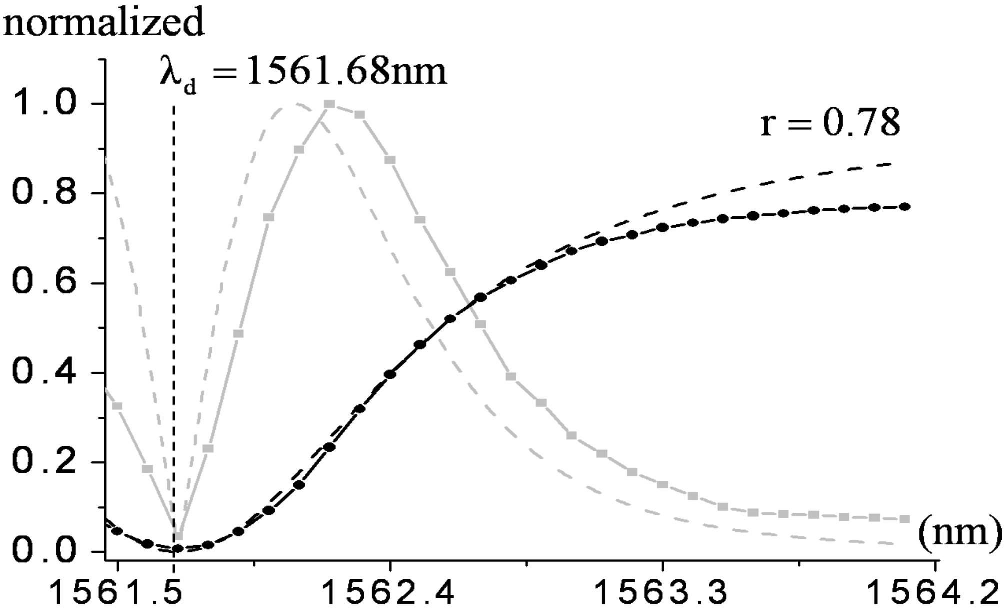

Figure 6.7: Normalized sensor reflectance slope *vs* corresponding EO strength. (solid black line: experimental slope, dashed black line: fitted slope of r = 0.78, solid gray line: experimental EO strength, dashed gray line: simulated EO strength).

Another fiber probe shows r = 0.78 of the Fresnel field coefficient compared to that of the ideal free-space case (r = 0.95). The extracted, normalized EO strength from the fitted reflectance slope of r = 0.78 is presented in Fig. 6.7. The probe was positioned 200 µm above the DUT where the strongest x tangential field component could be interrogated with the sensor crystal. The experimental EO signal peak was observed at a wavelength 'bias' of 1562.2 nm, where it experienced the highest slope of the modulation response. The 0.1 nm deviation of the measured EO peak compared to the simulation is likely due to the enhancement of the phase retardation being reduced by the non-zero resonance dip due to the imperfect HR coatings (*i,e,*. small practical δ) on the resonant probe. Also, as the wavelength shifted from the destructive wavelength, λ_d, the signal decreased in response due to the decrease in the reflection slope, while noise increased in response to the increased reflected light intensity. The signal and noise levels converged to a finite value as the slope flattened [24].

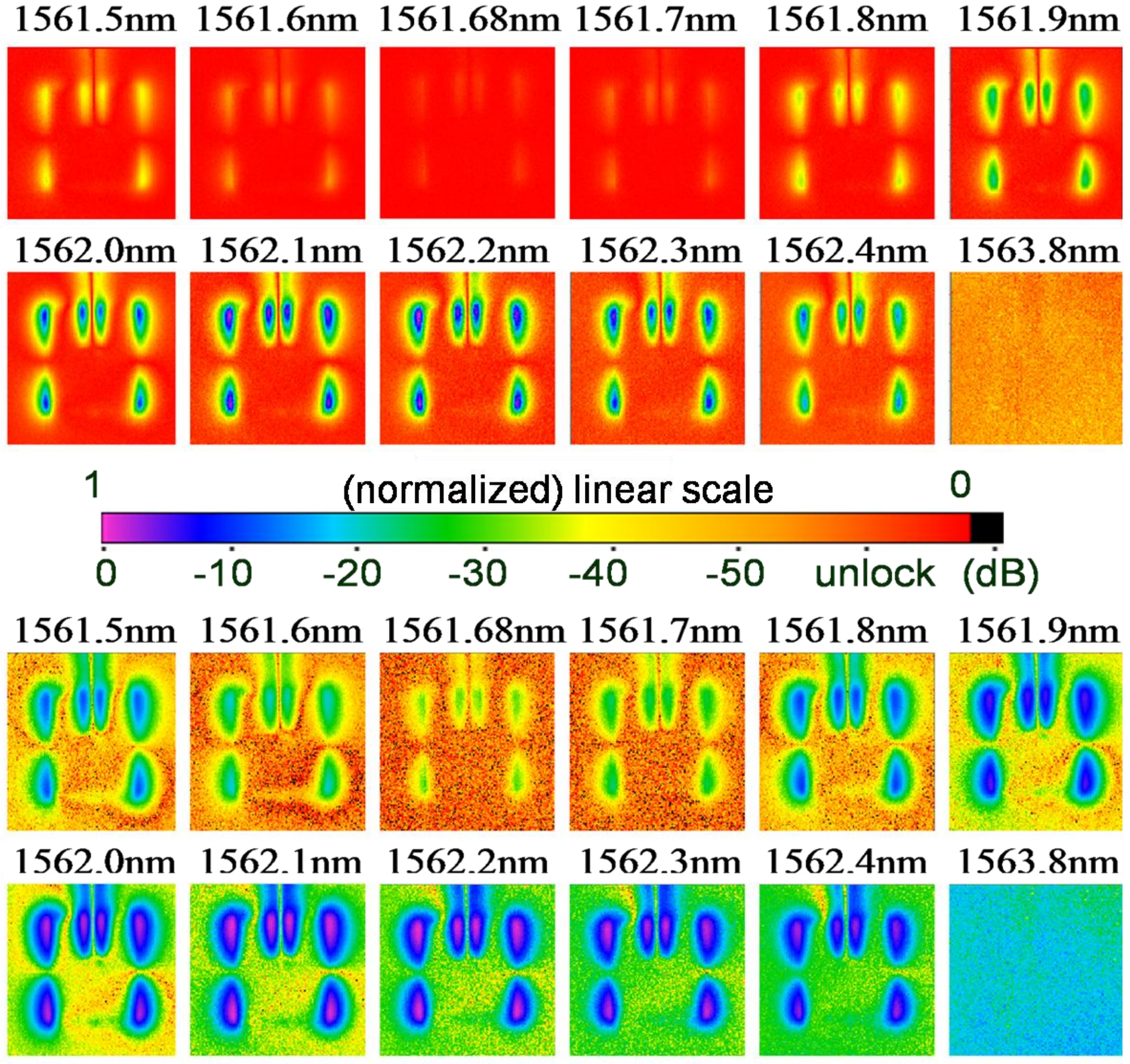

Figure 6.8: Evolution of horizontal transverse electric field mapping at the various spectral biases in Fig. 6.7 (normalized log scale: 0 dB = -52.5 dBm).

A complete set of 12 field-mapping scans for the biases of interest is presented in Fig. 6.8. The strongest signal is measured in the 1562.1~1562.3-nm wavelength band, but the corresponding noise is not minimum in that range. For instance, the SNR at 1562.2 nm is ~30 dB (purple: 0 dB to green:~ -30 dB), but it is ~34 dB (strong blue:-6 dB to yellow:~ -40 dB) at 1561.9 nm. This SNR improvement is from the more abrupt reflected power reduction than the signal drop. Thus, the new bias point, 1561.9 nm, provides a greater portion of signal per unit power, yielding a modulation-depth enhancement. By this principle, the SNR can be improved, although the absolute signal level decreases.

Figure 6.9 presents the evolution of the signal and noise floor at the 12 spectral bias check points of Fig. 6.8. Each signal level was read using the peak value at the same location along the edge of the DUT that produced the highest electric field. While the signal levels have strong stable values, the noise floor has inherent fluctuations (~ ±3 dB), and thus the noise level was determined by averaging the sampled values from the relatively uniform low-field area in the center of the DUT.

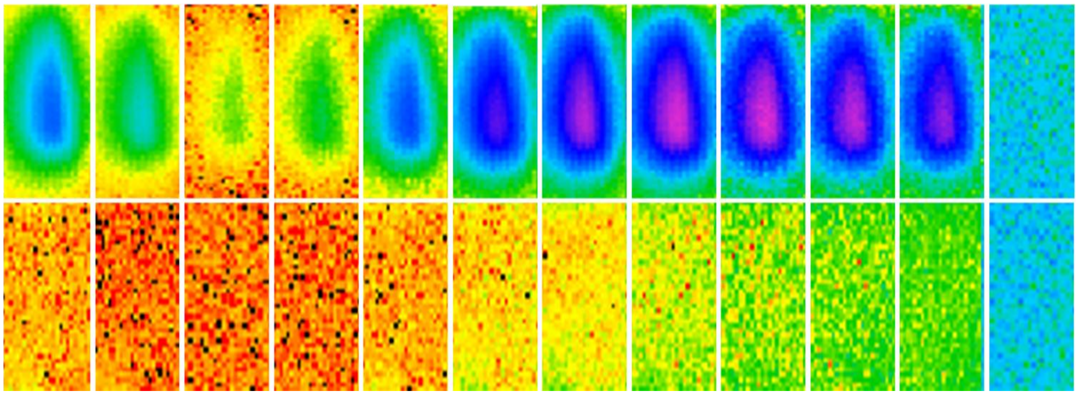

bias (nm)	1561.5	1561.6	1561.68	1561.7	1561.8	1561.9	1562.0	1562.1	1562.2	1562.3	1562.4	1563.8
signal (dBm)	-64.3	-70.2	-81	-77.7	-63.2	-58.3	-53.8	-52.7	-52.5	-53.0	-54.1	~-74
noise (dBm)	~-95	~-100	~-100	~-100	~-95	~-92	~-86	~-84	~-82	~-81	~-80	~-74
SNR (dB)	~31	~30	~19	~22	~32	~34	~32	~31	~29.5	~28	~26	~0

Figure 6.9: Evolution of the strongest signal regimes and noise floors at the various spectral biases in Fig. 6.7.

The minimum SNR occurs when the bias does not experience the spectral slope. The 1563.8 nm bias is the case having highest noise floor without signal. The SNR is also ideally zero at the bias of the minimum resonant transmission (λ_d) and practically very small because of very low noise floor and imperfect spectral bias positioning at sharp λ_d. The measured minimum power reflectance to the detector is ~ 0.9% of the input power to the resonance-based probe. This small reflection comes from an imperfect resonant cavity in the fiber-coupled configuration and corresponds to the practical power offset δ. This configuration is virtually the same as the case in the LO sideband-modulation modeling presented in Fig. 6.3. Hence, the optimum SNR band is expected to be very close to $\lambda_{d.}$

For the conventional EOS case with a pair of polarizers, the optimum SNR was found just ~ 2° off from the minimum transmission angular bias 90° [41,48]. The optimum SNR band in our resonance based EO system is in the 1561.8~1562.0-nm band as seen in Fig. 6.9. Since the mode spacing (*i.e.*, λ_d *to* λ_{d+1}) for our 52 µm $LiTaO_3$ sensor plate is 10.76 nm at 1562 nm, just a 1~3% offset of the mode from λ_d yields the practical peak SNR band. Although 1561.8 nm should lead to a better SNR than 1561.9 nm or 1562.0 nm bias theoretically, the practical noise floor at 1561.8 nm is limited by the instrumental and EMI noise floor of the lock-in amp. Hence, we choose 1561.9 nm for the optimum SNR bias point maintaining appropriate absolute signal levels.

6.5. Combined Optimization

The enhancement of SNR in EO sensing by shifting the modulation bias points was possible without field distortions. This is because the nearly infinitesimal nature of RF sensing is immune to the nonlinearity, while the intense nature of the LO laser source modulation severely distorts the fields when the voltage bias shifts from the half transmission point. The actual EO modulation efficiency was proportional to the product of both the LO and RF modulations. The severe nonlinearity induced mainly by an EOM was mitigated as the minute EO sensing modulation was reduced. We shifted the peak EO spectral bias (1562.2 nm) to the wavelength that optimized the SNR (1561.9 nm) and then explored how much we could shift of the voltage bias to increase the EOM modulation efficiency without suffering nonlinear distortion.

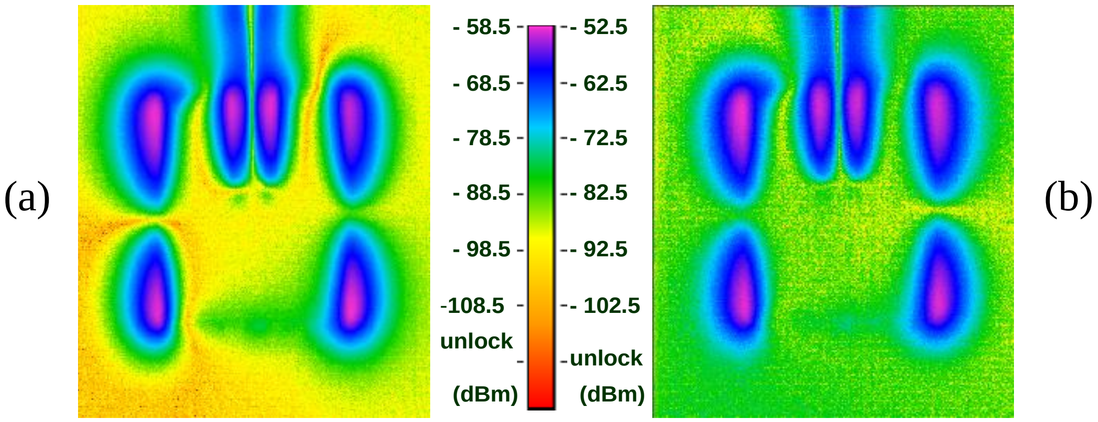

Figure 6.10: Comparison of horizontal transverse electric field mapping (a) LO-RF-combined optimization scan, (b) conventional scan.

Figure 6.10 shows the SNR comparison for the previous bias combination (EOM bias: c, EOS bias: 1562.2 nm) and the optimized combination (EOM bias: **d**, EOS bias: 1561.9 nm). The optimized bias enhances by ~10 dB the SNR compared to the previously determined value of 30 dB. Further shifting of the voltage bias to the point ***e*** shows a noticeable nonlinearity.

6.6. Summary

We have presented a methodology to enhance EO signal modulation depth by simple re-position of bias points without increasing system complexity. The optimization procedures to enhance SNR by simply shifting both EOM-LO/EOS-RF modulation bias points were presented in an optical-heterodyne down-mixing systems. Practically modified modeling, with the minimal transmission-extinction consideration, explains how modulation depth can be increased per unit power. This approach worked well for the RF EO sensing case where the nonlinearity was not a big limitation, unlike the LO-EO modulation which requires the differential-nonlinearity-compensation technique. The overall optimization is the interplay of LO/RF-EO modulation so proper combination of both biases gives SNR enhancement over a conventional case. To realize optimum enhancement, a trade-off between nonlinearity-induced field distortion and SNR enhancement was explored, attaining ~10-dB SNR enhancement without field distortion.

CHAPTER 7

A PRACTICAL COMPARISION OF THE ELECTRICAL AND PHOTONIC DOWN-CONVERSION METHODS

7.1 Introduction

Down-mixing measurement techniques in general have been very useful tools for shifting high frequency sensing information to a lower, baseband regime. Two down-mixing techniques that employ cw lasers, as optical sources, were introduced in previous chapters. One, presented in chapter 4, is the electrical conversion method, and its principle and field mapping results were demonstrated for the UHF band. The other technique, an alternative to the electrical method, is the photonic conversion technique, which requires amplitude-modulated light as a down-conversion source, as described in chapter 5. Each system has different conversion media and principles. By understanding these features, the advantages of each system have been exploited by comparing the field distributions from the same radio frequency identification (RFID) antenna. Consequently, criteria for choosing between the electrical and optical heterodyne-mixing methods in potential applications are identified and described in detail.

7.2 Principle and Experimental Setup

The experimental scheme for the heterodyne-down-mixing EO sensing is shown in Fig. 7.1. The system is designed to switch between electrical (Fig. 7.1 (a)) and photonic (Fig. 7.1 (b)) down-conversion methods in order to facilitate a comparison between the two in an otherwise identical environment. The systems are tested using the same type of resonance-based sensing probe that was used in previous chapters. A glass ferrule was used to mate the probe sensor tip with a single-mode optical fiber. A fiber-pigtailed, distributed-feedback laser diode, manual polarization controller, optical circulator, and fiber-pigtailed photodiode were then spliced together with the probe to form a continuous, low-loss, enclosed optical path.

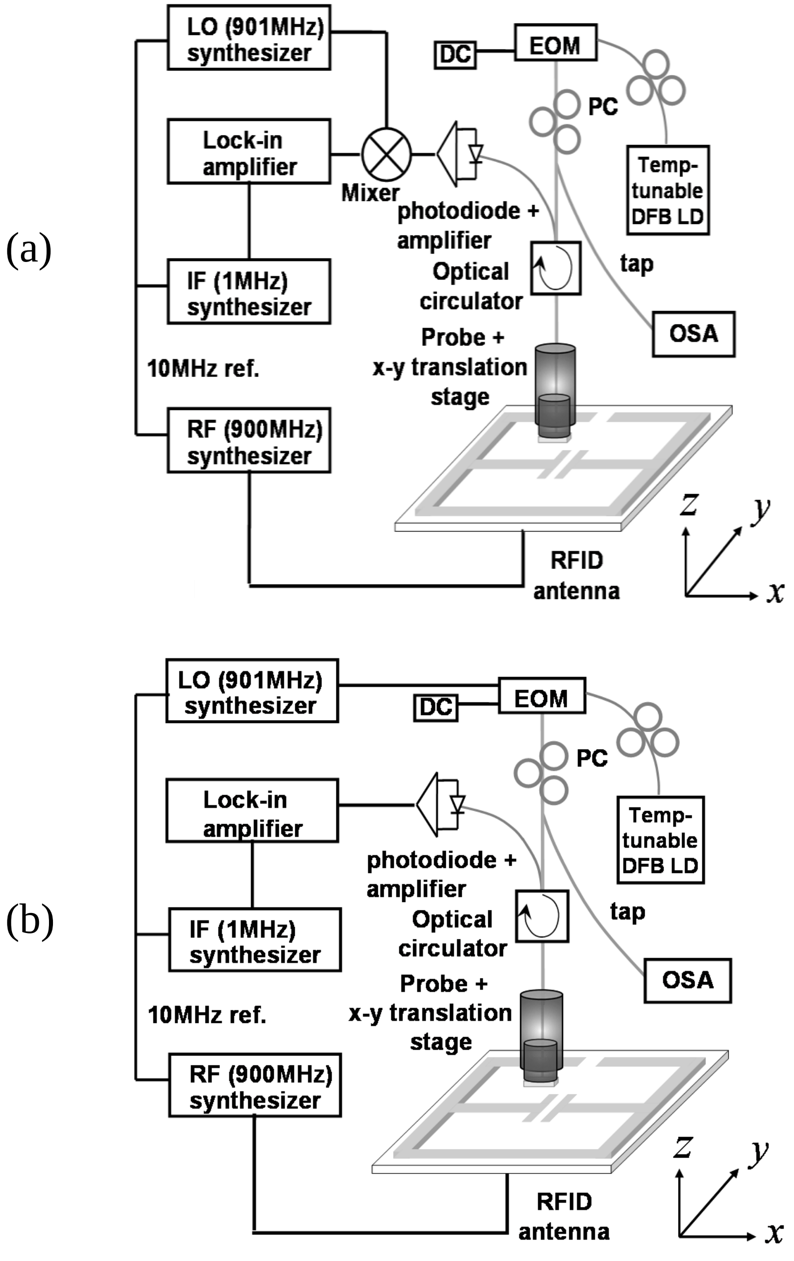

Figure 7.1: Experimental schematics for the (a) electrical-down-conversion and (b) photonic down-conversion, resonance-based, EO sensing techniques. (DFB LD: distributed feedback, continuous-wave laser diode; EOM: electro-optic modulator; PC: polarization controller; OSA: optical spectrum analyzer). The gray and black lines are optical fibers and electrical connections, respectively.

The down-mixing techniques utilized with EO sensing convert electrical-domain information emitted by the DUT at microwave frequencies to electrical-domain information at an IF in the 1 kHz to few-MHz range at the photodetector output. This signal is detected by a lock-in amplifier operating in a low-noise-floor regime. In photonic down-conversion, as observed previously, optical sidebands are introduced by a conventional Mach-Zehnder EO modulator, and these sidebands mix with the RF signal to be measured in the EO probe. The resulting optical sideband, separated from the carrier by the IF, is received by the photodetector and, bypassing the electrical mixer, input directly to the lock-in (Fig. 7.1(b)). In electrical down-conversion, the EO modulator has no RF input and thus does not impart sidebands on the optical probe beam. The small sideband induced on the optical beam by the signal to be measured in the EO probe is received by the photodiode and mixed with an electrical LO of similar frequency in the mixer, with the IF again input to the lock-in (Fig. 7.1(a)). In operating both heterodyne-down-mixing EO sensing systems, we have chosen to conduct near-field scans on the same rectangular RFID antenna, designed for use in a mobile handheld scanner at 900 MHz, as was used in chapter 4.

7.3 Probe Characterization

In order to compare the electrical and photonic down-mixing systems fairly, the same resonance-based fiber pig-tailed EO probe described in chapter 6 is employed. Utilizing the same probe, both conversion systems sense the same RF field before down-converting. Thus, the respective down-converted IF signals from the two systems yield the performance of each conversion scheme.

The sensitivity of the EO probe within the heterodyne-down-mixing measurement systems has a strong spectral dependency due to the resonant nature of the etalon. Considering that SNR depends on factors such as laser noise, which will increase and decrease along with the light intensity on the photodetector, it was valuable to consider the optimization of the probe operating point when maximizing the measurement SNR in chapter 6. The resonance-based modulation slope (*i.e.,* the reflectance) and corresponding EO sensitivity are re-visited versus spectral bias in Fig. 7.2 (re-drawn Fig. 6.7 with optimal bias band), along with a simulation using the equivalent Fresnel field reflection (*r* = 0.78) that is fit using the experimental curve. The probe was positioned at the point where the strongest transverse component was measured, and its sensitivity and reflectance both normalized. Here it can be seen that the EO signal modulation is maximized by adjusting the laser wavelength to the highest slope of the reflection spectrum, although the corresponding noise level will be larger than if a lower light level was used. Hence, for low noise, the spectral bias is optimum when it is close to the destructive wavelength λ_d.

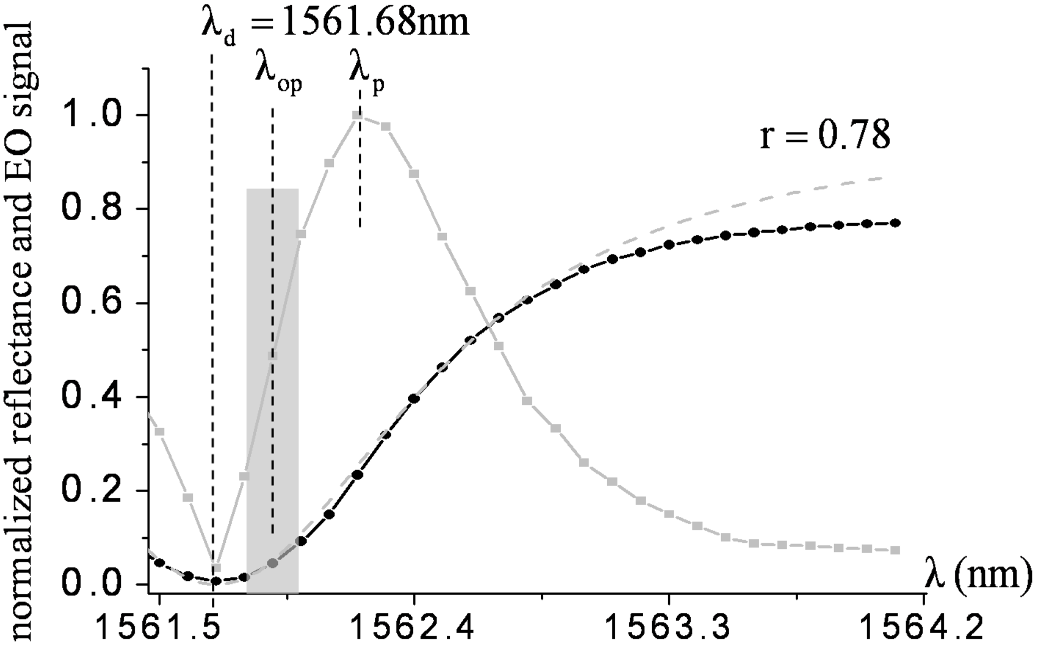

Figure 7.2: (Re-drawn Fig. 6.7 with optimal bias band) Reflectance slope and corresponding EO strength (solid black line: experimental reflectance slope; dashed gray line: fitted slope with coating reflectivity *r* = 0.78; gray solid line: normalized experimental EO strength; shaded area: optimum bias band).

To investigate which spectral bias provides the optimum signal-modulation depth (*i.e.,* SNR), the laser wavelength was swept from λ_d (1561.68 nm) to λ_p (1562.2 nm) with 0.1 nm incremental steps. The shaded band in Fig. 7.2 including λ_{op} provides the optimal spectral biases to achieve the highest SNR.

7.4 EO Sensing by Electrical Down-conversion

To scrutinize the evolution of the SNR, the EO probe was used to map the electric field above the capacitively-loaded dipole located in the center of the rectangular RFID antenna at each wavelength. The optical axis of the probe is set along the *x*-axis to sense the horizontal transverse electric fields. As shown in Fig. 7.3, although the peak signal (-51.8 dBm), with an SNR of ~30 dB, is achieved at the wavelength λ_p of Fig. 5, an improved SNR of ~35 dB is realized at λ_{op} (1561.9 nm). This optimum spectral band (shaded area in Fig. 7.2) and bias (=λ_{op}) can also be calculated by exploring the reflectance and its derivative. A detailed quantitative modeling and analysis have been described in chapter 6.

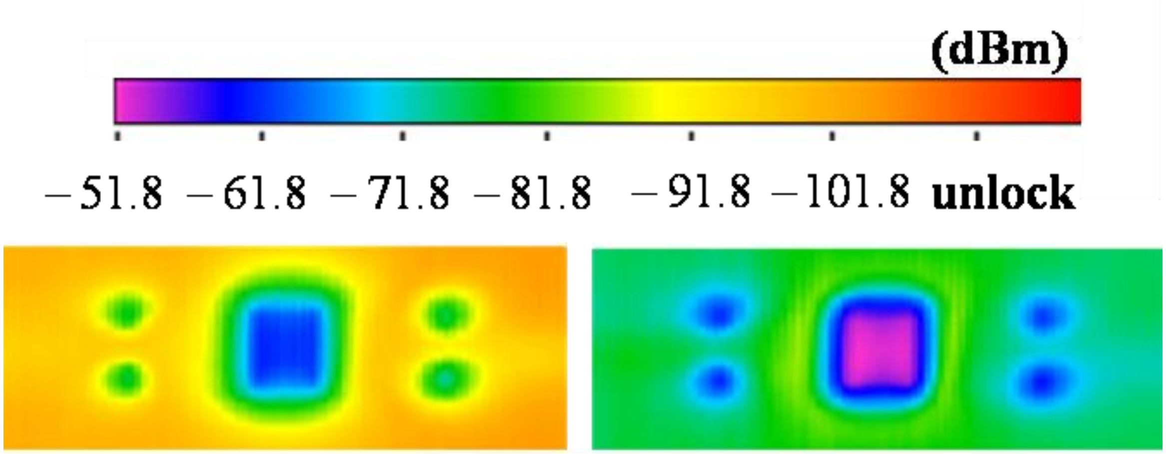

(a) λ_{op} = 1561.9 nm (b) λ_p = 1562.2 nm

Figure 7.3: Horizontal (*x*-component) electric-field distributions over the capacitively-loaded terminal using (a) a spectral bias for optimum SNR or (b) a spectral bias for peak EO signal.

During these tests of the electrical down-conversion system and the resonant probe, a cw optical power of 9 mW was delivered to the probe, and the return signal, with a 900 MHz sideband, was demodulated by the fast photodiode. The RF was measured on a spectrum analyzer to have a power of -44.8 dBm, and this signal was down-converted to a 1 MHz IF using 0 dBm of a 901 MHz LO. The -51.8 dBm of peak signal level at λ_p was obtained from the microwave mixer. Although the mixer had 7 dB of conversion loss, it maintained the overall SNR of the measurement, and the absolute value of the signal could be changed with the LO power level. The optimum SNR was ~35 dB when the laser was tuned to λ_{op}, with a -58.2 dBm maximum signal level. That is, a smaller signal at the mixer output is observed for the same radiated RF signal when using λ_{op}, but the power-sensitivity of the probe has actually increased by 5 dB.

7.5 EO Sensing by Photonic Down-conversion

As described in chapters 5 and 6, the photonic down-conversion can also be used to mix the EO-probe cw modulation down to a narrow-band, low-frequency IF. Here, the optical-heterodyne technique is compared with the electrical-down-conversion case under identical experimental conditions to determine if advantages exist to either methodology.

As mentioned earlier, the LO signal in this case is delivered along with the optical beam as a sideband on the light beam, and thus the $LiTaO_3$ probe mixes the LO and RF components, creating a beat frequency on the light modulation due to the additional RF from the DUT. With the DC bias still applied to the EO modulator at the half-wave voltage (V_π), applying an RF at the LO frequency (14 dBm @ 901MHz) yields the same 9 mW of average optical-beam power to the probe as in the electrical down-conversion case. This is a conventional heterodyne configuration where the EO modulator is operated at the 50% point of the sine-squared transmission curve to minimize nonlinearity of the modulation [24].

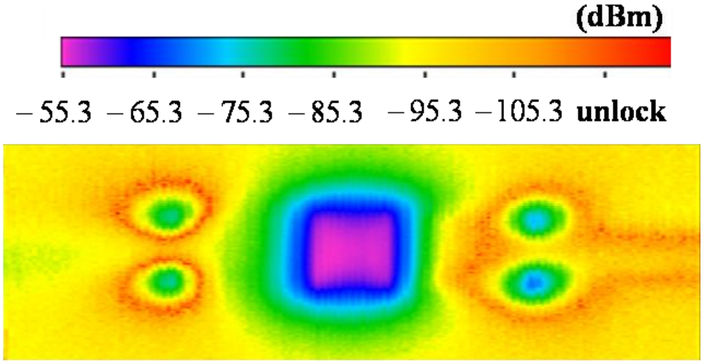

Figure 7.4: Horizontal (*x*-component) electric-field distributions over the capacitively-loaded terminal measured using a resonant EO probe and photonic down-conversion.

The field mapping result for this case is presented in Fig. 7.4. The SNR is ~40 dB when the operating wavelength is again optimized for the resonant probe at λ_{op}, with a -

55.3 dBm signal level. The signal is thus ~3 dB higher than for the electrical mixing results, and the SNR and sensitivity are observed to increase by ~5 dB.

It should also be possible to enhance the efficiency of a photonic-down-conversion EO measurement by, among other actions, enhancing the Mach-Zehnder-EO-modulator modulation depth. There have been numerous attempts to do this by lowering the EO modulator DC bias to suppress the carrier more rapidly than the modulation sidebands [47]. Although this technique indeed increases the sensing signal strength per unit beam power, measured field distributions become severely distorted due to the nonlinearity of the EO modulation function at that bias point. That is, with the EO modulator DC bias set close to the minimum transmission point (*e.g.*, on either side, but relatively close to point *b* in Fig. 7.5), one direction of the RF driving signal will yield a more quadratic output than the other.

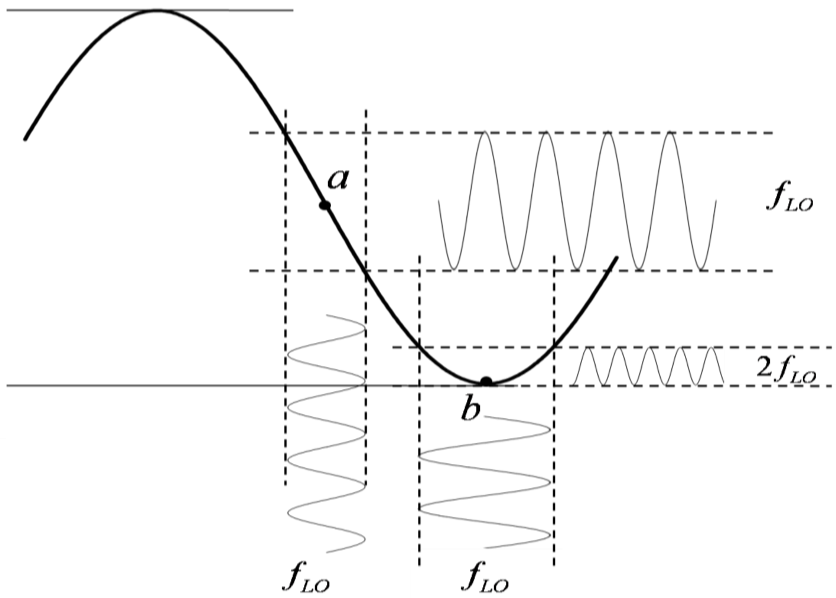

Figure 7.5: Optical intensity output from the Mach-Zehnder EO modulator vs. driving signal. Modulator output swings at 50% (point *a* for V_π) and minimum (point *b* for $2V_\pi$) light-transmission DC-bias points.

Asymmetric EO-modulator output-intensity swings in the generation of the LO signal with the Mach-Zehnder EO modulator lead to significantly different EO measurement sensitivities for the electric-field vector components of opposite phase.

However, the unbalanced EO sensitivity can be overcome by balancing the LO swings on either side of the DC operating point, as illustrated in Fig. 7.5 for two instances, points ***a*** and ***b***.

Besides DC-biasing the EO modulator at its 50% transmission intensity, V_π (Fig. 7.5, point ***a***), operating the device at its precise minimum transmission intensity, $2V_\pi$ (Fig. 7.5, point ***b***), also makes the LO oscillations balanced. For a single LO-modulation cycle at any static bias, the dynamic bias passes the static bias twice. The maximum (or the minimum) exists during the upper half (or lower half) across the static bias. While balanced upper/lower half swings around the V_π bias reproduce an output modulation intensity with minimal nonlinearity, operating at the minimum transmission bias at $2V_\pi$ allows the same LO oscillation to have two minimum points whenever the dynamic bias passes this static bias point. As a result, the upper/lower-half oscillations around the V_π bias become upper swings only around the minimum transmission bias. Since these swings are balanced and identical, the original LO period gets ‘folded in half,’ resulting in efficient generation of the second-order harmonic of the LO driving frequency [30].

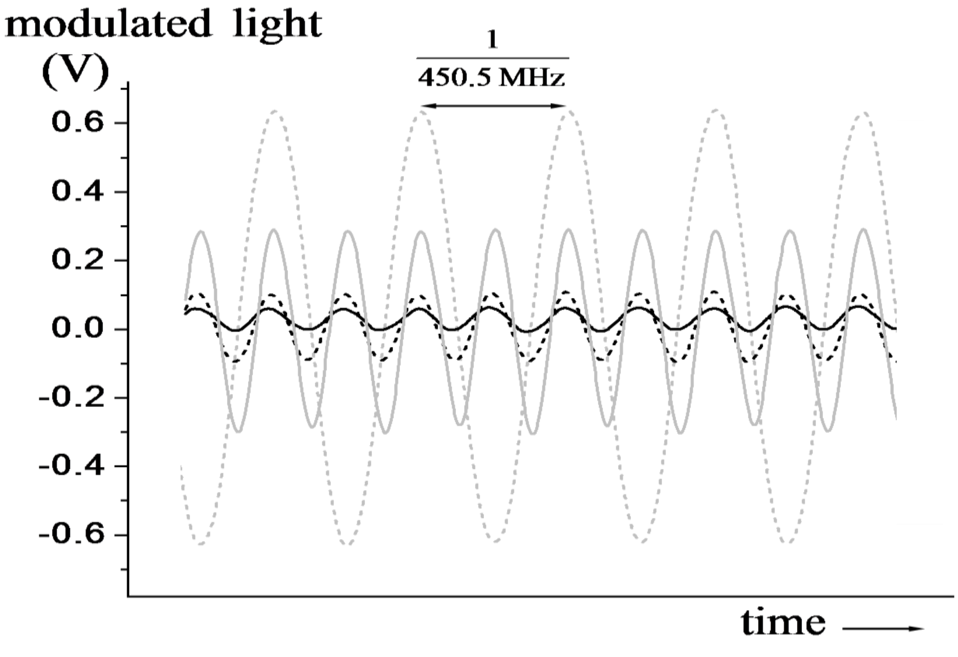

Figure 7.6: Modulated light waveforms from the 1% tap of Fig. 7.1(b) with LO/2 = 450.5 MHz (dashed gray: fundamental swing with 14 dBm; solid gray/dashed black/solid black: second-order harmonic swing with 19/14/9 dBm Mach-Zehnder input, respectively). DC components are not coupled from the photodetector.

As depicted in Fig. 7.5, the second-order harmonic output at $2V_{\pi}$, even with a larger LO power input, is significantly smaller than that of the fundamental LO frequency generated when biased at V_{π}. However, the second-order harmonic here has superior modulation depth, as determined by the carrier and amplitude-modulated-side-band ratio. The carrier is significantly suppressed in this second-order harmonic operation, or in other words, the modulation is enhanced per unit output optical power. The smaller relative second-order harmonic amplitude can be increased by bigger input oscillation spans (*i.e.*, LO power levels to the Mach-Zehnder). This balanced second-order harmonic modulation is experimentally demonstrated *vs.* LO driving power in Fig. 7.6.

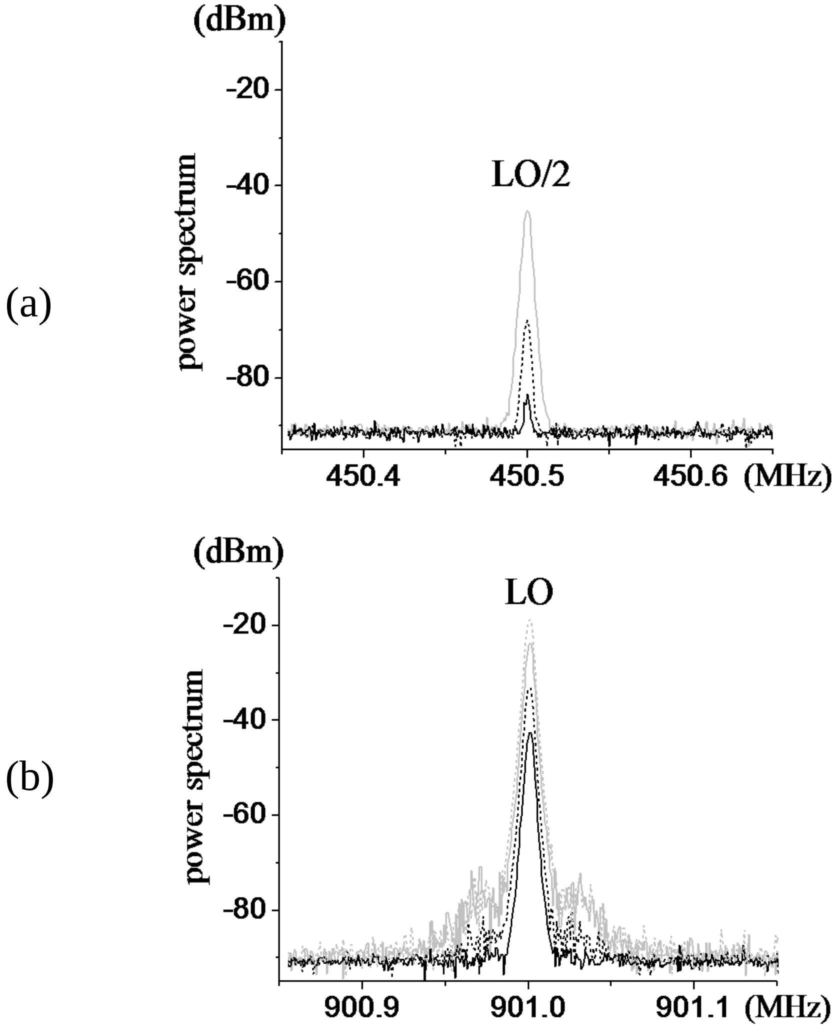

Figure 7.7: Electrical spectrum of components in Fig. 7.6. (a) fundamental component of LO/2 at 450.5 MHz; (b) fundamental component of LO at 901 MHz and second-order harmonic components, LO/2 at 450.5 MHz (where style of each line represents the corresponding line in Fig. 7.6).

The fundamental LO (at 901 MHz) can be replaced by the more efficient second-order harmonic signal. Thus, the EO modulator is driven with an RF at LO/2 (at 450.5 MHz), and the modulation strength is compared with that from conventional, fundamental modulation. The DC is tuned to a bias that yields the minimum carrier transmission at the fundamental (now LO/2), and the second-order harmonic is maximized. The contrast of the fundamental and second-order harmonic versus power levels input to the EO modulator, as seen in Figs. 7.7 and 7.8, serves to determine the appropriate LO power range. The second-order harmonic intensities are 20-30 dB stronger than the intensity of the fundamental.

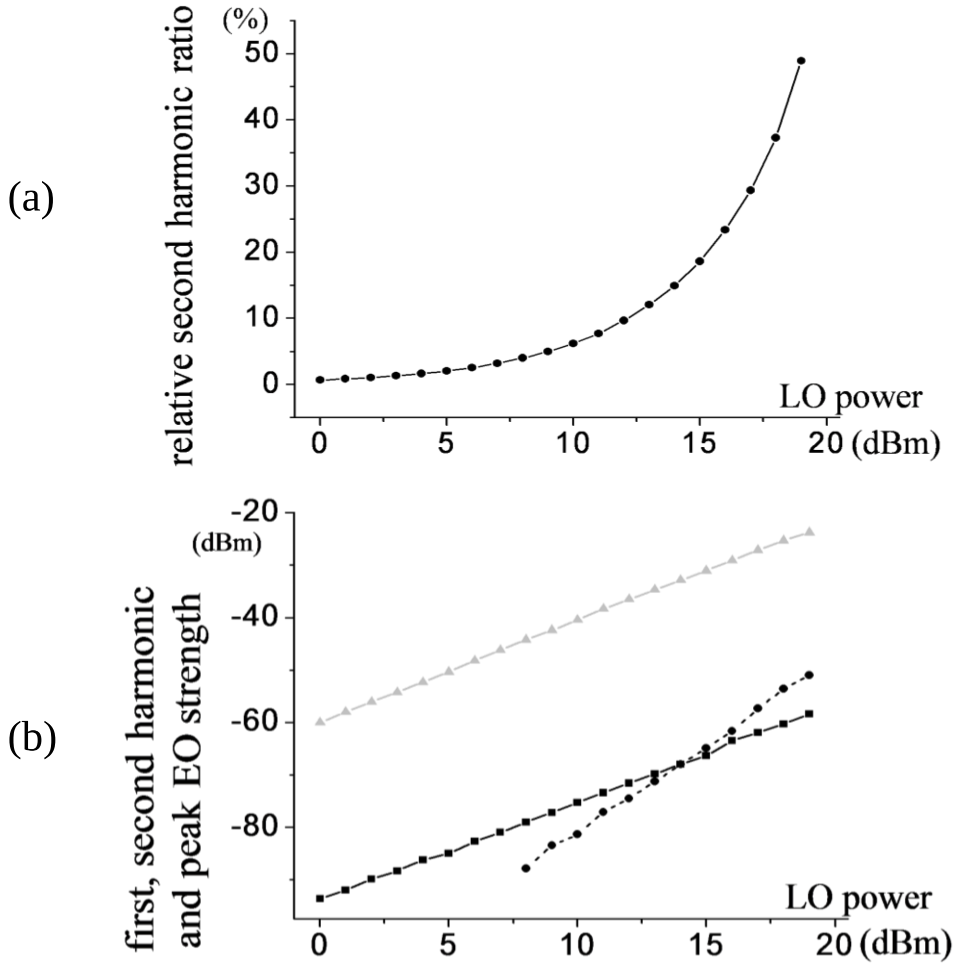

Figure 7.8: Nonlinearity performance versus LO power levels. (a) relative second-order harmonic optical-sideband-power ratio to conventional-fundamental 50% power with 14 dBm LO power; (b) fundamental component power of LO/2 at 450.5 MHz (dashed), second-order harmonic component power of LO at 901 MHz (gray), and peak EO signal levels using second harmonic LO (solid black).

Compared to the fundamental of the LO (14 dBm at 901 MHz) at the 50%-transmission operating point (dashed gray plot in Fig. 7.7(b)), the second-order harmonic of the LO/2 is weaker by ~14 dB for the same LO power (dashed black plot in Fig. 7.7(b)). This is not because the conversion to the second-order harmonic is inefficient, but because the total modulated optical power, operating at the minimum transmission bias, is smaller than in the conventional case. The relative second-order harmonic-modulated optical power compared to the fundamental of the LO at 50 %-transmission operation is presented in Fig. 7.8(a).

This optical power is mostly (≥ 99%) the second-order harmonic component due to the huge scale gap (or conversion efficiency) between the fundamental and second-order harmonic as shown in Fig. 7.8(b). The fundamental components (dashed line in Fig. 7.8(b)) increase more rapidly for higher LO power than the second-order harmonic components (gray line in Fig. 7.8(b)). This indicates that the EO-probing sensitivity using the second-order harmonic would be rather inefficient for a high LO power due to the less-efficient second-order harmonic conversion. Thus, the ~2 dB increment of the second-order harmonic (or EO signal) per 1 dB step of LO relationship begins to roll off for higher driving levels [30].

The optical modulation at the second-order harmonic is directly related to the EO signal sensitivity in photonic down-conversion. The EO signal (black line in Fig. 7.8(b)), at the strongest tangential *x*-component position, is presented with respect to the corresponding second-order harmonics. The EO signal is ~35 dB lower uniformly over the wide LO power range investigated.

Electro-optic field-mapping measurements were also made using the minimized-carrier, EO-modulator output intensity and second-order harmonic LO. The microwave driving signal to the Mach-Zehnder EO modulator at the LO/2 frequency is varied from +19 to +9 dBm, and the corresponding field scan for the +19 dBm LO level is seen in Fig. 7.9(a). Although the absolute peak signal level decreases for lower LO powers, as seen in Fig. 7.8(b), the noise level also decreases proportionally with the lower optical output power (Fig. 7.8(a)). Thus, the SNR values remain comparable until the reduced noise floor reaches the instrument noise limit (-125 dBm ±5 dB for the lock-in amplifier at our IF). In contrast, as the LO power is increased significantly above +19 dBm, the SNR would degrade as the second-order harmonic-generation efficiency diminished.

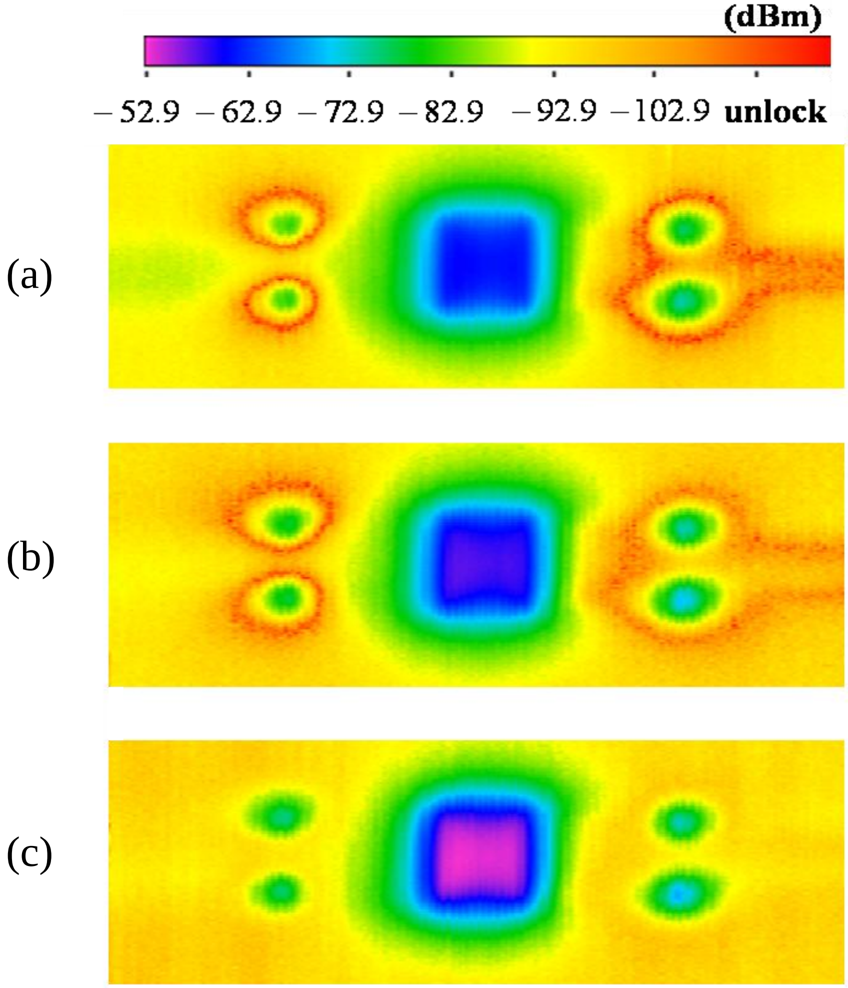

Figure 7.9: Horizontal (*x*-component) electric-field distributions over the capacitively-loaded terminal of the RFID DUT. (a) second-order harmonic of LO/2 at 450.5 MHz, +19 dBm; (b) fundamental of LO at 901 MHz, +14 dBm; (c) second-order harmonic of LO/2 at 450.5 MHz, +9 dBm and with ~26 dB of optical gain.

The low signal and noise levels attained using the tiny optical intensities at the LO optical sidebands, can be readily raised by optical amplification. Since the second-order harmonic power with a +9 dBm RF input to the Mach-Zehnder EO modulator at LO/2 is only ~5% of the input in the conventional fundamental case, as in Fig. 7.8(a), an optical gain of 20 from an erbium-doped fiber amplifier brings the power back to that of the conventional photonic-down-mixing case. The field-mapping result when an optical amplifier is added to the optical beam path after the Mach-Zehnder EO modulator is shown in Fig. 7.9(c). The signal level has risen from -77.1 dBm to -52.9 dBm. Using the gain to obtain the same optical power level as in the 50%-transmission, conventional EO-modulation case, a 2-3 dB higher signal level is observed for the second-order harmonic-LO, EO-measurement method. This is because the modulation depth was enhanced through suppression of the optical carrier, while the noise floor was maintained due to use of the same optical power.

This method would be even more useful when measuring higher microwave frequencies, since the modulation depth of an EO modulator degrades as it is operated closer to its bandwidth limit [30]. Since the EO-probing measurement would also take place at twice the microwave frequency input to the Mach-Zehnder EO modulator, field-mapping could be accomplished at a frequency of twice the rated bandwidth of the EO modulator. All components in the optical system would also remain the same, so that only the driving frequency would have to be increased in order to increase the measurement frequency. Considering the high expense of modulators with millimeter-wave operating frequencies, photonic-down-mixing EO-field measurements at the second-order harmonic of the Mach-Zehnder driving frequency would realize substantial cost benefits [30].

7.6 System Comparison

The fundamental difference between the electrical and photonic down-conversion techniques can be understood by their respective mixing mechanisms. Although both systems eventually deliver IF components to a low frequency read-out instrument, such as a lock-in amplifier, the two IF components are attained by quite different procedures. These IF components are generally the baseband levels that are down-converted from two comparable microwave band levels. These microwave components are also delivered over the optical carrier typically through an optical fiber (*i.e.,* as in a Radio over Fiber system). Thus, there should subsequently be two down conversions: optical to microwave and microwave to baseband.

Each down-conversion is realized by the square law behavior of a nonlinear detector or mixer that is typically implemented with a diode. A slow diode is only capable of detecting the nonlinear product of two comparable beating components, shown in envelope modulation. In the electrical down-conversion case, the first stage photodetector (*i.e.*, photodiode) demodulated the RF components cast as an envelope of the optical carrier. Then, the purely electrical RF component associated with the additional electrical LO component through an electrical mixer (*i.e.*, electrical diode) was down-converted.

Table 7.1:

Comparison of the electrical and photonic down-conversion methods.

	Electrical down-conversion	Photonic down-conversion
Measurement bandwidth limit	limited by detector and mixer	limited by EOM
Useful bandwidth	better for lower band (<~1GHz)	better for higher band (>~5GHz)
Bandwidth enhancement	not available	significantly enhanced using higher harmonics
Mixing medium	electrical mixer (electrical diode)	EO sensor+photodetector (photo diode)
SNR with same optical power (9mW)	typically ~35dB	typically ~40dB
Signal level scaling	scalable according to mixer LO power	impossible for fixed gain detector
Laser power usage (insertion loss)	no insertion loss	~4dB EOM insertion loss + 3 dB (50%) bias loss
Noise susceptibility (EMI)	sensitive	relatively less sensitive
Optical management concern	easy to manage (only laser)	less easy to manage (laser+EOM)
Cost concern	effective for lower band	effective for higher band

In considering the differences between the electrical- and photonic-down-conversion methods in EO field probing, one may recognize that, with the former technique, the laser input intensity could have been increased without concern for exceeding the damage threshold of the EO modulator. However, this intensity was reduced to the same level (~ 9 mW) as that used in the photonic-down-conversion measurements to enable a relative comparison between the two. Hence, the power reduction resulting from a considerable inherent insertion loss, as well as other losses, was avoided in the photonic-down-conversion system, implying that the electrical down-conversion could have taken advantage of higher optical power levels. Furthermore, the signal strength from the IF port of the mixer could readily be scaled by increasing the LO power level to the electrical mixer. This would then behave in a similar fashion as an RF amplifier after the fixed-gain photodetector in the electrical-down-conversion case. This system is also relatively inexpensive for lower-frequency applications and easier to manage in all applications, as it allows for the elimination of several optical components.

The photonic down-conversion method exhibited a small advantage in SNR performance per unit optical power. In addition, the system sensitivity and measurement bandwidth could be extended by utilizing a Mach-Zehnder EO modulator with wider bandwidth – an expensive alternative – or by use of the second-order harmonic LO-sideband generation described in Sect. 7.5. For very high frequencies, this system will also likely become more cost-effective, as the requirement for a fast detector and microwave-mixer pair increases cost compared to a fast EO modulator and a slow detector for the optical IF.

Finally, measurements with both the electrical and optical down-conversion techniques displayed decent SNR performance (35-43 dB), suitable for characterizing microwave near-field patterns in a wide variety of applications.

7.7 Summary

Two simplified electro-optic-sensing-system embodiments, using either electrical- or photonic-down-conversion techniques to create a low-frequency, IF representation of RF signals, have been demonstrated. By utilizing a resonant probe optimized for efficient operation, the performance of each measurement configuration has been compared by exploring the electric-field radiation from an RFID near-field-reader antenna in the UHF band. The measurement bandwidth in the photonic-down-conversion system has been extended through novel use of nonlinear dynamics during the process of creating an LO-sideband on the optical probe beam, all without eroding the SNR, as demonstrated in example field-mapping scans. Advantages of each system can be exploited depending on the desired application.

CHAPTER 8

BANDWIDTH ENHANCEMENT OF ELECTRO-OPTIC FIELD SENSING USING PHOTONIC DOWN-MIXING WITH HARMONIC SIDEBANDS

8.1 Introduction

For pursuing an ultra wide sensing bandwidth, the photonic down-mixing technique was recommended due to the feasibility of amplitude-modulating an optical source at high frequency and its immunity to the EMI environment. Besides these advantages, it is also possible for harmonic sidebands of an electro-optic modulator's driving frequency to be used as the local oscillator in a photonic down-mixing process, in order to significantly enhance the bandwidth of near-field, electro-optic, microwave measurements. This concept has been introduced, in chapter 7, with a low frequency UHF-band antenna as an example DUT. In this chapter, the concept of utilizing the second- and even third-order-harmonic modulation sidebands on a laser-diode output are developed, with heterodyne down-conversion of microwave signals taking place within an electro-optic sensor crystal. The measurement bandwidth of an electro-optic microwave probe can thus be enhanced by as much as a factor of three with respect to the use of conventional, fundamental-harmonic sidebands. Carrier-sideband analysis from the measured optical spectrum indicates that millimeter-wave-frequency local-oscillator sidebands can be created using a Ku-band electro-optic modulator, and that the electro-optic-signal-modulation depth can be enhanced by suppressing the light-beam carrier component. Transverse near-field distributions from high frequency patch antennas are extracted using both second- and third-order-harmonic sidebands. Finally, a multiple cascaded, carrier-suppression method to enhance both the sensitivity and bandwidth, even up to the Ka-band region, of electro-optic sensing techniques is presented. The typical bandwidth limitations, low signal-modulation depth, and high laser-induced noise in millimeter-wave electro-optic-sensing applications have been overcome by suppressing the carrier portion of the optical-interrogation beam.

8.2 Motivation

With the use of high-order harmonics of the repetition rate of an ultrafast-pulsed laser for creating an LO signal, it is found that the measurement bandwidth of EO probing can in principal be extended to the terahertz range, although literally a price is paid for this capability through the greater expense of the laser source compared to a cw laser diode. In previous work using the pulsed-laser-harmonic LO generation, the 1,250th harmonic of an 80-MHz-repetition-rate pulsed laser was mixed with the 100.003-GHz output of a millimeter-wave frequency multiplier [14], yielding an IF signal with $f_{IF} = 3$ MHz at the output of the probe-beam photodetector. The resulting electrical amplitude and phase of the IF were measured using the narrow-band input of a lock-in amplifier.

While having a large number of uniform spectral harmonics from the ultrafast laser allows access to LO-sideband frequencies with millimeter-wave separation from the carrier wavelength, when employing a cw laser diode it is more difficult to achieve a reasonably high-power LO-sideband at such high frequencies. This is due to the limitations and costs of millimeter-wave, commercial-grade EOMs and the high-frequency signal sources necessary to drive them. In this chapter, we present an alternative to the creation of optical sidebands at the fundamental driving frequency of an EOM for use as the local oscillator in EO photonic-down-mixing test-and-measurement applications. Either by driving an EOM at a frequency of $f_{LO}/2$ and operating the device at a DC-bias point where it efficiently produces a second-order harmonic intensity modulation, or by utilizing an input signal of frequency $f_{LO}/3$ and overdriving the EOM to produce a third-order harmonic intensity modulation, LO signals can be generated at up to three times the rated fundamental frequency of the EOM. The effectiveness of utilizing these harmonic sidebands as LO frequencies to photonically down-mix microwave signals is evaluated through comparisons of EO experimental measurements on X-, K- and Ka-band patch antennas.

8.3 Bandwidth of Modulator Sideband Generation with Fundamental-Drive Frequency

The double sidebands (DSB) imparted onto the output of a cw, telecommunications-qualified, distributed-feedback laser using a conventional Mach-Zehnder type EOM can be used as the LO for mixing down, within an EO probe, a signal at f_{RF} to one at f_{IF} [24,45,49], as described previously. The frequency components generated by the ac driving signal and the DC bias point on the modulator transmission function determine the bandwidth. That is, the modulated light output is predominantly determined by the frequency and amplitude of the ac-driver swings along the modulation function around a given DC bias point. Typically, to avoid the creation of RF-harmonic information on a cw optical beam, the DC bias is set at the symmetric point ***a*** on the sine-squared intensity-modulation function shown in Fig. 8.1(a).

To enhance the EO-sensing component, which is the signal at f_{IF}, for a given RF condition, it is important to maximize the LO sideband component per unit light power. For an intensity modulator driven about point ***a*** with +14 dBm of RF power, the amplitude-modulated light has DSB around the carrier (Fig. 8.1(b)), and the modulation depth can be specified by the ratio of the carrier and sideband. The average power of the modulated beam at the EOM output, which is dominated by the carrier component, is ~10 mW for all the driving frequencies. Measured with 0.01 nm resolution on an optical spectrum analyzer at the output of a 1% tap from the EOM, the carrier power level is maintained, while the low-level sideband power decreases rapidly for higher frequencies: from 25% to 18.6%, 13.1%, and 7.6% for modulation frequencies of 5.241, 10.482, 15, and 25 GHz, respectively. Overall, the sideband degradation follows a slope of -0.41 dB/GHz over the C- to K-band microwave regions. Thus, when an optical sideband is conventionally generated using a fundamental-driving frequency harmonic in an EOM, a relatively large amount of the carrier wavelength remains in the beam, the modulation depth is relatively small, and the intensity of the sidebands decreases rapidly with increasing frequency.

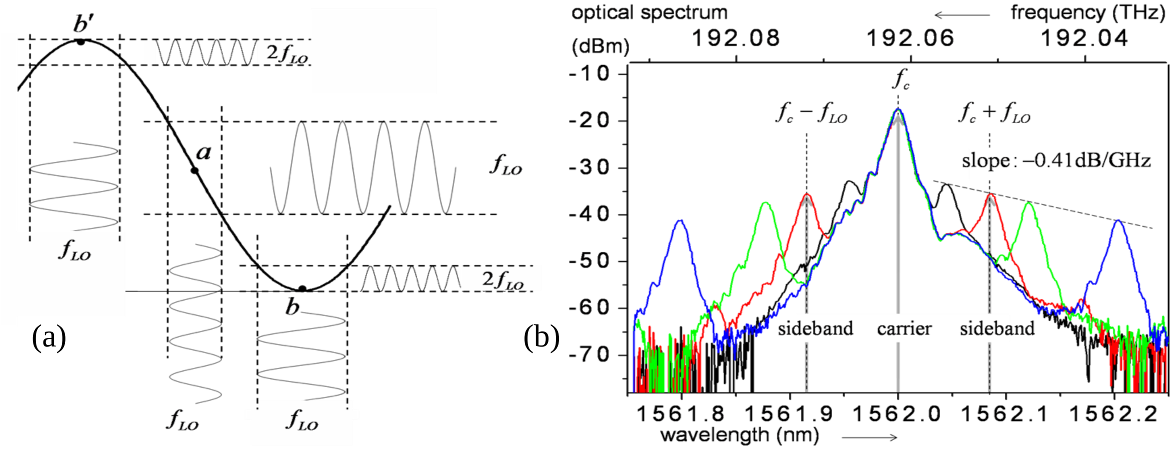

Figure 8.1: (a) Amplitude modulations at three symmetric DC-bias points of a sine-squared modulation function. The input sinusoids are drawn with vertical time axes and the modulation outputs with horizontal time axes. (b) modulated spectra and evolution of modulation depth at operating point ***a*** for several fundamental driving frequencies (Black, red, green and blue: f_{LO} = 5.241, 10.482, 15, 25 GHz, respectively; input LO drive power is +14 dBm).

8.4 Second-order-harmonic Intensity Modulation for Local-oscillator Bandwidth Enhancement

Operating an EOM at the minimum-transmission dc-bias point of its sine-squared modulation curve was a presented technique in chapter 7 for suppressing a carrier signal, as the ac part of the driving signal, which normally provides the LO for the photonic down-mixing, yields a predominant amplitude-modulated transmission at the second harmonic of the driving frequency, with a carrier that is significantly suppressed. The suppressed carrier significantly enhances the modulation depth, while the second harmonic of the driving frequency creates a doubled-LO-frequency sideband for down-mixing. Although this harmonic sideband-generation scheme produces a nonlinear output, the second-order component is dominant and actually serves as an efficient down-mixing source for enhanced-frequency sensing without signal distortion.

As the input oscillates to the maximum ***b'*** and minimum ***b*** values of the sine-squared curve, the output is rectified compared to operation at point ***a*** in Fig. 8.1(a). That is, the periodic output cycles are still balanced and identical, but the original LO driving period gets 'frequency doubling effect' resulting in efficient generation of sidebands at the second-order harmonic of the EOM driving frequency. Although both bias points ***b*** and ***b'*** in Fig. 8.1(a) are seen to fold the original LO period in half, operation at point ***b*** minimizes the carrier intensity, while operating at point ***b'*** maximizes the carrier intensity and minimizes the modulation efficiency (or sideband-to-carrier ratio). Illustrating the suppression of the optical-carrier intensity when biasing the EOM at point ***b***, the black curve in Fig. 8.2(a) shows the LO sidebands achieved when the driving frequency is at $f_{LO/2}$. The suppressed carrier in the second-order harmonic case transforms the DSB modulation (black plot in Fig. 8.1(b)) to a single-sideband (SSB) modulation with equal sideband amplitudes. This indicates that a nearly full modulation depth is achieved at 2 $f_{LO/2}$, or twice the driving frequency. As the carrier is suppressed enough to be essentially negligible, each sideband becomes effectively an adjacent band to the other, yielding a second-order harmonic with greatly improved modulation depth.

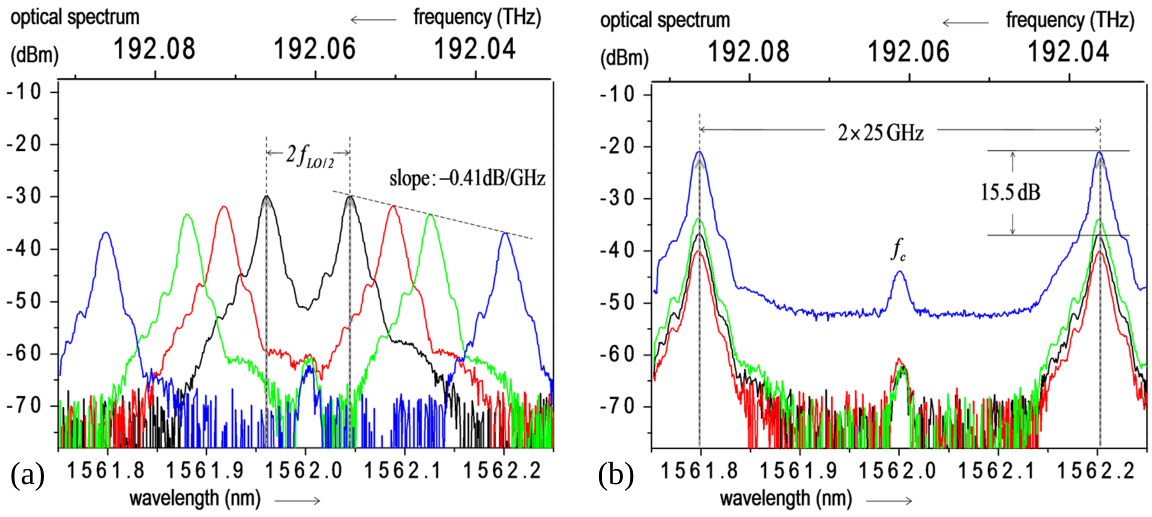

Figure 8.2: (a) Modulated spectra and evolution of modulation depth for several driving frequencies (Black, red, green and blue: $f_{LO/2}$ = 5.241, 10.482, 15, and 25 GHz, respectively; +14 dBm LO drive power) at the second-order harmonic operating points (bias ***b*** in Fig. 8.1(a)). (b) modulated spectra and change in modulation depth for various driving power levels (Red, black and green: +11, +14, and +17 dBm, respectively, at 25 GHz. Blue: optically amplified black spectrum).

As the sidebands decrease in intensity in Fig. 8.1(b), the modulation efficiency, already poor due to the strong carrier intensity, decreases further, and the sidebands cannot function as the LO past about 15 GHz for our Ku-band EOM. However, in the SSB case, the carrier is suppressed, and the matched sets of sidebands, now essentially without a carrier, have equal intensity. Consequently, even though the modulation slope still degrades by -0.41 dB/GHz (Fig. 8.2(a)), the intensities of the optical sidebands at the second-order harmonic are sufficient to serve as the LO out to much greater frequencies than the 15 GHz of the DSB case, operating at point ***b***. The light intensity due to the carrier does not noticeably change for higher driving frequencies (Fig. 8.2(a)) or larger drive-signal amplitudes (Fig. 8.2(b)). In the latter, the RF drive power has been increased in 3 dB increments from +11 to +17 dBm, to the maximum available power at 25 GHz that was readily available. While the sideband intensity increases much more than that of the carrier with increasing RF-driving power, it was necessary to utilize optical amplification of the EOM output with an Er-doped fiber amplifier to create an SSB sideband strong enough to use as an LO signal. The second-order-harmonic LO intensity was thus boosted by 15.5 dB, effectively extending the photonic heterodyne capability of the system completely through the microwave Q-band (33-50 GHz).

Although an increasingly large EOM-drive input power would result in diminishing benefits for operation at point ***a***, overdriving is actually beneficial in the second-order-harmonic-generation case, with higher input-oscillation amplitudes nonlinearly increasing the output-modulation amplitude and yielding the higher optical-sideband intensity. The relative optical-sideband intensity ratios for operation at ***b*** compared to conventional operation at ***a*** (input signal at 5.241 GHz), with EOM-drive power as a variable for the former and +14 dBm for the latter, are shown in Fig. 8.3(a). The second-order-harmonic optical-sideband power when using the maximum safe EOM-drive input of +26 dBm becomes comparable to the optical power level in the conventional EOM operation at point ***b***. The corresponding spectra of the fundamental- and second-order-harmonic modulations with comparable modulated output power are presented in Fig. 8.3(b). The red and black plots both yield a 10.482 GHz LO for optical down-mixing, the former via DSB operation at point ***a*** and the latter via SSB operation at point ***b***.

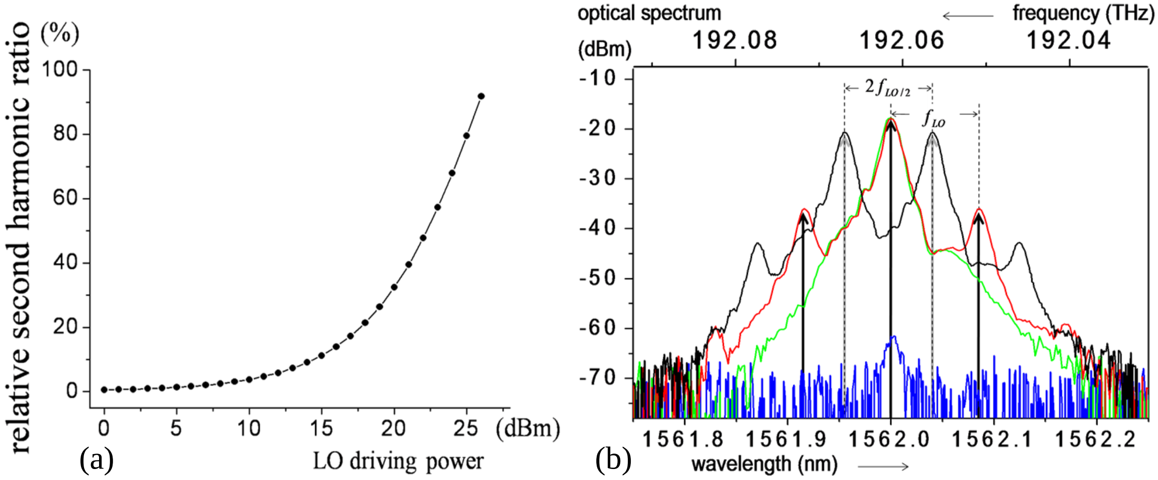

Figure 8.3: (a) Ratio of second-order-harmonic optical-sideband power (driven at 5.241 GHz, operating point ***b***) to fundamental optical-sideband power (driven at 10.482 GHz and +14 dBm, operating point ***a***) vs. EOM-drive power for the former. (b) comparison of DSB (red: driven by +14 dBm at 10.482 GHz; green: drive power off) and SSB (Black: driven by +26 dBm at 5.241 GHz; blue: drive power off) modulated spectra for comparable optical power.

8.5 Third-order-harmonic Intensity Modulation for Local-oscillator Bandwidth Enhancement

Without switching to an EOM of higher bandwidth or increasing the EOM drive frequency, the bandwidth of the optical LO sidebands can also be increased even further through the nonlinear-dynamic behavior of the EOM. Specifically, overdriving the EOM while it is biased at the 50% transmission position ***a*** of Fig. 8.1(a) produces the next higher odd-order harmonic [50]. This can be interpreted as nonlinear generation in a perfect centro-symmetric optical media (*i.e.*, $\chi^{(2)} = 0$, as in optical fibers), so that the next nonlinearity is given by the third-order harmonic. Figure 8.4(a) illustrates this harmonic generation for large-amplitude, EOM-input signals. Biasing at the exactly symmetric point ***a***, the two second-order harmonics at operating points ***b*** and ***b'*** cancel each other out, as they are out of phase with equal amplitude. While this is true in a precisely symmetric condition, for high frequency bands it is not technically trivial to fully suppress the second-order-harmonic sideband generation.

Figure 8.4(b) shows the combinations of the fundamental, second- and third-order-harmonic spectra when the EOM is driven by a signal at $f_{LO/3}$. Each of the spectra has essentially the same average output power, while the carrier depletes rapidly for higher EOM-drive power to yield a larger nonlinearity and sideband for the same output power. The black plot (driven with +26 dBm at $f_{LO/3}$) contains multiple major third-order harmonic components as indicated by the vertical dashed lines in Fig. 8.4(b). The energy at this frequency can then be used to extend the bandwidth of an EOM to three times its rated maximum frequency for generating LO sidebands.

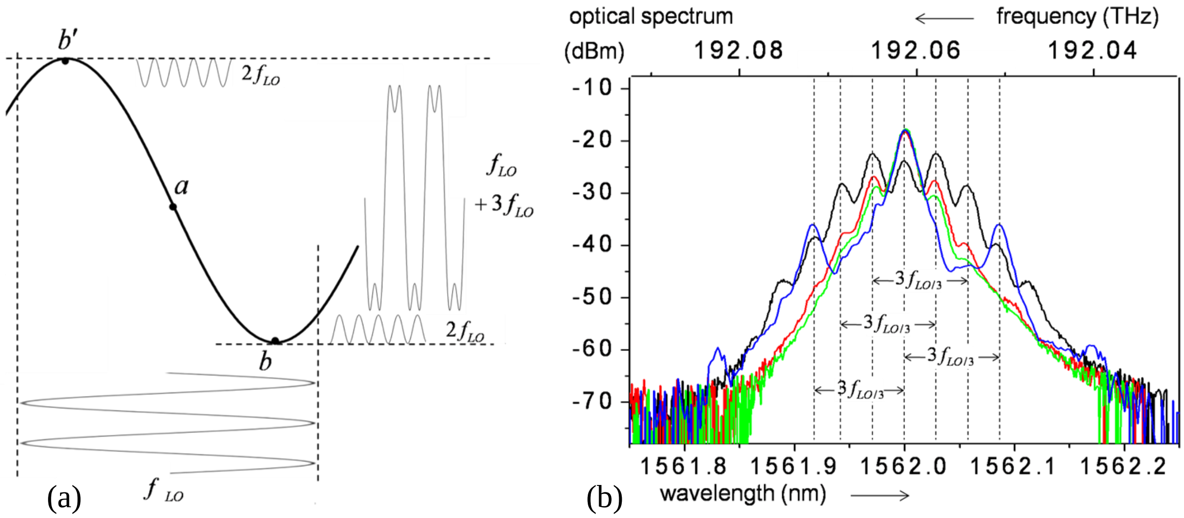

Figure 8.4: (a) Overdriven amplitude modulations using the symmetric bias point, ***a***. (b) modulated spectra and evolution of modulation depth for several EOM-input-drive power levels (Green, red and black: +18, +22 and +26 dBm, respectively, at $f_{LO/3}$. Blue: +14 dBm at f_{LO} for comparison).

8.6 Photonic down-conversion EO Sensing with Higher-order Harmonics

Compared with using an ultrafast pulsed laser, an EOM has a limited modulation bandwidth, and its use becomes the greatest factor increasing the cost for high frequency measurement applications extending up into the millimeter-wave regime. Conventionally, in EOM applications such as Radio over Fiber (ROF) systems, a high degree of system linearity is preferred to reduce the impact of nonlinear distortion (*i.e.*, harmonic or intermodulation distortion) and to deliver modulated RF information via an optical carrier using fiber. Thus, mitigating signal distortion induced by the nonlinear response of the EOM is one of the main concerns in ROF systems [51]. However, for EO probing, the RF signal is the radiation field from the DUT. Because the LO is used only as a beating source for the IF-down-mixing, where the IF contains the signal information, a strong and precise LO component is more important than its harmonic-order origin. Thus, the nonlinearity in the EOM operation is not detrimental, but beneficial for enhancing the bandwidth of the EO measurement without RF-signal distortion.

To demonstrate the utilization of second- and third-order-harmonics of the EOM-drive frequency in EO sensing, we adopted the photonic-down-mixing platform used previously for vector-RF-electric-field sensing with the fiber-mounted, micro-cavity-EO sensor [24]. The experiment was arranged so that the entire laser-beam path was enclosed within optical fiber, and the probe light beam with the LO modulation was passed down the fiber to a $LiTaO_3$ EO probe tip. The probe was raster-scanned over an X-band-patch-antenna device-under-test (DUT) (resonance frequency of 10.485 GHz) using a computer-controlled translation stage, and the probe light, now with the optically-mixed sidebands, was reflected back up the fiber and directed by an optical circulator to a photodetector for demodulation.

The evolution of the peak EO signal levels for three cases – mixed down using each of the first three harmonics of the EOM-drive signal – versus LO drive power are presented in Fig. 8.5(a). The signal builds up at 0.96 dB per 1 dB at the fundamental LO drive frequency, and this slope becomes steeper for the two higher-order harmonics, 1.76 dB per 1 dB and 2.60 dB per 1 dB of EOM-drive power for the second- and third-order harmonics of LO/2 and LO/3, respectively. The higher-order harmonics have the higher thresholds to emerge, but they then grow faster according to these slopes. Although the intercept points for the second- and third-order are expected to be +31.7 dBm and +29.06 dBm of the respective LO power, both cases pass their 1-dB suppression points before they reach the EOM maximum safe input power.

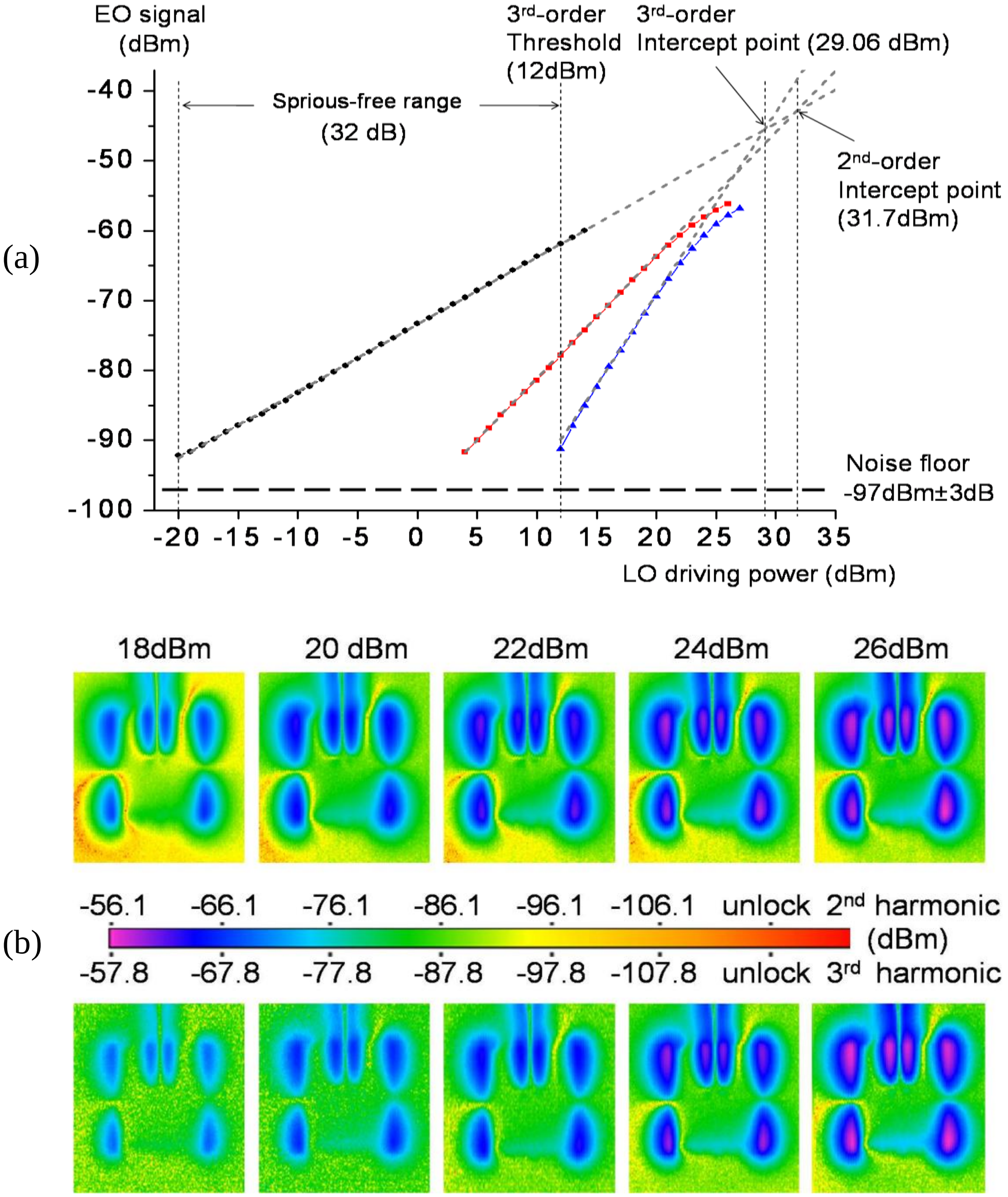

Figure 8.5: (a) Down-mixed EO-signal strengths using the first three modulation harmonics as the LO, versus modulator driving power (Black, red and blue: fundamental-, second- and third-order, respectively). (b) EO field maps of the transverse near-field distribution (horizontal polarization) from an X-band patch antenna for different modulator-drive powers, (as indicated, +18 to +26 dBm). The top (bottom) scans use the second (third)-order harmonic LO sideband to mix down the signal frequency to f_{IF}. As amplitude and phase are measured simultaneously in this EO measurement technique, the two terms may be combined together to illustrate the temporal nature of the sinusoidal microwave electric field around the patch antenna.

The horizontal transverse electric-field distributions 200 µm above the DUT antenna are shown in Fig. 8.5(b) versus EOM-drive power for both the second- and third-order harmonic LO cases. The field distributions are virtually the same as those found using the fundamental LO previously [24]. Furthermore, the field distribution for the entire driving power range – even beyond the 1 dB suppression power level – is uniform when mixing with either of the higher-order-harmonic LO frequencies, demonstrating that noninvasive near-field EO measurements can be extended to frequencies up to two and three times that of the EOM-drive frequency without loss of fidelity.

In Fig. 8.5(b), the utility of the field-mapping technique becomes apparent, as one is able to isolate highly detailed field information on the microwave DUT. In this case, since the length of the antenna is designed to be a half-wavelength at the resonance frequency, the potential reaches its maximum value at the edges of the patch, close to the recessed feed line and at the farthest extent from the feed. The transverse field of Fig. 8.5(b), in a pattern expected from the potential distribution, has its peak amplitude outside the antenna conductor near the corners of the patch and within the gaps between the patch and the feed line. Here the probe captures the electric field component that is parallel to the plane of the patch.

8.7 Harmonic-photonic-heterodyne EO probing applied to a K-band Antenna array

As the response of the EOM is consistently rolling off as the driving frequency increases past the X-band maximum at 12.5 GHz, use of a fundamental LO sideband at driving frequencies up into the K-band (18-26.5 GHz) limits the sensitivity of the EO measurements. Thus, the second-order harmonic LO sideband has been utilized in the characterization of two orthogonal transverse electric fields of a 2 × 2 array of patch antennas having a resonant frequency of 18.535 GHz. As with the horizontal field component in the single, X-band patch antenna, each of the array patches (positioned in the four corners of the viewing window) has fields at their corners that are out of phase with their neighboring fields (Fig. 8.6(b)). However, each of the patches cycles through its field maxima in phase with the other three, indicating that the interconnects and reactive parasitic circuit effects were chosen so as to maintain a constant phase between each radiating element. One can also notice the feed microstrip, entering the window from the left-center and supporting the field of the incident signal, as well as the nodes in the center of the window where the input is divided into individual incident signals for the four antennas.

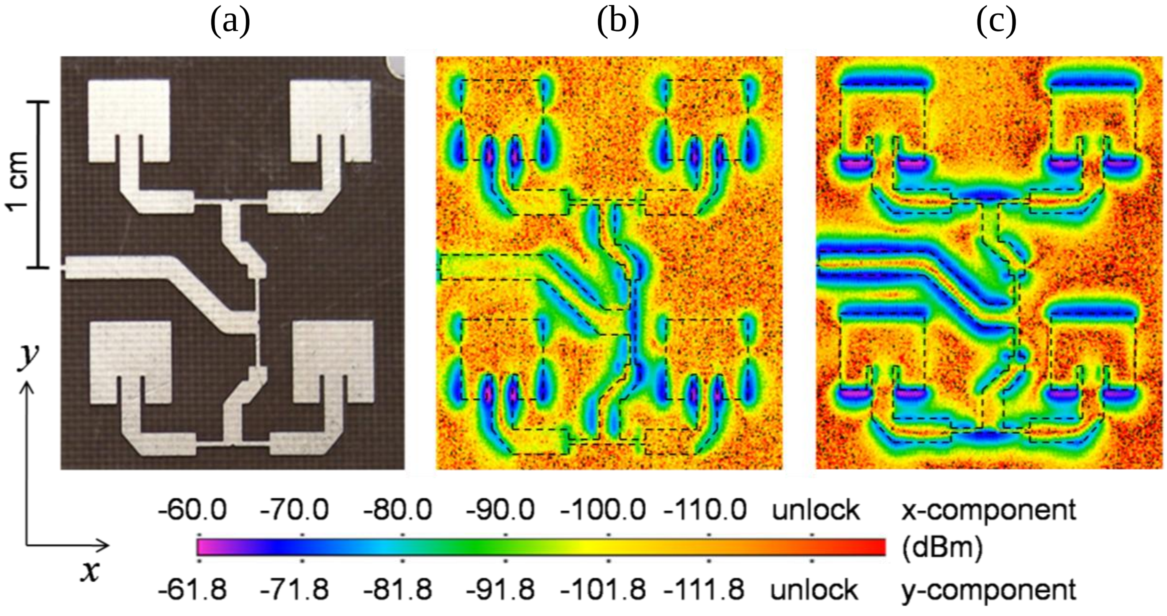

Figure 8.6: (a) 2 × 2 array of K-band patch antennas. (b) horizontal (*x*-component) EO field amplitude maps of (a) using 2nd order harmonic LO for amplitude-phase animation. (c) vertical (*y*-component) EO field amplitude maps of (a) using 2nd order harmonic LO for amplitude-phase animation). (EOM-LO: +26 dBm at 9.266 GHz, DUT-RF: +10 dBm at 18.535 GHz).

Now, the field is strongest at the top and bottom edges of each patch, and while all of the four patches are still in phase with each other, the strong fields within each individual patch are also in phase. This confirms that the vertical direction will correspond to the polarization of the antenna in the far field, as these field components will add together coherently as they propagate.

8.8 Millimeter-wave Near-field sensing with Multi-stage Optical-carrier suppression

Although the EO sensitivity decreases for measurements at higher frequencies due to the degradation of modulation depth, this can be contained reasonably well by utilizing suppression techniques on the carrier components. Here three cascaded carrier-suppression techniques, each employing a different mechanism, are presented. The field mapping data for a millimeter-wave antenna is then demonstrated using the multi-stage optical-carrier suppression.

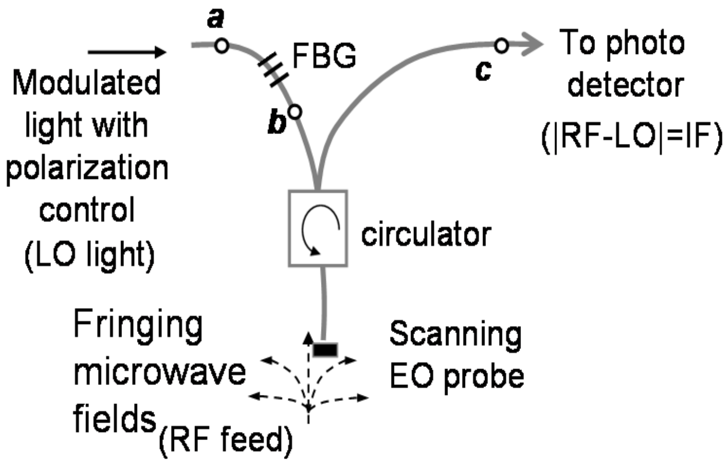

Figure 8.7: Optical heterodyne electro-optic sensing sub-system with multi stage carrier suppression. (Points ***a***, ***b*** and ***c*** are the three carrier suppression stages investigated).

Figure 8.7 is the sensing section of the optical-heterodyne EOS system, and points ***a***, ***b*** and ***c*** were the multiple carrier-suppression points to be investigated. For the first suppression stage at point ***a***, operating an EOM at the minimum-transmission dc-bias point of its sine-squared modulation curve was a good technique for suppressing a carrier signal. This was because the ac part of the driving signal, which normally provides the LO for the photonic down-mixing, yielded a predominant amplitude-modulated transmission at the second-order harmonic of the driving frequency, with a carrier that was significantly suppressed. The suppressed carrier significantly enhances the modulation depth, while the second-order harmonic of the driving frequency creates a doubled-LO-frequency sideband for down-mixing. The solid-line spectrum in Fig. 8.8 represents the carrier-suppressed double sidebands when the EOM is driven with +11 dBm at 17.2985 GHz, a frequency that is LO/2 compared to the second-order harmonic EOM output.

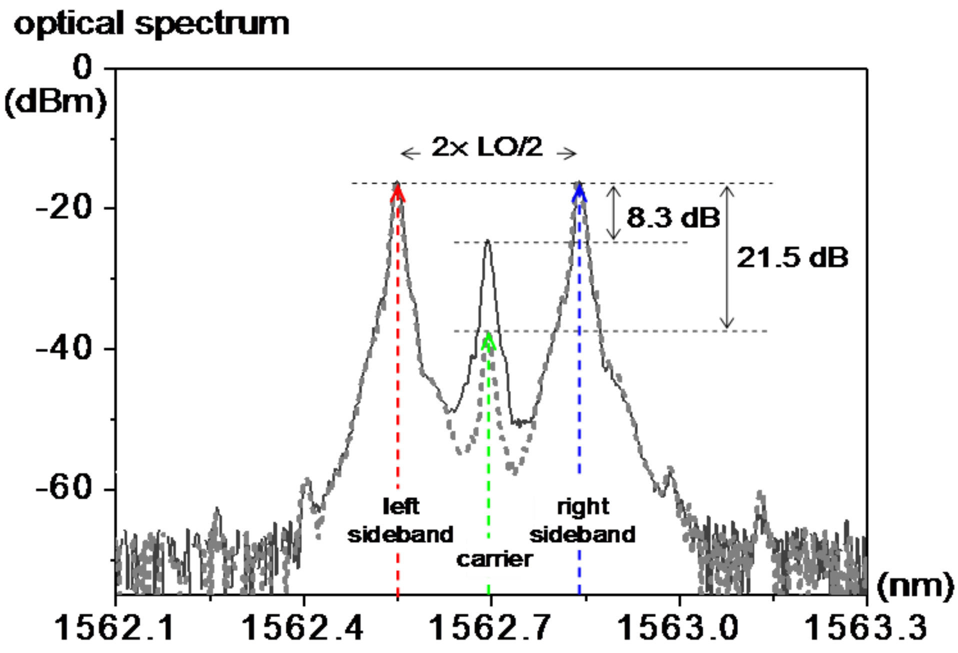

Figure 8.8: Carrier-suppressed LO spectra at stages ***a*** (solid plot) and ***b*** (dashed gray plot). (All spectra measured after 20 dB attenuation).

Since the bandwidth and modulation-depth-enhancement technique relies on the nonlinearity of an EOM, a larger LO/2 input will yield a more efficient second-order-LO harmonic. However, the damage threshold of the EOM and deficiencies of the drivers at higher frequencies will limit the modulation sideband of the second-order harmonic. However, the modulation depth is determined by the carrier-to-sideband ratio, and thus the modulation efficiency can be further enhanced by additional carrier suppression.

The modulated input spectrum (Fig. 8.8) at stage ***a*** of Fig. 8.7 shows a carrier-suppressed DSB with the second-order, LO harmonic sidebands. A higher frequency LO modulation yields a wider sideband separation, albeit with reduced amplitude. However, the wider sideband separation makes it easier to eliminate detrimental carrier components through filtering. For instance, the LO-sideband spacing for our Ka-band signal is 0.29 nm as shown in Fig. 8.8. A fiber Bragg grating (FBG) filter of 0.2 nm FWHM bandwidth accomplished 13.2 dB of additional carrier suppression at stage ***b***, as shown in Fig. 8.8, and thus the carrier-suppressed DSB spectrum essentially evolved into a single-sideband (SSB) case.

The prior two stages of carrier suppression enhanced the modulation depth of the LO sidebands that were used for mixing with the RF fields to be measured. The sensor itself yields an EO phase retardation when the signal RF electric field and the optical-beam interact (*i.e.*, EO effect) within the probe crystal. Typically, the phase modulation is transformed into a minute amplitude modulation using the slope at the 50% transmission point of the sine-squared amplitude-modulation slope for the EO sensor.

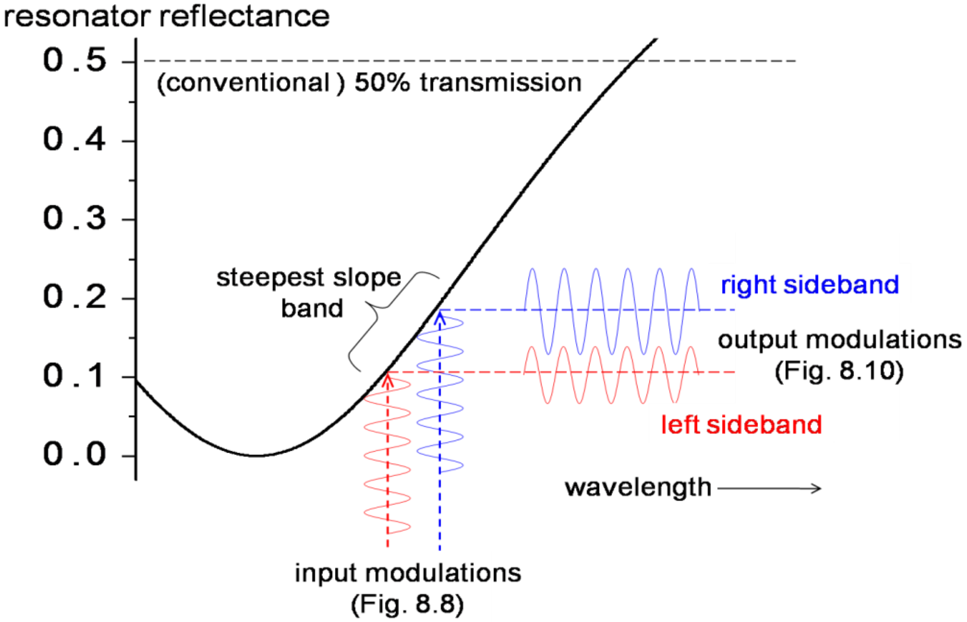

Figure 8.9: Principle of carrier suppressed electro-optic modulation for single sideband optical input. The carrier is much stronger at the conventional, 50% transmission point, while the slope and sidebands would be lower.

It was previously shown that an EO probe fabricated as a micro-cavity optical resonator offers a steeper intrinsic modulation slope without requiring conventional polarization optics to create the sine-squared modulation function. However, the resonator-based modulation slope has even more advantages over the conventional case, as it has its steepest slope around the minimum transmission regime. For the 52 μm-thick, x-cut, HR-coated $LiTaO_3$ wafer tip used previously, operating the LO sidebands around the steepest slope of the resonator curve yielded a more efficient secondary RF modulation with less carrier power (*i.e.*, average transmission) than the conventional 50% case (Fig. 8.9).

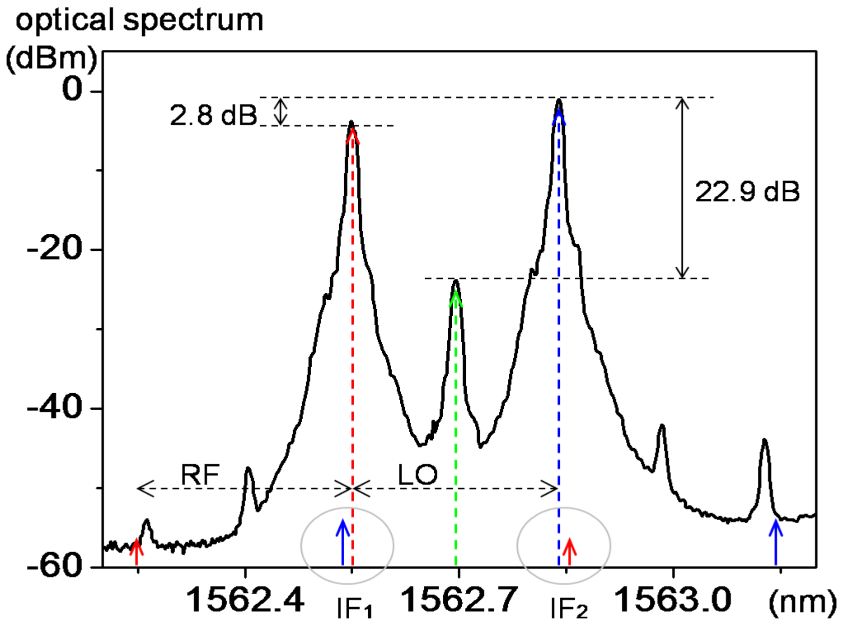

Figure 8.10: Electro-optic modulated LO and RF spectrum at stage ***c***. (LO:35.497 GHz, RF:35.5 GHz, and $IF_{1,2}$: 3 MHz).

Owing to the steep slope, both the left (red) and right (blue) LO sidebands yielded different transmission (or reflection) optical outputs. Although this slope difference causes a different modulation depth and signal level, the same slope polarity (*i.e.*, ascending in this case) allows the output modulation components to combine constructively in one common fiber path to the photodetector. The experimental spectrum of the left and right sidebands is shown in Fig. 8.10.

The two sideband spectra out of the EO probe sensor contain minute levels of the RF sideband components. The two dominant beating regions (within the circles in Fig. 8.10) of the millimeter-wave-scale difference frequency of |LO-RF| yield sub-sonic IF components at a frequency of 3 MHz. The overall IF is a constructive summation of the (IF_1) and (IF_2). The 35.497 GHz of the frequency-doubled LO is used to attain a 3 MHz IF when compared with the 35.5 GHz signal frequency of a Ka-band, 8 × 2 antenna array (Fig. 8.11(a)). The amplitude of the resulting down-mixed 3 MHz RF signal (transverse near-field components), demodulated in the low-frequency photodetector, are plotted versus position in Fig. 8.11 for a 2 × 2 section of the array. An SNR of >35 dB was achieved, allowing detailed resolution of the fields along the edges of the antennas and their feed network.

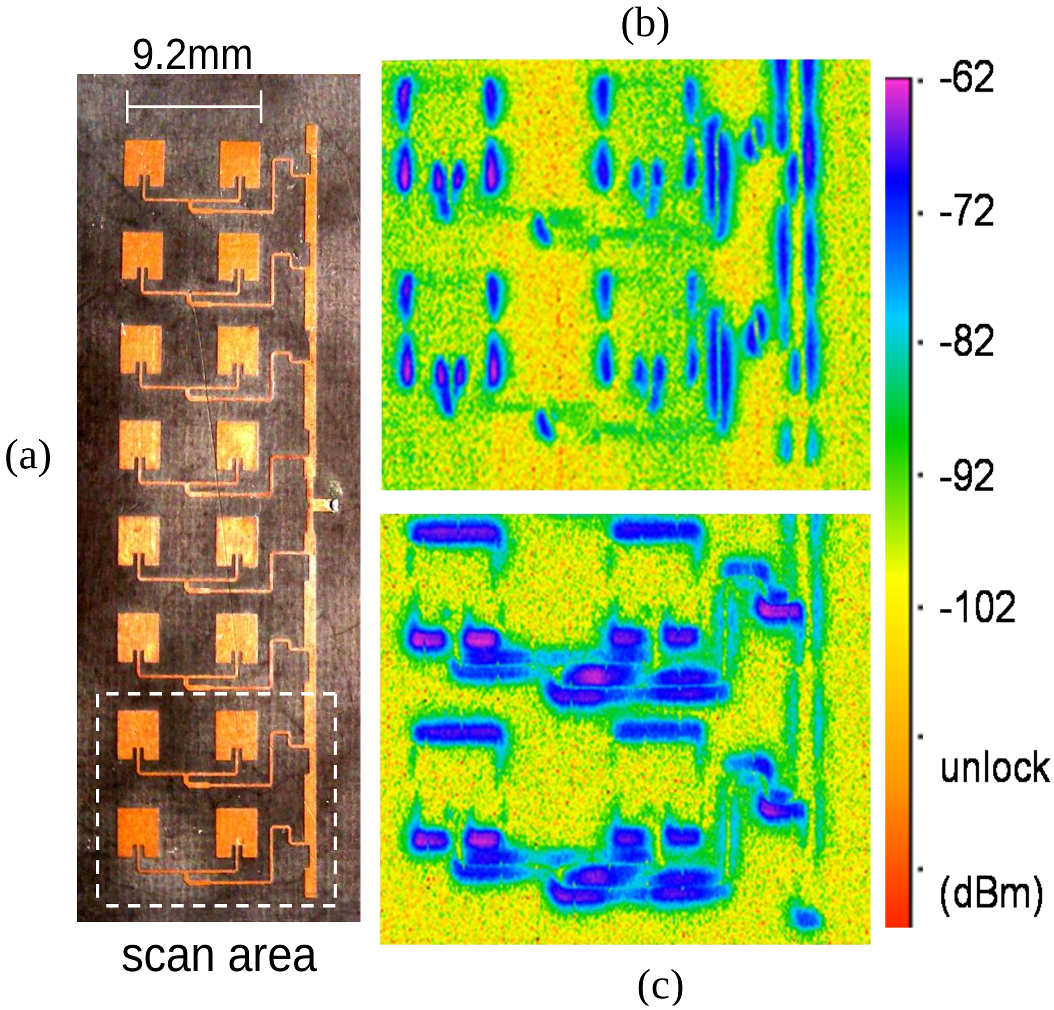

Figure 8.11: EO amplitude maps of the transverse field components of a Ka-band (35.5 GHz) patch-antenna array (P_{in} = +5 dBm). (a) photograph of 8 × 2 array; (b) horizontal transverse electric-field distribution; (c) vertical transverse electric-field distribution.

8.9 Summary

Utilizing higher-order harmonics during the operation of an EOM to generate a photonic LO, we have demonstrated that the finite bandwidth of a typical low-cost amplitude modulator can be expanded by two to three times, into the millimeter-wave regime. Both second- and third-order-harmonic regimes of the modulator can be used to extend operating bandwidths to millimeter-wave bands. In addition, a multi-stage optical-carrier suppression technique for millimeter-wave field measurements, enhancing the signal-modulation depth for both LO generation and EO sensing, was presented. The applications to the near-field analysis of high frequency microwave patch antennas (at the X-band) and arrays (at the K- and Ka- bands) were demonstrated.

CHAPTER 9

AN OPTICAL-FIBER-SCALE ELECTRO-OPTIC PROBE FOR MINIMALLY INVASIVE HIGH-FREQUENCY FIELD SENSING

9.1 Introduction

The previous chapters have focused on the techniques for improving sensitivity, system simplification and bandwidth enhancement in the EOS techniques rather than the invasiveness concern of the sensing scheme. In fact, the capability of minimally invasive detection of the electric near-field from a radiation source is one of the most distinguished and attractive features in EOS techniques [1,2,9]. The significantly lower intrusiveness of EO probing originates from the dielectric nature of the EO probe structure, as it avoids the use of highly field-disruptive metal components. Although such dielectric EO-probe antennas or sensors enable significantly lower invasiveness in near-field sensing than conventional metal-based devices, the cross-sectional size and volume of EO probes, including their crystals and support structure, are the main limitations to realizing an ideal minimum-invasiveness configuration. Generally, to increase the scanning mobility and spatial resolution, EO sensors are mounted on the fiber facet, which is terminated with a bulk ferrule and/or graded-index lens [3,14]. The typical size of such a termination scheme is the ~1-2 mm diameter of a ferrule or lens onto which a smaller sensor crystal is mounted. Such a termination scheme has a limit to its size due to the geometry required to re-direct the modulated beam back through the optical fiber.

In this chapter, we report what is likely the least-invasive fiber-based field probe assembled and employed to date. It eliminates all optical mounting components, resulting in a micro-EO-sensor tip, or micro-scale probe, being mounted directly at the end of a standard telecommunication fiber (model SMF-28). The significant size-reduction of the probe provides not only a diminished invasiveness, but it also eliminates the need for changing probes for other vector-field measurements, allowing a uniform probe sensitivity to be maintained. The full *x*-*y*-*z* vector field re-construction from a planar radiation antenna, attained using the same probe in different positions, is presented. In addition, the relative invasiveness of various scales of EO probes has been investigated via microwave network analysis and comparisons of near-field EO amplitude maps. Finally, a significantly improved spatial accessibility that is beneficial for probing fields around smaller devices and structures, especially in high frequency applications, is presented.

9.2 Structure of a Micro-cavity EO probe

A number of fiber-based EO probes have been reported by several groups [3,14,38,48]. All of these are based on a retro-reflection process employing dielectric mirrors [3,14,48] on the probe itself or on highly reflective surfaces inherent to the device under test (DUT) [38]. These fiber-based EO probes can be categorized into two main types: those that are directly fiber-mounted, and those that are attached to a ferrule and lens assembly, depending on how the optical beam diverges within the EO crystals [3,14,48]. The size of the EO crystal is the crucial factor in determining the mounting type, and a clear criterion was presented in Ref. 3. Crystals up to 1 mm thick can be directly mounted on a thermally-expanded-core fiber-end, because the increased numerical aperture of the expanded core allows one to achieve virtually a collimated beam within the crystal volume.

While thicker crystals increase the EO sensitivity, the coupling efficiency of the reflected beam back into the fiber core is typically degraded due to the divergence of the beam. Furthermore, an increased volume and interaction length of the crystal would nearly always be detrimental for invasiveness, primarily in the case of the former, and sensing bandwidth, in the case of the latter. Thus, the use of thin crystals that possess a small surface area is essential to minimizing invasiveness related to the probe volume. While probe sensitivity can be sacrificed when maximizing bandwidth and reducing invasiveness, the small interaction length within a thin crystal can be extended if an etalon is created and multiple Fabry-Perot round trips inside of the cavity are used for EO-phase-retardation enhancement [23,24].

The structure of a fiber-based micro EO probe is shown in Fig. 9.1(a). In this case, we again procured a 52-µm-thick x-cut $LiTaO_3$ wafer and coated it with five-layer high-reflection coatings on both of its larger surfaces. The wafer was diced to a ~0.2 mm × 0.2 mm area to fit onto the ~125 µm diameter of a standard fiber, and it was attached with ultra-violet curing optical cement. Because the crystal is very thin, the first few round-trip components of the light inside the micro-resonator can still be reasonably aligned back to the fiber without the need for an expanded-core. The use of a standard fiber and minute volume for a sensor crystal, without the need for ferrules, graded-index lenses, and glass alignment collars, also results in a significant reduction of the probe cost.

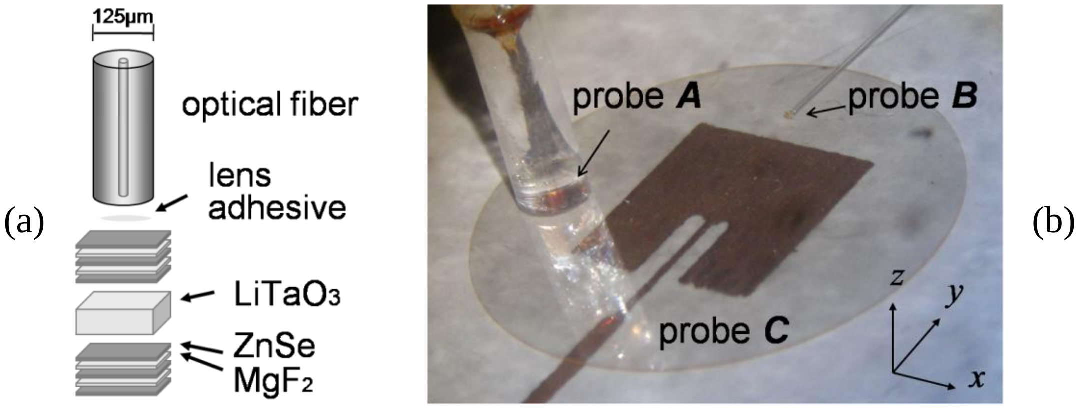

Figure 9.1: (a) Structure of a micro-cavity EO fiber probe. (b) photograph of three different $LiTaO_3$ EO sensors over an X-band patch antenna. ***A*** is a conventional resonance-based EO probe with a 1.8-mm-diameter ferrule mount [24], positioned with the fiber axis normal to the plane of the antenna. Probe ***B*** is the micro-scale probe of (a), mounted with the fiber axis parallel to the plane of the antenna. ***C*** is a thin (60 µm), circular wafer (diameter: 10 mm) of $LiTaO_3$ that covers the antenna and could be used with an expanded, free-space optical beam for rapid, large-area sensing. (invasiveness: ***C*** >> ***A*** > ***B***).

The detailed principle and performance of a resonance-based, fiber-coupled EO probe, as well as an entire photonic-down-mixing EO probing system, were discussed earlier, [and in Ref. 24]. Here, the EO interaction occurs only over a very confined area of the crystal cavity, determined by the mode-field diameter of the fiber, as well as the thickness of the crystal and the Q-factor of the resonator. Often for free-space, bulk-probe sensing, the EO interaction volume is significantly expanded so that the optical-sensing area can be increased to include a larger part, or even nearly the entire probe volume (*e.g.*, probe ***C*** in Fig. 9.1(b) is 60 μm thick, but has a 10 mm diameter). While this type of sensor can facilitate rapid sensing of field distributions over a large area, it can also influence the performance of the DUT, as shown later in Sect. 9.3.

While the length over which the volume of the light beam interacts with the microwave electric field in the EO crystal governs the EO sensitivity per unit optical and microwave intensity, the invasiveness is primary determined by the increase in capacitance (*i.e.*, volume and permittivity) due to the presence of the crystal. The optical-resonator cavity increases EO interaction length by keeping the photons inside of the cavity for a longer time without increasing the thickness and volume of the crystal, thus reducing the microwave-field distortion. Hence, the micro-cavity EO sensor mounted directly on a fiber facet helps to minimize invasiveness while maintaining a reasonable sensing quality.

9.3 Three component Vector-field mapping with a Minimally Invasive EO probe

To compare probe invasiveness between a conventional ferrule-supported probe and a micro-scale probe, an optical-heterodyne system for down-mixing of the optical beam and extracting the microwave amplitude and phase was adopted [24,30]. Using a configuration that kept the entire optical system the same except for the different fiber-based probes, the three independent, orthogonal vector electric-field components of the 10.485 GHz signal at the resonance frequency of an X-band patch antenna were measured. In this now familiar technique, a cw laser beam was modulated within an electro-optic modulator (EOM) at a frequency that became the local oscillator (LO), before that beam was again modulated by the DUT electric field in the EO sensor crystal. Here the second-order harmonic of a 5.421 GHz drive signal to an EOM was used to efficiently create the photonic LO [24]. The down-converted beating components (or intermediate frequency, IF) at 3 MHz (10.485 GHz minus 2×5.421 GHz) were used to reconstruct the original amplitude and phase of the electric fields from the DUT.

Generally, fiber probes are positioned vertically with respect to a DUT because of accessibility and invasiveness concerns (see probe ***A*** in Fig. 9.1(b)). This configuration enables the sensing of only certain vector field components, based on the orientation of the optic-axis of the crystal. For instance, an x-cut $LiTaO_3$ wafer has its optic-axis in the plane of the wafer, so the EO effect gets maximized as the electric field is applied along this axis. In this case, the x-cut $LiTaO_3$ fiber probe (the probe ***B*** placed as in Fig. 9.1(b)) can be used to measure two transverse (*i.e., x* and *y*) electric-field components. If one wishes to measure the normal (*i.e., z*) component, the probe has to be replaced with another one fitted with a z-cut crystal.

The characteristics of EO materials vary with the orientation of an optic-axis (*i.e.,* x- or z-cut). For instance, the induced birefringence due to an applied electric field E for x-and z-cut $LiTaO_3$ are $\Delta n_{x\text{-}cut}=(n_e^3 r_{33} - n_o^3 r_{13})E/2$ and $\Delta n_{z\text{-}cut}=n_o^3 r_{13} E/2$, respectively. Using the known values for the EO coefficients at 1558 nm [52], the EO-induced birefringence values per unit electric field (*i.e.,* EO figure of merit) are 97.1975 pm/V and 33.0794 pm/V for x-and z-cut, respectively. Thus, the x-cut probe has a nearly three times superior sensitivity as the z-cut probe for the same electric field, making it highly advantageous to utilize the x-cut configuration for measuring the two transverse and the normal field components. However, cumbersome re-alignment and sensitivity-calibration procedures would be necessary if one needed to switch between probes.

9.3.1 Minimally Invasive Three component Field mapping

Since the miniaturized EO probe of Fig. 9.1 has an increased accessibility to the DUT, full three-dimensional, directional-field sensing becomes possible with a single probe. For instance, placing the micro-scale probe ***B*** laterally as in Fig. 9.1(b), the vector field sensitivity is directed along the optical-axis. If the optical axis of probe ***B*** in Fig. 9.1(b) is set normal to the plane of the DUT, the probe measures the field in the z direction. To measure the transverse field components, the probe fiber would first be simply rotated around its longitudinal axis by 90º so that the optical axis of the EO crystal was parallel to, and sensitive to, the DUT field polarization along the *x* direction. To capture the *y* component of the field, the probe fiber would be rotated by 90º so that the fiber itself was made parallel to the *x* axis, with the crystal optic axis remaining in the plane of the DUT, both parallel and sensitive to its *y*-directed polarization. If this was attempted with probe ***A***, the ferrule diameter would limit the proximity that the probe could have to the DUT, and the parasitic capacitance presented by the probe would also increase.

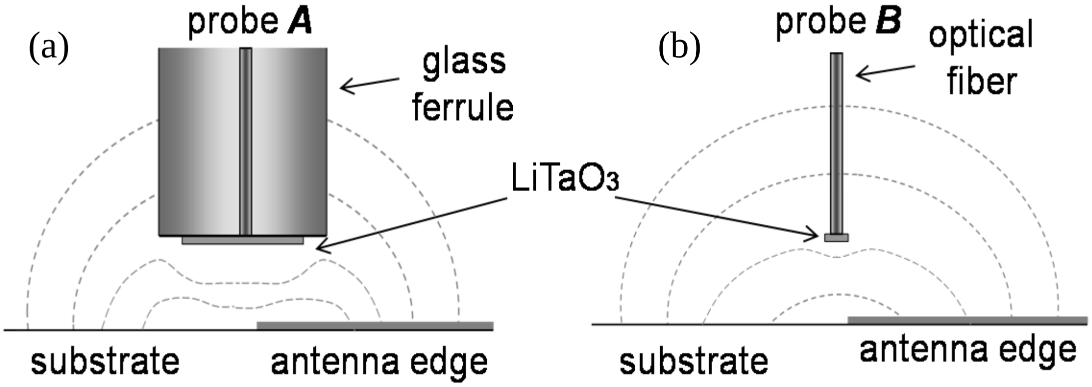

Figure 9.2: Concept of electric field distortions near the radiating edge of the sample patch antenna, (a) for ***A*** in Fig. 9.1 and (b) for probe ***B*** in Fig. 9.1. (Dashed lines are electric field flux).

To better understand the concept of field distortion due to dielectric probes having different sizes, examples of how electric-field flux changes due to the capacitance of EO probes are illustrated in Fig. 9.2. Finite-element simulations [*e.g.*, in 53] show that one result of substituting air with the volume and permittivity of dielectric probes is that the electric-field flux lines in the vicinity of the probe may deviate significantly, causing a field pattern to actually 'flatten' or take on a more distributed characteristic with respect to the pattern in air. When comparing the effect of the small, but still relatively large volume of probe ***A*** (as compared to the micro-scale probe), one would expect to observe a more widely distributed field measured by the former as compared to the latter. This is what is observed in a comparison of the measurement fidelity of the fields above the patch antenna for probes ***A*** and ***B*** (Figs. 9.3(a) and (b), respectively)**.** That is, probe ***B*** extracts an apparently more localized field distribution as compared to probe ***A***, a result of the fact that the increased area of high-permittivity material present in probe ***A*** compresses the field under the probe. All three orthogonal components of the electric-field vector from the patch antenna, as measured with the micro-scale probe, are shown in Figs. 9.3(b), (c), and (d).

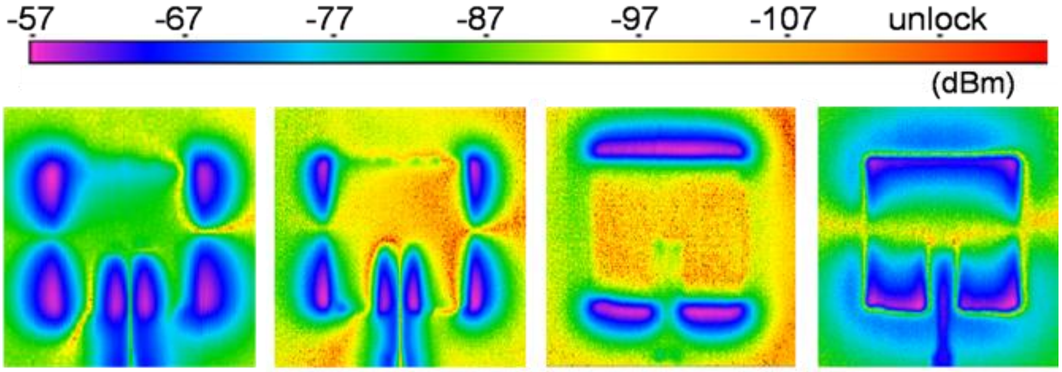

(a) (b) (c) (d)

Figure 9.3: EO field amplitude maps of the X-band patch antenna (a) horizontal (*x*-component) measured with probe ***A*** [from chapter.8] (b) horizontal transverse (*x*-component) measured with probe ***B*** (c) vertical transverse (*y*-component) measured with probe ***B*** (d) normal (*z*-component) measured with probe ***B.***

The *x*-*y*-*z* patterns are measured at a uniform height ~250 µm above the DUT, and thus the sensitivity for each of the measured components is the same, and the amplitude field plots in Fig. 9.3 (b-d) have the same scale and can be directly compared. This is a departure from all previous work with fiber-based field probes, in which either different probe materials, different crystal axes, or different probe positions (that presented different invasiveness profiles) were employed. The peak modulated signal level at the IF as measured on a lock-in amplifier read-out instrument is -57 dBm ±0.5 dB for each of the three field components. The significance of the field patterns for the patch antenna, which is not an objective of this thesis, is discussed in Ref. 2. From the current characterization, however, we can conclude that the micro-scale probe yields a substantially more detailed and accurate microwave near-field pattern.

9.3.2 Invasiveness Analysis versus Probe Size

The invasiveness of a radiation source is heavily influenced by the distance from the DUT to an EO sensor probe. The near-field regions may be categorized into two sub-regions based on invasiveness, distance and radiation patterns of the DUT. One is the reactive near-field region, within a wavelength of the DUT. The other one is the radiating near-field region, located before the conventional border of the Fresnel/Fraunhofer regions [5]. The fields within the reactive region are important in that they eventually determine the Fresnel to Fraunhofer distributions.

Although EO sensing, due to its photonically assisted, all-dielectric configuration, is the most promising experimental way to measure the fields that serve as the origin of the far-field pattern, the reactive near-field regime is highly susceptible and invasive to any material other than air. For instance, the X-band patch antenna used in Figs. 9.1 and 9.2 has a 10.485 GHz resonance frequency with a -11 dB return loss as measured with a vector network analyzer. The resonance characteristics of the DUT remain virtually the same when probes ***A*** and ***B*** are brought into the near field of the patch as shown in Fig. 9.1(b) (the antenna return loss for the case when air or either of the fiber-based probes is represented by the black curve in Fig. 9.4). However, the resonance dip frequency and degree of return loss are modified noticeably as the surface or volume of the probe increases.

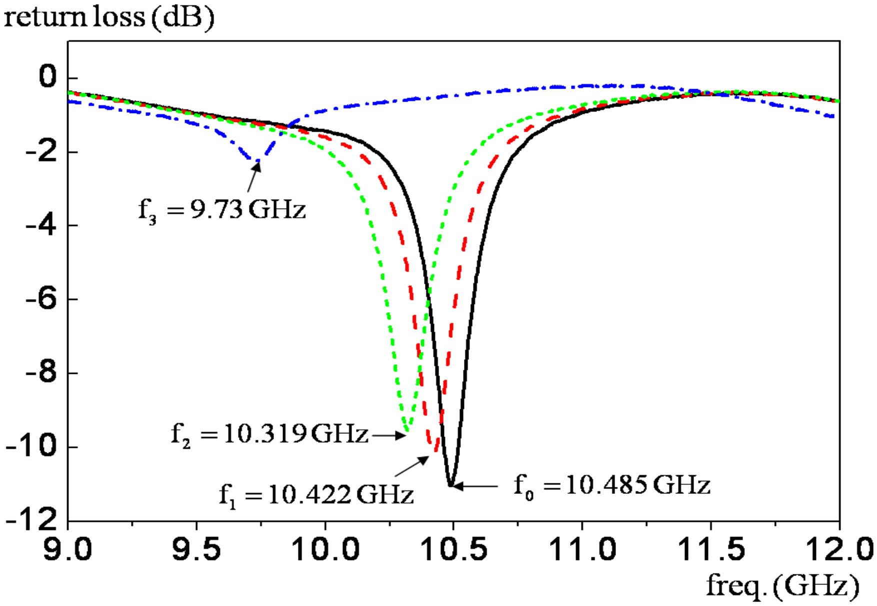

Figure 9.4: Evolution of the resonance performance of the X-band patch antenna in Fig. 9.1(b), where the small return-loss values correspond to the peak of the antenna radiation spectrum. Black curve: antenna, 200 μm below probe ***A*** or ***B***; red dashed curve: antenna covered with 150-μm-thick glass slide; green curve: antenna covered with 60-μm-thick $LiTaO_3$ wafer with 200 μm air gap; and blue curve: antenna covered with 60-μm-thick $LiTaO_3$ wafer with no air gap.

For instance, using a 150 μm thick glass slide, with a relatively low permittivity compared to most EO materials, to cover the entire DUT shifts the resonance frequency 63 MHz shorter (to the red line in Fig. 9.4). For more invasive materials like the 60 μm $LiTaO_3$ wafer probe ***C*** of Fig. 9.1(b), the resonance frequency decreases by 755 MHz (the blue line in Fig. 9.4). Covering the DUT with a high-permittivity wafer ruins the desired resonance frequency and radiation efficiency by degrading the quality of the match of the characteristic impedance of the antenna input. To mitigate the device invasiveness, one may tolerate a decrease in EO-sensor sensitivity by offsetting the wafer probe above the DUT and leaving an air gap between the probe and DUT. The field intensity decreases significantly (~1/(offset distance)^3) from the DUT [5], but of potentially greater concern is that the invasiveness of the probe ***C***, even with an offset of 200 μm, still shifts the antenna resonance to a frequency 133 MHz shorter than that of the unloaded or fiber-probe-loaded antenna (green line in Fig. 9.4).

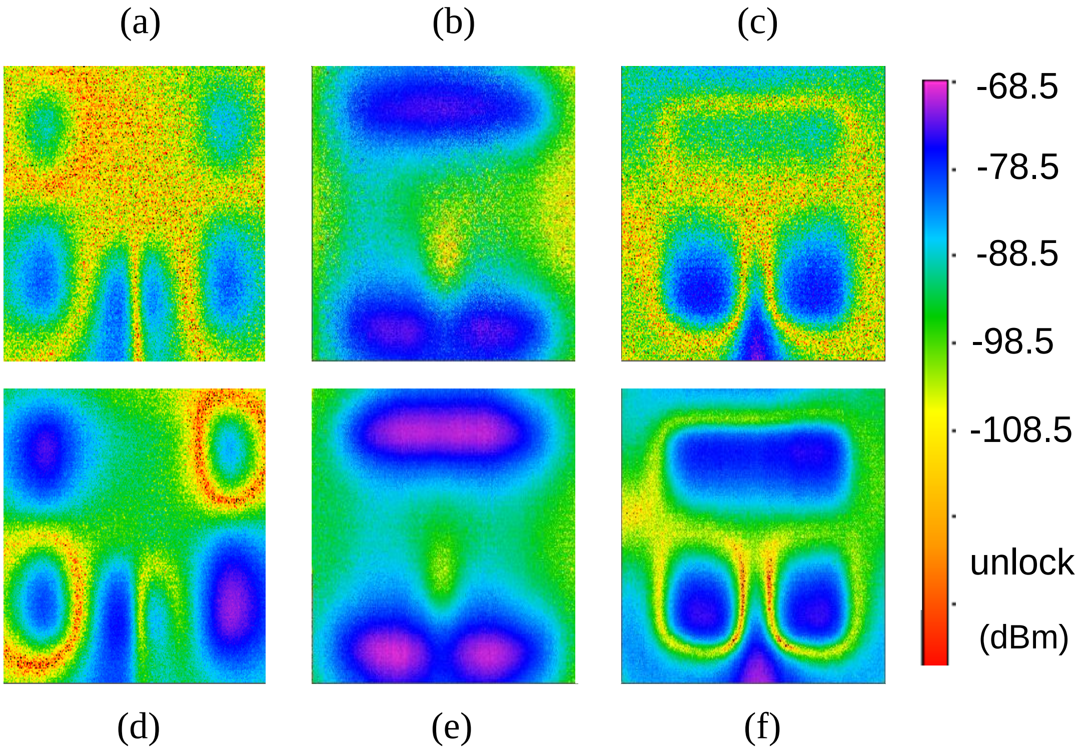

Figure 9.5: Distorted EO field amplitude maps measured under invasive conditions of the capacitively-loading wafer probe ***C*** on the X-band patch antenna. (a) *x*, (b) *y* and (c) *z* components at 10.485 GHz; (d) *x*, (e) *y*, and (f) *z* components at 10.319 GHz.

$LiTaO_3$ has a relatively higher invasiveness due to its higher microwave permittivity, so using the bulk configuration of this crystal affects the original field significantly. To investigate the field penetrating through the $LiTaO_3$ wafer, probe ***C*** was placed 200 μm above the DUT, and we measured the field distribution 250 μm above wafer ***C*** using the micro-scale probe ***B***. Figures 9.5(a), (b) and (c) are the *x*, *y* and *z* field components at 10.485 GHz of the original resonance frequency, respectively. Because of the resonance frequency shift and induced invasiveness by the wafer probe ***C,*** the measured fields are distorted with lower sensitivity. Even at the new shifted resonance frequency of 10.319 GHz, the fields are still distorted as observed in Fig. 9.5(d), (e) and (f).

The main advantage of using a bulk wafer probe is to decrease the scanning and data acquisition time rather than to enhance the sensitivity. The wafer probe that is larger than the DUT scale enables one to either scan a probe beam over the DUT without moving the probe, or to use a large, relatively high-power probe beam to capture a large area of the RF electric field at the same time, processing the EO detection in parallel with multi-channel image processing [49]. This technique allows even virtually live field images to be sensed, while avoiding the single probe-channel field mapping used in this paper.

The instantaneous live imaging is a true breakthrough where real-time monitoring of a DUT is essential. For broadband, non-resonant radiation devices such as microstrip line or co-axial cables, invasive is less a concern [49], although changes in impedance could still be significant. However, for most resonant devices, such as antennas, filters and resonators, it is crucial to keep the original radiation performance even for sensors that are placed in the reactive near-field region. Hence, sensing speed and invasiveness is a trade-off between live imaging with a bulk wafer probe and slow raster mapping with a micro-scale fiber probe.

9.3.3 Comparison of Spatial Accessibility

Besides its advantages in regards to low invasiveness, the micro-scale probe also offers greater potential accessibility to DUTs such as integrated-circuit packages (measurements between pins), circuits that possess air bridges or vias, and so forth. Thus, due to the miniaturized size of the fiber probe, sensing within gaps as narrow as 150 or 200 μm is feasible. For an example measurement, we probed the field in a plane underneath a wire-over-ground-plane structure, in which a 2.5-mm-diameter copper wire was suspended 0.8 mm over a ground plane. As seen in Fig. 9.6 (a) the probe ***B*** can easily be guided to the middle of the gap, where it is raster-scanned, sensing three standing-wave modes (Fig. 9.6 (b)). The fiber probe is set to sense the normal field and the DUT was fed at 10 GHz with an open termination. As expected for a 10-GHz standing-wave pattern in free-space, a 4.5 cm separation between three strong standing modes are observed. Probe ***A***, also seen positioned above the copper wire in Fig. 9.7 (a), had a diameter more than twice as large as the wire/ground-plane separation, and thus was useless for extracting the fields from the small space within the DUT.

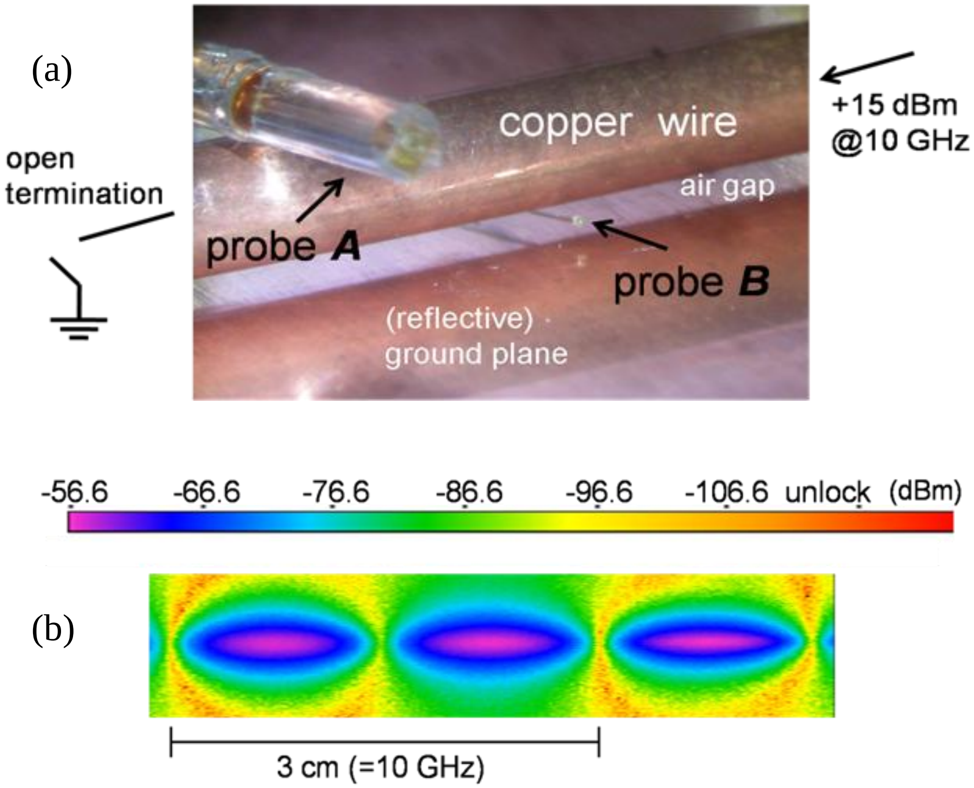

Figure 9.6: (a) Photograph of a copper transmission wire over a ground plane with probe ***A*** positioned over the top of the wire and probe ***B*** positioned in the air gap between the wire and ground plane. Probe ***B*** has much greater accessibility, as probe ***A*** would not fit under the wire in this structure. (b) standing-wave pattern of the normal electric field directed between the wire and ground plane.

9.3.4 Invasiveness and Spatial Resolution Advantages for Millimeter-wave Applications

The micro-scale probe becomes more valuable for higher frequency resonant devices. Generally, the size of an antenna decreases as the resonance wavelengths become smaller. For instance, Fig. 9.7 shows an array of 35.5-GHz patch antennas, such as those that might be found in a phased-array radar. Considering the sub-centimeter radiation wavelength and the half-wavelength of the unit antenna scale, the size of probe ***A*** is now comparable to an entire unit antenna, whereas the micro-scale probe ***B*** is not. Antenna performance is primarily evaluated by how efficiently it broadcasts the guided microwave power to the air. To realize such a radiation condition, the reflected power portion has to be minimized, and this can be achieved typically by implementing a quarter-wavelength impedance transformer into the signal's path in the same fashion as a quarter-wavelength anti-reflection layer in used in an optical coating. Such impedance matching networks are typically very narrow, as seen in Fig. 9.7 at the sections where the small line parallel to the *y*-axis enters the different patches. Thus, perturbations during probe scanning could alter the impedance (particularly the reactive part) of the matching network, causing serious resonances and a general degradation of the quality of operation of the device.

The measured field comparisons using probes ***A*** and ***B*** are presented in Fig. 9.7(b). Probe ***A*** clearly disrupted the field pattern, especially at the narrow matching lines as the probe captured data from the lines. However, fortunately the radiation pattern and performance was basically maintained except for in the matching-layer regions. This is because as the probe moved onto the radiation terminal edges where the radiation fields emerged, the matching layers were not greatly affected by the probe, for instance as compared to when the whole-wafer probe was used. However, it was still clear that the patterns from probe ***B*** were much more distinct and well-confined than the patterns from probe ***A***.

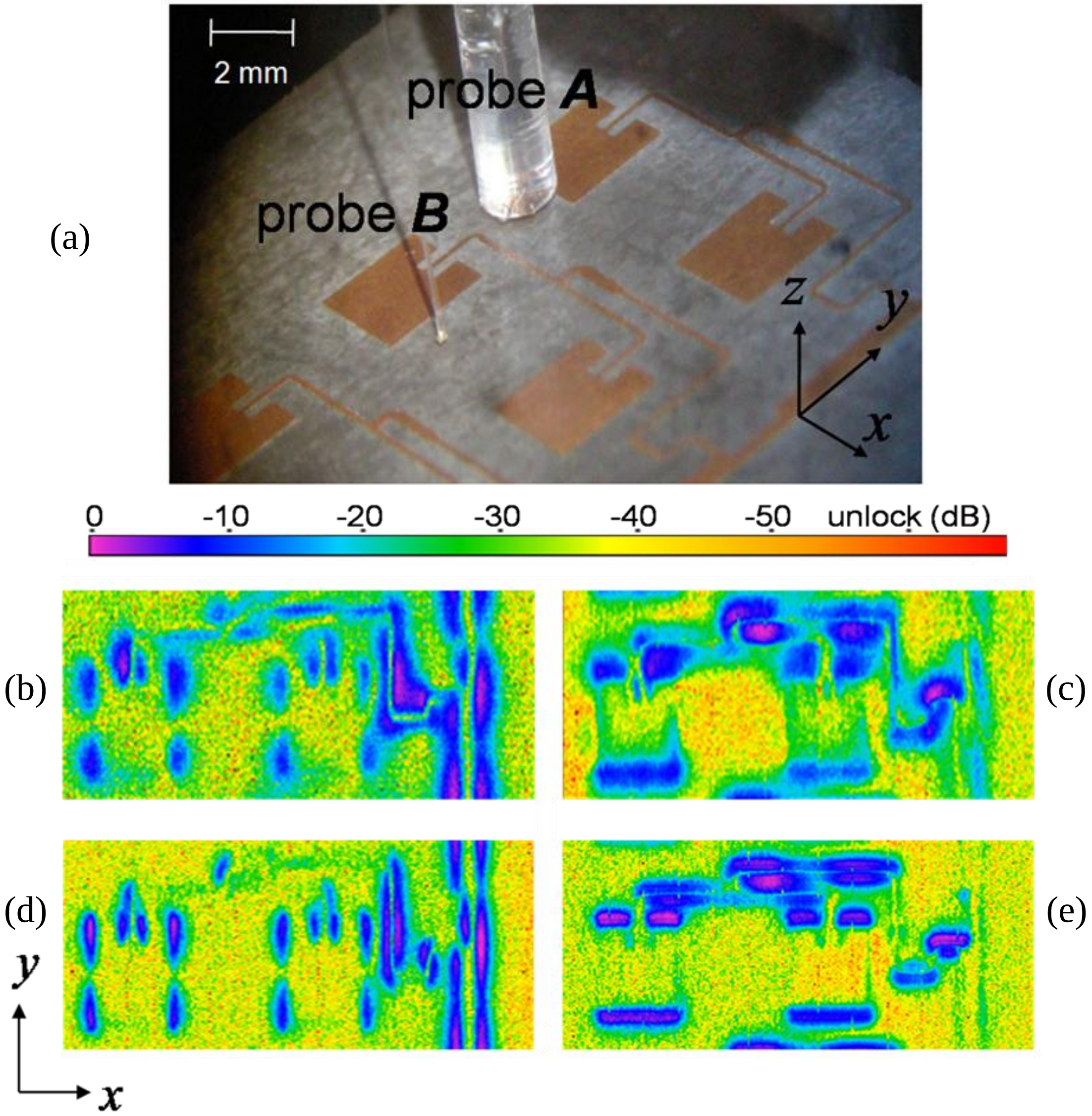

Figure 9.7: (a) Photograph of a Ka-band patch-antenna array with EO probes ***A*** and ***B***. (b) horizontal transverse (*x*-component) EO field amplitude map measured with probe ***A***, (c) vertical transverse (*y*-component) EO field amplitude map measured with probe ***A***, (d) and (e) are the cases of (a) and (b) with the probe ***B***.

9.4 Summary

A micro-cavity-resonator EO probe that has minimal intrusiveness in a fiber-based sensing scheme was proposed and demonstrated. The quantitative and qualitative relative invasiveness of the probe on the operation of an example antenna device-under-test was explored with respect to previously demonstrated fiber and wafer electro-optic sensors. The proposed probe yielded significantly less invasiveness with respect to conventional fiber and wafer-based sensors, as well as an improved scanning accessibility to the radiation devices, due to the dramatic reduction in volume of the dielectric material comprising the probe inserted into the near field of a device to be characterized. This accessibility enabled the reconstruction of the full three dimensions of near-electric fields with a single probe, thus eliminating the need for different probe crystals or multiple calibration procedures. Finally, the accessibility and invasiveness advantages of the micro-scale probe were demonstrated through the enhanced resolution of detailed images extracted from planar antennas, as well as the capability of reaching into circuit locations heretofore inaccessible.

CHAPTER 10

CONCLUSIONS

10.1 Summary of Achievements

This dissertation demonstrated how the various remaining challenges of the unique features of the EOS technique (*i.e.*, low sensitivity, system complexity, limited bandwidth and residual invasiveness) could be overcome through the use of innovative techniques employing an optical-fiber-scale, micro-resonator probe based on down-mixing with higher-order harmonics.

The detailed remaining challenges in conventional EOS technology were identified to be:

- Low sensitivity – The inherently low figures of merit in EO crystals and conventional single- or double-pass amplitude-sensing configurations that utilize a pair of polarizers yield low sensitivity. An EO sensitivity of 40 mV/(Hz)$^{1/2}$, achieved with a pulsed-laser, was previously reported by our lab.

- System complexity and management – The conventional set of polarization optics, such as polarizers and waveplates, associated with EOS measurements utilizing an ultrafast optical source is arguably cumbersome and expensive to manage within the system.

- Limited bandwidth – The sensing bandwidth is fundamentally limited by the modulation speed of an optical source. The bandwidth of a typical telecom-grade

EO modulator is 10~20 GHz, which becomes the sensing bandwidth when the optical down-mixing technique is used.

- Residual invasiveness – The size of an EO probe sensor is the main factor for undesirable residual invasiveness. A typical fiber-based probe has a 1~2 mm diameter, which causes potentially serious field distortion for millimeter-wave applications.

These shortcomings in the EO systems, throughout this dissertation, have been improved by following various techniques:

- Sensitivity enhancement with system simplification – Applying the intrinsic resonator characteristics of an EO crystal (as a Fabry-Perot etalon) to EO sensing applications demonstrated a sensitivity enhancement of > 10 dB compared to the conventional methodology. A simplified system embodiment was also devised and implemented, eliminating the need for virtually all conventional polarization components. Furthermore, this resonance-based scheme was especially advantageous for a fiber-based reflective mode of sensing, due to noise reduction advantages.

- Novel down-mixing methodology – High frequency applications of the resonance-based field-measurement techniques were also demonstrated through two respective electrical and photonic down-conversion techniques, using cost-effective optical–telecommunication-modulation technology. Each method was based on an electrical- or photo-diode detection scheme that down-converted high frequency information by the square-law property of nonlinear detectors. Both down-mixing techniques were also optimized by the carrier-suppression method for signal-to-noise ratio improvement as high as 10 dB. In addition, the merits and shortcomings of the two techniques were thoroughly compared.

- Bandwidth enhancement – For ultra-high frequency broadband sensing, another technique to expand the bandwidth, utilizing higher-order harmonics (up to the third-order) created during the operation of an EOM to generate a photonic beating source, was demonstrated. The bandwidth was expanded 2~3 times up to the millimeter-wave regime, with additional carrier suppressions to increase the signal-modulation depth. Applications to the near-field analysis of high frequency microwave patch antennas (at the X-band) and arrays (at the K- and Ka- bands) were demonstrated.

- Achievement of minimal invasiveness – Finally, using an optical-fiber-scale EO probe with a micro-cavity-resonator, minimal intrusiveness in a fiber-based EO probe for high-frequency (especially millimeter-wave) sensing was successfully demonstrated. The proposed probe yielded not only significantly less invasiveness with respect to conventional fiber and wafer-based sensors, but also an improved scanning accessibility to the radiation devices, due to the dramatic reduction in volume of the dielectric material comprising the probe to be inserted into the near field of a device. This accessibility enables the reconstruction of the full three dimensions of near-electric fields with a single probe, thus eliminating the need for different probe crystals or multiple calibration procedures.

Using combinations of these techniques, the most simple and efficient, as well as the least intrusive, high frequency EO implementations to date were developed.

10.2 Suggested Future Work

Rather than using a single-layer EO sensor with a balanced resonator, more sophisticated resonant structures, such as multi-stratified layers of EO materials, would provide further resonance-based sensitivity enhancement. As discussed in chapter 2, a single resonator determines the EO modulation efficiency for a given EO sensor wafer as a product of the EO amplitude-modulation slope and phase retardation. Due to the inevitable huge mismatch between the modulation slope and retardation in a resonator, there is a trade-off between the minimum transmission spectral bias where the EO retardation becomes maximum and the optimum EO spectral bias. In contrast to this trade-off due to the mismatch in a single resonator, distributed multi-stratified layers of EO materials enable separate controls of the modulation slope and phase retardation. Generally, in distributed Bragg EO layers, the modulation slope evolves into a curve with a much steeper slope than that of the EO phase retardation, whereas the EO modulation and retardation slopes change in the same fashion in a single EO layer. Thus the walk-off (*i.e.*, separation between the steepest slope point in modulation and the peak point in retardation) disadvantage can be reduced in the distributed structures.

In addition to enhancing the sensitivity by improvements in the resonant structures, the sensing bandwidth could be further expanded by the use of even higher (than third)-order harmonics in EOMs. In chapter 8, the finite bandwidth of a typical low-cost amplitude modulator can be expanded by two to three times with the respective second- and third-order harmonics. The fourth-order harmonic component would become strong enough due to its high threshold driving power that is close to the damage threshold of an EOM. Such limited nonlinearity for the fourth-order harmonic generation in single EOM can be overcome by cascading a second EOM, which imposes another identical amplitude-modulation envelope onto the output of the first EOM. For instance, the product of second-order harmonic throughput eventually evolves to the efficient fourth-order harmonic that significantly increases the sensing bandwidth of the EOS system even while using microwave hardware having much lower bandwidths.

APPENDICES

Appendix A

Analysis of Optical and Terahertz Multilayer Systems Using Microwave and Feedback Theory

The principles of microwave and feedback theory have been independently applied to the analysis of both optical and terahertz-regime multilayer systems. An analogy between the two approaches is drawn herein, and useful recursion relations, along with a signal-flow approach, are presented for both reflection and transmission cases. These relations, in terms of S-parameters, allow an exact analytical solution for even arbitrary, active, stratified structures, not only for any wavelength in the radio-frequency spectrum, but also for optical wavelengths. This approach also provides a bridge between the microwave and optical bands and leads to beneficial design solutions for intermediate bands such as the THz regime. Comparisons with conventional methodologies are provided using practical multilayer simulations. In addition, graphical design techniques from microwave theory are used along with examples for efficient design and understanding.

1. INTRODUCTION

The matrix approach has been the most widely used method to analyze optical multilayers because of its mathematical convenience for quantifying cascaded structures. Transmission-line theory in microwave systems with cascaded elements, on the other hand, has widely used non-matrix methods. These microwave approaches have been difficult to extend to optical applications due to the reliance in optics on the concept of refractive index. However, analogies between optical thin films and electrical transmission lines have been considered because of the similarity between the transmission impedance and refractive index of a layer [54]. This analogy enables optical multilayers to take advantage of conventional microwave circuit theory for stratified, planar-structure analysis [55-57].

One alternative to the matrix approach is called the signal-flow-graph technique, introduced by Mason [58] and widely used in the analysis of microwave circuits [59]. It has also found only limited use in optical engineering [60,61].

The inconvenience of utilizing impedance-based and signal-flow analyses for optical feedback is overcome by exploring the recursive relations of reflection and transmission of optical dielectric multilayers from the microwave perspective. An equivalent subsystem in a recursive format overcomes mathematical complexity and allows for the development of a simple programming algorithm. Since this approach manipulates each layer step by step and naturally provides the reflection and transmission for every layer, it enhances the understanding of the power flow though the layers.

2. MICROWAVE APPRAOCH

An arbitrary, optical, dielectric multilayer is shown in Fig. A.1(a). For the sake of simplicity, normal-incidence light from free space to a lossless medium is considered. Since the inhomogeneous discontinuity at each boundary, *k*, causes a partial field reflection (the Fresnel coefficient, r_k) based on refractive-index (n) differences, the two boundaries of a *k*-th layer create a unique phase-delay ($\delta_k = 4\pi\, n_k\, h_k/\lambda$) loop. This delay is determined by the refractive index (n_k) and the thickness (h_k) of the *k*-th layer, as well as the wavelength (λ). Such an optical-feedback system can be remodeled as a microwave transmission line in terms of the same phase delay and discontinuity. Each discontinuity can be expressed as a scattering matrix (Eq. 1, with *S* following the standard notation, the *k* values indicating the boundaries, and *Z* being impedance), with the round-trip phase delay for each of the *k* layers given in Eq. 2.

$$[S]^k = \begin{bmatrix} S^k{}_{11} & S^k{}_{12} \\ S^k{}_{21} & S^k{}_{22} \end{bmatrix} = \begin{bmatrix} r_k & t_k \\ t_k & -r_k \end{bmatrix} \qquad (1)$$

$$, \quad k = 1,2,\cdots,n+1$$

where $$r_k = \frac{n_k - n_{k-1}}{n_k + n_{k-1}} = \frac{Z_k - Z_{k-1}}{Z_k + Z_{k-1}}, \qquad t_k = \sqrt{1 - r_k{}^2}$$

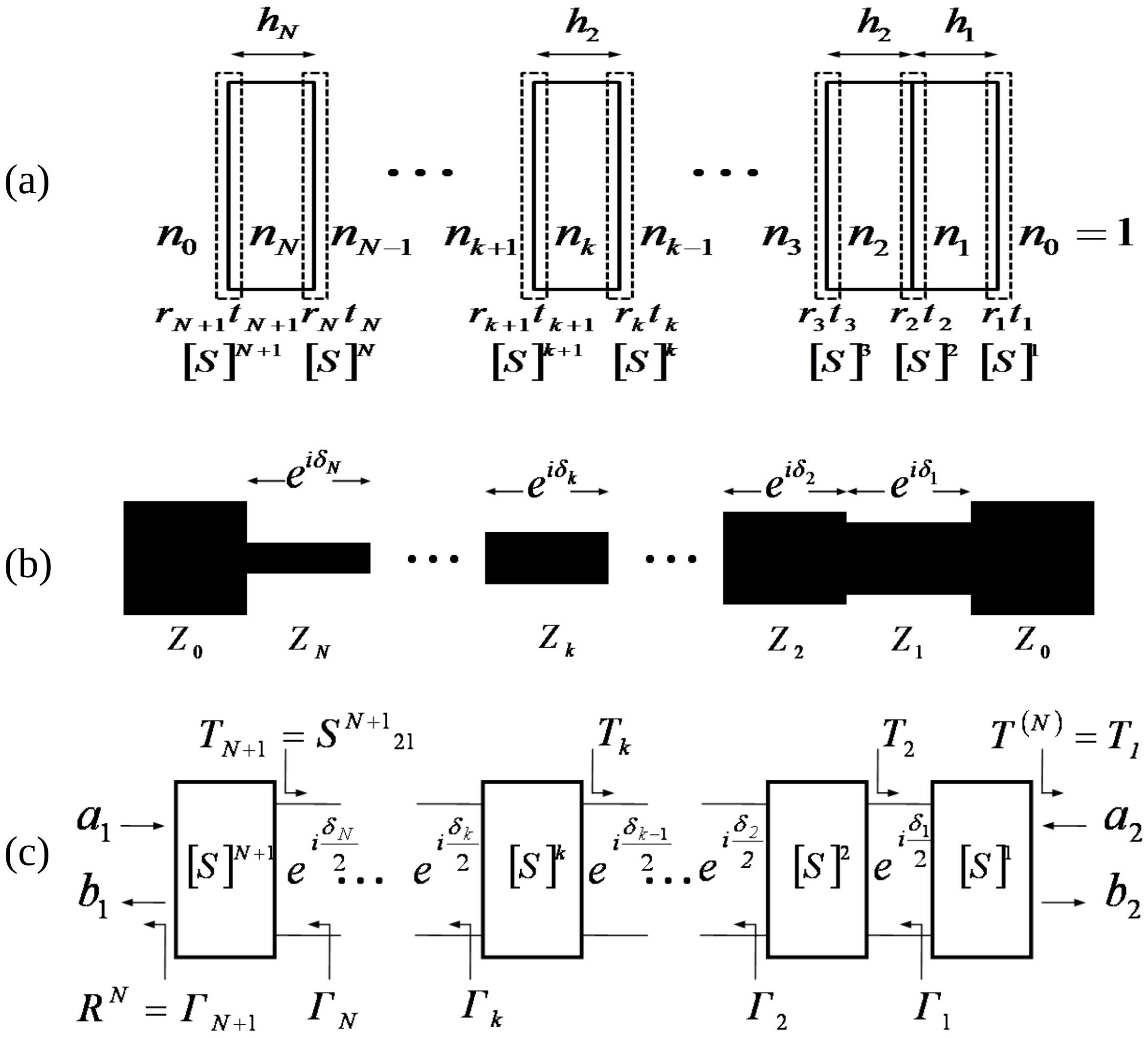

Figure A.1: Multiple Fabry-Perot etalon: (a) optical model, (b) transmission-line model (where $n_2 < n_1 < n_k < n_N$), and (c) equivalent network diagram.

$$\delta_1 = \frac{4\pi n_1 h_1}{\lambda}, \delta_2 = \frac{4\pi n_2 h_2}{\lambda}, \cdots, \delta_N = \frac{4\pi n_N h_N}{\lambda} \qquad (2)$$

At the k-th boundary, the reflectance is $R_k= r_k^2$, thus $T_k= t_k^2$ is the remaining transmittance for a lossless medium. (The conventional definition, $t_k=2n_k/(n_k-n_{k-1})$ is the Fresnel electric-field transmission coefficient. Here, t_k is a transmission field coefficient to satisfy the $R_k+T_k=1$ relation.) Z_0 is the characteristic impedance, which is typically 50

Ω and corresponds to free space in optics. Therefore, a typical glass layer (n =1.5) with thickness h_1 can, for example, be expressed as a 75 Ω impedance with phase delay $\delta_1/2$. (This analogy is valid when the conventional reflection coefficient $\Gamma_2= (Z_2-Z_1)/(Z_2+Z_1)= (n_2-n_1)/(n_2+n_1)$ from medium 1 to 2 is used. If the other convention, as in ref.2, $\Gamma_2= (Z_2-Z_1)/(Z_2+Z_1) = (Y_1-Y_2)/(Y_1+Y_2)= (n_1-n_2)/(n_1+n_2)$, is adopted, all the expressions in the article would be modified by replacing the term impedance with admittance and altering the Smith charts accordingly.)

According to classical circuit theory for a cascaded network, the equivalent impedance at a given position can be readily obtained. Since reflection originates from impedance (index in optics) discontinuities at boundaries, an equivalent reflection at a specific position can be extracted from the corresponding mismatches.

For the single-layer case, the overall reflection is associated with the S-parameter at the front boundary $[S]^2$, as well as the reflection at the interior boundary at the back of the layer, Γ_1. This relation is also valid for the double layer case in which the total reflection at the foremost boundary, Γ_3, is obtained from $[S]^3$ and Γ_2.

For the multiple, N-layer case, the total reflection at the k_{th} boundary (Γ_k) is generalized with $[S]^k$ and Γ_{k-1}. As a result, the total reflection at the N-th layer is

$$R^{(N)} = \Gamma_{N+1} = S^{N+1}{}_{11} + \frac{S^{N+1}{}_{12} S^{N+1}{}_{21} \Gamma_N e^{i\delta_N}}{1 - S^{N+1}{}_{22} \Gamma_N e^{i\delta_N}} \qquad (3)$$

where

$$\Gamma_N = S^N{}_{11} + \frac{S^N{}_{12} S^N{}_{21} \Gamma_{N-1} e^{i\delta_{N-1}}}{1 - S^N{}_{22} \Gamma_{N-1} e^{i\delta_{N-1}}} \quad ,\cdots,\ \Gamma_1 = S^1{}_{11}$$

The transmission also has recursive characteristics associated with any previous equivalent transmission. However, the transmission at each layer also has to include the previous equivalent reflection term. This is because each transmission shares identical feedback terms that are described using the reflection.

The generalized transmission can be written as

$$T^{(N)} = T_1 = \frac{S^1{}_{21} T_2 e^{i\frac{\delta_1}{2}}}{1 - S^2{}_{22} \Gamma_1 e^{i\delta_1}} \tag{4}$$

where

$$T_2 = \frac{S^2{}_{21} T_3 e^{i\frac{\delta_2}{2}}}{1 - S^3{}_{22} \Gamma_2 e^{i\delta_2}}$$

$$,\cdots, T_N = \frac{S^N{}_{21} T_{n+1} e^{i\frac{\delta_N}{2}}}{1 - S^{N+1}{}_{22} \Gamma_N e^{i\delta_N}},\ T_{N+1} = S^{N+1}{}_{21}$$

The superscripts on R and T indicate the number of layers. The expression using optical parameters can be obtained by simply replacing the S parameters using Eq. 1.

3. SIGNAL FLOW GRAPH APPROACH

Based on standard feedback theory, any arbitrary feedback network can be expressed conveniently with a signal-flow graph. An example for a double layer is given in Fig. A.2. Four basic topographical rules (branches in series, branches in parallel, elimination of self-loop, and node-splitting) are discussed by Dunn [60] for transforming such networks to a single path.

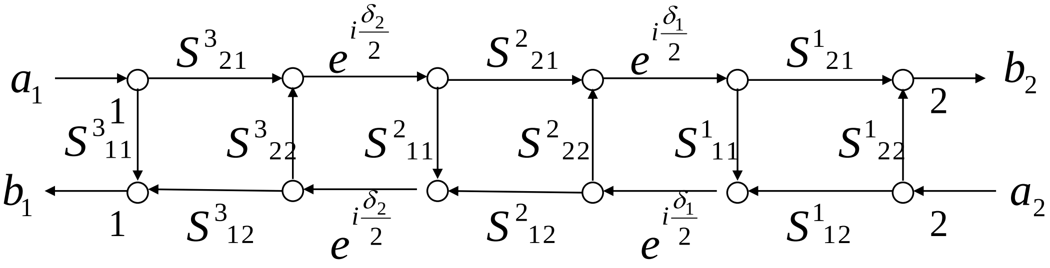

Figure A.2: Signal flow graph of a double-layer structure.

Such a transform is illustrated in Fig. 3, where excluding the reflective paths in Fig. A.2 results in the transmission-flow graph of Fig. 3(a). There is one forward transmission path ($S^3{}_{21}$- $S^2{}_{21}$- $S^1{}_{21}$) and three feedback-loop paths ($S^3{}_{22}$- $S^2{}_{11}$, $S^3{}_{22}$- $S^2{}_{21}$- $S^1{}_{11}$- $S^2{}_{12}$, $S^2{}_{22}$- $S^1{}_{11}$). A difficulty does arise due to the path containing the longest loop, $S^2{}_{12}$, but this can be eliminated by replacing $S^2{}_{11}$ and $S^1{}_{11}$ with Γ_2 and Γ_1. This technique discontinues the inter-relationship between the two layers, and thus each single-layer loop becomes independent as illustrated in Fig. 3(b). Likewise, the two single-layer loops can be transformed to one single-layer loop (Fig. 3(c)), and eventually, the double-layer transmission $T^{(2)}$(=T_1) is reformulated in terms of equivalent, prior-layer transmissions in the identical format of Eq. 4 (Fig. 3(d)). This provides a verification of the recursive pattern.

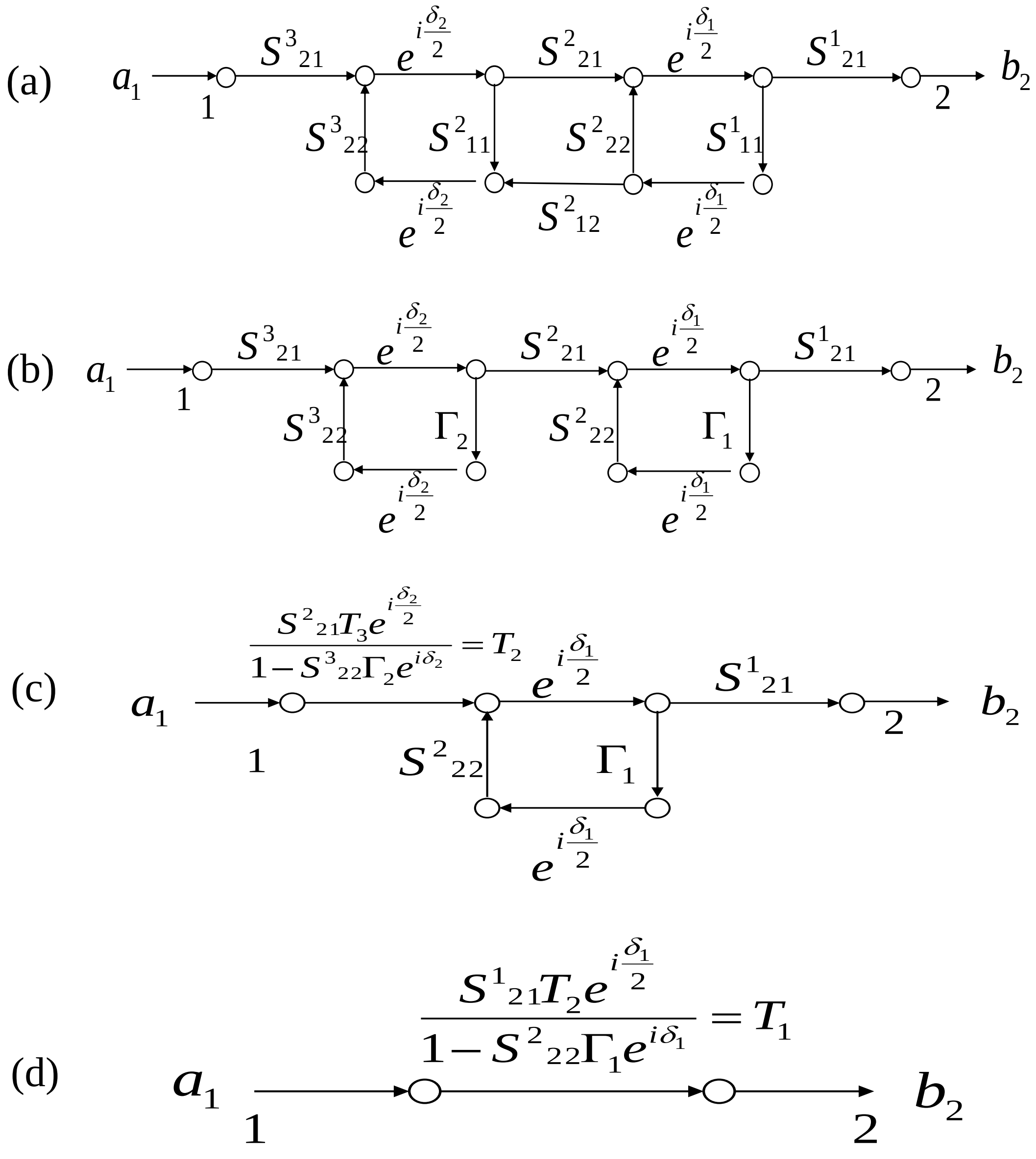

Figure A.3: Topographical transform of a double-layer transmission to a single equivalent-signal-flow graph. (a) transmission-flow graph of a double layer; (b) transform into two independent and equivalent layers; (c) elimination of the first independent feedback loop; (d) elimination of the second independent feedback loop.

4. MICROWAVE APPROACH FOR OPTICAL THIN-FILM LAYERS

Symmetric, quarter-wave dielectric layers are a standard prototype for high-reflectors in the optical regime. The contribution of each quarter-wavelength layer to a five layer reflector is analyzed here using a recursion formula. A graphical interpretation using microwave methods is also presented to demonstrate the ease of isolating each layer's contribution to the system's reflectance.

Although graphical techniques for optical multilayer systems that assist conceptual design have been reported, *e.g.*, by Apfel [62], the standard graphical tool for microwave engineering – the Smith chart – can be utilized to visualize optical design in a similar fashion. In microwave design, one of the primary goals is to maximize power flow by minimizing impedance mismatches, and the Smith chart has been a valuable tool to visualize the control of reflections. This impedance-reflection conversion as a function of microwave frequency is the essence of the Smith chart, and it can also be applied to the index-reflection conversion as a function of optical wavelength.

For example, a five-layer, quarter-wavelength optical system consisting alternately of zinc sulfide ($n_{odd} = n_H = 2.3$) and magnesium fluoride ($n_{even} = n_L = 1.35$), as shown in Fig. A.4, gives a power reflectance ($|\Gamma|^2$) of 0.9141. This value decreases to 0.7704 for a three-layer system (layers cba only in Fig. 4) and 0.4652 for a single layer (a only).

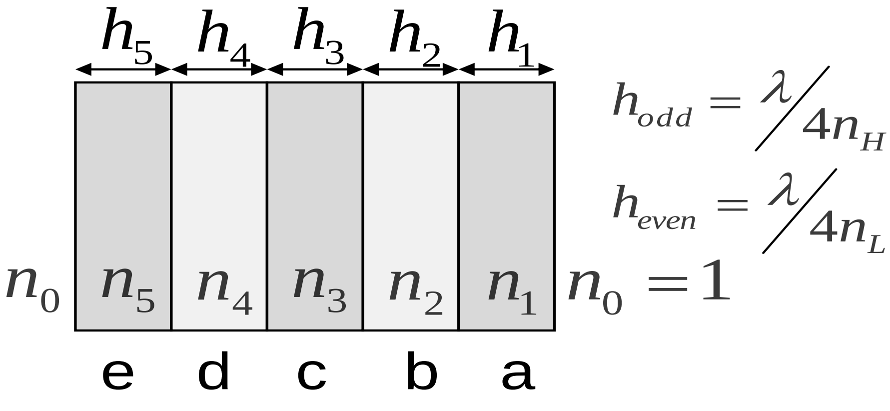

Figure A.4: Five-layer optical system with quarter-wavelength layers of zinc sulfide and magnesium fluoride, labeled **a-e**.

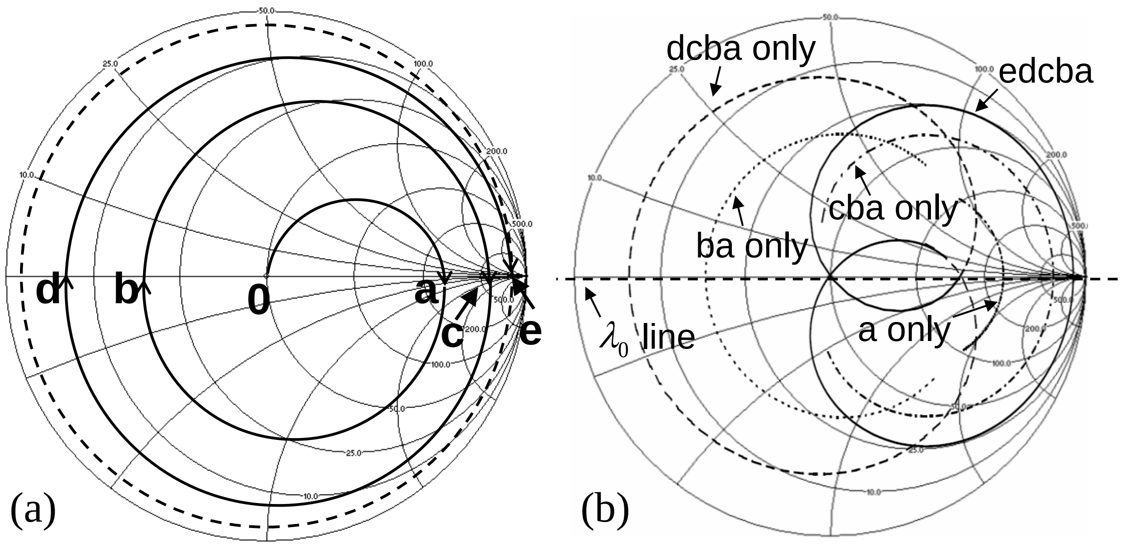

Figure A.5: (a) Evolution of optical reflection on a Smith chart for a cumulative quarter wavelength multiple stack of five elements at λ_o. (b) individual reflections on Smith chart for a cumulative quarter wavelength multiple stack of five elements, vs. wavelength (or frequency) $\left(0.7\lambda_0 \le \lambda \le 1.7\lambda_0\right)$.

The graphical explanation of this quarter-wave reflector is presented in Fig. A.5(a). Each layer makes a circular trace that starts from the equivalent reflection point from the previous layer. The radius of this trace is determined by the index of the corresponding layer. The circles are periodic with every half wavelength. This means the quarter-wavelength layers form semi-circles that push their traces toward the unity boundary in a spiral pattern. This spiral is achieved by alternating quarter-wave layers of high and low index material, and it approaches the unity circle as the number of layers increases. The dashed circle represents the final reflection after the fifth layer, e. The circle originates at the center (50 Ω point) and yields the same reflection with different phases.

Reflection traces for each of the five layers of the coating for a broad wavelength band are given in Fig. A.5(b). Reflections at the λ_o line also appear in Fig. A.5(b), which explains why $\Gamma_b < \Gamma_a$, $\Gamma_d < \Gamma_c$. When the number of quarter-wave layers increases, the reflection is observed to be higher, but the reflection bandwidth is shown to decrease, as expected. The reason for this is that fewer wavelengths can adequately satisfy the quarter-wavelength condition as the number of spiral turns increases. The use of the Smith chart thus offers excellent design advantages. For instance, the graphical transition of the reflection trace with additional layers can be easily predicted based on the index and thickness of a layer.

The reflection at a specific frequency can be readily moved to other points simply by adding layers with appropriate parameters. Each additional layer gives an inscribed circle with a half-wavelength period. A larger refractive index results in a smaller diameter. This is fundamentally the same as series stub tuning in microwave theory. Unfortunately, parallel stub tuning cannot be realized in optics because the reactive part of the refractive index in dielectric materials is typically negligible and difficult to manipulate. This graphical tuning method allows a designer to observe the tuning range of single additional layers with a given index of refraction. This also determines the number of layers necessary to reach the final tuning objective.

5. PRACTICAL MULTILAYER ANALYSES

In order to evaluate the recursion formula presented in Eq. (4), we have chosen the example of a practical, 17-layer mid-infrared reflector. The example optical reflector was designed to have a maximum reflectance at a wavelength of 5 μm with zero reflectance at 4.5 μm and 5.5 μm. This specification was achieved by an optimization method using layer perturbation in a computation-intensive Monte Carlo approach [63].

Given the refractive index and the thickness in terms of wavelength for each layer, the power reflectance is also computed using the expressions in Eq. 3. Figure 6 shows the results from the recursion analysis; they are observed to be identical to those of the conventional method. The specified design spec in ref. 63 (85 % reflection at 5 μm center wavelength with a 1 μm null bandwidth) was realized using a diverse set of 17 asymmetric optical layers. This optical design simulation was reproduced using purely the microwave and feedback approaches.

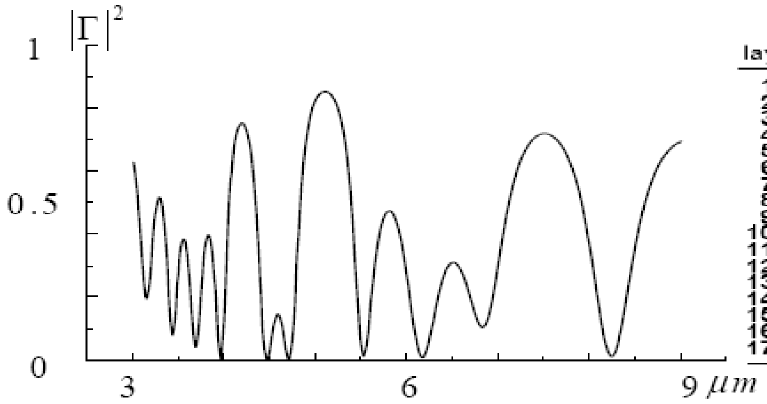

From Air

layer	n	thickness (λ)
1:	2.30	.2181
2:	1.75	.1923
3:	1.45	.2350
4:	1.75	.2755
5:	2.30	.4681
6:	1.75	.4281
7:	1.45	.2416
8:	1.75	.0510
9:	2.30	.6649
10:	1.75	.4476
11:	1.45	.2651
12:	1.75	.1410
13:	2.30	.3962
14:	1.75	.3329
15:	1.45	.2025
16:	1.75	.0340
17:	2.30	.2696

To Glass

Figure A.6: Power reflectance vs. wavelength for a 17-layer reflector designed for a 5-μm wavelength [63] ,using the recursion expression in Eq. (3).

The microwave approach for a multilayer system may best be suited for the THz region – the underutilized band between the microwave and infrared portions of the spectrum. Thus, a computational example for a THz mirror previously designed with a transfer-function method is chosen [64] for comparison with the recursion analysis. The mirror consists of 25 ceramic layers of a Bragg-grating stack to be used with a broadband THz source, such as those that employ ultrafast lasers in the generation of a signal. Since the THz generator was an optical-based source, the simulation of the reflection performance was compared in Ref. 11 to the experiment using a purely optical approach. Power-transmittance results across the THz spectral range, computed using the recursion methodology developed herein, are shown in Fig. 7. A wide high reflectance region that matches that from the previous design [64] is observed.

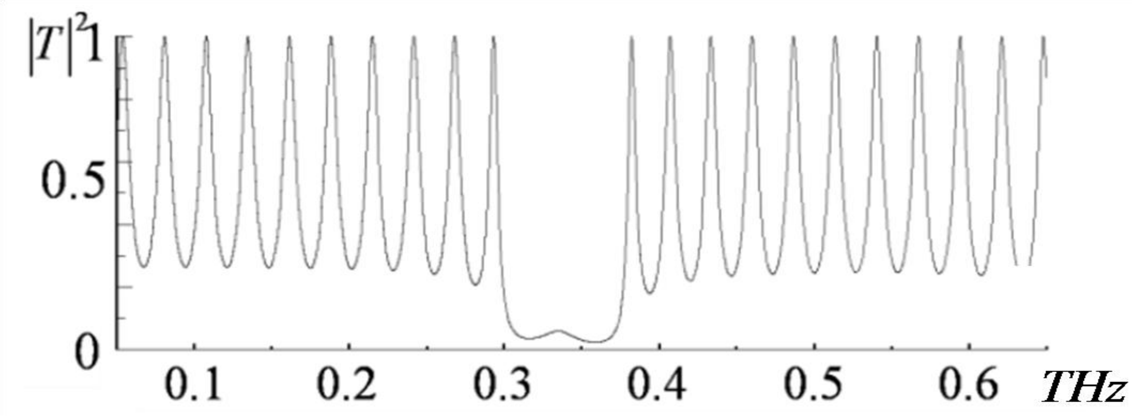

Figure A.7: Power transmittance of a practical 25-layer reflector for wideband THz beams [suggested in Ref. 64] (n_{odd} = 3.17, n_{even} = 4.16, h_{odd} = 73 μm, h_{even} = 51 μm), computed with the recursion expression in Eq. (4).

Appendix B

A Method for Spectro-temporal and Echo Responses of Arbitrary Optical Multilayer Systems

In general optical multilayer systems with arbitrary different thicknesses, refractive indices and number of layers, a comprehensive numerical method to calculate not only steady-state spectral responses but also their spectro-temporal responses is presented. The transient evolution of spectrum until it reaches its steady-state spectral response is investigated by modifying signal processing and feedback theory to arbitrary stratified multilayer systems. This modeling based on feedback analysis enables to explore highly complicated sub-groups of the round trips associated with the layout of layers. Furthermore, the finger print of a system - the impulse response – is obtained by the modeling and its application to the reflection echo or transmission pulse train analyses is presented. The Fourier transformation of initial and complete impulse responses provide also temporally transient and steady-state spectral responses, respectively. Finally, an experimental demonstration of an impulse response and its spectral response using ultrafast optical pulses are followed.

1. INTRODUCTION

Multiple arrays of optical dielectric media have been an essentially fundamental structures to control a transmission (or reflection) of continuous-wave (CW) light. For designs of multilayer systems to control the light propagation for a certain wavelength or band, the decent material, thickness and number of layers have to be properly deployed. Such designs have been readily pursued by the conventional transfer matrix technique.

The transmission characteristics of the multilayer systems rely on interferometric superposition of detoured (or round- tripped) components based on multilayer layout.

Thus the steady-state transmission is guaranteed only the accumulation of the whole transmission components is realized. This condition can be satisfied with CW or at least quasi-CW sources because mostly only initial dominant components govern the whole transmission.

As the light is operated in a pulsed mode and the pulse duration is not long enough to be considered as a quasi-cw condition, the transmission characteristic begins to be degraded. This criteria for a quasi-cw condition is so heavily related with the multilayer structure and wavelengths. The conventional transfer matrix technique is challenging to provide the temporal responses of the entire spectrum (*i.e.,* spectro-temporal response) and there have been no clear methods to analyze this in optical multilayers.

The optical multilayer systems could be interpreted as feedback systems where solid theories such as the signal flow graph and discrete signal processing techniques are commonly used. In this paper, we employ and utilize such numerical tools to the arbitrary optical layer analysis. First, a method to compute the transmission (reflection) function of multilayers, from the point of feedback approach, is presented. Second, a technique to compute the transient responses until they reach the steady-state spectral responses is followed. This transient analysis method was developed by modifying the Z-transformation in discrete signal processing theory for the application to the arbitrary optical multilayers.

The modified Z-transformation technique provides not only spectro-tempotal response but also the impulse response of the multilayer. This is a very powerful tool to analyze multilayer systems based on reflected (or transmitted) echoes for the short pulse input trigger pulses. Finally, the experimental demonstration of echo analysis using ultrafast short pulses is presented and the spectral response of a multilayer system is discussed by exploring the relation of temporal and spectral Fourier transform pair.

2. METHODS FOR STEADY-STATE SPECTRAL RESPONSES OF A MULTILAYER SYSTEM

Prior to the transient analysis of a multilayer system, the steady-state transfer function for both reflection and transmission is discussed based on feedback theory. For a single layer case, the overall reflectance is associated with reflectance at the front boundary r_2, as well as the reflectance at the inner boundary, r_1. This relation is also valid for the double layer case in which the total reflectance at the foremost boundary R^2 is obtained from r_3 and R^1.

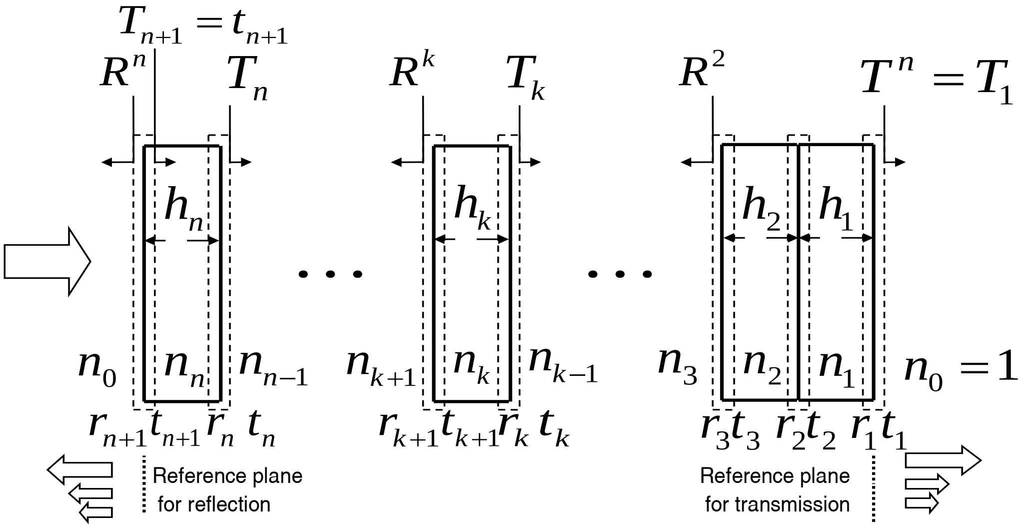

Figure B.1: Optical *n*-layer system with arbitrary indices and thicknesses.

This recursive relation can be extended to the multiple, *n*-layer case as shown in Fig.1. The total reflectance at the k_{th} boundary (R^{k-1}) is generalized with r_k and R^{k-2}. As a result, the total reflectance at the n^{th} layer is

$$R^{(n)} = r_{n+1} + \frac{(t_{n+1})^2 R^{(n-1)} e^{i\delta_n}}{1 + r_{n+1} R^{(n-1)} e^{i\delta_n}} \qquad (1)$$

where

$$R^{(n-1)} = r_n + \frac{(t_n)^2 R^{(n-2)} e^{i\delta_{n-1}}}{1 + r_n R^{(n-2)} e^{i\delta_{n-1}}}, \ \cdots \ , \ R^1 = r_2 + \frac{(t_2)^2 r_1 e^{i\delta_1}}{1 + r_2 r_1 e^{i\delta_1}}$$

$$r_k = \frac{n_k - n_{k-1}}{n_k + n_{k-1}} \qquad t_k = \sqrt{1 - r_k{}^2}$$

and

$$\delta_1 = \frac{4\pi n_1 h_1}{\lambda}, \delta_2 = \frac{4\pi n_2 h_2}{\lambda}, \cdots, \delta_n = \frac{4\pi n_n h_n}{\lambda}$$

$$, \quad k = 1, 2, \cdots, n+1$$

At *k*-th boundary, the reflected beam is $R_k = r_k^2$ thus $T_k = t_k^2$ is the rest transmitted beam for a lossless medium. The transmittance also has recursive characteristics associated with any previous equivalent transmittance. However, the transmittance at each layer also has to include the previous equivalent reflectance (*i.e.,* feedback) terms. This is because transmissions share the identical feedback terms described using reflectance.

The generalized transmittance is written as

$$T^{(n)} = T_1 = \frac{t_1 T_2}{1 + r_2 r_1 e^{i\delta_1}} \qquad (2)$$

where $$T_2 = \frac{t_2 T_3}{1 + r_3 R^1 e^{i\delta_2}} \quad ,\cdots, T_n = \frac{t_n t_{n+1}}{1 + r_{n+1} R^{n-1} e^{i\delta_n}}$$

The superscripts on *R* and *T* indicate the number of layers.

3. APPLICATION OF FEEDBACK THEORY TO THE TRANSIENT MULTILATER ANALYSIS

3.1. Single layer

A Fabry-Perot etalon can be interpreted as an optical feedback system having a single closed loop created by its two boundaries. Hence, it can be reformulated in standard feedback transfer function format. For instance, the CW field transmission as in Eq.(2) is a closed loop feedback system with various discrete time delays of δ_n.

The Z transform is the most widely used method to analyze such a discrete feedback system and Eq.(2) for a single etalon layer can be re-expressed in Z transform format as in Eq.(3) which is an infinite power series, with z being a complex variable.

$$T = \frac{forward\ terms}{1 - feedback\ terms} = \frac{t_1\ t_2}{1 + r_1 r_2 e^{i\delta}} \equiv \frac{a_1}{1 - a_2 z^{-1}} = \sum_{k=0}^{\infty} a_1 \left(a_2 z^{-1}\right) \qquad (3)$$

where the forward/feedback and phase delay terms are defined as $a_1 \equiv t_1\ t_2$, $a_2 \equiv -r_1\ r_2$ and $z^{-1} \equiv exp(i\delta)$, respectively. This expression is a discrete feedback system with unit constant phase delay z^{-1} of a single closed feedback loop. The phase delay δ is determined by the refractive index and thickness of the layer as well as the operation wavelength.

For instance, Fig. B.2.(a) is the impulse response of an example thin glass layer ($n_1=1.5$, $h_1=0.1mm$) with balanced coatings ($R=0.7=r_1^2=r_2^2$), obtained from infinite series format in Eq.(3) at a constructive wavelength of 1μm. Each line component indicates transmitted field strength with phase and delay information at n^{th} beam. For the constructive wavelength, all transmitted components are in-phase and fading away at an equal rate and delay step.

Accumulation of each component yields a step response. Fig. B.2.(b) is the intensity step response obtained from the intensity summation of Fig. B.2.(a). As opposed to this, a different pulse train, with alternate phase, is obtained at a destructive wavelength. The poor transmission due to this destructive wavelength is shown in Fig. B.2.(d)

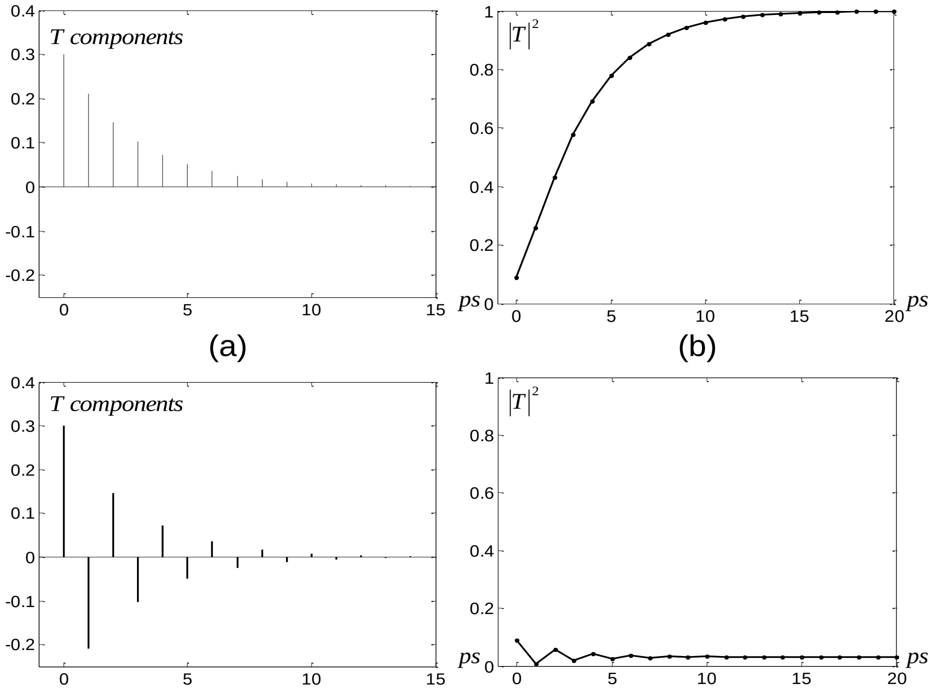

(a) (b)
(c) (d)

Figure B.2: Temporal responses of a Fabry-Perot etalon (a) constructive impulse response, (b) constructive step response, (c) destructive impulse response, (d) destructive step response.

Figure B.2(b and d) are the step responses of an ideally instantaneous input CW beam. For the finite beam duration, such as pulsed operation in lasers, the transient rising and falling response can be readily attained by impulse response analysis. As a pulsed beam escapes from the layer, the earliest beam components begin to cut off in order. Hence, the transmission intensity at certain time is the summation of the components that the pulsed-window contains at that moment. Fig. B.3(a) is the constructive transient response for 50 ps of square pulsed beam with the bare and various high-reflection coated glass slide used in Fig. B.2. The transient responses heavily get prolonged for the stronger feedback loops (*i.e.*, higher reflections at boundaries).

Transformation of impulse response to the frequency domain is spectral response of the system itself. The spectrum is centered at input frequency f_0 (λ_0 in wavelength) and the transmission can be constructive or destructive based on input frequencies. For example, Fig. B.3(b) is steady-state spectral responses for CW beam with the same coating cases at the constructive wavelength of 1 μm.

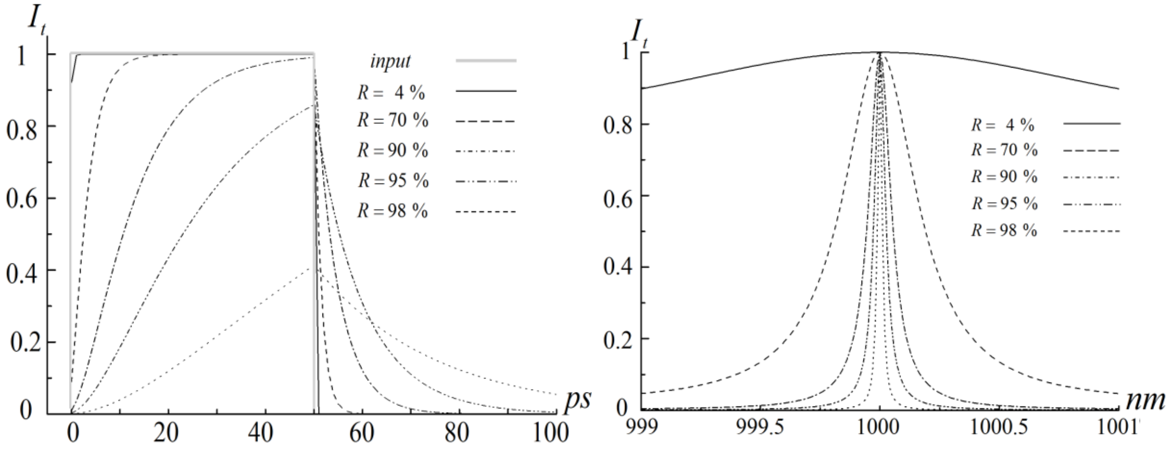

Figure B.3: (a) Temporal response of an etalon, (b) steady-state spectral response of an etalon.

Noticing that impulse response is in time order and its frequency domain transform is spectrum, taking transform of the entire impulse response gives a steady-state spectral response as shown in Figs B.2 and B.3. The center frequency of the spectrum is the input frequency f_0. This approach could be a powerful method to analyze temporal responses taking a transform from only the early part of the impulse trains for CW beams.

The spectro-temporal response can be obtained by taking the discrete Fourier transform of the partial beginng impulse components before reaching the steady-state regime. The spectral component $T_n(\omega,n)$ after n-th impulse component is expressed as Eq.(4) and the power spectrum is the conjugate square of $T_n(\omega,n)$. Hence, the evolution of $|T_n(\omega,n)|^2$ as another function of n (*i.e.*, discrete timing sequence) is the spectro-temporal transmission response of the systems.

$$T_n(\omega,n) = \Im\left(\sum_{k=0}^{n} a_1\left(a_2 z^{-1}\right)^k\right) \qquad (4)$$

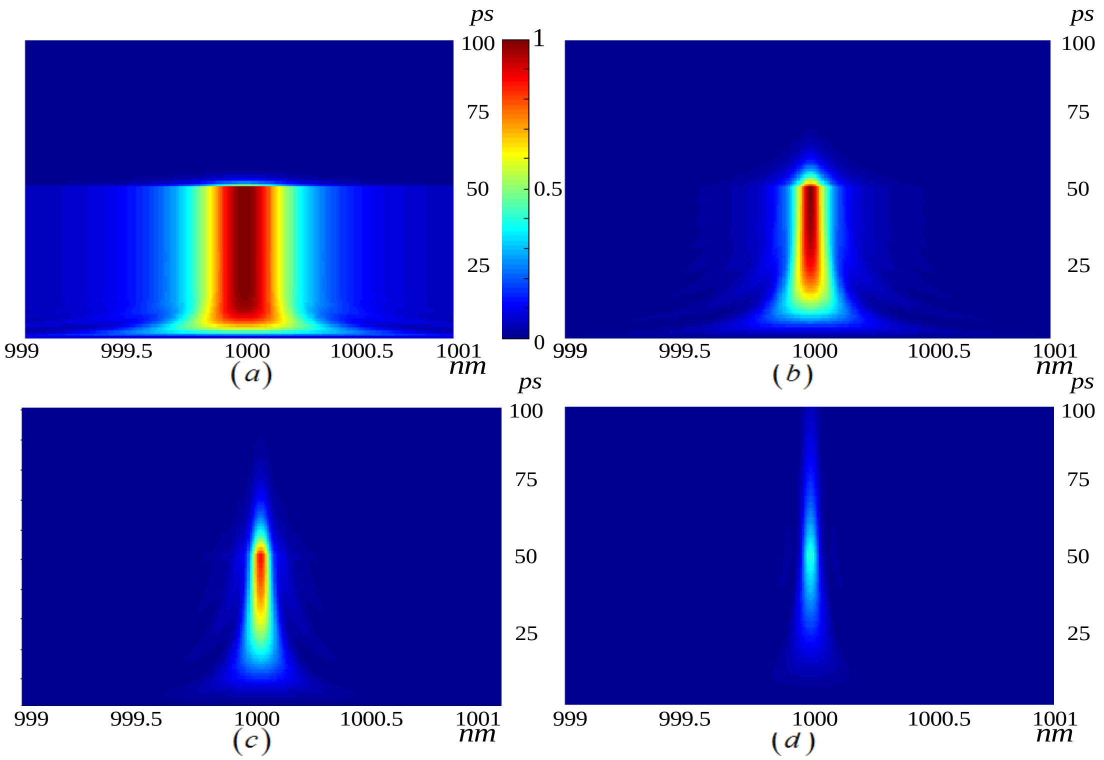

Figure B.4: Spectro-temporal response of an etalon with various coatings.
(a) R = 70%, (b) R = 90%, (c) R = 95%, (d) R = 98%.

In case of pulsed mode, the starting value *k* has to be modified with respect to the pulse duration. The evolution of $|T_n(\omega)|^2$ from 0 (single pass tramsmission) to n is the sepctro-temporal response up to n-th round trip time. After 50 ps of the example pulse, the beam begins to cut off so the earliest components have to be excluded in the tramsformation. The round trip time is 1 ps for the example thin glass layer ($n_1 = 1.5, h_1$

= 0.1mm) and the spectro-temporal responses until 100th round trip (100 ps) for the same coatings in Fig. B.3 are presented in Fig. B.4.

2.2. Multilayer system

The transient spectral response method of a single optical layer with feedback theory based impulse response can be extended to the arbitrary multilayers. As an example, we present a modeling and result for the three layer system in Fig. B.5. The example three layers were chosen to have the same thickness but different refractive indices to make different time delays per each layer.

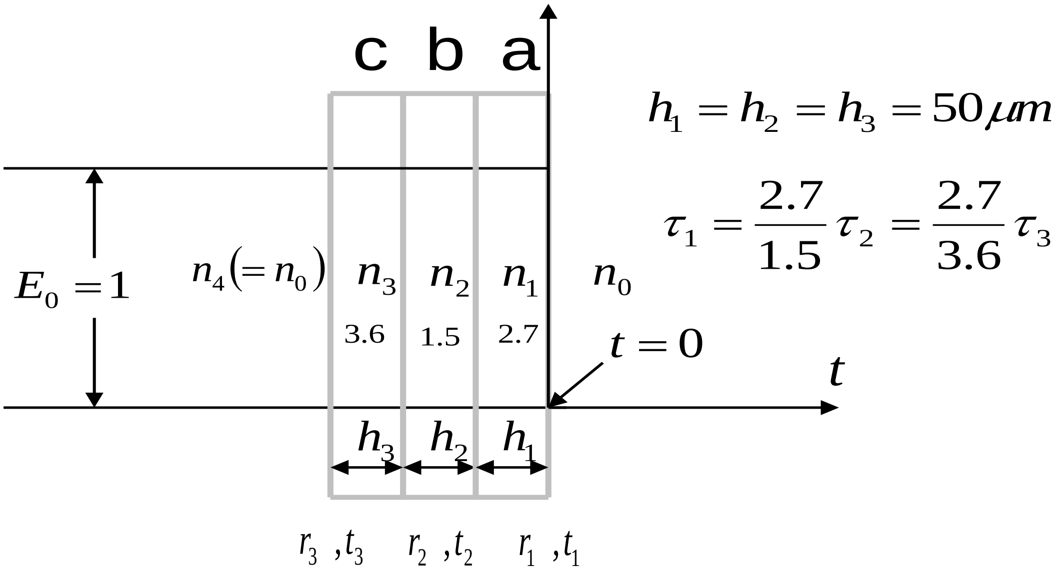

Figure B.5: Three layer system with different time delays.

Using Eq.(2), the three layer transfer function $T_1^{(3)}$ can be reformulated as Eq.(5) with a feedback loop terms.

$$T_1^{(3)} = \frac{t_4 t_3 t_2 t_1}{1 - (\text{first} + \text{second} + \text{third})\text{order feedback terms}} \qquad (5)$$

where

first order feedback terms = $-\left(r_1 r_2 e^{i\delta_1} + r_2 r_3 e^{i\delta_2} + r_3 r_4 e^{i\delta_3}\right)$

second order feedback terms = $-\left(r_1 r_3 e^{i(\delta_1+\delta_2)} + r_2 r_4 e^{i(\delta_2+\delta_3)} + r_1 r_2 r_3 r_4 e^{i(\delta_1+\delta_3)}\right)$

third order feedback terms = $-\left(r_4 r_1 e^{i(\delta_1+\delta_2+\delta_3)}\right)$

As shown in Fig. B.5, the relative delay between layers is $\tau_1=2.7\tau_2/1.5=2.7\tau_3/3.6$. These differences of time delay scale raise the biggest challenge for a discrete sampling analysis. The possible combinations of the delay differences result in the finer delays. Since each delay is discrete, there exists the smallest common discrete step determined by the various combinations of each difference.

In this case, the smallest sampling step τ_s is $\tau_1/36$. This allows each phase delay in some integer times of the finest step phase delay δ_s such as $\delta_1=9\,\delta_s$, $\delta_2=5\,\delta_s$ and $\delta_3=12\,\delta_s$. Considering the finer scaled phase term $exp(i\delta_s)$ as z^{-1}, a new expression of $T_1^{(3)}$, in terms of z, is obtained as Eq.(6).

$$T^{(3)} = \frac{A}{1-a_5 z^{-5} - a_9 z^{-9} - a_{12} z^{-12} - a_{14} z^{-14} - a_{17} z^{-17} - a_{21} z^{-21} - a_{26} z^{-26}} \quad (6)$$

where a_5= 0.11765, a_9= 0.13127, a_{12}= 0.23274, a_{14}= -0.18919,
a_{17}= -0.16149, a_{21}= -0.03055, a_{26}= 0.25969 and A= 0.67559

There are numerous computational tools to handle the standard Z transform. Here, functions in the Matlab tool are chosen for the impulse and step responses computations. The first delay component, from the single-path component referenced at $t = 0$ plane, is a round trip in layer b which is $\tau_2 = 5\tau_s$. Similarly, the second delay component is $\tau_1 = 9\tau_s$ associated with a round trip in layer a. The third delay is $2\tau_2$ with another reduction factor $r_2\, r_3$ because of one more turn in layer b. The fourth delay is $\tau_3=12\tau_s$ due to one turn in layer c. The first delay associated with the two cavities is the fifth delay $\tau_1+\tau_2$ and has a reverse phase because of $-r_2\, r_4$.

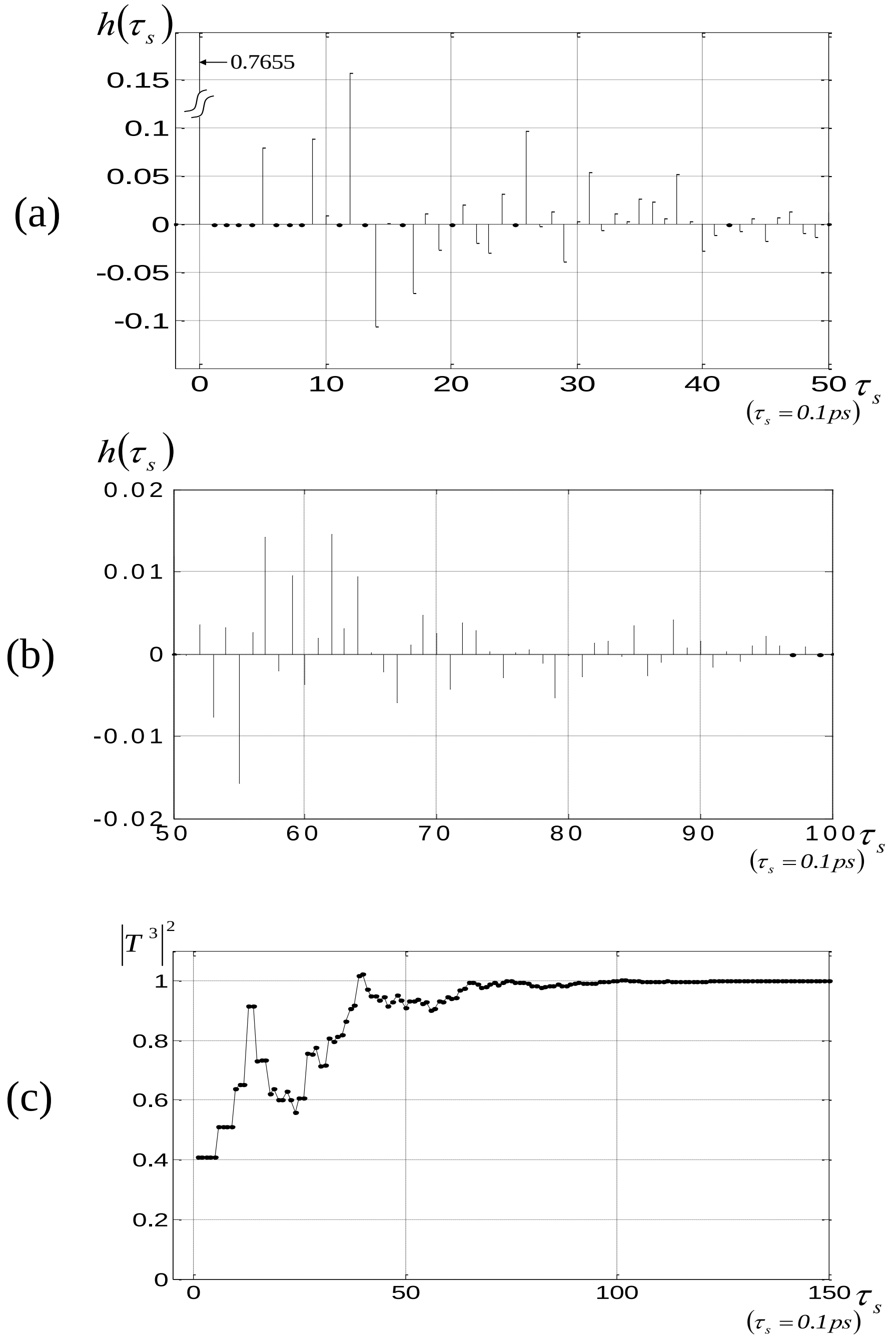

Figure B.6: Three layer system with different time delays. (a) transmission impulse response in first $50\tau_s$ window, (b) transmission impulse response in second $50\tau_s$ window, (c) transmission step response.

The impulse response naturally reveals such polarity (phase) information to the far extended delays. In Fig. B.6.(a), the 40 delay components exist in the first $50\tau_s$ window with amplitude and phase information. The next $50\tau_s$ windows are filled with generally weaker delay components with more diverse paths, with fewer empty slots (the black dots) seen in Fig. B.6.(b).

Fig. B.6.(c) shows the step response of this system. The two spikes are observed in $12\sim14\tau_s$ and $38\sim40\tau_s$ windows because two notable components that have opposite phases are in those windows. The second spike even slightly exceeds the input strength but such a transient overshoot is physically possible in such high order dynamics.

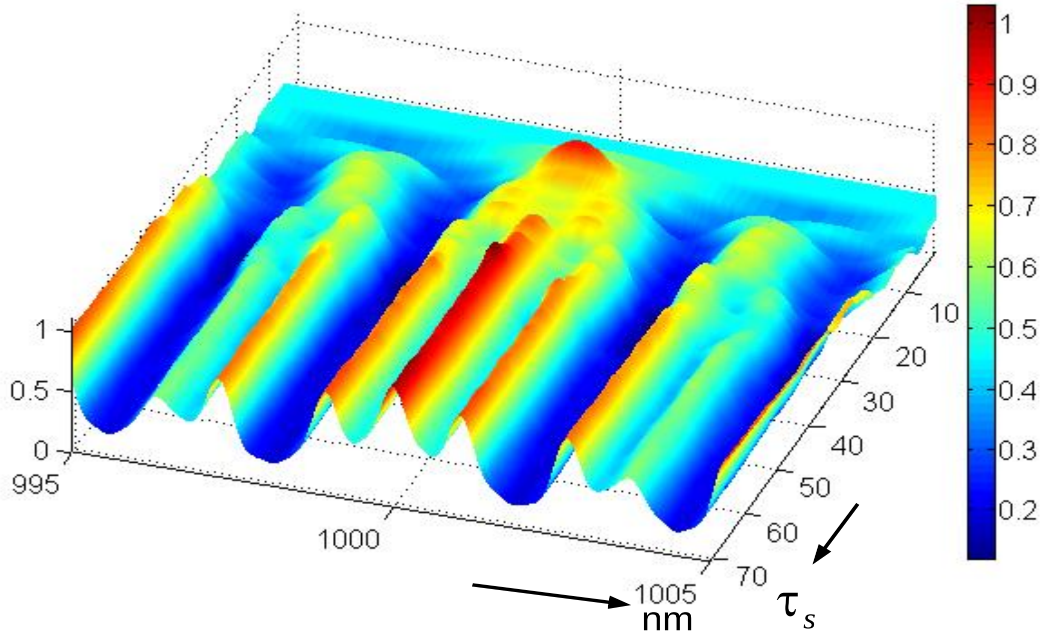

Figure B.7: Spectro-temporal response of three layer system with different time delays.

The spectro-temporal response of this three layer system is obtained by $|T^{(3)}{}_n(\omega,n)|^2$ in Fig. B.7 up to $70\tau_s$ of timing window with 10 nm of spectral span. This is $|T^{(3)}{}_k(\omega,k)|^2$ from $k=0$ to 70 and the angular frequency ω was rescaled in wavelength domain centered from the input wavelength λ_0. The cross section at the designed input resonant wavelength of 1 μm is the same as in Fig. B.6.(c). This also presents so diverse transient behaviors at other wavelengths.

4. NUMERICAL METHOD OF MULTILATER ECHO ANALYSIS

In practical applications, the reflected echoes with a pulsed ultrafast pulsed laser or Tera-hertz input beam are crucial clues to analyze the inside structures of the multilayer samples [65,66]. The echo components are basically the impulse response of a system obtained from its reflective transfer function, as covered in the previous section for the transmission case.

Here, the same three layer system is used with a new reference plane at the most left foremost boundary $t = 0$. The design wavelength of 1 μm is now deconstructive for a CW reflection case.

Table B.1: Components of first ten delays in three layer system.

order	delay (τ)	path	value
1	12	$t_4r_3t_4$	-0.280218
2	17	$t_4t_3r_2t_3t_4$	0.161470
3	22	$t_4t_3r_2(-r_3)r_2t_3t_4$	0.018996
4	24	$t_4r_3(-r_4)r_3t_4$	-0.065217
5	26	$t_4t_3t_2r_1t_2t_3t_4$	-0.238465
6	27	$t_4t_3r_2(-r_3)r_2(-r_3)r_2t_3t_4$	0.002235
7	29	$t_4r_3(-r_4)t_3r_2t_3t_4$ $+t_4t_3r_2t_3(-r_4)r_3t_4$	0.075160
8	31	$t_4t_3r_2(-r_3)t_2r_1t_2t_3t_4$ $+t_4t_3t_2r_1t_2(-r_3)r_2t_3t_4$	-0.056109
9	32	$t_4t_3r_2(-r_3)r_2(-r_3)r_2(-r_3)r_2t_3t_4$	0.000263
10	34	$t_4t_3r_2t_3(-r_4)t_3r_2t_3t_4$ $+t_4r_3(-r_4)t_3r_2(-r_3)r_2t_3t_4$ $+t_4t_3r_2(-r_3)r_2t_3(-r_4)r_3t_4$	-0.012812

The transfer function for reflection can be reformulated as Eq.(7) from the recursive Eq.(1). The transfer function for reflection has the identical denominator to that of the transmission case because reflection shares the same closed feedback loops. So, the coefficient, *a*, in the denominator are identical to Eq.(6). The complexity of the nominator originated from the multiple forward paths unlike the single forward coefficient *A* as defined as Eq.(6) in the transmission case.

$$R^{(3)} = \frac{b_0 - b_5 z^{-5} - b_9 z^{-9} - b_{12} z^{-12} - b_{14} z^{-14} - b_{17} z^{-17} - b_{21} z^{-21} - b_{26} z^{-26}}{1 - a_5 z^{-5} - a_9 z^{-9} - a_{12} z^{-12} - a_{14} z^{-14} - a_{17} z^{-17} - a_{21} z^{-21} - a_{26} z^{-26}} \qquad (7)$$

where b_0=0.56522, b_5=0.06650, b_9=0.07420, b_{12}=0.41177,
b_{14}=-0.10693, b_{17}=-0.28571, b_{21}=-0.05405, b_{26}=0.45946

The first delay *12τ_s* came after the first reflection at the *t=0* plane. The second and third delays, $17\tau_s$ and $22\tau_s$, are one and two turns of the layer b via layer c, respectively. The first 10 delay components are summarized in Table. B.1.

For higher delay orders, beams generally get smaller with longer paths and the empty delay slots are less appeared. Also, the multi-paths exist in the same time slot and the order 7 in Table. B.1 is the first case.

(a)

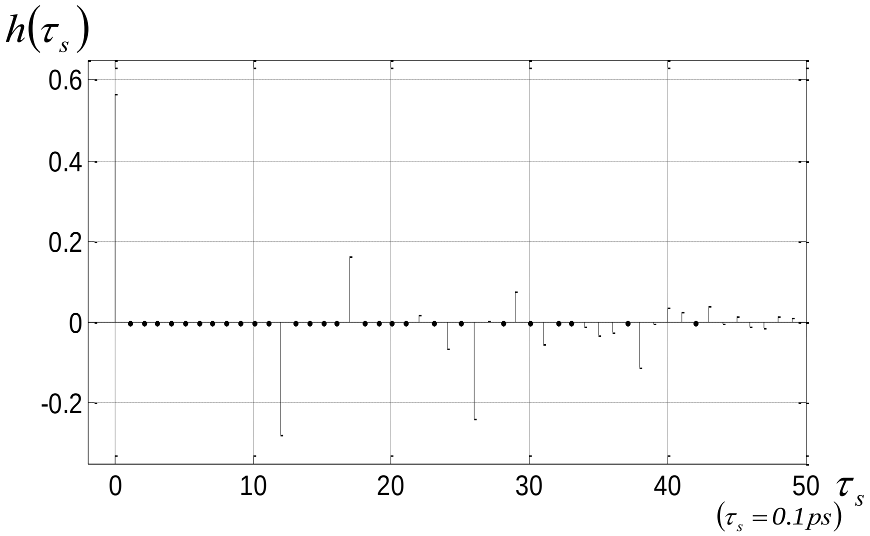

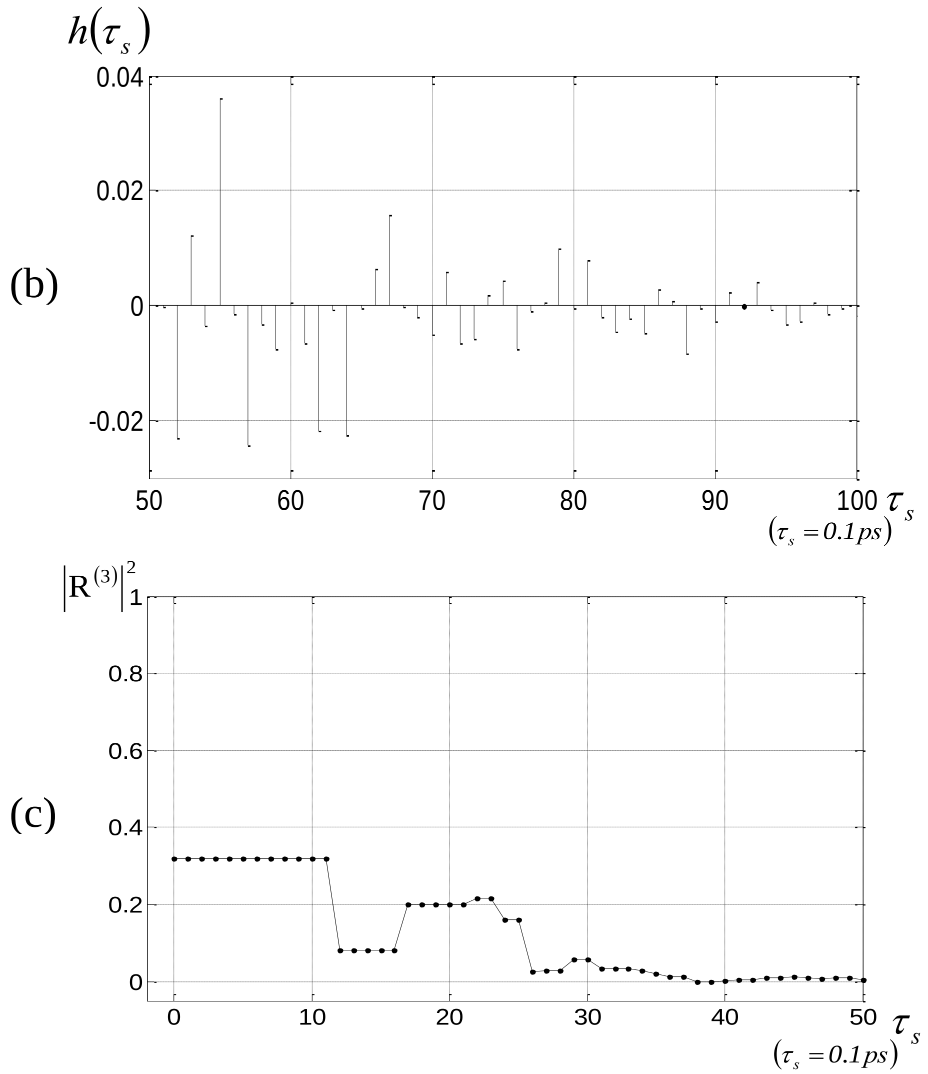

Figure B.8: The three layer system with different time delays. (a) reflection impulse response in first $50\tau_s$ window, (b) reflection impulse response in second $50\tau_s$ window, (c) reflection step response. (The black dots in (a and b) are empty or extremely tiny sampling time spot).

The frequent sign changes in the impulse response cause rapid deconstructive step responses as shown in Fig. B.8(c). Such a resonance-based steady-state value requires CW or at least quasi-CW beams and its impulse decomposition gives a clue for the CW transfer response.

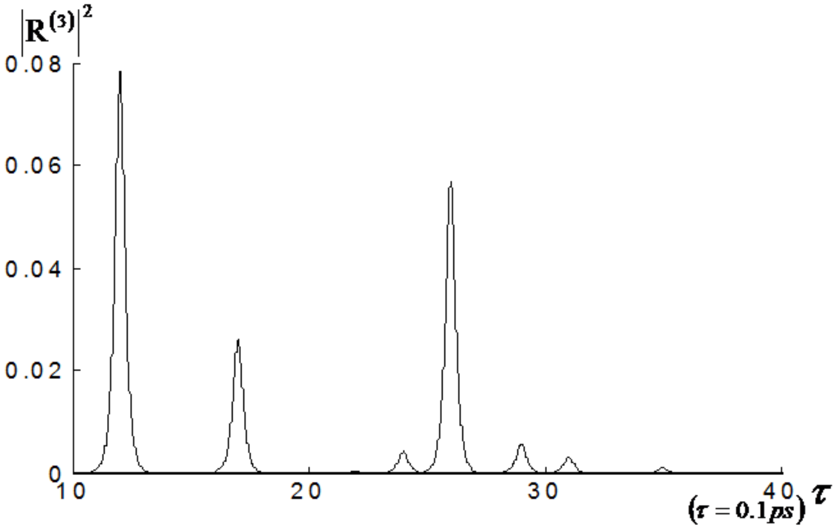

Figure B.9: Intensity echoes reflected from the three layer system.

Although the impulse response is an ideal mathematical methodology, the ultrafast optical pulses – the shortest human invented sources – is most likely the best practical source for an impulse source. With a femtosecond scale pulse, the impulse response allows to calculate the intensity echoes from the system. For example, the computed intensity echoes of the detoured pulses for a practical 50 fs secant hyperbolic pulse are in Fig. B.9. Unlike the impulse echoes, the intensity echoes do not contain phase information due to the conjugate square operation. Thus, the intensity echoes are independent of the wavelengths if refractive indices remain the same, *i.e*. no dispersion.

5. APPLICATION TO THE PRACTICAL ECHO AND SPECTRUM ANYLYSIS IN MULTILAYER

In this session, a three layer system with two same sample layers with air gap is analyzed numerically and experimentally by use of the modeling and an ultrafast laser, respectively. The multilayer system to be analyzed is in Fig. B.10. Two layers of the same $LiTaO_3$ sample are separated by a spacer.

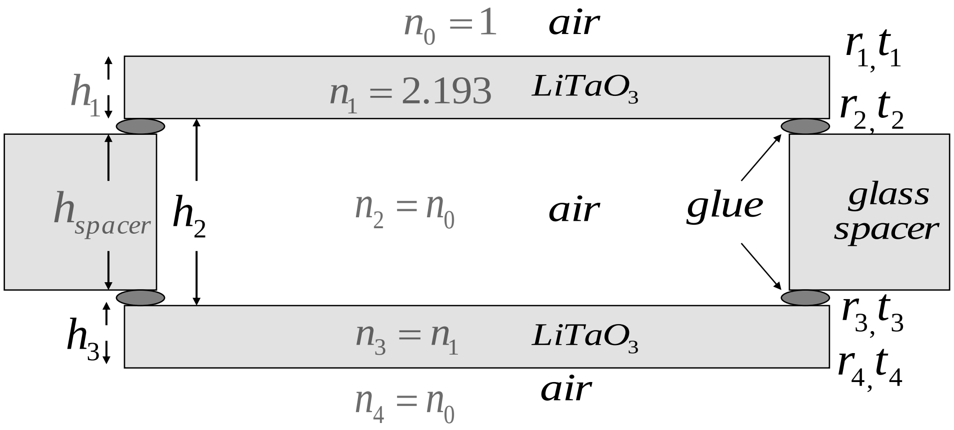

Figure B.10: The three layer system of the $LiTaO_3$.

In most of multilayer cases, the time delay based on the physical property of each layer is not the same as those of others. For instance, the thickness of the spacer h_{spacer} ~ 156 μm in the air makes a longer delay than the single layer delay τ_{rt} ~ *804 fs* in the $LiTaO_3$ samples. Such different delays make multiple paths to have different delays. As a result, a high number of micro-beams with different separations are generated.

For example, in case of the sample in Fig. B.10, the measured τ_{rt} and delay in the air gap τ_{gap} are shown in Fig. B.11(b). The sample was inserted at one of the optical path in an autocorrelator. Thus the other optical pulse acts as a trigger pulse to provide multiple correlation sequences which contain pulse separation and relative intensity strength. The τ_{gap} *~1167 fs* gives the overall gap thickness $h_2=175\ \mu m$ associated with the spacer and glue on both sides.

Taking the common sampling step τ_s to cover all the possible combinations of the delays, as described in session 2.2. For instance, because of the $\tau_{gap} \approx 1.45\tau_{rt}$ and $\tau_{gap} = 29/20\tau_{rt}$, any combinations of two delays are expressed in the unit of $1/20\tau_{rt}$. Defining the sampling delay as $\tau_s \equiv 1/20\ \tau_{rt} = 40.2\ fs$, expression of $T_1^{(3)}$ in the feedback format is in Eq.(8) in terms of $z^{-1} \equiv exp(i\delta_s)$.

$$T^{(3)} = \frac{A}{1 - a_{20}z^{-20} - a_{29}z^{-29} - a_{40}z^{-40} - a_{49}z^{-49} - a_{69}z^{-69}} \qquad (8)$$

where a_{20}= 0.29586, a_{29}= 0.14793, a_{40}= -0.021883, a_{49}= -0.29586, a_{69}= 0.14793 and A= 0.72642

The intensity of *h(t)* is presented in Fig. B.10(a). The first component without delay is referenced at the 0 delay position, so the second component with two delay paths is positioned at $20\tau_s$. The third component is due to the τ_{gap}, so it is positioned at $29\tau_s$ and the fourth one is due to three paths of $2\tau_{rt}$. The two paths of the τ_{rt} and τ_{gap} make the fifth component positioned at τ_{rt} + τ_{gap}, and so forth.

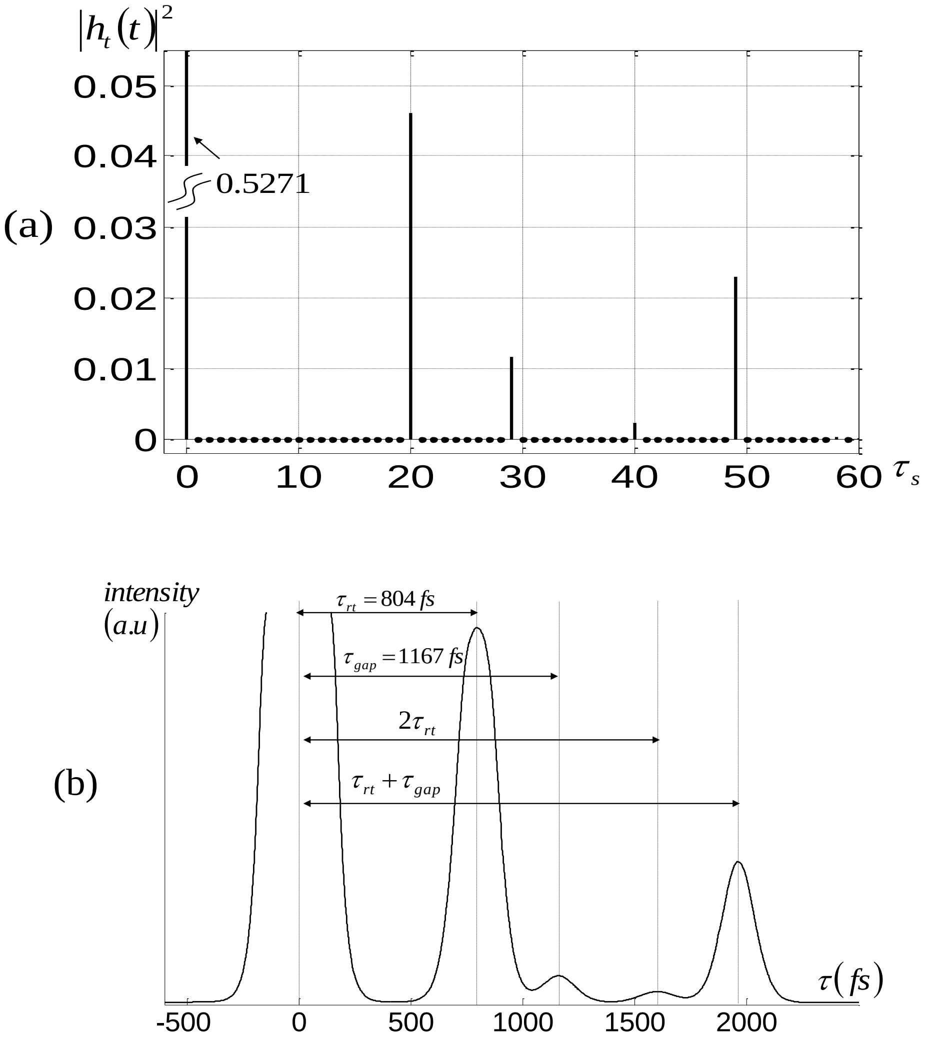

Figure B.11: The transmission pulses (a) intensity components by simulation (b) experimental components by correlations.

These multiple pulses are the origins of the spectral response and the computed spectrum for 20 nm window of a typical Ti-sapphire laser is presented in Fig. B.12.

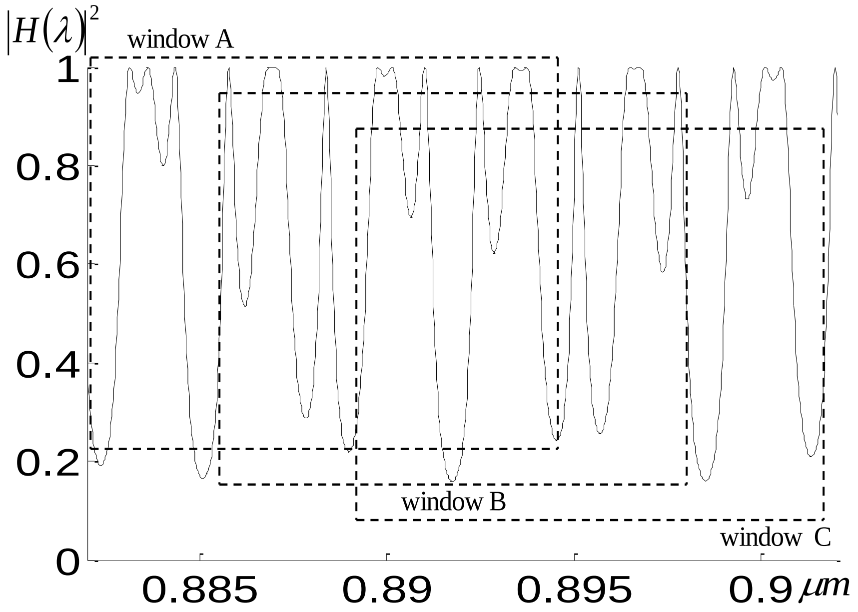

Figure B.12: The simulated spectrum of three layer system.

Since the our Ti-sapphire laser pulses have 10 nm of a finite spectral bandwidth on secant-hyperbolic envelope, we split the 20 nm band to explore into three sub-windows and observed the spectral features inside of the envelope for each window. Comparisons of the simulation with envelope consideration and experimental data for the three windows are shown in Fig. B.13.

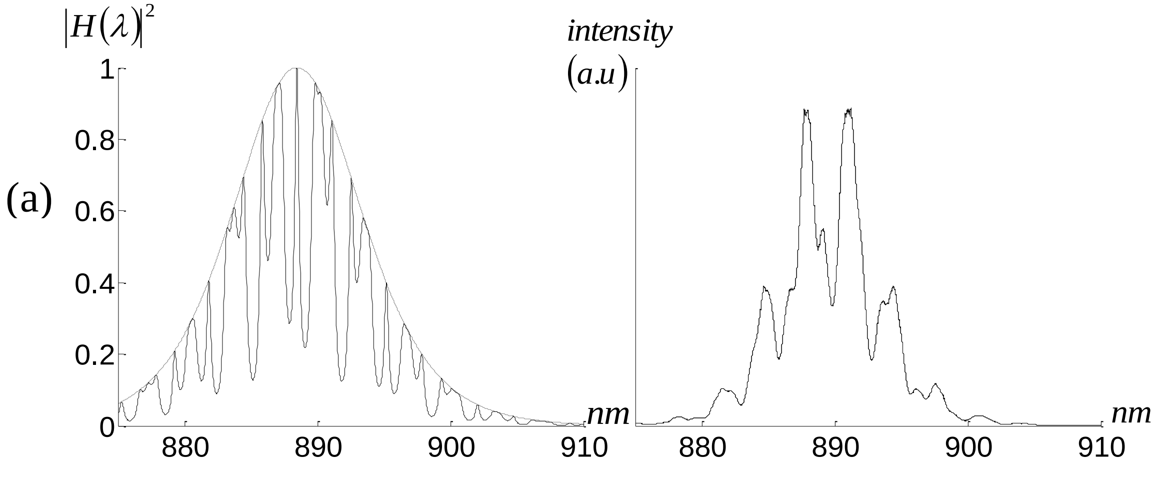

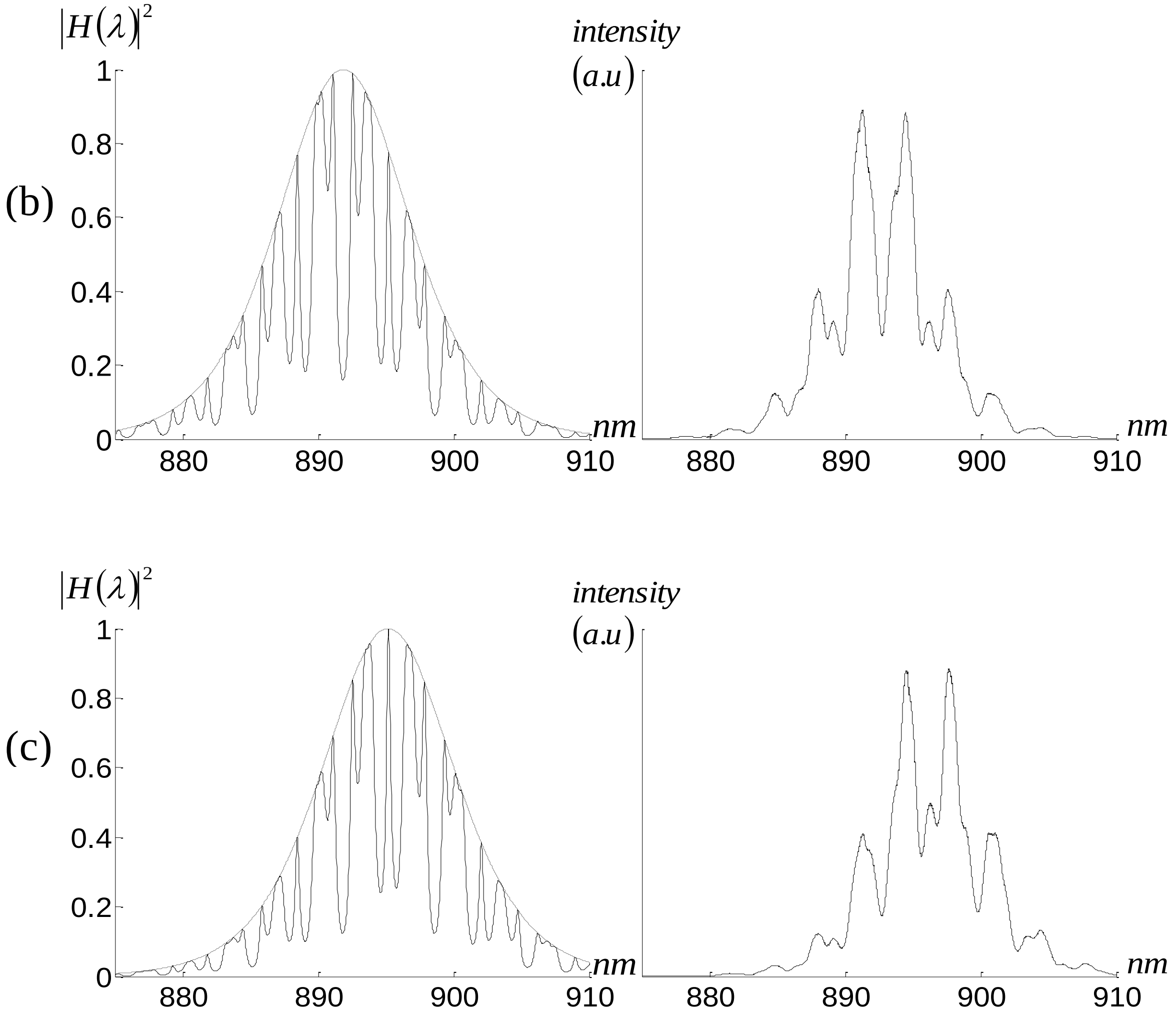

Figure B.13: The simulated spectrum vs experimental spectrum (a) window A (b) window B (c) window C.

The spectrum of this three layer system in Fig. B.13 can be read by scanning the spectral window of an ultrafast laser. Thus the actual spectrum can be extracted by compensating the envelope. Considering that the spectrum analyzer used here has a poor sub-nm resolution, the fine spectral features are not as fully observed as those of the wide parts. Although a ~1 nm offset is also observed by spectrum analyzer calibration offset, the experimental data basically shows the expected spectral patterns, because the data have the same relative mode spacing and arrays of fine and course patterns as well as depth of modulations.

Although the spectrum based on quasi-impulse response is not from the temporal interferometric resonances such as CW spectrum, because each pulse is separated from its neighbor, it has the same spectrum as the CW case. This method makes it possible to obtain the real time measurements of spectral responses, none the less, without the need for a tunable CW laser. Moreover, the faster pulsed input will increase the quality of quasi-impulse behavior as well as the wider spectral coverage.

Appendix C[1]

Compact Mobile RFID Antenna Design

1. INTRODUCTION

Radio-frequency identification (RFID) plays a major role in ubiquitous sensor networks because of its ability to input and output data wirelessly. Active circuitry, one of the main RFID components, is being integrated to minimize the size of the sensor technology, where the dimensions of the antenna are determined by the wavelength of its operating frequency. Much research on minimizing the size of antennas for RFID tags has been done, but research on antennas of RFID readers hasn’t been as active [67].

In the design of antennas for mobile handsets, size reduction is often more important than gain or radiation pattern. Usually it is difficult to match small antennas, even if lumped elements are employed, because small antennas such as a short dipole or a small loop are quite reactive. We present the design of and experimental results on small planar loop antennas for applications in mobile RFID readers in the Ultra-high frequency band (UHF, 860~960 MHz). A small loop antenna has been realized by bending a folded-dipole, providing the advantage that the structure can increase the antenna input resistance. A capacitive load is created inside the loop antenna through a parasitic patch formed in the center of the antenna, lowering the resonance frequency and increasing the electrical length of the structure. The current distribution of the antenna is the same as a loop antenna, and its radiation patterns are omni-directional. The proposed antenna, a small, planar, circular loop antenna in a given perimeter of $\sim\lambda_0/(2\pi)$ at 910 MHz (the center of the UHF band), is easy to tune and it can be formed in various shapes [68].

---

[1] Appendix C was provided by Prof. Jeong-Jin Kang.

In addition to RFID-antenna design, we have also investigated novel means of antenna characterization. Antennas are primarily evaluated by their radiation performance. Since in many practical applications one is only interested in radiation effects where the distance from the antenna to the observer is very much greater than the largest dimension of the transmitting antenna, a relative-distance-insensitive angular-radiation distribution (far-field) is usually considered as an antenna pattern. In the far-field, electric and magnetic fields propagate as an electromagnetic wave and are generally orthogonal to each other and to the direction of propagation. The fields are uniquely related to each other via free-space impedance and decay as $1/r$.

For antennas whose sizes are comparable to the wavelengths used in UHF RFID, the approximate boundary between the far field and the near field region is commonly given as $r = 2D^2/\lambda$, where D is the maximum antenna dimension. In contrast to a far-field pattern, the near field components have different angular and radial dependence (*e.g.*, $1/r^3$) [69], and the near-field is not typically considered to be farther away than a few wavelengths from the antenna. Hence, the near-field should not be neglected in the case of RFID analysis because most of the tapping range is within one wavelength (30 cm for 1 GHz) of the tag.

2. ANTENNA DESIGN AND FABRICATION

This section considers a few simple attachable antennas that are suitable for minimization. It also explains a way of adjusting input impedance and reactance.

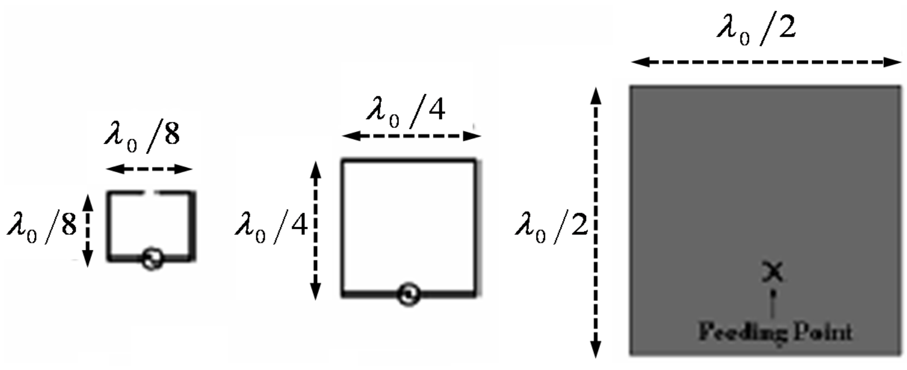

(a) (b) (c)

Figure C.3: Planar Antennas (a) dipole (b) loop (c) patch.

Fig. C.1 shows three types of antennas that could be built in a plane: a dipole, a loop, and a patch antenna. The resonant frequency of each antenna relies on its dimensions. The electric length of a dipole antenna becomes short when the wavelength is twice as long as the length of the antenna. The same thing happens when the wavelength is as long as the length of a loop antenna. A patch antenna's dielectric constant often decides the resonant frequency of the antenna, but most of the time, when the length of the antenna is as long as a half wavelength, it resonates. So it is ideal to use a dipole antenna which has the smallest size among these.

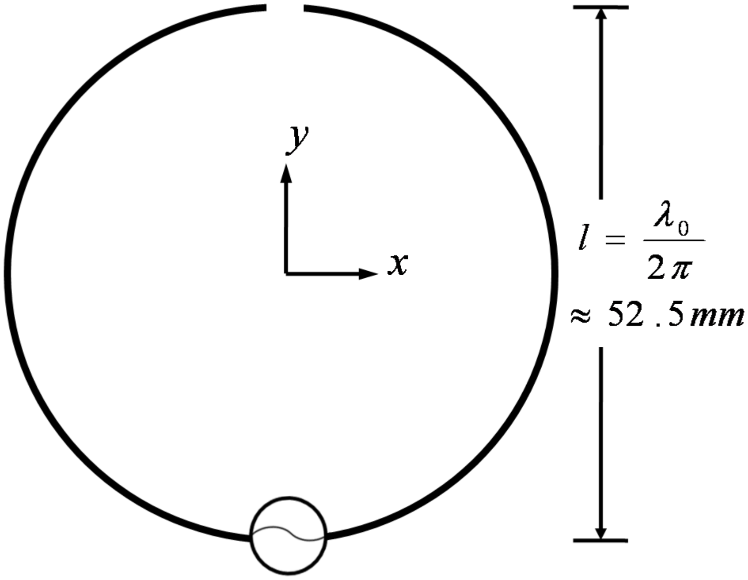

Figure C.4: Dimensions of a circular dipole antenna.

The proposed antenna design is basically a conventional $\lambda_0/2$ dipole antenna that is transformed to a circular structure so it is capable of being minimized. Fig. C.2 shows the dimensions of an antenna to be manufactured with its resonant frequency at 910 MHz. It has a total circular electrical length of $\lambda_0/2$ with a perimeter l ($=\lambda_0/(2\pi)$) at 910 MHz. The dimensions of this design are close to those of a dipole antenna shown in Fig. C.1(a), and it has a structure that is capable of being reduced.

In the case of simple, folded dipoles, the impedance is generally mismatched throughout the operating band. Hence, a method to improve the impedance match and reduce the incident power dissipation, which increases the effective bandwidth, is required. There is a way to adjust the input impedance of a planar dipole antenna which adopts a basic structure of a folded dipole antenna. We employ the T-match topology shown in Fig. C.3(a). The T-match can be decomposed into two different modes: the *antenna mode,* and the *transmission line mode*. The input impedance of an antenna can be calculated from analyzing currents flowing in both of the modes.

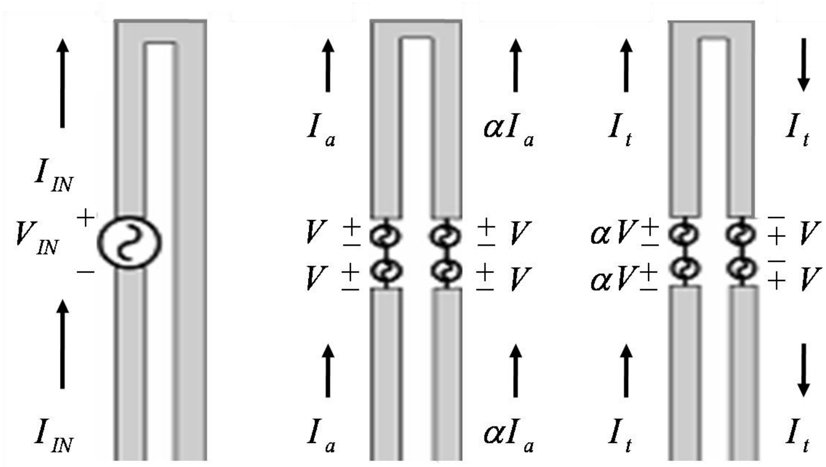

(a) (b) (c)

Figure C.3: Folded dipole antenna (a) antenna mode (b) transmission line mode (I_a) (c) transmission line mode (I_t).

The currents of the antenna mode and the transmission line mode are expressed as Eqs. (1-a) and (1-b), respectively.

$$I_a(1+\alpha) = \frac{2V}{Z_a} \qquad (1-a)$$

$$I_t = \frac{V(1+\alpha)}{Z_t} \qquad (1-b)$$

The sum of the input voltages and currents are calculated by superposition and the input impedance is expressed in Eq. (2). The equivalent circuit is shown in Fig. C.4 [70].

$$Z_{IN} = \frac{V_{IN}}{I_{IN}} = \frac{2V(1+\alpha)}{I_t + I_a} = \frac{2(1+\alpha)^2 Z_t Z_a}{2Z_t + (1+\alpha)^2 Z_a} \qquad (2)$$

If the total length of a folded-dipole antenna is close to a half wavelength, then $Z_t = j\infty$, and the input impedance is expressed as (3) [71].

$$Z_{IN} \cong (1+\alpha)^2 Z_a \qquad (3)$$

The term $(1+\alpha)^2$ plays an important role in increasing the input impedance, which may be increased up to 50 Ω by adjusting the distance between two dipole antennas.

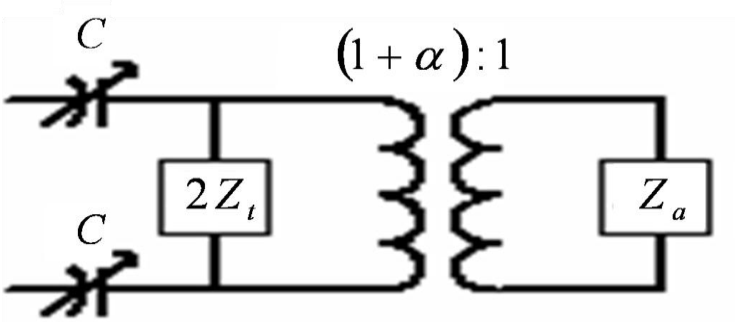

Figure C.4: Equivalent circuit of a folded-dipole antenna.

Based on this topology, the input impedance has been noticeably increased. When a dipole antenna and a folded dipole antenna are tested under the same conditions, the higher input impedance (> *50* Ω) of the folded dipole antenna traces into the middle of the Smith chart, and the resonant frequency occurs near there. Here, the implanting of an additional device was investigated to control the resonant frequency of the antenna for further optimization.

Applying capacitive loading to an antenna is one of many ways to control its resonant frequency. An antenna gains extra electrical length and increased resistance against reflection of waves through the addition of a disk-shaped capacitor-plate [68,72]. This forms capacitive loading inside of the antenna and reduces the resonant frequency by providing extra electrical length. The capacitive load is mounted on the antenna by plating metal traces with an open-circuit gap. This is the complete proposed dipole antenna, and its full manufactured dimensions were presented previously in chapter 4 (Fig. 4.9).

The resonant frequency of the antenna is measured to be ~910 MHz, which is in the middle of the UHF band for RFID. The resonance frequency could be tuned by manipulating the electrical length of the capacitive load and the size of the parasitic patch on the other side of the substrate. The matching quality was observed to be good, giving ~22 dB return loss at the resonance frequency as previously shown in chapter 4 (Fig. 4.10).

BIBLIOGRAPHY

[1] K. Yang, G. David, S. Robertson, J.F. Whitaker, and L.P.B. Katehi, “Electro-optic Mapping of Near-field Distributions in Integrated Microwave Circuits,” *IEEE Trans. Microwave Theory Tech.*, vol. 46, pp. 2338-2343, Dec. 1998.

[2] K. Yang, J.G. Yook, L.P.B. Katehi, and J.F. Whitaker, “Electrooptic Mapping and Finite-Element Modeling of the Near –Field Pattern of a Microstrip Patch Antenna,” *IEEE Trans. Microwave Theory Tech.*, vol. 48, pp. 228-294, Feb. 2000.

[3] H. Togo, N. Shimizu, and T. Nagatsuma, “Near-Field Mapping System Using Fiber-Based Electro-Optic Probe for Specific Absorption Rate Measurement,” *IEICE Trans. Electron.*, vol. E90–C, pp. 436-442, Feb. 2007.

[4] E.M. Godshalk, “Characterization of surface mount packages at microwave frequencies using wafer probes,” *IEEE MTT-S International Microwave Symposium Digest*, pp. 1887-1890, Jun. 2000.

[5] A.G. Yaghjian, “An Overview of Near-Field Antenna Measurements,” *IEEE Trans. Antennas Propagat.*, vol. AP-34, pp. 30-45, Jan. 1986.

[6] J.A. Valdmanis and G.A. Mourou, “Subpicosecond electro-optic sampling: Principles and applications,” *IEEE J. Quantum Electron.*, vol. 22, pp. 69-78, 1986.

[7] J.A. Valdmanis, “1 THz-bandwidth prober for high speed devices and intergrated circuits,” *Electro. Lett.*, vol. 23, pp. 1308-1310, Nov. 1987.

[8] B.H. Kolner and D.M. Bloom, “Direct electro-optic sampling transmission line signals propagating on a GaAs substrate,” *Electron. Lett.*, vol. 20, pp. 818-819, 1984.

[9] K. Yang, T. Marshall, M. Forman, J. Hubert, L. Mirth, Z. Popovic´, L.P.B. Katehi, and J.F. Whitaker, “Active-Amplifier-Array Diagnostics Using High-Resolution Electrooptic Field Mapping,” *IEEE Trans. Microwave Theory Tech.*, vol. 49, pp. 849-857, May. 2001.

[10] J. A. Deibel, “A Study of Nonlinear Optical Polymers for Use in Ultrafast Electro-Optic Sampling Measurements” Ph.D thesis, Univ. of Michigan, 2004.

[11] M. Lee, H.E. Katz, C. E. Douglas, M. Gill, P. Gopalan, J.D. Heber, and D.J. McGee, “Broadband modulation of light by using an electro-optic polymer,” *Science*, vol. 298, pp. 1401-1403, Nov. 2002.

[12] J.A. Valdmanis, “Electro-optic measurement techniques for picosecond materials, devices, and integrated circuits,” *Semiconductors and Semimetals.*, vol. 25, pp. 52-54, Jan. 2000.

[13] K. Yang, “Application of Ultrafast Optical Techniques to the Characterization of mm-Wave Integrated Circuits and Radiating Structures,” PhD thesis, Univ. of Michigan, 2001.

[14] K. Yang, L. P. B. Katehi, and J. F. Whitaker, “Electro-optic field mapping system utilizing external gallium arsenide probes,” *Appl. Phys. Lett.*, vol. 77, pp 486-488, Jul. 2000.

[15] L. Duvillaret, S. Rialland, and J.L. Coutaz, “Electro-optic sensors for electric-field measurements. i. theoretical comparison among different modulation techniques,” *J. Opt. Soc. Am. B.*, vol. 19, pp. 2692-2703, Nov. 2002.

[16] L. Duvillaret, S. Rialland, and J.L. Coutaz, “Electro-optic sensors for electric-field measurements. ii. choice of the crystals and complete optimization of their orientation,” *J. Opt. Soc. Am. B.*, vol.19, pp. 2704-2715, Nov. 2002.

[17] R. M. Reano, J.F. Whitaker, and L.P.B. Katehi, “Vector-component isolation of an arbitrary modulating electric field in zincblende electro-optic probes,” *J. Opt. Soc. Am. B* vol. 22, pp. 1719-1722, Aug. 2005.

[18] Z. Jiang, and X.-C. Zhang, “Terahertz imaging via electrooptic effect,” *IEEE Trans. Microwave Theory Tech.*, vol.47, pp. 2644-2650, Dec, 1999.

[19] K. J. Weingarten, M.J.W. Rodwell, and D. M. Bloom, “Picosecond optical sampling of GaAs integrated circuits,” *IEEE J. Quantum Electron*., vol. 24, pp. 198-220, Feb. 1988.

[20] K. Yang, G. David, J.G. Yook, I. Papapolymerou, L.P.B. Katehi, and J.F. Whitaker, “Electro-optic mapping and finite-element modeling of the near-field pattern of microstrip patch antenna,” *IEEE Trans. Microwave Theory Tech.*, vol. 48, pp. 288-294, Feb. 2000.

[21] K. Yang, L. P. B. Katehi, and J. F. Whitaker, “Electric field mapping system using an optical-fiber-based electro optic probe.” *IEEE Microw. Wireless Compon. Lett*., vol.11, pp. 164-166, Apr. 2001.

[22] D.J. Lee, and J. F. Whitaker, “Simplified Electro-Optic Probing Utilizing the Fabry-Perot Effect,” *IEEE Lasers and Electro-Optics Society (LEOS)*, pp. 116-117, Oct 2007.

[23] D.J. Lee, and J. F. Whitaker, “A Simplified Fabry–Pérot Electrooptic-Modulation Sensor,” *IEEE Phot. Tech. Lett*., vol. 20, pp. 866-868, May 2008.

[24] D.J. Lee, M.H. Crites, and J.F. Whitaker, “Electro-Optic Probing of Microwave Fields Using a Wavelength-Tunable Modulation Depth,” *IOP Meas. Sci. Tech*., vol. 19, pp. 115301-115310, Sep. 2008.

[25] J.J. Kang, D.J. Lee, C.C. Chen, J.F. Whitaker, and E.J. Rothwell, “Compact Mobile RFID Antenna Design and Analysis Using Photonic-assisted Vector Near-field Characterization,” *IEEE International Conference on RFID*, pp. 81-88, Apr. 2008.

[26] D.J. Lee, J.J. Kang, C.C. Chen, and J. F. Whitaker, “Vector Near-Field Measurement System Using an Electro-Optic Microcavity and Electrical Down-conversion,” *IEEE MTT-S International Microwave Symposium Digest*, pp. 1589-1592, Jun. 2008.

[27] J.J. Kang, D.J. Lee, J.F. Whitaker, and E.J. Rothwell, “Mobile RFID antenna design and near field characterization using an electro-optic field mapping system,” *Proc. of the Institute of Webcasting, Internet Television and Telecommunication (IWIT),* vol.5, pp. 91-95, Dec. 2007.

[28] D.J. Lee, J.J. Kang, and J.F. Whitaker, “Vector Near-Field Measurements Using Optimized Electrical and Photonic Down-Conversion,” *IEEE Trans. Microwave Theory Tech.*, vol. 56, pp. 3231-3238, Dec. 2008.

[29] D.J. Lee, and J.F. Whitaker, “Optimization of Electro-Optic Sideband Modulation in Optical-Heterodyne-Down-Mixed Sensing of Microwave-Fields,” *submitted to Applied Optics,* Nov. 2008.

[30] D.J. Lee, and J.F. Whitaker, “Bandwidth Enhancement of Electro-Optic Field Sensing Using Photonic Down-Mixing with Harmonic Sidebands,” *Opt. Express*, vol. 16, pp. 14771-14779, Sep. 2008.

[31] D.J. Lee, and J.F. Whitaker, “An optical-fiber-scale electro-optic probe for minimally invasive high frequency sensing,” *Opt. Express*, vol. 16, pp. 21587–21597, Dec. 2008.

[32] A.Yariv, and P.Yeh, *Optical Waves in Crystals*. Ch.8. John Wiley and Sons.1984.

[33] A. J. Vickers, R. Tesser, R. Dudley, and M. A. Hassan, “Fabry-Perot enhancement electro-optic sampling,” *Opt. Quantum Electron.*, vol. 29, pp. 661-669, Mar.1997.

[34] P. O. Mueller, S. B. Alleston, A. J. Vickers, and D. Erasme, “An External Electrooptic Sampling Technique Based on the Fabry–Perot Effect,” *IEEE J. Quantum Electron.*, vol. 35, pp. 7-11, Jan. 1999.

[35] S. Wakana, T. Ohara, M. Abe, E. Yamazaki, M. Kishi, and M. Tsuchiya, “Fiber-Edge Electrooptic/Magnetooptic Probe for Spectral-Domain Analysis of Electromagnetic Field,” *IEEE Trans. Microwave Theory Tech.*, vol. 48, pp. 2611-2616, Dec. 2000.

[36] O. Mitrofanov, A. Gasparyan, L.N. Pfeiffer, and K. W. West, “Electro-optic effect in an unbalanced AlGaAs/GaAs microresonator,” *Appl. Phys. Lett.*, vol. 86, pp. 202103-1-3, May. 2005.

[37] K.Sasagawa, and M. Tsuchiya, “An Electrooptic Sensor with Sub-millivolt Sensitivity Using a Nonlinear Optical Disk Resonator,” *Microwave Phot.* vol.12, pp. 355-358, Oct. 2005.

[38] S. M. Chandani, “A Fiber-Based Probe for Electrooptic Sampling,” *IEEE Phot. Tech. Lett.*, vol. 18, pp. 1290-1292, Jun. 2006.

[39] D. Le Quang, D. Erasme, and B. Huyart, “Fabry–Perot enhanced real-time electro-optic probing of MMICs,” *Electron. Lett*., vol. 29, pp. 498–499, 1993.

[40] O. Mitrofanov, “Laser excess noise reduction in optical phase-shift measurements,” *Appl. Opt.*, vol. 42, pp. 2527-2531, May 2003.

[41] S. Mitani, E. Yamazaki. M. Kishi, and M. Tsuchiya, “EDFA-enhanced sensitivity of RF magneto-optical probe,” *International Topical Meeting on Microwave Photonics*, pp. 255-258, Sep. 2003.

[42] K. Sasagawa and M. Tsuchiya, “Modulation depth enhancement for highly sensitive electro-optic RF near-field measurement,” *Electron. Lett.*, vol. 42, pp. 1357-1358, Nov. 2006.

[43] D.J. Lee, and J.F. Whitaker, “Analysis of Optical and Terahertz Multilayer Systems Using Microwave and Feedback Theory,” *Micro. and Opt. Tech. Lett*., scheduled to be published, May. 2009.

[44] W. K. Kuo, C. H. Pai, and S. L. Huang, Tech Dig. *4th Pacific Rim Conf. on Lasers and Electro-Optics*, pp. 474-475, 2001.

[45] K. Sasagawa, M. Tsuchiya, and M. Izutsu, “Electrooptic probing based on photonic downconversion,” *Eighth Int. Symp. Contemporary Photon. Tech. Dig.,* pp. 29-30, Jan. 2005.

[46] D.J. Lee, and J.F. Whitaker, “A method for Spectro-temporal and echo responses of arbitrary optical multilayer systems,” *to be submitted* (*J. Opt. Soc. Am. B*), Jan. 2009.

[47] K. Sasagawa, M. Tsuchiya, and M. Izutsu, “Sensitivity Eenhancement of Electrooptic Probing Based on Photonic Downconversion by Sideband Management,” *Conference on Lasers and Electro-Optics (CLEO)*, pp. 1185-1187, May 2005.

[48] S. Wakana, E. Yamazaki, S. Mitani, H. Park, M. Iwanami, S. Hoshino, M. Kishi, M. Tshuchiya, “Performance evaluation of fiber-edge magnetooptic probe,” *J. Lightwave Technol.* vol. 21, pp. 3292-3299, Dec. 2003.

[49] K. Sasagawa, A Kanno, T. Kawanishi, and M. Tsuchiya, “Live Electrooptic Imaging System Based on Ultraparallel Photonic Heterodyne for Microwave Near-Fields,” *IEEE Trans. Microwave Theory Tech.* vol.55, pp. 2782-2791, Dec. 2007.

[50] B. H. Kolner and D. W. Dolfi, “Intermodulation distortion and compression in an integrated electrooptic modulator,” *Appl. Opt.* vol.26, pp. 3676-3680, Sp. 1987.

[51] B. Masella and X. Zhang, “Linearized optical single sideband Mach-Zehnder electro-optic modulator for radio over fiber systems,” *Opt. Express.*, vol. 16, pp. 9181-9190, Jun. 2008.

[52] J. L. Casson, K. T. Gahagan, D. A. Scrymgeour, R. K. Jain, J. M. Robinson, V. Gopalan and R. K. Sander, “Electro-optic coefficients of lithium tantalite at near-infrared wavelengths,” *J. Opt. Soc. Am. B,* vol. 21, pp. 1948-1952, Nov. 2004.

[53] J.A. Deibel, and J. F. Whitaker, “A fiber-mounted polymer electro-optic-sampling field sensor,” *IEEE Lasers and Electro-Optics Society (LEOS)*, pp. 786-787, 2003.

[54] R. Guenther, *Modern Optics,* Chap.3, John Wiley & Sons, 1990.

[55] L. Young, “Synthesis of Multiple Antireflection Films over a Prescribed Frequency Band,” *J. Opt. Soc. Am*., vol. 51, pp. 967-974, Sep. 1961.

[56] L. Young and E. G. Cristal, “Low~Pass and High~Pass Filters Consisting of Multilayer Dielectric Stacks,” *IEEE Trans. Microwave Theory & Tech*., vol. 48, pp. 75-80, Feb. 1966.

[57] P. Baumeister, “Application of microwave technology to design an optical multilayer bandpass filter,” *Appl. Opt*., vol. 42, pp. 2407-2414, May 2003.

[58] S. J. Mason, “Feedback theory—some properties of signal flow graphs,”’ Proc. IRE, vol 41, pp. 1144–1156, 1953; vol. 44, pp. 920–926, Jul. 1956.

[59] G. Gonzalez, *Microwave Transistor Amplifiers Analysis and Design*, Ch.2, Prentice Hall, New Jersey, 1997.

[60] M. H. Dunn, “Use of Flow Graphs in the Analysis of Optical Cavities,” *Appl. Opt*. vol 10, pp. 1393-1397, Jun. 1971.

[61] D. Minkov, “Flow-graph Approach for Optical Analysis of Planar Structures,” *Appl. Opt*. vol. 33, pp. 7698-7703, Nov. 1994.

[62] J. H. Apfel, “Graphics in optical coating design,” *Appl. Opt.*, vol. 11, pp. 1303-1312, Jun. 1972.

[63] W. J. Wild and H. Buhay, “Thin-film multilayer design optimization using a Monte Carlo approach,” *Opt. Lett*., vol. 11, pp. 745-747, Nov. 1986.

[64] F. Rutz, M. Koch, L. Micele, and G. de Portu, “Ceramic dielectric mirrors for the terahertz range,” *Appl. Opt*., vol. 45, pp. 8070-8073, Nov. 2006.

[65] J.B. Jackson, M. Mourou, J.F. Whitaker, I.N. Duling III, S.L. Williamson, M. Menu, and G.A. Mourou, “Terahertz imaging for non-destructive evaluation of mural paintings,” Opt. Comm., vol. 281, pp. 527-532, Nov. 2007.

[66] C.C. Chen, D.J. Lee, and J.F. Whitaker, "Terahertz Characterization of Interfacial Oxide Layers and Voids for Health Monitoring of Ceramic Coatings," *submitted to Conference on Lasers and Electro-Optics (CLEO)*, Dec. 2008.

[67] B.T. Yoon, et al., "Cognition Distance of Mobile RFID," *Korea Electomagnetic Engineering Society*, vol. 16, pp. 61-65, Jul. 2007.

[68] J.J. Kang, Y.T. Lim, W.S. Park, B.M. Kang, and E.J. Rothwell "Folded Dipole Loop Antenna of Mobile RFID Reader for USN," *Proceedings of the International Conference on Ubiquitous Convergence Technology (ICUCT) 2007 of IEEK*, pp. 55-59, Nov. 2007.

[69] P. V. Nikitin, K. V. S. Rao, and S. Lazar, "An Overview of Near Field UHF RFID," *IEEE International Conference on RFID*, pp. 167-174, Mar. 2007.

[70] H. K. Schuman, "Modeling Folded Dipoles and Feedlines for Radiation and Scattering," *IEEE Trans. Antennas Propagat.*, vol. 38, pp. 30-39, Jan. 1990.

[71] R.W. Lampe, "Design Formuas for an Asymmetric Coplanar Strip Folded Dipole," *IEEE Trans. Antennas Propagat.*, vol. AP-33, pp. 1028-1031, Sep. 1985.

[72] I.M. Park, H.S. Chu, and C.H. Cho, "Design of Electrically minimized Antenna," *Korea Electomagnetic Engineering Society*, vol. 16, pp. 13-21, Apr. 2005.